Quantum nonadiabatic dynamics of clusters and molecules

A Thesis submitted for the degree of
Doctor of Philosophy

By
Rajagopala Reddy Seelam

School of Chemistry
University of Hyderabad
Hyderabad 500046
India

December 2013

Statement

I hereby declare that the matter embodied in this thesis is the result of investigations carried out by me in the School of Chemistry, University of Hyderabad, Hyderabad, under the supervision of Prof. Susanta Mahapatra.

In keeping with the general practice of reporting scientific observations, due acknowledgment has been made whenever the work described is based on the findings of other investigators.

(Rajagopala Reddy Seelam)

December 2013
Hyderabad-500046

Certificate

Certified that the work embodied in this thesis entitled "Quantum nonadiabatic dynamics of clusters and molecules" has been carried out by Mr. Rajagopala Reddy Seelam under my supervision and the same has not been submitted elsewhere for a degree.

December 2013
Hyderabad-500046

(Prof. Susanta Mahapatra)
Thesis supervisor

Dean
School of Chemistry
Prof. C. R. Rao Road
University of Hyderabad
Hyderabad-500046, India

Acknowledgments

I would like to express my deep sense of gratitude to **Prof. Susanta Mahapatra** for his excellent guidance and constant encouragement throughout my research work and introducing me to this fascinating field of vibronic coupling. I admire his vast knowledge and skill in theoretical chemistry and I thank him for the discussions and assistance in writing manuscripts. The experience that I gained in the last five years through his suggestions, comments and even critiques will help me in all my future endeavors.

I would like to thank Prof. M. Durga Prasad, Prof. M. V. Rajasekharan and Prof. T. P. Radhakrishnan for their lectures on Quantum chemistry, Molecular spectroscopy and Mathematics. I wish to thank Prof. K. C. Kumara Swamy for financial support over six months. I thank Prof. G. N. Patwari, School of Chemistry, IIT Bombay, for fruitful discussions on a joint collaborative project.

I extend my sincere thanks to the former and present Deans, School of Chemistry, for providing all necessary facilities to carry out my research work. I also thank all the faculty members for their assistance during my graduate years. I would like to extend my thanks to Council of Scientific and Industrial Research (CSIR), New Delhi for financial support and Center for Modelling Simulation and Design (CMSD) for computational facilities.

I express my heartfelt thanks to my labmates Dr. T. Venkatesan, Dr. B. Jayachander, Dr. V. Sivaranjana Reddy, Dr. Tanmoy Mondal, Dr. Susanta Ghanta, Dr. T. Rajagopal Rao, Tanmoy Roy, S Nagaprasad Reddy, Rudraditya Sarkar, Sugata Goswami, N. Krishna Reddy, S. Subrahmanyam, Arpita Ghosh, Aleem, Arun and Dr. B. Saritha, C. Sridhar Reddy and Dinesh Thakur of Prof. M. D. P. group for many fruitful discussions, help and their warm company on various occasions. Their association will remain forever in my memory.

I thank Mrs. Gitashree Mahapatra (madam), Anusha and Anish for providing me a homely feeling in several occasions.

I would like to thank all my friends Krishna (kitta), School (Phani, Tiru, Anji, Vijay etc.), B. Sc (Nagaraju, Krishna Prasad, Chandu, V. Rajasekhar, Pidugu, Anil, N. Prasad, N. Rajasekhar etc.), M. Sc (A. Srinu, K. V. Subrahmanyam, K. Hemachandra, Nanda, Gangadhar etc), Ph. D (Sasi, Yasin, Tirupati Reddy, Ramanjeneya Reddy, Siva Reddy Alla, Anand, Pavan, Ramu, Obaiah, Aswin (ACRHEM), Naveen, P. Kishore (Bhaskar lab), Krishna Chari, Ganesh, Ramesh, Sivaprasad (DBR lab), Swamy Maloth,

Praveen, Rajesh, Naisa Chandu, Chandu (AS lab), Ashok, Santosh (AS lab), G. Ramesh anna (TPR lab), Hari, Gupta, Kesav, Durga Prasad, Kishore (MJS lab), Sivaram (MJS lab), Sudheer, S. Babu, Rama Krishna, Phani Pavan anna, Nagarjuna Reddy, Rmesh Reddy, B. Sekhar Reddy anna (DB lab), Santosh anna (DB lab), Veera Raghaviah, Chandu (DB lab), Gurubramham, Nagarjuna (KM lab), Narayana, Venu, Shakti Vel, Madhu, B. Rama Krishna (RS lab), DK anna, Rama Raju, Balu, Nagaraju, G. Sekhar Reddy (KM lab), Srinu naik, Karunakar, Vikranth, Satish, Srinivasa Reddy, Vijayender Reddy, Kishore Reddy, A. Bharani, Durgesh, Venkat Rao (life sciences), Satyanarayana (Physics) and Sriram (Physics) etc.), without them my life would have been boring.

Throughout my life I have been lucky enough to be surrounded by lot of wonderful friends. Therefore, it is indeed a difficult task to mention them all here. But I acknowledge **each and every one** of them from the bottom of my heart for helping me to get through the difficult times, all the support, entertainment and the caring they have provided.

I use this opportunity to thank Sri N. Narsi Reddy, correspondent of Vikas educational institutions, Vissannapeta, for the financial aid during the 2001-2006 time period. I extend my thanks to chemistry teachers Rajesh Reddy and Pratapa Reddy. My journey towards this Ph. D would not have been possible with out their support.

Lastly, and most importantly, I thank my parents and extended family members for their love, care and unconditional support.

December 2013 (**Rajagopala Reddy Seelam**)
Hyderabad - 500046

Glossary

aug-cc-pVDZ	augmented correlation-consistent polarized Valence Double-ζ
aug-cc-pVTZ	augmented correlation-consistent polarized Valence Triple-ζ
aug-cc-pVQZ	augmented correlation-consistent polarized Valence Quadrapule-ζ
ADT	adiabatic to diabatic transformation
B3LYP	Becke 3-Parameter (exchange), Lee, Yang and Parr
BO	Born-Oppenheimer
BH	Born-Haung
BZ	Benzene
CA	crude adiabatic
CASSCF	complete active space self consistent field
CBS	complete basis set
CC	coupled cluster
CCSD(T)	coupled cluster singles and doubles with triple excitations
cc-pVDZ	correlation-consistent polarized Valence Double-ζ
CG	Clebsch-Gordon
CIs	conical intersections
CRD	cavity ringdown
DFT	density functional theory
DIBs	Diffuse interstellar bands
DOF	degrees of freedom
DVR	discrete variable representation
ECP	effective core potentials
EOM-CCSD	equation of motion-coupled cluster singles and doubles
FC	Franck-Condon
FWHM	full width at the half maximum
G3B3	Gaussian-3 variant with B3LYP
HFBz	hexafluorobenzene
HO	Harmonic oscillator
HOMO	highest occupied molecular orbital
IREP	irreducible representation
JT	Jahn-Teller
LIF	laser-induced fluorescence
LVC	linear vibronic coupling
m-DFBz	meta-difluorobenzene

Continued in next page

– **continued from previous page**

MCTDH	multi-configuration time-dependent Hartree
MFBz	monofluorobenzene
MO	molecular orbital
MP2	Møller-Plesset perturbation theory
MRCI	multi-reference configuration interaction
o-DFBz	ortho-difluorobenzene
OVGF	outer valence Greens function
PAHs	polycyclic aromatic hydrocarbons
PESs	potential energy surfaces
PFBz	pentafluorobenzene
PJT	pseudo-Jahn-Teller
QVC	quadratic vibronic coupling
RT	Renner-Teller
REMPI	resonance enhanced multiphoton ionization
RHF	restricted Hartree-Fock
ROMP2	restricted open shell Møller-Plesset perturbation theory
R2C2PI	resonant two-color two-photon ionization
SPFs	single particle functions
TDDFT	time-dependent density functional theory
TFBz	1, 3, 5 trifluorobenzene
UHF	unrestricted Hartree-Fock
UMP2	unrestricted second - order Møller- Plesset perturbation
UB3LYP	Unrestricted Becke 3-Parameter (exchange), Lee, Yang and Parr
UCCSD(T)	unrestricted coupled cluster singles and doubles with triple excitations
VC	vibronic coupling
VDEs	vertical detachment energies
VEEs	vertical excitation energies
WP	wave packet

Contents

1 Introduction

1.1 Vibronic coupling

The Adiabatic approximation often called as clamped nuclei approximation, concerns the separability of electronic and nuclear motions [1–3]. This approximation allows to generate the so called adiabatic PESs by calculating electronic energies at various fixed nuclear positions. This approximation is based on the fact that the electronic motion is much faster than the nuclear motion as the nucleus is 1836 times heavier than electrons. The cross coupling terms of the molecular Hamiltonian, also called as nonadiabatic coupling elements, arise due to the coupling of electronic and nuclear motions. While the nonadiabatic coupling elements completely ignored in the BO approximation [1, 4], the diagonal elements of this coupling operator are retained in BH approximation [5]. The BO approximation received wide accolades from the molecular physicists and chemists and treated as the cornerstone in the the molecular physics and chemistry. This approximation holds good provided the PESs are well separated and the nuclear motion confines to a single PES [6–9]. When the PESs are degenerate or near degenerate, the nonadiabatic coupling elements diverge at the degeneracy points and supersedes the nuclear mass effect. Therefore, they can not be ignored any more, leading failure of well celebrated BO approximation [1–3, 10–14].

Two types of degeneracies are identified from dependence of electronic energy on the nuclear coordinate near their vicinity. In the first case, electronic states cross and resemble a double cone topography, popularly known as CIs. In the second, the states do not cross but coincide and result in a glancing topography leading to Renner effect or RT coupling. Electronic degeneracies in molecules mostly yield CIs. While point group symmetry allows a classification of different types of CIs, the RT case is unique for the degenerate electronic states of linear polyatomic molecules.

1.1.1 Conical intersections

PESs of diatomic molecules will not cross unless the electronic states in question differ either in their symmetry properties or in their spin multiplicity. This statement is called noncrossing rule and proposed by Wigner and von Neumann [15]. When spin-orbit coupling is excluded, minimum two DOF are required for two electronic states to be degenerate. Due to availability of three or more DOF, electronic states of ploy atomic molecules often violates this rule. When two PESs cross, they form a hyperline in the multidimensional nuclear coordinate space of polyatomic molecules and is called as CI. Teller [16] pointed out in 1937 that CIs may give rise to exceptionally fast radiationless

transitions.

Molecular point group symmetry generally plays a decisive role for the existence of CIs. The CIs of electronic PESs are classified into (i) symmetry required or enforced, (ii) accidental symmetry allowed and (iii) accidental same-symmetry intersections. Symmetry-enforced electronic degeneracy is exhibited by the JT systems. For example, a doubly degenerate E state in D_{3h} symmetry configuration splits into A_1 and B_2 when distorted to C_{2v} and forms CIs at the original undistorted D_{3h} configuration. Conical intersections which are not required by symmetry are accidental intersection. While accidental intersection corresponds to two states of distinct spatial symmetry is known as *accidental symmetry-allowed (different symmetry)* CI, the CI between two electronic states of same symmetry is called as same-symmetry accidental CI. Symmetry-allowed (and accidental) CIs are ubiquitous in molecular systems. The $\widetilde{a}^3B_{2u}$ -$\widetilde{b}^3B_{1u}$ CI of B_4 provide such an example. CIs of states of same spatial symmetry are very rare. It has been shown by Yarkony and coworkers that the excited electronic states of methyl mercaptan of $^1A''$ symmetry indeed possess such intersections [17, 18].

Based on the shape and orientation of the PESs, CIs are further classified as *peaked* and *sloped* CI [19–21]. *Peaked* CIs appear when both the PESs are elliptical cones pointing towards each other with a common tip. In this case, the crossing point is the minimum of the upper PES and the topology at this point looks like a double cone. At *slopped* CIs, both the PESs have downhill slope and touch each other at the crossing point in branching space. Here, the crossing point is always at higher energies compared to the minimum of the upper PES and the crossing appear as a seam of intersections. While a large variety of photochemical reactions via excited-state reaction pathways are controlled by *peaked* CIs, the *sloped* CIs are key factor for the unsuccessful chemical reactions and arrange decay channels for the ultrafast nonradiative deactivation of excited states [20, 21].

Seams of the CI can also be categorized based on the dimension of the branching space, η, for intersection of two PESs with $\eta = 2$, 3 or 5 [22]. Among them $\eta = 2$ is the most common case of a two state CI for even electronic molecular system in a non-relativistic situation.

CIs of electronic PESs have now emerged to be the paradigm of triggering strong nonadiabatic effects leading to blurring of vibrational level structure of molecular electronic states, various ultrafast molecular processes [17, 18] and also serve as the "bottleneck " in photophysical and photochemical transitions [23–25]. They are also referred to as *photochemical funnels* in the literature [26]. The book edited by Domcke, Yarkony and Köppel represents an excellent collection of articles in this emerging area of chemical dynamics [17, 18].

The first evidence of CIs came from JT active systems [16]. The JT effect is a unique vibronic coupling mechanism that prevails in complex electronic spectra of symmetric molecules, according to which, the nonlinear nuclear configurations of polyatomic systems in electronic degenerate state (Γ) are unstable and distort spontaneously to remove the degeneracy along a nontotally symmetric mode [27,28]. The symmetry of the nontotally symmetric mode (ε) such that it contains in the direct product of $\Gamma \otimes \Gamma$. This VC

is called as $(\Gamma \otimes \epsilon)$-JT coupling model. The $(E \otimes e)$-JT effect, that is, perturbation of a doubly degenerate electronic state (E) by a doubly degenerate vibrational mode (e), has been extensively studied for molecules with trigonal symmetry [2, 10, 11, 27–31]. In tetragonal systems, the JT perturbation of an E state is caused by the nondegenerate vibrational modes of b symmetry, known as $(E \otimes b)$-JT effect.

PJT effect is the interaction between the degenerate and non degenerate electronic states in a molecule that is pronable to JT or RT effect. In 1957, Öpic and Price [32], observed structural distortions and splitting of energy term when two or more electronic states are very close in energy (pseudo degenerate). While the JT effect is the source of instability in high symmetry configuration of any polyatomic molecules in degenerate states, the PJT effect is the only source of instability and distortions of high-symmetry configurations of any polyatomic system in nondegenerate states [33, 34].

1.1.2 Glancing interactions

A situation analogous to the JT effect in nonlinear polyatomic molecules also occurs in linear molecules in their degenerate states and is known as RT effect [35]. The RT effect in degenerate Π electronic states of linear molecules represents one of the best known examples of vibronic coupling in molecules. Upon bending the molecule, an additional dipole moment is set up in the molecular plane which lifts the electronic degeneracy. The interaction between the vibrational and electronic angular momentum behaves singularly at the linearity and breaks the adiabatic approximation. While the JT effect is linear in lowest order coupling terms, the RT effect is quadratic in nuclear displacements. Renner in his original theory treated the vibronic coupling problem in perturbative approach by expanding the lowest order of the Hamiltonian in a Taylor series around the linear configuration. Later his work has been expanded to include higher order terms of Taylor expansion [36], to allow for electronic spin [37], for the effect of molecular rotation [38], Δ electronic states [39] and four atomic molecules [40] have also been considered. In all the above reference perturbation method is used. Among the nonperturbative, i.e numeric approaches, the reader is directed to the works of Brown *et al.* [41] and Jungen *et al.* [42]. All the above mentioned works successfully explained the interactions in an isolated doublet Π or Δ electronic state of many triatomic molecules. The perturbative methods known to fail when the respective nonadiabatic coupling is strong enough. Moreover, the interaction between different electronic states are not accounted in these approaches. The quadratic vibronic coupling approach developed by H. Köppel, Domcke and Cederbaum appears to provide a systematic way to understand the multimode dynamics in linear polyatomic molecules [43]. Historically, it is understood that the RT effect is the source for instability of degenerate electronic states in linear polyatomic molecules. It was recently proved that, contrary the above belief, PJT is the source of the instability of the degenerate electronic states in linear polyatomic molecules [2, 33, 34].

All these couplings (JT, RT and PJT) have been theoretically analyzed over the years, gradually increasing the degree of complexity of the systems investigated. The theoretical approach is generally based on the so-called LVC scheme, often augmented by (selected or all) QVC terms [2,10,11,31]. This relies on the use of a diabatic electronic

basis, where the potential energy coupling matrix is expanded in a Taylor series in suitable displacement coordinates, and linear or quadratic terms are retained. The pertinent coupling constants and the nuclear motion are computed within an *ab initio* quantum dynamical scheme. Vibrational structures in various electronic spectra have been studied as time independent observables. Time dependent quantities of interest are often electronic populations in the interacting manifold of states. Strong nonadiabatic couplings manifest themselves typically in diffuse (under low resolution) or very irregular (under high resolution) spectral structures and in a femtosecond electronic population dynamics, thus signaling internal conversion processes proceeding on the same timescale as the nuclear motion [2].

1.2 Current state of research

Atomic clusters are the aggregates of few to a few thousands of atoms. Due to their small size, the properties of the clusters are in general different from those of the corresponding material in the macroscopic bulk phase. For example the all boron and carbon clusters displays wide variety of geometrical structures in contrast to their bulk phase. While boron in its elemental form present in 3-dimensional networks, its clusters B_n (where n=3-20) are planar or quasi planar. Similarly the carbon clusters also displays astonishing geometries depending on the number of carbon atoms. Elemental clusters are studied in gas phase and in solid state both experimentally and theoretically, because chemical and physical properties are of great fundamental interest. Theory played an important role in the development and application of cluster science. Since many cluster properties (*e.g.* cluster geometries, binding energies and energy barriers) can not be easily measured in the experiment, theoretical models and computational methods have been very useful in helping to interpret the geometry and spectroscopic (UV-visible and photoelectron spectroscopy) and mass spectroscopic data. The field of clusters also serves as an exciting test ground for validity of the theoretical methods. While there are several computational studies on the structure and thermodynamical parameters on both boron [44] and carbon [45, 46] clusters, study of detailed topography of their energetically low-lying electronic states and structure of the spectral bands is still missing in the literature. As a part of this thesis, the photodetachment spectroscopy of B_n^- with n=4, 5 and 7 (see Chapters 3 and 4) and absorption spectroscopy of carbon cluster C_{15} is studied theoretically by *ab initio* quantum dynamical methods. It is found that vibronic coupling is an important mechanism in the dynamics of excited electronic states of these clusters. Consequently fingerprints of electronic nonadiabatic effect for example, overlapping and broad band structure, excitation of nontotally symmetric vibrational mode etc are derived.

1.2.1 Boron clusters

Relative to its next door neighbor carbon, boron is just one electron short, but the difference that makes is substantial. While carbon is very essential to life, boron is not. There

are countless organic compounds having innumerable uses, but there are fewer examples of boron derivatives. The number of applications for these boron compounds in electronics, catalysis, organic synthesis, diagnostic and therapeutic medicine, while growing has been limited [47–49]. Nevertheless, because boron is a little different, with a diverse set of structural and bonding characteristics, chemists remained fascinated with the prospects of striking it rich with new families of functional boron compounds, particularly all boron clusters. It was found that boron has defied conventional bonding concepts that are central to carbon compounds. Boron exhibits sp^2 hybridization in most of its compounds, leaving one unhybridized p orbital unoccupied. In this bonding picture, boron has more bonding orbitals than available electrons, so it is considered "electron deficient". Boron adapts a multicentered bonding strategy that involves sharing electrons across BBB or BHB units, which necessitates formation of cluster compounds [47, 48]. Boranes are hydrocarbon equivalents, but they appear in all kinds of polyhedral structures.

Boron forms different types of clusters ranging from boranes, carboranes metalloboranes and all-boron clusters. The structure and bonding in boranes is very well understood from the contribution of many researchers Stock [50], Dilthey [51], Pitzer [52], Nobel prize winning three centered two electron (3c - 2e) model of Lipscomb [53], Pauling [54], Longuet-Higgins [55], Wade (also known as Wade's rules) [56], Jemmis *et al.* (see Ref. [57] and references therein) and the famous MNO of the latter rule is very helpful in understanding the structure of boranes and carboranes.

The bare all boron clusters have been studied both theoretically and experimentally during the past decade [44, 49, 58–65]. Boron clusters have been studied by mass [62–65] and photoelectron spectroscopy [44] experiments to understand the structure and bonding properties. To the surprise of the scientific community, the structure of bare boron clusters (B_n where n=3-20) were shown to be planar or quasi planar [44, 67]. The planar or quasi planar geometries of boron clusters are established from extensive photoelectron spectroscopy measurements by Wang et al aided by *ab initio* electronic structure calculations by Boldyrev et al [44]. Their stability is explained based on aromaticity, anti aromaticity and conflict aromaticity. As bare boron clusters have planar or quasi planar structure and show aromaticity or antiaromaticity like hydrocarbons, these are projected to be potential compounds as ligands for inorganic chemistry or building blocks of new solids [44]. Recent Computational studies upon designing potential sandwich like complexes based on the bare all-boron units B_3 [71], B_6^2 [72], B_7 [73], B_8^2 [74] and the successful synthesis of the triple-decker (Cp^*ReH_2) B_5Cl_5 and $(Cp^*)^2B_6H_4Cl_2$ [75] compounds containing B_5Cl_5 and $B_6H_4Cl_2$ structural units provide hope that many more compounds with bare boron building blocks may be synthesized in the future.

Wang et al have measured photodetachment spectrum at different photon wavelengths of 355, 266, and 193 nm. These studies revealed the vibronic band structures of the energetically low-lying electronic states of the corresponding neutral clusters with varying degree of energy resolution. While the combined experimental and computational efforts (stated above) unraveled rich information on the equilibrium structure and properties of the ionic and neutral boron clusters, detailed topography of their energetically low-lying electronic states and a detail study of the structure of the photodetachment bands are still missing in the literature. As a part of this thesis, the photodetachment spec-

troscopy of B_n^- with n=4, 5 and 7 (see Chapters 3 and 4) is studied theoretically by doing extensive *ab initio* quantum dynamical methods and by setting up suitable vibronic Hamiltonian. It is found that vibronic coupling is an important mechanism in the dynamics of excited electronic states of these clusters. Consequently fingerprints of electronic nonadiabatic effect for example, overlapping and broad band structure, excitation of nontotally symmetric vibrational mode etc are derived.

1.2.2 Carbon clusters

DIBs are a set of ubiquitous absorption features observed in the spectra of stars in the universe, that are caused by the absorption of light by the interstellar medium in ultraviolet, visible and infrared region of the electromagnetic spectrum [76]. For the origin and history of this subject, we direct the readers to the recent review by McCall *et al.* [76]. Over 500 DIBs are observed to date. The origin of DIBs is not known unambiguously and is a subject of major debate in the astrophysical observations. Because of their widths (ranging from a fraction to several angstroms wide), as well as their observed asymmetric profiles and substructure, the unresolved rotational contours of gaseous polyatomics are often considered. Origin of the DIBs were long believed to be due to PAHs [77] and other large carbon-bearing molecules [78]. The gas phase spectral measurements in the laboratory with support from theoretical studies of nuclear dynamics offer valuable aid to the astronomers in unraveling the mystery of the DIBs.

Douglas in his seminal paper, suggested that the bare carbon chains C_n, where n may lie in the range 5-15 [78] could show spectroscopic features consistent with the DIB observations as their electronic transitions take place in the visible region of the spectrum (the majority of the DIBs lying in the 400-800 nm region with a few others to the red) and the spectrum gets broadened due to intramolecular processes. The first spectroscopic detection of C_3 in comets in the year 1881 [79] triggered curiosity among the astronomers, chemists and physicists on the structure and spectroscopy of carbon chains. Maier *et al.* investigated the spectroscopy of linear carbon chains extensively with the aid of wide variety of spectroscopic techniques ranging from neon matrix studies, CRD, R2C2PI, LIF, trapped ion photofragmentation, and electron photodetachment processes [80–83] and concluded that absorptions of the carbon chains comprising upto 12 atoms do not correspond to any of the stronger DIB features.

The following criteria are furnishes by Mayer *et al.* for a species to be a potential DIB carrier, "(a) absorptions in the 400-800 nm range, (b) oscillator strength f values in the 1-10 range, and (c) an excited electronic-state lifetime longer than a few picoseconds so that intramolecular broadening would still be compatible with the typical half-widths of the narrower DIBs (i.e., a few wave numbers)" [10]. The longer chains with an odd number of carbon atoms of length 15, 17, 19 and 21 are expected to satisfy the first two criteria because their transitions are in the 400-800 nm range and their f values scale with the chain length. It remains to be seen by doing nuclear dynamics study, whether the excited electronic state of $^1\Sigma_u^+$ symmetry has a lifetime longer than a few picoseconds to satisfy the third condition listed above. Taking the mentioned facts into consideration the electronic structure and dynamics of C_{15} cluster are studied (see Chapter 5) in an

attempt to examine its potentiality as a DIB carrier.

1.2.3 Perfluoro effect

Fluorine atom substitution in the benzene (Bz) ring leads to a stabilization of the σ orbitals which consist mostly the fluorine orbitals. In a more general context this phenomenon is known as perfluoro effect in the literature [85]. Spectroscopic [88, 89] and photophysical [86, 87] studies on FBz molecules have revealed that the features of the electronic absorption and emission bands and lifetimes of fluorescence emission strongly depends on the number of substituted fluorine atoms. For example, C_6F_n with n $\leq$ 4 exhibit structured $S_1 \leftarrow S_0$ absorption band, large quantum yield and nanosecond lifetime of fluorescence. On the other hand, C_6F_n with n=5 and 6 exhibit structureless $S_1 \leftarrow S_0$ absorption band [88,89], low quantum yield [86,87], picosecond and nanosecond lifetime of fluorescence emission [90]. Furthermore, a biexponential decay of fluorescence is observed for the latter molecules [90].

Early work from this group on the FBz molecules have settled the ambiguities over the justification of the origin of additional bands and several other issues mentioned above for C_6F_n with n upto 5 [91]. It is established that along vibronic coupling, perfluoro effect [85] also plays important role on the dynamics of the low-lying excited electronic states of these FBz molecules. In case of HFBz (where all the hydrogen atoms are replaced by fluorine atoms and the perfluoro effect is expected to have the maximum impact), there exist no clear-cut understanding of the origin of the additional bands (when compared to Bz) and several anomalous experimental observations about its fluorescence lifetime and biexponential decay dynamics in gas phase absorption spectrum [89]. Furthermore, the additional band (C-band) observed in HFBz, unlike PFBz, exhibits a twin structure and there is no unambiguous interpretation exists for the observed twin to date. The above mentioned unresolved issues on the observed optical absorption spectrum of HFBz prompted us to study its absorption spectrum theoretically in order to provide a comparative account on the impact of fluorine atom substitution on the optical absorption spectrum of Bz (see Chapter 6).

1.3 Outline of the thesis

The theoretical background of vibronic interactions in polyatomic molecules is presented in Chapter 2. The concept adiabatic and diabatic electronic basis is introduced. Construction of diabatic electronic Hamiltonian utilizing elementary symmetry selection rules is elaborated with few representative examples. The strategy to estimate the parameters of the electronic Hamiltonian, in particular, is described in each chapter. Technical details of the first principles quantum dynamics calculations are also discussed.

Photo-induced electron detachment spectroscopy of anionic boron clusters, B_4^-, B_5^-, and B_7^-, is theoretically investigated by performing electronic structure calculations and nuclear dynamics simulations. While the electronic potential energy surfaces and their coupling surfaces of neutral B_4, B_5 and B_7 clusters are constructed in Chapter 3, the

details of the nuclear dynamics calculations on these electronic states are presented in Chapter 4. Electronic structure calculations are carried out at the CASSCF-MRCI level of theory employing the aug-cc-pVTZ basis set. Using the calculated electronic structure data suitable vibronic Hamiltonians are constructed utilizing a diabatic electronic basis and displacement coordinates of the normal vibrational modes. The theoretical results are discussed in relation to those recorded in recent experiments.

In Chapter 4, the photodetachment bands of anionic boron clusters, B_n (n = 4, 5 and 7) are theoretically examined. The model Hamiltonians developed through extensive *ab initio* quantum chemistry calculations in chapter 3 are employed for the required nuclear dynamics study. While the precise location of vibronic lines and progression of vibrational modes within a given electronic band is derived from time-independent quantum mechanical studies, the broad band spectral envelopes and the nonradiative decay rate of electronic states are calculated by propagating wave packets in a time-dependent quantum mechanical framework. The theoretical results are in good accord with the experiment to a large extent. The discrepancies between the two can be partly attributed to the inadequate energy resolution of the experimental results and also to the neglect of dynamic spin-orbit interactions and computational difficulty related with detachment channels involving multi-electron transitions in the theoretical formalism.

While the studies of boron clusters in Chapters 3 and 4 are of importance in material chemistry, in Chapter 5 structure and dynamics of odd numbered carbon chains are studied in connection to their astrophysical relevance. The absorption spectrum of a state of Σ_u^+ symmetry of the carbon chains consisting of 15, 17, 19 and 21 carbon atoms is expected to be a DIB carrier provided it is long lived (upto $\sim$ 2 ps). Theoretical study of nuclear dynamics in the $S_5{}^1\Pi_g$, $S_6{}^1\Pi_u$, $S_7{}^1\Sigma_u^+$ and $S_{12}{}^1\Sigma_g^+$ electronic states of C_{15} is carried out to examine the nonradiative decay dynamics of its $^1\Sigma_u^+$ electronic state. The findings are presented in this Chapter.

In Chapter 6, theoretical study of the photoabsorption spectroscopy of HFBz is presented. The chemical effect due to fluorine atom substitution on the electronic structure of Bz saturates in HFBz. State-of-the-art quantum chemistry calculations are carried out to establish potential energy surfaces and coupling surfaces of five energetically low-lying electronic (two of them are orbitally degenerate) states of HFBz. Coupling of these electronic states caused by the JT and PJT type of interactions is examined. The impact of these couplings on the nuclear dynamics of the participating electronic states is thoroughly investigated by quantum mechanical methods and the results are compared with those observed in the experiments. The complex structure of the $S_1 \leftarrow S_0$ absorption band is found to originate from very strong nonadiabatic coupling between the S_2 (of $\pi\sigma^*$ origin) and S_1 (of $\pi\pi^*$ origin) electronic state. While S_2 state is orbitally degenerate and JT active, the S_1 state is nondegenerate. These states form energetically low-lying CIs in HFBz. These CIs are found to be the mechanistic bottleneck of the observed low quantum yield of fluorescence emission, non overlapping absorption and emission bands of HFBz and contribute to the spectral width. Justification is also provided for the observed two peaks in the second absorption (the unassigned "c band") band of HFBz. The peaks observed in the third, fourth and fifth absorption bands are also identified and assigned.

Final conclusions and prospects of the current thesis is presented in Chapter 7.

References

[1] C. J. Ballhausen and A. E. Hansen, Ann. Rev. Phys. Chem. **23**, 15 (1972).

[2] H. Köppel, W. Domcke, and L. S. Cederbaum, Adv. Chem. Phys. **57**, 59 (1984).

[3] G. Fisher, *Vibronic coupling*, Academic press, London (1984).

[4] M. Born and R. Oppenheimer, Ann. Phys. **84**, 457 (1927).

[5] M. Born and K. Haung: *Dynamical Theory of Crystal Lattices*, Oxford University Press, New York (1954).

[6] R. G. Bray and M.J. Berry, J. Chem. Phys. **71**, 4909 (1979).

[7] J. Ford, Advan. Chem. Phys. **24**, 155 (1973).

[8] D. F. Heller and S. Mukamel, J. Chem. Phys. **70**, 463 (1979).

[9] W. H. Miller *Dynamics of molecular collisions*, Plenum. Press, New York , (1976).

[10] H. Köppel, L.S. Cederbaum, and S. Mahapatra, *Theory of the JahnTeller Effect*, in *Handbook of high-resolution spectroscopy*, John Wiley & Sons, (2011).

[11] S. Mahapatra, Acc. Chem. Res. **42**, 1004 (2009).

[12] M. Baer, *Beyond Born-Oppenheimer: electronic non-adiabatic coupling terms and conical intersections*, John Wiley and Sons, (2006).

[13] M. S. Child in *Atom-Molecular collision theory*, edited by R. B. Bernstein, Plenum press, New York, (1979).

[14] B. DiBartolo, *Radiationless processes*, PLenum press, New York, (1980).

[15] J. von Neumann and E. P. Wigner, Physik. Z. **30**, 467 (1929).

[16] E. Teller, J. Phys. Chem. **41**, 109 (1937).

[17] *Conical Intersections: Electronic Structure, Dynamics and Spectroscopy*, edited by W. Domcke, D. R. Yarkony, and H. Köppel (WorldScientific, Singapore, 2004).

[18] *Conical Intersections: Theory, Computation and Experiment*, W. Domcke, D. R. Yarkony, H. Köppel, Eds., (World Scientific: Singapore, 2011).

[19] G. J. Atchity, S. S. Xantheas, K. Ruedenberg, J. Chem. Phys. **95**, 1862 (1991).

[20] A. Migani and M. Olivucci, Chapter 6, In; *Conical Intersections: Electronic Structure, Dynamics and Spectroscopy*, edited by W. Domcke, D. R. Yarkony, and H. Köppel (WorldScientific, Singapore, 2004).

[21] M. J. Paterson, M. A. Robb, L. Blancafort and A. D. DeBellis, J. Phys. Chem. A **109**, 7527 (2006).

[22] W. Domcke, D. R. Yarkony, Annu. Rev. Phys. Chem. *63*, 325 (2012).

[23] M. A. Robb, F. Bernardi, and M. Olivucci, Pure and Appl. Chem. **67**, 783 (1995).

[24] F. Bernardi, M. Olivucci, and M. A. Robb, Chem. Soc. Rev. **25**, 321 (1996).

[25] *Conical intersections in photochemistry, spectroscopy and chemical dynamics*, Chem. Phys. **259**, 121-337 (2000).

[26] J. Michl and V. Bonacic-Koutecky, *Electronic Aspects of Organic Photochemistry* (Wiley, New York, 1990).

[27] H. A. Jahn and E. Teller, Proc. Roy. Soc. London, Ser. A **161**, 220 (1937).

[28] H. A. Jahn, Proc. R. Soc. London, Ser. A **164**, 117 (1938).

[29] R. Englman, *The Jahn-Teller Effect in Molecules and Crystals* (Wiley, New York, 1972).

[30] I. B. Bersuker and V. Z. Polinger, *Vibronic Interactions in Molecules and Crystals* (Springer-Verlag, Berlin, 1989).

[31] I. B. Bersuker, *The Jahn-Teller Effect* (Cambridge University Press, 2006).

[32] U. Öpik and M. H. L. Pryce, Proc. R. Soc. London, Ser. A **238**, 425 (1957).

[33] P. Garcia-Fernandez and I. B. Bersuker, Int, Jou, Quant, Chem, **112**, 3025 (2012).

[34] I. B. Bersuker, Chem. Rev. *113*, 1351, (2013).

[35] R. Renner, Z. Phys. **92**, 172 (1934).

[36] J. A. Pople and H. C. Longuet-Higgins, Mol. Phys. **1**, 372 (1958).;R. N. Dixon, Mol. Phys. **9**, 357, (1965).

[37] J. A. Pople, Mol. Phys., bf 3, 16, (1960).

[38] J. T. Hougen, J. Chem. Phys. **36**, 1874 (1962).

[39] A. J. Merer and D. N. Travis, Can. J. Phys. **43**, 1795, (1965).

[40] A. N. Petlin and A. A. Kiselev, Int. J. Quantum. Chem. *6*, 701 (1972).

[41] T. Barrow, R. N. Dixon and G. Duxbuty, Mol. Phys. *27*, 1217 (1974).

[42] Ch. Jungen and A. J. Merer, Mol. Phys. *40*, 95 (1980).

[43] H. Köppel, W. Domcke and L. S. Cederbaum, J. Chem. Phys. **74**, 2946 (1981).

[44] A. N. Alexandrova, A. I. Boldyrev, H. J. Zhai, and L. S. Wang, Coord. Chem. Rev. **250**, 2811 (2006).

[45] W. Weltner, Jr. and R. J. van Zee, Chem. Rev. **89**, 1713 (1989).

[46] A. V. Orden and R. J. Saykally, Chem. Rev. **98**, 2313 (1998).

[47] N. N. Greenwood, A. Earnshaw, *Chemistry of the elements*, second ed., Butterworth-Heinemann, Oxford/Auckland/Boston/Johannesburg/ Melbourne/New Delhi, (2001).

[48] F. A. Cotton, G.Wilkinson, C.A. Murillo, M. Bochmann, *Advanced inorganic chemistry*, sixth ed., John Wiley & Sons, New York, (1999).

[49] R. N. Grimes, J. Chem. Educ. **81**, 657 (2004).

[50] A. Stock, C. Massanez, Chem. Ber. **45** 3539 (1912); A. Stock, *Hydrides of Boron and Silicon*, Cornell University Press, Ithaca, NY, 1933.

[51] W. Dilthey, Z. Angew. Chem. *34*, 596 (1921).

[52] K. S. Pitzer, J. Am. Chem. Soc. *67*, 1126 (1945).

[53] W. H. Eberhardt, B. Crawford, W.N. Lipscomb, J. Chem. Phys. *22*, 989 (1954).

[54] L. Pauling, S. Weinbaum, Z. Kristallogr. **87**, 181 (1934).

[55] H. C. Longuet-Higgins, M. deV. Roberts, Proc. R. Soc. (Lond.) **224A**, 336 (1954).

[56] K. Wade, Chem. Commun. 792 (1971).

[57] E. G. Jayasree and E. D. Jemmis, Acc. Chem. Res. **36**, 816 (2003).

[58] H. Kato and K. Yamashita, Chem. Phys. Lett. **190**, 361 (1992).

[59] I. Boustani, Int. J. Quantum Chem. **52**, 1081 (1994).

[60] A. Ricca and C.W. Bauschlicher Jr., Chem. Phys. **208**, 233 (1996).

[61] I. Boustani, Phys. Rev. B. **55**, 16426 (1997).

[62] L. Hanley, J. L. Whitten, and S. L. Anderson, J. Phys. Chem. **92**, 5803 (1988).

[63] L. Hanley and S. L. Anderson, J. Phys. Chem. **91**, 5161 (1987).

[64] S. A. Ruatta, P. A. Hintz, and S. L. Anderson, J. Chem. Phys. **94**, 2833 (1991).

[65] P. A. Hintz, S. A. Ruatta, and S. L. Anderson, J. Chem. Phys. **92**, 292 (1992).

[66] M. Kobayashi, I. Higashi, and M. Takami, J. Solid State Chem. **133**, 211 (1997).

[67] B. Kiran, S. Bulusu, H.J Zhai, S. Yoo, X. C. Zeng and L. S. Wang. Proc. Natl. Acad. Sci. USA. **102**, 961 (2005).

[68] H. J. Zhai, L. S. Wang, A. N. Alexandrova, A. I. Boldyrev, and V. G. Zakrzewski, J. Phys. Chem. A **107**, 9319 (2003).

[69] H. J. Zhai, L. S. Wang, A. N. Alexandrova, and A. I. Boldyrev, J. Chem. Phys. **117**, 7917 (2002).

[70] H-J Zhai, L-S Wang, A. N. Alexandrova and A. I. Boldyrev, J. Phys. Chem. A **108**, 3509 (2004).

[71] Li-Ming Yang, J. Wang, Y. B. Ding and C. Sun, J. Phys. Chem. A **111**, 9122 (2007).

[72] A. N. Alexandrova, A. I. Boldyrev, H-J Zhai, L-S. Wang, J. Chem. Phys **122**, 054313, (2005); Q.S. Li, Q. Jin, J. Phys. Chem. A **107**, 7869, (2003).

[73] Q. S. Li, L. F. Gong, J. Phys. Chem. A **108**, 4322,(2004).

[74] A. N. Alexandrova, H-J Zhai, L-S Wang, A. I. Boldyrev, Inorg. Chem. 43, 3552, (2004); S. D. Li, J. C. Guo, C. Q. Miao, G. M. Ren, Angew. Chem., Int. Ed. **44**, 2158, (2005).

[75] B. Le Guennic, H. Jiao, S. Kahlal, J-Y Saillard, J-F Halet, S. Ghosh, M. Shang, A. M. Beatty, A. L. Rheingold, T. P. Fehlner, J. Am. Chem.Soc. **126**, 3203, (2004); S. Ghosh, A. M. Beatty, T. P. Fehlner, J. Am. Chem. Soc. **123**, 9188, (2001).

[76] B. J. McCall and R. E. Griffin, Proc. R. Soc. A **469**, 0604, (2012)

[77] T. P. Snow, A. G. G. M. Tielens, 'The Diffuse Interstellar Bands' Klüwer Acad. (1995).

[78] A. E. Douglas, Nature, **269**, 130, (1977).

[79] W. Huggins, Proc. R. Soc. Landon **33**, 1 (1982); G. Herzberg, Astophys. J. **96**, 314 (1942).

[80] J. P. Maier Chem. Soc. Rev. **17**, 45, (1988).

[81] J. P. Maier Chem. Soc. Rev. **26**, 21, (1997).

[82] J. P. Maier J. Phys. Chem. A **102** 3462 (1998).

[83] E. B. Jochnowitz and J. P. Maier, Annu. Rev. Phys. Chem. **59**, 519 (2008).

[84] C. A. Rice and J. P. Maier, J. Phys. Chem. A **117**, 5559 (2013).

[85] C. R. Brundle, M. B. Robin, and N. A. Kuebler, J. Am. Chem. Soc. **94**, 1466 (1972).

[86] D. Phillips, J. Chem. Phys. **46**, 4679 (1967).

[87] G. L. Loper, and E. K. C. Lee, Chem. Phys. Lett. **13**, 140 (1972).

[88] M. B. Robin, *Higher Excited States of Polyatomic Molecules*, Vol. III (Academic, New York, 1975), and references therein.

[89] J. Philis, A. Bolovinos, G. Andritsopoulos, E. Pantos, and P. Tsekeris, J. Phys. B: At. Mol. Phys. **14**, 3621 (1981).

[90] D. V. O'connor, M. Sumitani, J. M. Morris, and K. Yoshihara, Chem. Phys. Lett. **93**, 350 (1982).

[91] Ph.D thesis of Tanmoy Mondal submitted to School of Chemistry, University of Hyderabad, November (2010).

2 Theoretical methodology

2.1 Born-Oppenheimer approximation and adiabatic representation

Quantum chemistry and dynamics of a molecular system can be described theoretically by the following time independent Schrödinger equation

$$\mathcal{H}(q,Q)\Psi(q,Q) = \mathcal{E}\Psi(q,Q) \tag{2.1}$$

where the vibronic wavefunction and energy are represented by $\Psi(q,Q)$ and $\mathcal{E}$, respectively, and the molecular Hamiltonian $\mathcal{H}$ in the absence of spin-orbit interaction is given by

$$\mathcal{H}(q,Q) = \mathcal{T}_{el}(q) + \mathcal{T}_N(Q) + \mathcal{U}(q,Q) + \mathcal{V}(Q) \tag{2.2}$$

where q and Q collectively represent electronic and nuclear coordinates, respectively. $\mathcal{T}_{el}$ and $\mathcal{T}_N$ are electronic and nuclear kinetic energy terms, respectively. $\mathcal{U}(q,Q)$ includes the repulsion energy between the electrons and attraction energy between the electrons and nuclei. $\mathcal{V}(Q)$ is the potential energy of interaction between the nuclei. The Schrödinger equation (2.1) can not be solvable because the Hamiltonian Eq. (2.2) doesnt allow a separation of variables q and Q. To solve this problem of nonseparability of electronic and nuclear motions, one of the most fundamental approximation known as adiabatic approximation is proposed and it consists of computing the electronic wavefunctions for fixed positions of the nuclei. The rationale for this approximation derives from the much heavier mass (slower motion) of the nuclei relative to the electrons. The electronic motion is treated with the nuclei held at fixed positions and then the slower motion of the nuclei is monitored using a potential energy established by the moving cloud of electrons. This is also called as clamped nuclei approximation [1, 2].

In the so called clamped nuclei approximation, the orthonormal electronic eigenfunctions $\psi_n(q;Q)$ and electronic energy $\mathcal{V}_n(q;Q)$ at a fixed nuclear position are calculated by solving electronic Schrödinger equation

$$\mathcal{H}_{el}(q,Q)\psi_n(q;Q) = (\mathcal{T}_{el}(q) + \mathcal{U}(q,Q))\psi_n(q;Q) = \mathcal{V}_n(q;Q)\psi_n(q;Q) \tag{2.3}$$

The molecular wavefunction within adiabatic theorem can be written as a product of electronic eigenfunction ($\psi_n(q;Q)$) which in addition to electron coordinates is parametrically dependent on nuclear coordinates and nuclear eigenfunction ($\chi(Q)$) which is

dependent only on the nuclear coordinates.

$$\Psi_i(q,Q) = \sum_n \psi_n(q;Q)\chi_{ni}(Q) \tag{2.4}$$

By inserting the expression for vibronic wavefunction $\Psi_i(q,Q)$ into Eq. (2.1), one readily obtains the following coupled differential equations

$$\left[\mathcal{T}_N(Q) + \mathcal{V}_n(q;Q) + \mathcal{V}(Q) - \mathcal{E}\right]\chi_n(Q) = \sum_m \Lambda_{nm}(Q)\chi_n(Q) \tag{2.5}$$

where

$$\sum_m \Lambda_{nm}(Q) = -\int dq \psi_n^*(q;Q)\left[\mathcal{T}_N(Q), \psi_m(q;Q)\right] \tag{2.6}$$

defines the coupling of electronic states n and m through the nuclear kinetic energy operator and is termed as the nonadiabatic coupling matrix of the adiabatic electronic representation. The nuclear kinetic energy operator takes non-diagonal form in this representation. The quantity $\Lambda_{nm}(Q)$ can be expressed as [1, 3]

$$\Lambda_{nm}(Q) = -\sum_i \frac{\hbar^2}{M_i} A_{nm}^{(i)}(Q)\frac{\partial}{\partial Q_i} - \sum_i \frac{\hbar^2}{2M_i} B_{nm}^{(i)}(Q) \tag{2.7}$$

where M_i are nuclear masses and

$$A_{nm}^{(i)}(Q) = \langle \psi_n(q;Q)|\nabla_i|\psi_m(q;Q)\rangle \tag{2.8}$$

and

$$B_{nm}^{(i)}(Q) = \langle \psi_n(q;Q)|\nabla_i^2|\psi_m(q;Q)\rangle \tag{2.9}$$

represents the derivative coupling vector and scalar coupling, respectively. Depending on the choice made in the molecular wavefunction and nonadiabatic coupling term, three approximations are evolved. They are BO, BH and CA approximations [4].

BO approximation

If Λ_{nm} in Eq. (2.5) is approximated to zero, then that approximation is called as BO approximation [2, 4, 5]. The molecular wavefunction is given by

$$\Psi_i^{BO}(q,Q) = \sum_n \psi_n(q;Q)\chi_{ni}^{BO}(Q)$$

The electronic and nuclear Hamiltonians are given by

$$\left[\mathcal{T}_{el}(q) + \mathcal{U}(q,Q) - \mathcal{V}_n(q;Q)\right]\psi_n(q;Q) = 0$$

and

$$[\mathcal{T}_N(Q) + \mathcal{V}(Q) + \mathcal{V}_n(q;Q) - \mathcal{E}]\,\chi_{ni}^{BO}(Q) = 0.$$

BH approximation

If the diagonal terms of the nonadiabatic operator Λ_{nm} are retained while off-diagonal terms set to zero, then that approximation is called as BH approximation [2, 4, 6]. The diagonal part of the nonadiabatic operator is given by

$$\Lambda_{nn} = -\sum_i \frac{\hbar^2}{M_i} A_{nn}^{(i)}(Q)\frac{\partial}{\partial Q_i} - \sum_i \frac{\hbar^2}{2M_i} B_{nn}^{(i)}(Q) \tag{2.10}$$

Since the electronic wavefunction chosen to be real and $A_{mn}^{(i)}$ is an anti-hermitian operator, the following relations apply.

$$A_{mn}^{(i)} = -A_{nm}^{(i)}$$

For diagonal terms $m = n$, then the above equation become

$$\begin{aligned} A_{nn}^{(i)} &= -A_{nn}^{(i)} \\ 2A_{nn}^{(i)} &= 0 \\ A_{nn}^{(i)} &= 0 \end{aligned}$$

The molecular wavefunction and electronic Schrödinger equation in BH approximation are same as that of the BO approximation. The nuclear Schrödinger equation differs from BO approximation and is given by

$$\left[\mathcal{T}_N(Q) + \mathcal{V}_n(q;Q) + \mathcal{V}(Q) - \mathcal{E} + \sum_i \frac{\hbar^2}{2M_i} B_{nn}^{(i)}\right] \chi_{ni}(Q) = 0. \tag{2.11}$$

CA approximation

In this approximation the molecular wavefunction is expanded in a basis of electronic functions corresponds to a fixed nuclear configuration. The molecular wavefunction is given by [1, 2]

$$\Psi_i^{CA}(q,Q) = \sum_n \psi_n(q;Q_0)\chi_{ni}^{CA}(Q) \tag{2.12}$$

The electronic Hamiltonian is given by

$$\begin{aligned} \mathcal{H}_{el} &= \mathcal{T}_{el}(q) + \mathcal{U}(q,Q) \\ &= \mathcal{T}_{el}(q) + \mathcal{U}(q,Q_0) + \Delta\mathcal{U}(q,Q) \\ &= \mathcal{H}_{el}(q,Q_0) + \Delta\mathcal{U}(q,Q) \end{aligned} \tag{2.13}$$

The nuclear Schrödinger equation is given as

$$[\mathcal{T}_N(Q) + \mathcal{V}_n(Q_0) + \mathcal{V}(Q) - \mathcal{E} + \langle n|\Delta\mathcal{U}(q,Q)|n\rangle]\,\chi_{ni}^{CA}(Q) = 0 \tag{2.14}$$

In the adiabatic representation, the potential energy matrix is diagonal, while the nuclear kinetic energy matrix is non-diagonal due to coupling between electronic states,

2.2 Breakdown of BO approximation and diabatic representation

From the electronic Schrödinger equation Eq. 2.3

$$\begin{aligned} \langle\psi_m(q;Q)|\mathcal{H}_{el}(q;Q)|\psi_n(q;Q)\rangle &= \langle\psi_m(q;Q)|\mathcal{V}_n(q,Q)|\psi_n(q;Q)\rangle \\ \langle\psi_m(q;Q)|\mathcal{H}_{el}(q;Q)|\psi_n(q;Q)\rangle &= \mathcal{V}_n(q,Q)\delta_{mn} \end{aligned}$$

Differentiating the above equation with respect to Q

$$\begin{aligned} \frac{\partial}{\partial Q}[\langle\psi_m(q;Q)|\mathcal{H}_{el}(q;Q)|\psi_n(q;Q)\rangle] &= \frac{\partial\mathcal{V}_n(q,Q)}{\partial Q}\delta_{mn} \\ \langle\frac{\partial}{\partial Q}\psi_m|\mathcal{H}_{el}(q;Q)|\psi_n\rangle + \langle\psi_m|\frac{\partial\mathcal{H}_{el}(q,Q)}{\partial Q}|\psi_n\rangle + \langle\psi_m|\mathcal{H}_{el}(q,Q)|\frac{\partial}{\partial Q}\psi_n\rangle &= 0 \\ \mathcal{V}_n\langle\frac{\partial}{\partial Q}\psi_m|\psi_n\rangle + \langle\psi_m|\frac{\partial\mathcal{H}_{el}(q;Q)}{\partial Q}|\psi_n\rangle + \mathcal{V}_m\langle\psi_m|\frac{\partial}{\partial Q}\psi_n\rangle &= 0 \end{aligned} \tag{2.15}$$

Since ψ_m and ψ_n are orthogonal to each other

$$\langle\psi_m|\psi_n\rangle = 0$$

Differentiating the above equation with respect to Q

$$\begin{aligned} \langle\psi_m|\frac{\partial\psi_n}{\partial Q}\rangle + \langle\frac{\partial\psi_m}{\partial Q}|\psi_n\rangle &= 0 \\ \langle\frac{\partial\psi_m}{\partial Q}|\psi_n\rangle &= -\langle\psi_m|\frac{\partial\psi_n}{\partial Q}\rangle \end{aligned}$$

Substituting the above equation in Eq. 2.15

$$-\mathcal{V}_n\langle\psi_m|\frac{\partial\psi_n}{\partial Q}\rangle + \mathcal{V}_m\langle\psi_m|\frac{\partial\psi_n}{\partial Q}\rangle + \langle\psi_m|\frac{\partial\mathcal{H}_{el}(q;Q)}{\partial Q}|\psi_n\rangle = 0$$
$$\langle\psi_m|\frac{\partial\mathcal{H}_{el}(q;Q)}{\partial Q}|\psi_n\rangle + (\mathcal{V}_m - \mathcal{V}_n)\langle\psi_m|\frac{\partial\psi_n}{\partial Q}\rangle = 0$$
$$\langle\psi_m|\frac{\partial}{\partial Q}|\psi_n\rangle = \frac{1}{(\mathcal{V}_n - \mathcal{V}_m)}\langle\psi_m|\frac{\partial\mathcal{H}_{el}(q,Q)}{\partial Q}|\psi_n\rangle$$

Using the above equation, $A^{(i)}_{nm}(Q)$ can be expressed as [1, 7, 8]

$$A^{(i)}_{nm}(Q) = \frac{\langle\psi_m(q;Q)|\nabla_i\mathcal{H}_{el}(q;Q)|\psi_n(q;Q)\rangle}{\mathcal{V}_n(Q) - \mathcal{V}_m(Q)}, \tag{2.16}$$

where $\mathcal{H}_{el}$ represents the electronic Hamiltonian for fixed nuclear configuration. When the two surfaces $\mathcal{V}_n(Q)$ and $\mathcal{V}_m(Q)$ become degenerate, the derivative coupling elements of Eq. (2.16) exhibit a singularity. This results discontinuity in both the electronic wavefunction and the derivative of energy at the point of degeneracy and making the adiabatic representation unsuitable for the computational study of the nuclear dynamics. The derivative coupling, $A^{(i)}_{nm}(Q)$, becomes extremely large at near-degeneracy or at degeneracy of different electronic PESs eventually breaking down the BO approximation. Typical phenomena associated with a violation of the BO approximation are inelastic atom-atom collisions and the radiationless decay of excited electronic states [8, 9]. To overcome this singularity in the derivative coupling operator, the adiabatic basis functions are replaced by smooth, slowly varying functions of nuclear coordinates and correspond to potential energy surfaces which may cross at the avoided crossings of adiabatic PESs. These functions are called as diabatic basis [1, 10–13]. The diabatic basis are constructed by a suitable unitary transformation of the adiabatic basis functions.

$$\phi(q;Q) = \mathbf{S}(Q)\ \psi(q;Q), \tag{2.17}$$

Where $\phi(q;Q)$ and $\psi(q;Q)$ are electronic eigenfunctions in diabatic and adiabatic representations, respectively. $\mathbf{S}(Q)$ is the transformation matrix which reads as

$$\mathbf{S}(Q) = \begin{pmatrix} \cos\theta(Q) & \sin\theta(Q) \\ -\sin\theta(Q) & \cos\theta(Q) \end{pmatrix} \tag{2.18}$$

The matrix $\mathbf{S}(Q)$ is called the ADT matrix and $\theta(Q)$ defines the transformation angle. The required condition for such transformation is that the first-order derivative couplings of Eq. (2.8) vanishes in the new representation for all nuclear coordinates [15, 16] i.e.,

$$\int dq\psi^*_n(q;Q)\frac{\partial}{\partial Q_i}\psi_m(q;Q) = 0. \tag{2.19}$$

This requirement yields the following differential equations for the transformation matrix [15, 17, 18]

$$\frac{\partial \mathbf{S}}{\partial Q_i} + \mathbf{A^{(i)}}\mathbf{S} = 0, \tag{2.20}$$

where the elements of the first-order derivative coupling matrix $\mathbf{A^{(i)}}$ are given by Eq. (2.8). A unique solution of the above equation can be obtained only when starting from a finite subspace of electronic states [16]. Therefore, for polyatomic molecular systems rigorous diabatic electronic states do not exist [16]. Approximate schemes are therefore developed to construct diabatic electronic states [18–20].

2.3 Quasi Diabatic Hamiltonian

In all the theoretical studies presented in this thesis assume a diabatic basis is already constructed. The diabatic basis results a diagonal form of nuclear kinetic energy operator and the coupling between the electronic states is described by the off-diagonal elements of the potential energy operator. The PESs are smooth, crossing curves in diabatic basis in contrast to the adiabatic basis in which the PESs are non crossing and exhibit a discontinuity at the avoided crossing. The vibronic Hamiltonian of the final states of the ionized/excited species is constructed in terms of the dimensionless normal coordinates of the electronic ground state of the corresponding (reference) anion or neutral species. The mass-weighted normal coordinates (q_i) are obtained by diagonalizing the force field and are converted into the dimensionless form [14] by

$$Q_i = (\omega_i/\hbar)^{\frac{1}{2}} q_i, \tag{2.21}$$

where ω_i is the harmonic frequency of the i^{th} vibrational mode. These actually describes the normal displacement coordinates from the equilibrium configuration, $\mathbf{Q} = 0$, of the reference state. The vibronic Hamiltonian describing the photoinduced molecular process is then given by [1]

$$\mathcal{H} = (\mathcal{T}_\mathcal{N} + \mathcal{V}_0)\mathbf{1}_n + \mathcal{W}(Q). \tag{2.22}$$

In the above equation $(\mathcal{T}_\mathcal{N} + \mathcal{V}_0)$ defines the Hamiltonian for the unperturbed reference ground electronic state, with

$$\mathcal{T}_\mathcal{N} = -\frac{1}{2}\sum_i \omega_i \left[\frac{\partial^2}{\partial Q_i^2}\right], \tag{2.23}$$

and

$$\mathcal{V}_0 = \frac{1}{2}\sum_i \omega_i Q_i^2, \tag{2.24}$$

describing the kinetic and potential energy operators, respectively. All vibrational motions in this reference electronic state are generally, to a good approximation, assumed to be harmonic. The quantity $\mathbf{1}_n$ is a $(n \times n)$ (where n is the number of final electronic states) unit matrix and $\mathcal{W}$ in Eq. (2.22) describes the change in the electronic energy

upon ionization/excitation. This is a $(n \times n)$ non-diagonal matrix. The term $\mathcal{W}$(Q) is expanded in a Taylor series in terms of normal coordinates as [21–23]

$$\mathcal{W}(Q) = W_0(Q) + \sum_{i\alpha} V_i^{(\alpha)} Q_i^{\alpha} + \frac{1}{2} \sum_{ij} \sum_{\alpha\beta} V_{ij}^{(\alpha\beta)} Q_i^{\alpha} Q_j^{\beta} + ... \tag{2.25}$$

The indices i and j run over the number of normal vibration modes. α and β runs over the components of the irreducible representations. m and n are electronic state numbering, respectively. The electronic potentials V_i^{α} and $V_{ij}^{\alpha\beta}$ are given by

$$\begin{aligned} V_i^{\alpha} &= \left. \frac{\partial V}{\partial Q_i^{\alpha}} \right|_{Q_0} \\ V_{ij}^{\alpha\beta} &= \left. \frac{\partial^2 V}{\partial Q_i^{\alpha} Q_j^{\beta}} \right|_{Q_0} \end{aligned}$$

While the diagonal elements of the electronic Hamiltonian, $\mathcal{W}_{nn}$, describe the diabatic potential energy surfaces of the electronic states, the off-diagonal elements $\mathcal{W}_{nm}$ are the coupling surfaces between mth and nth electronic states [1, 21, 23] and are given by

$$\mathcal{W}_{nm} = \sum_{kk'} \sum_{i\alpha} \langle n|V_i^{\alpha}|m\rangle Q_i^{\alpha} + \frac{1}{2} \sum_{kk'} \sum_{ij} \sum_{\alpha\beta} \langle n|V_{ij}^{\alpha\beta}|m\rangle Q_i^{\alpha} Q_j^{\beta} \tag{2.26}$$

where k and k' are the indices for the components of the electronic states m and n, respectively. To setup the molecular Hamiltonian, one needs to evaluate the integrals $\langle n|V_i^{\alpha}|m\rangle$ and $\langle n|V_{ij}^{\alpha\beta}|m\rangle$. This can be easily accomplished by employing group theory. The terms V_i^{α} and $V_{ij}^{\alpha\beta}$ transform according to the transformation properties of Q_i^{α} and $Q_i^{\alpha} Q_j^{\beta}$ [21]. A truncation of the Taylor series expansion given in Eq. (2.26) at the first and second order terms leads to the LVC and QVC schemes, respectively [1, 22, 23].

2.3.1 LVC

let β and γ be the n^{th} and m^{th} electronic states. The first order potential V_i^{α} given in Eq. (2.26) transforms according to Q_i^{α} where α be the symmetry of the vibrational mode Q_i. Let i, k and k' be the indices for the components of α, β and γ. The matrix element $\langle n|V_i^{\alpha}|m\rangle$ can be reduced by using Wigner-Eckart theorem as follows [21]

$$\langle n|V_i^{\alpha}|m\rangle = \left(\begin{array}{cc|c} \alpha & \beta & \gamma \\ i & k & k' \end{array} \right)^* \langle n||V^{\alpha}||m\rangle \tag{2.27}$$

It should be noted that index for the normal mode number is dropped. The index i should not be confused with the index i in Eq. (2.26). The matrix elements $\left(\begin{array}{cc|c} \alpha & \beta & \gamma \\ i & k & k' \end{array} \right)$ are

called as CG coefficients, which in turn depends only on the symmetry properties. These CG coefficients are also called as V coefficients and are tabulated for each molecular point group in Ref. [24]. The matrix elements $\langle n||V^{\alpha}||m\rangle$ is called as reduced matrix element, as it is independent of i, k and k'. The integral Eq. (2.27) is non-zero if and only if the symmetric direct product of β and γ contains α. i.e $\alpha \in \beta \otimes \gamma$. For non-degenerate electronic states, only totally symmetric vibrational modes a_1 are active in first order in diagonal elements. For degenerate states, the direct product obtains some non-totally symmetric vibrations, in addition to the totally symmetric modes, causes Jahn-Teller distortions.

Now let us calculate the matrix elements of the Hamiltonian for $S_2{}^1E_{1g}$ state of HFBZ. Then $m = n = S_2$, β=E_{1g} and $\gamma = E_{1g}$. k and k' runs over θ and ϵ, the two components of the degenerate electronic state E_{1g}. The symmetric direct product $[E_{1g} \otimes E_{1g}] = [E_{1u} \otimes E_{1u}] = A_{1g} + E_{2g}$. Hence, the linear coupling in the electronic state $S_2{}^1E_{1g}$ is possible only along the normal modes of symmetry a_{1g} and e_{2g}.

When $\alpha = a_{1g}$, then $i = 1$ and with aid of V coefficients given in page no. 109 of Ref. [24], the Eq. (2.27) becomes

$$\begin{aligned}
\langle n|V_i^{\alpha}|m\rangle &= \left(\begin{array}{ccc|c} A_{1g} & E_{1g} & E_{1g} \\ 1 & k & k' \end{array}\right)^{*} \langle n||V^{A_{1g}}||m\rangle \\
&= \frac{1}{\sqrt{2}}\delta_{kk'}\langle n||V^{A_{1g}}||m\rangle \\
&= \kappa\delta_{kk'}
\end{aligned}$$

where $\kappa = \frac{1}{\sqrt{2}}\langle n||V^{A_{1g}}||m\rangle$. The matrix elements of the Hamiltonian for $S_2{}^1E_{1g}$ state along a_{1g} modes hence can be given by pre multiplying with $\langle k|$ and post multiplying with $|k'\rangle$

$$\mathcal{W}_{nn} = \begin{array}{c|cc} & \theta & \epsilon \\ \hline \theta & \kappa Q & 0 \\ \epsilon & 0 & \kappa Q \end{array}$$

When $\alpha = E_{2g}$, then i runs over θ and ϵ and with the aid of the V coefficients given in Table. 3.1 of page no. 30 of Ref. [24], the JT matrix Hamiltonian is given as

$$\begin{aligned}
\mathcal{W}_{nn}^{E\otimes e} &= \sum_{kk'}\sum_{i}\langle n|V_i^{e_{2g}}|n\rangle Q_i^{e_{2g}} \\
&= \sum_{kk'}\sum_{i}\left(\begin{array}{ccc|c} E_{2g} & E_{1g} & E_{1g} \\ i & k & k' \end{array}\right)^{*} \langle n||V^{E_{2g}}||n\rangle Q_i^{e_{2g}}
\end{aligned}$$

The nonzero V coefficients are

$$\begin{pmatrix} E_{2g} & E_{1g} & E_{1g} \\ \theta & \theta & \theta \end{pmatrix} = -\begin{pmatrix} E_{2g} & E_{1g} & E_{1g} \\ \theta & \epsilon & \epsilon \end{pmatrix} = \frac{1}{2}$$
$$\begin{pmatrix} E_{2g} & E_{1g} & E_{1g} \\ \epsilon & \theta & \epsilon \end{pmatrix} = \begin{pmatrix} E_{2g} & E_{1g} & E_{1g} \\ \epsilon & \epsilon & \theta \end{pmatrix} = \frac{1}{2}$$

The matrix elements of the Hamiltonian for $S_2{}^1E_{1g}$ state along e_{2g} modes with $\lambda = \frac{1}{\sqrt{2}}\langle n||V^{E_{2g}}||n\rangle$, hence can be given by

$$\mathcal{W}_{nn} = \begin{array}{c|cc} & \theta & \epsilon \\ \hline \theta & \lambda Q_\theta & \lambda Q_\epsilon \\ \epsilon & \lambda Q_\epsilon & -\lambda Q_\theta \end{array}$$

2.3.2 QVC

Let α and β are the symmetries of the normal modes of vibration and i and j are the indices for the components of α and β, respectively. The electronic states m and n are represented by ψ and χ and their components are represented by indices k and k'. The evaluation of the matrix elements $\langle n|V_{ij}^{\alpha\beta}|m\rangle$ requires more effort. The quantity $V_{ij}^{\alpha\beta}$ transform according to $Q_i^\alpha Q_j^\beta$.

$$\langle n|V_{ij}^{\alpha\beta}|m\rangle = \sum_{\rho l}\begin{pmatrix} \alpha & \beta & \rho \\ i & j & l \end{pmatrix}\langle n|T_l^\rho|m\rangle$$

Where T_l^ρ represents some irreducible representations which are the symmetric direct product of ψ and χ. Now, applying Wigner-Eckert theorem, the above integral reduced to the following

$$\langle n|V_{ij}^{\alpha\beta}|m\rangle = \sum_{\rho l}\begin{pmatrix} \alpha & \beta & \rho \\ i & j & l \end{pmatrix}\begin{pmatrix} \rho & \psi & \chi \\ l & k & k' \end{pmatrix}\langle n||T^\rho||m\rangle \tag{2.28}$$

Where the stars on the CG coefficients have been removed, since the later turned out to be real. Now let us use the above equation, to construct the QVC Hamiltonian for $S_2{}^1E_{1g}$ state of HFBz. $\psi = \chi = E_{1g}$; and since selection rule for ρ is given by

$$[E_{1g} \otimes E_{1g}] = A_{1g} + E_{2g}$$

When $\rho = A_{1g}$,

$$\begin{aligned}
\langle n|V_{ij}^{\alpha\beta}|m\rangle &= \left(\begin{array}{cc|c} \alpha & \beta & A_{1g} \\ i & j & 1 \end{array}\right)\left(\begin{array}{cc|c} A_{1g} & E_{1g} & E_{1g} \\ 1 & k & k' \end{array}\right)\langle n||T^{\rho}||m\rangle \\
&= \frac{1}{\sqrt{2}}\delta_{kk'}\left(\begin{array}{cc|c} \alpha & \beta & A_{1g} \\ i & j & 1 \end{array}\right)\langle n||T^{\rho}||m\rangle \\
&= \frac{1}{\sqrt{2}}\delta_{\alpha\beta}\delta_{jj}\frac{1}{\sqrt{2}}\delta_{kk'}\langle n||T^{A_{1g}}||m\rangle \\
&= \frac{1}{2}\delta_{\alpha\beta}\delta_{jj}\delta_{kk'}\langle n||T^{A_{1g}}||m\rangle \\
&= \gamma\delta_{\alpha\beta}\delta_{jj}\delta_{kk'}
\end{aligned}$$

where

$$\gamma = \frac{1}{2}\langle n||T^{A_{1g}}||m\rangle \tag{2.29}$$

From the above equation, it is clear that all vibrational modes are active in second order and transform as A_1 representation. When α is not a degenerate mode the molecular Hamiltonian can be written as

$$\mathcal{W}_{nn} = \begin{array}{c|cc} & \theta & \epsilon \\ \hline \theta & \gamma Q_{\alpha}^2 & 0 \\ \epsilon & 0 & \gamma Q_{\alpha}^2 \end{array}$$

When α is a degenerate mode the molecular Hamiltonian can be written as

$$\mathcal{W}_{nn} = \begin{array}{c|cc} & \theta & \epsilon \\ \hline \theta & \gamma(Q_{\theta}^2 + Q_{\epsilon}^2) & 0 \\ \epsilon & 0 & \gamma(Q_{\theta}^2 + Q_{\epsilon}^2) \end{array}$$

When $\rho = E_{2g}$

$$\langle n|V_{ij}^{\alpha\beta}|m\rangle = \left(\begin{array}{cc|c} \alpha & \beta & E_{2g} \\ i & j & l \end{array}\right)\left(\begin{array}{cc|c} E_{2g} & E_{1g} & E_{1g} \\ l & k & k' \end{array}\right)\langle n||T^{E_{2g}}||m\rangle$$

From the direct product table, it can be seen that E_{2g} contained in the following products,

$$E_{1g} \otimes E_{1g} = E_{1u} \otimes E_{1u} = E_{2g} \otimes E_{2g} = E_{2u} \otimes E_{2u}$$

Hence, all the degenerate vibrational modes are quadratically JT active. By substituting

required V coefficients in the above equation, the matrix elements for the quadratic part of the JT Hamiltonian can be obtained, and are given below.

$$\mathcal{W}_{nn} = \begin{array}{c|cc} & \theta & \epsilon \\ \hline \theta & \eta(Q_\theta^2 - Q_\epsilon^2) & 2\eta Q_\theta Q_\epsilon \\ \epsilon & 2\eta Q_\theta Q_\epsilon & -\eta(Q_\theta^2 - Q_\epsilon^2) \end{array}$$

where $\eta = \frac{1}{4}\langle n||T^{E_{2g}}||m\rangle$

2.3.3 For molecules without degeneracy

When the molecular point group of the molecule which is under study is non-degenerate, then the construction of the molecular Hamiltonian is straight forward. The Taylor series expansion Eq. (2.26) is more complicated by the tensor potentials (product of three of more vectors). But in case of non-degenerate molecules, these tensor potentials becomes simple vectors. The Eq. (2.26) can be written as the following,

$$\mathcal{W}_{nn}(Q) = W_0(Q) + E_n + \sum_i \kappa_i^{(n)} Q_i + \sum_{ij} \gamma_{ij}^{(n)} Q_i Q_j + ... \tag{2.30}$$

and

$$\mathcal{W}_{nn'}(Q) = W_{nn'}(0) + \Sigma_i \lambda_i^{(nn')} Q_i + ..., \tag{2.31}$$

respectively. The intrastate (κ and γ) and the interstate (λ) coupling parameters are given by

$$\kappa_i^{(n)} = (\partial W_{nn}/\partial Q_i)_0 \tag{2.32}$$

$$\lambda_i^{(nn')} = (\partial W_{nn'}/\partial Q_i)_0 \tag{2.33}$$

$$\gamma_{ij}^{(n)} = \frac{1}{2}[(\partial^2 W_{nn}/\partial Q_i Q_j)_0] \tag{2.34}$$

Here E_n denotes the vertical ionization energy of the n^{th} excited electronic state from the reference state. Possible coupling between the states is assessed by employing the symmetry selection rule

$$\Gamma_m \times \Gamma_{Q_i} \times \Gamma_n \supset \Gamma_A, \tag{2.35}$$

where Γ_m, Γ_n and Γ_{Q_i} refer to the IREPs of the electronic states m, n and the i^{th} vibrational mode, respectively. Γ_A denotes the totally symmetric representation.

2.4 Simulation of eigenvalue spectrum

Assume that a molecule initially in the state Ψ_0 is excited by some operator $\hat{T}$ into a manifold of vibronically coupled electronic state. According to Fermi's golden rule, the excitation spectrum is described by function

$$P(E) = \sum_v \left| \langle \Psi_v^f | \hat{T} | \Psi_0^i \rangle \right|^2 \delta(E - E_v^f + E_0^i), \tag{2.36}$$

where the quantity $\hat{T}$ represents the transition dipole operator that describes the interaction of the electron with the external radiation of energy E during the photoionization process. $|\Psi_0^i\rangle$ is the initial vibronic ground state (reference state) with energy E_0^i and $|\Psi_v^f\rangle$ corresponds to the (final) vibronic state of the photoionized/excited molecule with energy E_v^f. The reference ground electronic state is approximated to be vibronically decoupled from the other states and it is given by

$$|\Psi_0^i\rangle = |\Phi^0\rangle |\chi_0^0\rangle, \tag{2.37}$$

The final vibronic state $|\Psi_v^f\rangle$ in the coupled electronic manifold of n interacting states can be written as

$$|\Psi_v^f\rangle = \sum_n |\Phi^n\rangle |\chi_v^n\rangle, \tag{2.38}$$

where $|\Phi\rangle$ and $|\chi\rangle$ represent the diabatic electronic and vibrational part of the wavefunction, respectively. The superscripts refer to the ground and excited states. With the help of Eqs. (2.37-2.38), the excitation function Eq. (2.36) can be rewritten as

$$P(E) = \sum_v \left| \sum_n \tau^n \langle \chi_v^n | \chi_0^0 \rangle \right|^2 \delta(E - E_v^f + E_0^i), \tag{2.39}$$

where

$$\tau^n = \langle \Phi^n | \hat{T} | \Phi^0 \rangle \tag{2.40}$$

represent the matrix elements of the transition dipole operator of the final electronic state n. In diabatic basis, these elements depends very weakly on nuclear coordinates Q. Hence, in the study of photoinduced processes presented in this thesis, we consider the transition dipole operator elements as constants. This approximation is called as Condon approximation [25].

2.4.1 Time-independent approach

The time-independent vibronic Schrödinger equation

$$\mathcal{H}|\Psi_n^f\rangle = E_n|\Psi_n^f\rangle, \tag{2.41}$$

is solved by expanding the vibronic eigenstates $\{|\Psi_n^f\rangle\}$ in the direct product harmonic oscillator basis of the electronic ground state [1]

$$|\Psi_n^f\rangle \;=\; \sum_{\{|K_i\rangle\}} a^n_{K_1,\ldots,K_l}|K_1\rangle|K_2\rangle\ldots|K_l\rangle|\phi_n\rangle \tag{2.42}$$

Here K^{th} level of i^{th} vibrational mode is denoted by $|K_i\rangle$. $|\phi_m\rangle$ is the electronic wavefunction. For each vibrational mode, the oscillator basis is suitably truncated in the numerical calculations. In practice, the maximum level of excitation for each mode is estimated from the convergence behavior of the spectral envelope. The Hamiltonian matrix expressed in a direct product Harmonic oscillator basis is highly sparse and is tri-diagonalized by the Lanczos algorithm [26]. The diagonal elements of the resulting eigenvalue matrix give the position of the vibronic lines and the relative intensities are obtained from the squared first components of the Lanczos eigenvectors [1, 13]. These calculations are simplified by employing the generalized Condon approximation in a diabatic electronic basis [25], that is, the matrix elements of $\hat{T}$ in the diabatic electronic basis are treated to be independent of nuclear coordinates and have the equal modulus.

To reflect the inherent broadening of the experimental vibronic spectrum, the stick vibronic lines obtained from the matrix diagonalization calculations are usually convoluted [1] with a Lorentzian line shape function

$$L(E) \;=\; \frac{1}{\pi}\;\frac{\frac{\Gamma}{2}}{E^2+(\frac{\Gamma}{2})^2}\;\;, \tag{2.43}$$

with a FWHM Γ.

2.4.2 Time-dependent approach

Use of Fourier representation of the Dirac delta function, $\delta(x) = \frac{1}{2\pi}\int_{-\infty}^{+\infty} e^{ixt/\hbar}$, in the golden rule equation transforms Eq. (2.36) into the following useful form, readily utilized in a time-dependent picture

$$P(E) \approx 2Re\int_0^\infty e^{iEt/\hbar}\langle\Psi_i(0)|\tau^\dagger e^{-i\mathcal{H}t/\hbar}\tau|\Psi_i(0)\rangle dt, \tag{2.44}$$

$$\approx 2Re \int_0^\infty e^{iEt/\hbar}\, C_i(t)\, dt. \tag{2.45}$$

In Eq. (2.44) the elements of the transition dipole matrix $\tau^\dagger$ is given by, $\tau^f = \langle \phi^f | \hat{T} | \phi^i \rangle$. The quantity $C_f(t) = \langle \Psi_f(0) | \Psi_f(t) \rangle$, is the time autocorrelation function of the WP initially prepared on the f^{th} electronic state and, $\Psi_f(t) = e^{-i\mathcal{H}t/\hbar}\, \Psi_f(0)$.

In the time-dependent calculations, the time autocorrelation function is damped with a suitable time-dependent function before Fourier transformation. The usual choice has been a function of type

$$f(t) \;\; = \;\; exp[-t/\tau_r] \;\; , \tag{2.46}$$

where τ_r represents the relaxation time. Multiplying $C(t)$ with $f(t)$ and then Fourier transforming it is equivalent to convoluting the spectrum with a Lorentzian line shape function (cf., Eq. (2.43)) of FWHM, $\Gamma = 2/\tau_r$.

2.4.3 Propagation of wave packet by MCTDH algorithm

The matrix diagonalization approach becomes computationally impracticable with increase in the electronic and nuclear degrees of freedom. Therefore, for large molecules and with complex vibronic coupling mechanism this method often becomes unachievable. The WP propagation approach within the MCTDH scheme has emerged as a very promising alternative tool for such situation [27–30]. This is a grid based method which utilizes DVR combined with fast Fourier transformation and powerful integration schemes. The efficient multiset ansatz of this scheme allows for an effective combination of vibrational degrees of freedom and thereby reduces the dimensionality problem. In this ansatz the wavefunction for a nonadiabatic system is expressed as [28–30]

$$\Psi(Q_1, ..., Q_f, t) \;\; = \;\; \Psi(R_1, ..., R_p, t) \tag{2.47}$$

$$\;\; = \;\; \sum_{\alpha=1}^{\sigma} \sum_{j_1=1}^{n_1^{(\alpha)}} ... \sum_{j_p=1}^{n_p^{(\alpha)}} A^{(\alpha)}_{j_1,...,j_p}(t) \prod_{k=1}^{p} \varphi_{jk}^{(\alpha,k)}(R_k, t) | \alpha \rangle, \tag{2.48}$$

Where, R_1,..., R_p are the coordinates of p particles formed by combining vibrational degrees of freedom, α is the electronic state index and $\varphi_{jk}^{(\alpha,k)}$ are the n_k SPFs for each degree of freedom k associated with the electronic state α. Employing a variational principle, the solution of the time-dependent Schrödinger equation is described by the time-evolution of the expansion coefficients $A^{(\alpha)}_{j_1,...,j_p}$. In this scheme all multi-dimensional quantities are expressed in terms of one-dimensional ones employing the idea of mean-field or Hartree approach. This provides the efficiency of the method by keeping the size of the basis optimally small. Furthermore, multi-dimensional SPFs are designed

by appropriately choosing the set of system coordinates so as to reduce the number of particles and hence the computational overheads. The operational principles, successes and shortcomings of this schemes are detailed in the literature [28–30]. The Heidelberg MCTDH package [27] is employed to propagate WPs in the numerical simulations for present molecules. The spectral intensity is finally calculated using Eq. (2.44) from the time-evolved WP.

Here we provide a brief overview on the memory requirement for the MCTDH method. The memory required by standard method is proportional to N^f, where N is the total number of grid points or primitive basis functions and f is the total number of degrees of freedom. In contrast, memory needed by the MCTDH method scales as

$$memory \quad \sim \quad fnN + n^f \tag{2.49}$$

where, n represent the SPFs. The memory requirements can however reduced if SPFs are used that describe a set of degrees of freedom, termed as *multimode* SPFs. By combining d degrees of freedom together to form a set of $p{=}f/d$ particles, the memory requirement changes to

$$memory \quad \sim \quad f\tilde{n}N^d + \tilde{n}^f \tag{2.50}$$

where $\tilde{n}$ is the number of multimode functions needed for the new particles. If only single-mode functions are used i.e. $d{=}1$, the memory requirement, Eq. (2.50), is dominated by n^f. By combining degrees of freedom together this number can be reduced, but at the expense of longer product grids required to describe the multimode SPFs.

References

[1] H. Köppel, W. Domcke, and L. S. Cederbaum, Adv. Chem. Phys. **57**, 59 (1984).

[2] G. Fisher, *Vibronic coupling*, Academic press, London (1984).

[3] B. H. Lengsfield and D. R. Yarkony, Adv. Chem. Phys. **82**, 1 (1992).

[4] C. J. Ballhausen and A. E. Hansen, Ann. Rev. Phys. Chem. **23**, 15 (1972).

[5] M. Born and R. Oppenheimer, Ann. Phys. **84**, 457 (1927).

[6] M. Born and K. Haung: *Dynamical Theory of Crystal Lattices*, Oxford University Press, New York (1954).

[7] H. Köppel, L.S. Cederbaum, and S. Mahapatra, *Theory of the JahnTeller Effect*, in *Handbook of high-resolution spectroscopy*, John Wiley & Sons, (2011).

[8] S. Mahapatra, Acc. Chem. Res. **42**, 1004 (2009).

[9] M. Baer, *Beyond Born-Oppenheimer: electronic non-adiabatic coupling terms and conical intersections*, John Wiley and Sons, (2006).

[10] W. Lichten, Phys. Rev. **131**, 229 (1963).

[11] F. T. Smith, Phys. Rev. **179**, 111 (1969).

[12] T. F. O'Malley, Adv. At. Mol. Phys. **7**, 223 (1971).

[13] H. Köppel and W. Domcke: in *Encyclopedia of computational chemistry* edited by P. v. R. Schleyer, Wiley, New York (1998), p 3166.

[14] E. B. Wilson Jr., J. C. Decius, and P. C. Cross, *Molecular vibrations*, McGraw-Hill, New York (1955).

[15] M. Baer, Chem. Phys. Lett. **35**, 112 (1975).

[16] C. A. Mead, D. G. Truhlar, J. Chem. Phys. **77**, 6090 (1982).

[17] M. Baer, Chem. Phys. **15**, 49 (1976).

[18] V. Sidis, Adv. Chem. Phys. **82**, 73 (1992).

[19] T. Pacher, L. S. Cederbaum and H. Köppel, Adv. Chem. Phys. **84**, 293 (1993).

[20] A. Thiel and H. Köppel, J. Chem. Phys. **110**, 9371 (1999).

[21] H. Barentzen, *Lectures on group theory and its applications in solid-state problems*, Max-Plank Institut für festkörperforschung, Stuttgart, Germany (2007).

[22] I. B. Bersuker, *The Jahn-Teller effect*, Cambridge University Press, Cambridge, U.K (2006).

[23] R. Englman, *The Jahn-Teller effect in molecules & cristals*, John Wiley & Sons Ltd, London (1972)

[24] J. S. Griffith, *The irreducible tensor method for molecular symmetry groups*, Dover publications Inc, New York (2006).

[25] W. Domcke, H. Köppel, and L. S. Cederbaum, Mol. Phys. **43**, 851 (1981).

[26] J. Cullum and R. Willoughby, *Lanczos algorithms for large symmetric eigenvalue problems*, Birkhäuser, Boston (1985), Vols. I and II.

[27] G. A. Worth, M. H. Beck, A. Jäckle, and H. -D. Meyer, *The MCTDH Package*, Version 8.2, (2000), University of Heidelberg, Heidelberg, Germany. H. -D. Meyer, Version 8.3 (2002), Version 8.4 (2007). See http://mctdh.uni-hd.de.

[28] H. -D. Meyer, U. Manthe, and L. S. Cederbaum, Chem. Phys. Lett. **165**, 73 (1990).

[29] U. Manthe, H. -D. Meyer, and L. S. Cederbaum, J. Chem. Phys. **97**, 3199 (1992).

[30] M. H. Beck, A. Jäckle, G. A. Worth, and H. -D. Meyer, Phys. Rep. **324**, 1 (2000).

3 Theoretical study of photodetachment spectra of anionic boron clusters. Structure

3.1 Introduction

The electronic structure and properties of anionic, neutral and cationic boron clusters have received considerable attention in theoretical and experimental research during the past decade [1–8]. The electron deficiency in the p orbitals of boron atom and its short covalent radius give rise to its unusual, highly coordinated bonding properties. The complex chemistry of boron atom characterized by formation of planar (quasi-planar) and three-dimensional bonding networks and even elementary boron exists in variety of allotropic forms with B_{12} icosahedron as a common structural motif [9]. The three-dimensional bonding network, planarity, multiple aromaticity (σ and π) are the important contributors to the novel and diverse chemistry of boron when compared to the much understood chemistry of carbon. Apart from the fundamental importance, the boron clusters are also potential candidate in advanced technological applications as optoelectronic materials (see ref. [10] and citations therein).

In order to understand the chemistry viz, the structure and bonding properties, boron clusters have been studied by mass spectroscopy [5–8] and photoelectron spectroscopy [11] experiments. In recent years, the latter in combination with *ab initio* electronic structure calculations have been very successful in elucidating the structure and bonding of many small and medium sized boron clusters [11]. Contrary to the expectations, the small boron clusters have been found to possess planar geometry at the equilibrium global minimum of their PESs (see ref. [12] and citations therein). Wang and co-workers have carried out extensive photoelectron spectroscopy measurements on boron clusters, B_n (n=3-20) and established their planar (or quasi-planar) equilibrium geometries aided by electronic structure calculations by Boldyrev and co-workers [11]. In all cases the measurements by Wang and co-workers [11] were carried out at three different photon wavelengths 355, 266 and 193 nm, which revealed the vibronic band structure of the energetically low-lying electronic states of the neutral clusters with varying degree of energy resolution [11].

The computational study so far focused on the search for the global minimum (equilibrium) geometry of the electronic ground state and calculations of the VDEs at the global minimum configuration [11]. This exercise has largely helped in identifying the novel bonding properties of the global minimum structure as well as the excited electronic

states and to correlate them with the observed band structures of the photodetachment spectrum [13–15]. Spin contamination in the HF wavefunction is a common problem for the open-shell boron clusters [19]. Hybrid DFT based methods are therefore generally employed to search for the global minimum configuration of these clusters [20, 21]. Methods based on the CASSCF theory orbitals and CC theory are also used for the purpose [11]. More accurate calculations of the structure of B_4, B_5 and B_7 clusters and their anions, VDEs, electron affinities and thermochemical parameters are also performed recently at the CCSD(T) level of theory [17,18]. In Ref. [17] the adiabatic electron affinity and the equilibrium structure of B_4 and B_4^- are calculated at the UCCSD(T)/aug-cc-pVTZ level of theory, the vibrational frequencies are calculated at CCSD(T)/aug-cc-pVDZ level of theory. While the electron affinity of B_4 is calculated by the CCSD(T) method extrapolated to CBS limit, the VDE of B_4^- is calculated at the CCSD(T)/aug-cc-pVQZ level of theory [17]. Ref. [18] used CCSD(T) extrapolated to the CBS limit to predict the adiabatic electron affinities for B_5 and B_7 and VDEs for B_5^- and B_7^- with geometries calculated at the MP2/aug-cc-pVTZ theoretical level. These quantities are also calculated with the G3B3 structures and frequencies [18]. The VDEs of B_4^-, B_5^- and B_7^- are also calculated by the OVGF method [22–24].

While the combined experimental and computational efforts (stated above) yield rich information on the equilibrium structure and properties of the ionic and neutral boron clusters, detailed information on the topography of their energetically low-lying electronic states and nuclear dynamics on them are not known till date. In the recent past we made some efforts to understand the photodetachment band structures of B_3^- [25]. In the present chapter, we attempt to investigate the structure and dynamics of the low-lying electronic states of B_4, B_5 and B_7 clusters and provide a theoretical basis for understanding the observed photodetachment bands of B_4^-, B_5^- and B_7^-. MRCI calculations are carried out to establish the energetically low-lying PESs of these highly correlated boron clusters. Curve crossings of the electronic states and strong anharmonicity of the potential energy functions in the neighborhood of these crossings are established. The importance of the intersystem crossing mediated by spin-orbit interactions is also discussed.

Model vibronic Hamiltonians are developed in this chapter with the aid of the calculated *ab initio* electronic structure data using various state-of-the-art electronic structure methods. While the details of structural study are presented here, the nuclear dynamics is investigated employing the developed Hamiltonians in Chapter 4. The theoretical results are discussed in relation with the experimental photodetachment spectrum of B_4^- [13], B_5^- [14] and B_7^- [15].

3.2 Electronic structure of boron clusters

3.2.1 B_4^-

The ground vibrational level of the electronic ground state of B_4^- is treated as the reference state in the photodetachment spectroscopy study presented in Chapter 4. The

Table 3.1: Optimized equilibrium geometry parameters of the electronic ground state of B_4^-. The results available in the literature [13, 17] are also included in the table for comparison. The units for electronic energy, bond length and bond angle are hartree, angstrom and degrees, respectively.

Parameters for B_4^-	$\widetilde{X}^2B_{1u}$					$\widetilde{X}^2A_g$	
	Ref [13]^a	Ref [17]^b	This work^c			Ref [13]^a	This work^c
			UB3LYP	ROMP2	UCCSD(T)		
E_{total}	-99.227	-98.947	-99.236	-98.909	-98.947	-99.217	-99.226
R(B1-B2)	1.568	1.583	1.564	1.579	1.583	1.578	1.574
R(B1-B3)	-	1.659	1.643	1.647	1.659	-	2.103
$\angle B1-B2-B3$	63.50	63.20	63.38	62.82	63.30	84.30	83.84
$\angle B2-B1-B4$	-	116.80	116.62	117.18	116.80	-	96.16
$\angle B2-B1-B3$	-		58.31	58.59	58.40	-	48.08

^{a} UB3LYP/6-311+G*, ^{b} CCSD(T)/aug-cc-pVTZ, ^{c} aug-cc-pVTZ level of theory

electronic ground state of B_4^- is optimized by the UB3LYP density functional method [26] using the aug-cc-pVTZ basis set of Dunning [27]. The Gaussian03 [29] suite of program is used for this purpose. Although the results from B3LYP calculations generally suffer from spin contamination owing to the presence of a HF component in it, fortuitously, this choice of the optimization method in the present case has been found to minimize spin contamination in the wavefunction drastically as compared to that obtained at the UMP2 [30–32] level of theory. Expectation values of S^2 operator are 0.754 and 1.579, respectively, obtained by the two methods as compared to its exact expectation value of 0.75.

Two possible rhombus shaped equilibrium structures of B_4^- corresponding to the D_{2h} symmetry point group shown as found by Zhai *et al.* [13] are also obtained by us and are shown in Fig. 3.1. In Table 3.1, the equilibrium geometry parameters are compared with those obtained by Zhai *et al.* [13] and Nguyen *et al.* [17] with ours at UB3LYP/aug-cc-pVTZ level of theory. It can be seen from the table that both sets of data agree very well with each other. Although the two possible equilibrium structures are energetically close, the $\widetilde{X}^2B_{1u}$ structure is ~ 0.27 eV lower in energy and represents the global minimum on the potential energy surface. While the B-B distance remains almost identical in the two isomers, the B-B-B angle is significantly larger and approaches to a square configuration at the $\widetilde{X}^2A_g$ minimum (cf., Table 3.1. On hearing from the referees we have additionally performed calculations at ROMP2 and UCCSD(T) [33–37] level of theory and obtained optimized geometry and vibrational frequencies. The optimized equilibrium geometry data is given in Table 3.1 and they are in very good agreement with those obtained from the UB3LYP method. This comparison supports the small spin contamination found in the UB3LYP results.

At both the minimum energy configurations of the electronic ground state, the harmonic vibrational frequencies ω_i are calculated by diagonalizing the *ab initio* force constant matrix. The eigenvectors of the force constant matrix yield the mass-weighted normal coordinates of the vibrational modes. The latter are transformed to the dimensionless form $\mathbf{Q}$ by multiplying with $\sqrt{\omega_i}$ (in atomic units) [38]. The six vibrational degrees of freedom of B_4^- transform to the following IREPs of the D_{2h} symmetry point group.

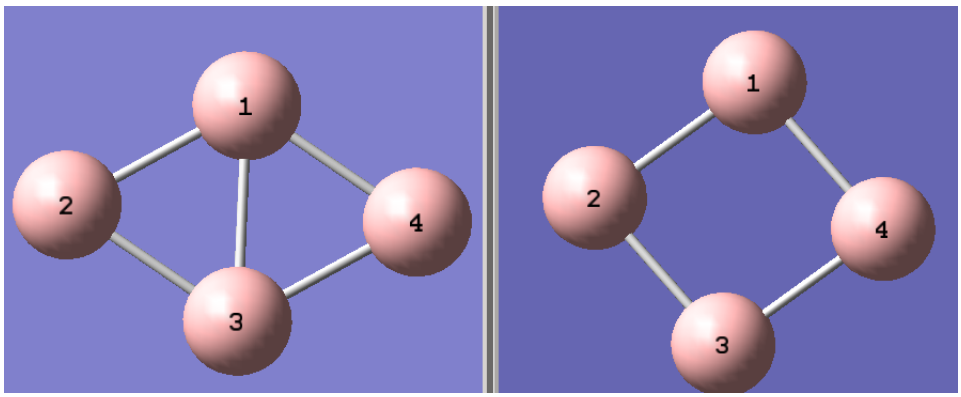

Figure 3.1: The geometry of the two low-lying isomers $\widetilde{X}^2B_{1u}$ (left) and $\widetilde{X}^2A_g$ (right) of B_4^-.

Table 3.2: Designation, symmetry, harmonic frequency (in cm^{-1}) calculated with different optimized equilibrium geometry of its electronic ground $\widetilde{X}^2B_{1u}$ state and description of the six vibrational modes of B_4^-. The results available in the literature [13, 17] are also included in the table.

Designation	Symmetry	Harmonic frequency (cm^{-1})					Description
		UB3LYP	ROMP2	UCCSD(T)	Ref [13]	Ref [17]	
ν_1	a_g	1141	1169	1126	1138	1142	ring stretch
ν_2	a_g	804	800	779	800	825	(2-4) B-B stretch and (1-3) B-B shrink
ν_3	b_{1u}	1013	1489	924	1008	815;	(1-4) and (2-3) B-B stretch
ν_4	b_{2u}	809	770	796	804	771	inplane bending
ν_5	b_{3u}	285	272	256	284	251	out of plane Butterfly bending
ν_6	b_{3g}	1043	1050	1032	1039	991	(1-2) and (3-4) B-B stretch inplane bending

[a] UB3LYP/ 6-311+G*, [b] CCSD(T)/aug-cc-pVDZ

$$\Gamma_{vib} = 2a_g + 1b_{3u} + 1b_{2u} + 1b_{1u} + 1b_{3g} \tag{3.1}$$

The description of these vibrational modes along with their harmonic frequencies calculated at UB3LYP/aug-cc-pVTZ level of theory, is given in Table 3.2. These vibrational frequencies are also calculated by the ROMP2 and UCCSD(T) level of theory. The frequencies available from the literature are also included in the table. It can be seen that the frequencies obtained by different methods are in very good accord with each other. The six vibrational modes are schematically shown in Fig. 3.2.

The electronic ground and excited PESs of neutral B_4 cluster are calculated along the dimensionless normal displacement coordinates ($\mathbf{Q}$) of the vibrational modes of the respective reference anionic clusters as discussed above. The MO sequence of the $\widetilde{X}^2B_{1u}$ electronic ground state of B_4^- obtained at the UB3LYP level of theory is given by

$$\begin{aligned} \alpha - MOs &: (1a_g)^1(1b_{1u})^1(2a_g)^1(1b_{2u})^1(3a_g)^1(2b_{1u})^1(2b_{2u})^1(4a_g)^1(1b_{3u})^1(1b_{3g})^1(3b_{1u})^1 \\ \beta - MOs &: (1a_g)^1(1b_{1u})^1(2a_g)^1(1b_{2u})^1(3a_g)^1(2b_{1u})^1(2b_{2u})^1(1b_{3u})^1(4a_g)^1(1b_{3g})^1 \end{aligned} \tag{3.2}$$

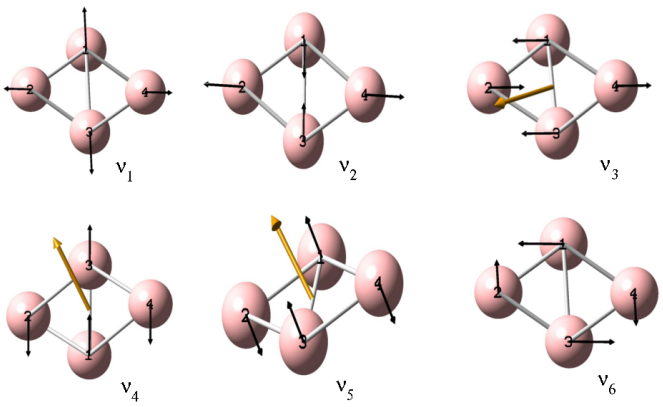

Figure 3.2: Schematic representation of the normal vibrational modes of B_4^-. The description of these modes are given in Table 3.2 in the text.

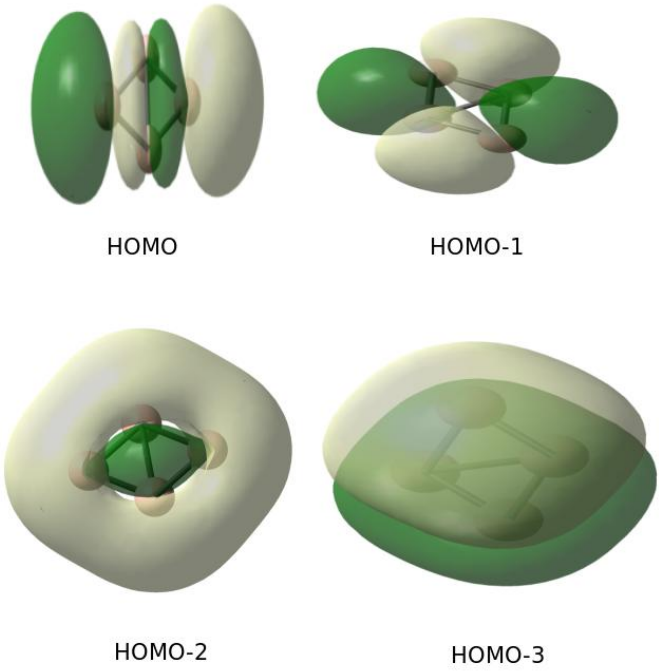

Figure 3.3: Schematic representation of the four valence type molecular orbitals of the electronic ground state of B_4^-.

The electronic ground and excited states of neutral B_4 are obtained by one electron detachment from the MOs listed above. For example, the singlet $\widetilde{X}^1A_g$, $\widetilde{A}^1B_{2u}$, $\widetilde{B}^1B_{2g}$ electronic states of B_4 result from the detachment of an electron from b_{1u}, b_{3g} and b_{3u} α-MOs of B_4^-, respectively. On the other hand, the triplet $\widetilde{a}^3B_{2u}$, $\widetilde{b}^3B_{1u}$ and $\widetilde{c}^3B_{2g}$ electronic states of B_4 result from the detachment of an electron from the b_{3g}, a_g and b_{3u}

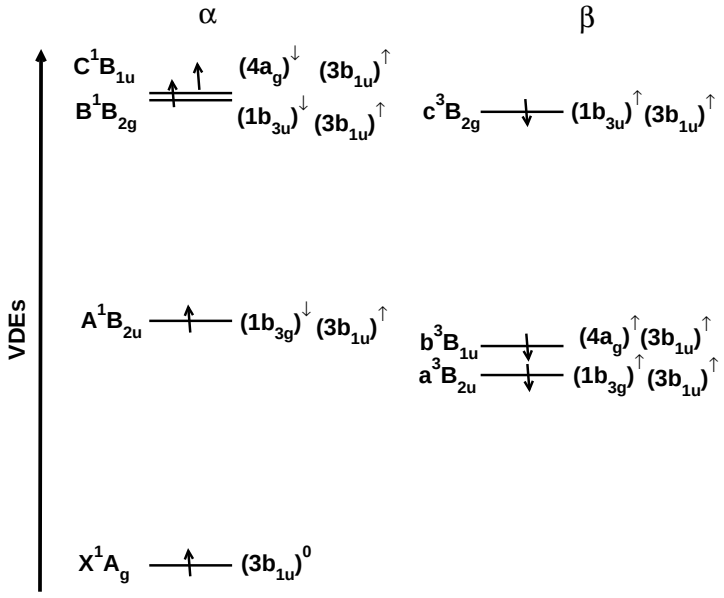

Figure 3.4: Schematic illustration of the formation of singlet and triplet electronic states of neutral B_4 cluster upon ionization from the α and β type of SCF canonical orbitals of B_4^-. The orbital occupation leading to the respective state symbol is also given. For example, the first singlet state $\widetilde{X}^1A_g$ formed by removing an α electron from the $3b_{1u}$ orbital. Similarly, the triplet $\widetilde{a}^3B_{2u}$ state is formed by removing an electron of β spin from the b_{3g} orbital (see text for details). The formation of rest of the electronic states is obvious from the diagram.

β-MOs of B_4^-, respectively. A pictorial illustration of the formation of various electronic states from the detachment of electrons from the MOs is shown in Fig. 3.4. Since the electronic states obtained by electron detachment from the above UHF type of orbitals may not be proper spin eigenstates, we generated the above states from the RHF type of MOs also. The orbital sequence obtained by optimizing the B_4^- at the ROMP2/aug-cc-pVTZ level of theory is given by

$$(1a_g)^2(1b_{1u})^2(2a_g)^2(1b_{2u})^2(3a_g)^2(2b_{1u})^2(2b_{2u})^2(1b_{3u})^2(1b_{3g})^2(4a_g)^2(3b_{1u})^1 \qquad (3.3)$$

The $\widetilde{X}^1A_g$ state results from the detachment of an electron from the HOMO $3B_{1u}$. Now we are left with two choices to detach an electron from the remaining MOs. If an electron with α spin is detached it will give rise to a singlet state, where as, a triplet state will result from the detachment of an electron with β spin. The VDEs (discussed below) obtained from both the UHF and RHF MOs are given in Table 3.3. It can be seen from the table that the energetic ordering of electronic states resulting from both the schemes is identical.

The four lowest canonical orbitals of the $\widetilde{X}^2B_{1u}$ isomer calculated at the UB3LYP/aug-

Table 3.3: Comparison of the VDEs (in eV) of B_4^- with available experimental and theoretical data [13]. The coefficients describe the contribution of the reference configuration for the particular state.

State	Co.eff of neutral B_4	Expt [13]	Ref [13] [a]	Ref [17] [b]	CASSCF-MRCI			OVGF
					UB3LYP	ROMP2	UCCSD(T)	
$\widetilde{X}^1A_g$	0.83	1.99	1.85	1.86	1.90	1.97	1.96	2.66
$\widetilde{a}^3B_{2u}$	0.80	3.08	3.14		3.21	3.19	3.21	3.07
$\widetilde{b}^3B_{1u}$	0.85	3.41	3.24		3.28	3.26	3.25	3.00
$\widetilde{A}^1B_{2u}$	0.81	-	4.03		3.94	3.87	3.89	4.38
$\widetilde{c}^3B_{2g}$	0.82	-	4.35		4.23	4.18	4.15	4.34
$\widetilde{B}^1B_{2g}$	0.82	4.39	4.65		4.42	4.37	4.34	3.53

[a] RCCSD(T) and EOM-CCSD methods with 6-311+G(2df), [b] CCSD(T)/aug-cc-pVQZ.

cc-pVTZ level of theory are shown in Fig. 3.3. The bonding nature of these MOs significantly dictates the shape and properties of the photodetachment spectrum. The HOMO orbital $3b_{1u}$ is an anti-bonding orbital formed by the p_σ orbitals of the two apex boron atoms (B2-B4). The antibonding nature of the $3b_{1u}$ MO pushes apart the atoms B2 and B4, significantly reducing the <B1-B2-B3 bond angle. This rhombus distortion enhances the bonding interaction between B1 and B3. As a result, the geometry changes significantly by the removal of the electron, leading to very broad photodetachment $\widetilde{X}^1A_g$ band. The HOMO-1 $1b_{3g}$ orbital is a bonding σ MO formed by the $2p_\sigma$ perpendicular orbitals of boron. The $2a_g$-HOMO-2 is a completely bonding σ orbital formed by the $2p_\sigma$ radial orbitals of the four boron atoms. The $1b_{3u}$-HOMO-3 is a completely bonding π MO formed by the $2p_\pi$ orbitals of boron

The adiabatic energies of the mentioned electronic states of the neutral B_4 cluster are calculated along the normal vibrational coordinates ($\mathbf{Q}$) of the respective anion. The calculations are carried out using CASSCF orbitals and MRCI method [39–41] employing the aug-cc-pVTZ basis set with the aid of MOLPRO suite of program [42]. The VDEs are calculated by taking the difference of the energies of the electronic ground state of the anion B_4^- with the ground and excited states of neutral B_4. Complementary calculations using the OVGF method [22–24] are also carried out to assess the validity of Koopman's theorem [43] for these highly correlated boron clusters.

To calculate the electronic ground state energies of B_4^- by the CASSCF-MRCI method, the active space is designed to consist of the $2a_g$, $1b_{3u}$, $2b_{2u}$, $1b_{1g}$, $2b_{1u}$, $1b_{2g}$, $1b_{3g}$ and $0a_u$ MOs pertinent to the D_{2h} symmetry designation. This includes 1, 1, 1, 0, 2, 0, 1, 0 occupied and 1,0,1,1,0,1,0,0 virtual orbitals and corresponds to a distribution of 11 electrons in 10 orbitals. The energies of the ground and excited electronic states of neutral B_4 are calculated by correlating 10 electrons in 10 orbitals as described above. This is sufficiently a large active space and expected to offer an accurate description of the electron correlation effects in B_4. The state symmetries, coefficient of the major configurations and VDEs computed at the D_{2h} symmetry configuration are given in Table 3.3. It can be seen from the table that the VDEs obtained by the present MRCI calculations using the CAS(11,10/10,10) are in good accord with the available theoretical and experimental data [13]. The VDE of the $\widetilde{X}^1A_g$ electronic state of B_4 is calculated by Nguyen *et al.* at the CCSD(T)/aug-cc-pVQZ level of theory is 1.86 eV. [17]. In the last column of Table 3.3 the VDEs obtained at the OVGF/aug-cc-pVTZ level of theory are

Table 3.4: The VDEs (in eV) of B_4^- are calculated with different active spaces are given below.

S.NO	Method	$\widetilde{X}^1A_g$	$\widetilde{a}^3B_{2u}$	$\widetilde{b}^3B_{1u}$	$\widetilde{A}^1B_{2u}$	$\widetilde{c}^3B_{2g}$	$\widetilde{B}^1B_{2g}$
1	MRCI(7,8)	2.010	3.353	3.269	3.996	4.180	4.371
2	MRCI(9,8)	2.070	3.321	3.196	3.916	4.241	4.434
3	MRCI(9,10)	1.853	3.153	3.282	3.852	4.433	4.567
4	MRCI(11,10)	1.903	3.207	3.283	3.935	4.228	4.421

Table 3.5: The VDEs (in eV) of B_4^- are calculated by varying basis sets and using (11,10) active space, are given below.

S.NO	Basis set	$\widetilde{X}^1A_g$	$\widetilde{a}^3B_{2u}$	$\widetilde{b}^3B_{1u}$	$\widetilde{A}^1B_{2u}$	$\widetilde{c}^3B_{2g}$	$\widetilde{B}^1B_{2g}$
1	cc-pVDZ	1.571	2.808	2.939	3.536	3.921	4.137
2	cc-pVTZ	1.819	3.113	3.170	3.797	4.122	4.320
3	cc-pVQZ	1.900	3.220	3.251	3.895	4.200	4.394
4	aug-cc-pVDZ	1.839	3.098	3.213	3.815	4.185	4.393
5	aug-cc-pVTZ	1.903	3.207	3.283	3.935	4.228	4.422
6	aug-cc-pVQZ	1.925	3.245	3.302	3.967	4.243	4.433

included. It can be seen that the Green's function results predict a conflicting energetic ordering of the $\widetilde{a}^3B_{2u}$ and $\widetilde{b}^3B_{1u}$ electronic states of B_4.

We also studied the dependence of these VDEs on the size of the CAS space as well as the choice of a basis set. While the VDEs calculated by, varying the size of active space with aug-cc-pVTZ basis set are tabulated in Table 3.4, the same calculated by active space (11, 10) and varying the basis sets are tabulated in Table 3.5. The CAS (11,10/10,10) and the aug-cc-pVTZ basis set are found to be a balanced compromise of the accuracy and the affordable computational cost. The VDEs along the distorted (from equilibrium at $\mathbf{Q}$=0) geometries of B_4^- to the energetically low-lying six electronic states of neutral B_4 are calculated. The number of CSFs for each state along the normal modes are tabulated in Table 3.6. These energies are equated with the adiabatic potential energies of these electronic states of B_4.

3.2.2 B_5^-

The equilibrium structure of B_5^- shown in Fig. 3.5, in its electronic ground state ($\widetilde{X}^1A_1$) converges to the C_{2v} symmetry point group. This equilibrium geometry is optimized in the present study at the MP2 level of theory employing the aug-cc-pVTZ basis set. The optimized equilibrium geometry parameters are given in Table 3.7 along with those available in the literature [14].

The harmonic vibrational frequencies and the dimensionless normal displacement coordinates ($\mathbf{Q}$) at this equilibrium minimum configuration are also calculated by the same technique as described above for B_4^-. The nine vibrational degrees of freedom of

Table 3.6: The number of CSFs for the ground $\widetilde{X}^2B_{1u}$ of B_4^- and excited states $\widetilde{X}^1A_g$, $\widetilde{A}^1B_{2u}$, $\widetilde{B}^1B_{2g}$, $\widetilde{C}^1B_{1u}$, $\widetilde{a}^3B_{2u}$, $\widetilde{b}^3B_{1u}$, $\widetilde{c}^3B_{2g}$ of B_4 radical on distorting the anion geometry, at CASSCF-MRCI(11,10)/(10, 10) are tabulated here.

S.NO	PG	CSFs							
		$\widetilde{X}^2B_{1u}$	$\widetilde{X}^1A_g$	$\widetilde{A}^1B_{2u}$	$\widetilde{B}^1B_{2g}$	$\widetilde{C}^1B_{1u}$	$\widetilde{a}^3B_{2u}$	$\widetilde{b}^3B_{1u}$	$\widetilde{c}^3B_{2g}$
ν_1-ν_2	D_{2h}	3484	2540	2420	2396	2420	3716	3716	3724
ν_3	C_{2v}	6940	4956	4816	4816	4816	7440	7440	7380
ν_4	C_{2v}	6948	4960	4960	4840	4792	7352	7432	7448
ν_5	C_{2v}	6968	4960	4960	4812	4840	7432	7352	7468
ν_6	C_{2h}	6968	4960	4840	4792	4840	24540	24540	24540

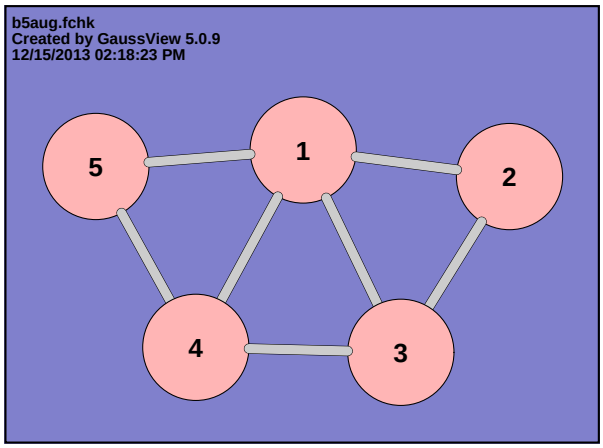

Figure 3.5: The optimized geometry of $\widetilde{X}^1A_1$ of B_5^-.

B_5^- transform to the following IREPs of the C_{2v} symmetry point group.

$$\Gamma_{vib} = 4a_1 + 1a_2 + 1b_1 + 3b_2 \tag{3.4}$$

The nature of these vibrational modes and their harmonic frequencies are also given in Table 3.8 and compared with the literature data [18]. These vibrational modes are schematically shown in Fig. 3.6.

At the equilibrium configuration of the $\widetilde{X}^1A_1$ electronic ground state, B_5^- possesses the following MO sequence

$$(1a_1)^2(1b_2)^2(2a_1)^2(2b_2)^2(3a_1)^2(4a_1)^2(3b_2)^2(5a_1)^2(6a_1)^2(4b_2)^2(1b_1)^2(7a_1)^2(5b_2)^2. \tag{3.5}$$

Detachment of an electron from $5b_2$, $7a_1$, $4b_2$, $6a_1$, $1b_1$ and $5a_1$ MOs, respectively, creates the ground $\widetilde{X}^2B_2$ and excited $\widetilde{A}^2A_1$, $\widetilde{B}^2B_2$, $\widetilde{C}^2A_1$, $\widetilde{D}^2B_1$ and $\widetilde{E}^2A_1$ electronic states of neutral B_5. A schematic representation of the 6 low-lying canonical MOs of B_5^- is presented in Fig. 3.7. The HOMO ($5b_2$) of B_5^- is a bonding orbital within the triangular wings B1-B2-B4 and B1-B3-B5 in the global minimum structure. Detachment of

Table 3.7: Optimized equilibrium geometry parameters of the electronic ground state of B_5^-. The results available in the literature [14,18] are also included in the table for comparison. Electronic energies and bond lengths are given in hartree and angstrom units, respectively.

Parameters	Ref [14][a]	Ref [18][b]	This work[c]
E_{total}	-124.081	-123.780	-123.685
R(B1-B2,B5)	1.738		1.729
R(B1-B3,B4)	1.614		1.610
R(B2-B3)	1.577		1.574
R(B3-B4)	1.579		1.576

[a] B3LYP/ 6-311+G*, [b] only energy is reported at CCSD(T)/CBS(DTQ) level of theory, [c] MP2/aug-cc-pVTZ.

Table 3.8: Designation, symmetry, harmonic frequency (in cm^{-1}) and description of the normal vibrational modes of B_5^-

		This work[a]	Ref [14][b]	Ref [18][c]	description
ν_1	a_1	1210	1259	1186	(3-4) B-B stretch
ν_2	a_1	956	965	947	Ring stretch
ν_3	a_1	764	719	754	inplane bending
ν_4	a_1	601	638	583	inplane bending
ν_5	a_2	373	374	379	out of plane bending
ν_6	b_1	208	253	189	out of plane bending
ν_7	b_2	1200	1067	1201	inplane bending
ν_8	b_2	952	998	931	inplane bending
ν_9	b_2	547	582	519	inplane bending

[a] MP2/aug-cc-pVTZ, [b] B3LYP/6-311+G*, [c] MP2/aug-cc-pVDZ

an electron from this orbital should result in geometry relaxations within these wings. HOMO-1 ($7a_1$) orbital is a strong bonding MO. However, the observed PES spectrum shown in panel b of Fig. 4.7 was relatively sharp with a very short vibrational progression. This suggests that the A state cannot be well described by the simple removal of an electron from the $7a_1$ orbital of B_5^-, consistent with the multi-configurational nature of this transition. HOMO-3 ($4b_2$) is a strong bonding orbital. The broad width of B band was consistent with the strongly bonding nature of the this orbital.

Similar to the study of B_4^- in the previous section, the adiabatic energies of the mentioned electronic states of the neutral B_5 cluster are calculated along the normal vibrational coordinates ($\mathbf{Q}$) of the anion. The CASSCF/MRCI calculations have been carried out in order to calculate electronic ground and energetically low-lying excited states of the neutral B_5 cluster. As mentioned before, the equilibrium geometry of B_5^- in its $\widetilde{X}^1A_1$ electronic state converges to the C_{2v} symmetry point group. A CAS space is therefore constructed in terms of the a_1, b_1, b_2 and a_2 electronic MOs of the C_{2v} symmetry point group. In this case the CAS space includes 3, 1, 2, 0 occupied and 1, 1,

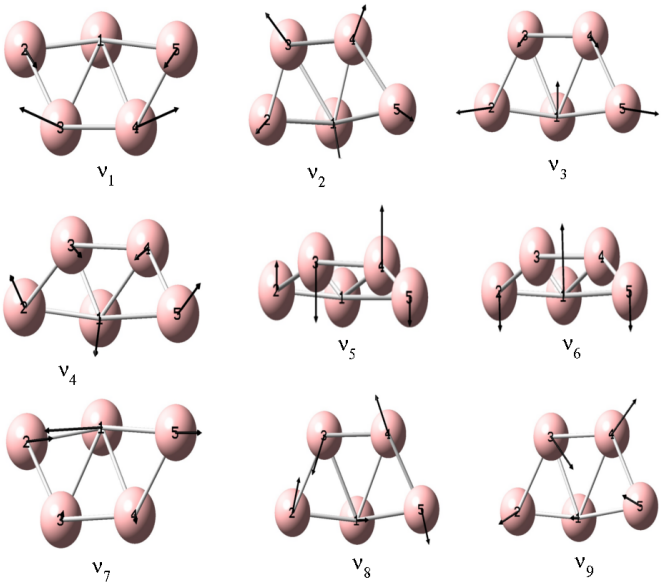

Figure 3.6: Same as Fig. 3.2 of the normal vibrational modes of B_5^-

Table 3.9: Comparison of the VDEs (in eV) of B_5^- with available experimental and theoretical data [14]. The coefficients describe the contribution of the reference configuration for the particular state. It can be seen from this table the coefficient for the $\widetilde{A}^2A_1$ state is 0.59. This implies strong electron correlation effects in B_5 molecular system.

State	Co.eff neutral B_5	Expt [14]	Ref [14] *a*	Ref [18] *b*	CASSCF-MRCI	OVGF
$\widetilde{X}^2B_2$	0.80	2.40 ±0.02	2.36	2.47	2.28	2.35
$\widetilde{A}^2A_1$	0.59	3.61 ±0.02	4.00		3.53	4.06
$\widetilde{B}^2B_2$	0.75	4.33 ±0.05	4.51		4.41	4.53
$\widetilde{C}^2A_1$	0.64	4.7-6.2	5.78		4.96	5.79
$\widetilde{D}^2B_1$	0.78	4.7-6.2	5.25		5.24	5.37
$\widetilde{E}^2A_1$	0.58	*c*	-		5.64[c]	-

[a] ROVGF/ 6-311+G(2df), [b] CCSD(T)/ CBS level, [c] This is a shake up state obtained by one electron detachment followed by electron transition.

1, 1 virtual orbitals in that order. A set of 12 electrons are correlated in 10 orbitals for B_5^- and 11 electrons are correlated in 10 orbitals for electronic states of neutral B_5. The state symmetries of B_5, coefficient of the dominant configuration and VDE values are given in Table 3.9. The experimental and theoretical VDE results from the literature as well as those obtained at the OVGF/aug-cc-pVTZ level of theory are also included in the table. It can be seen from the table that the VDE values obtained by the MRCI method generally agree well with the experimental and other theoretical [14] estimates.

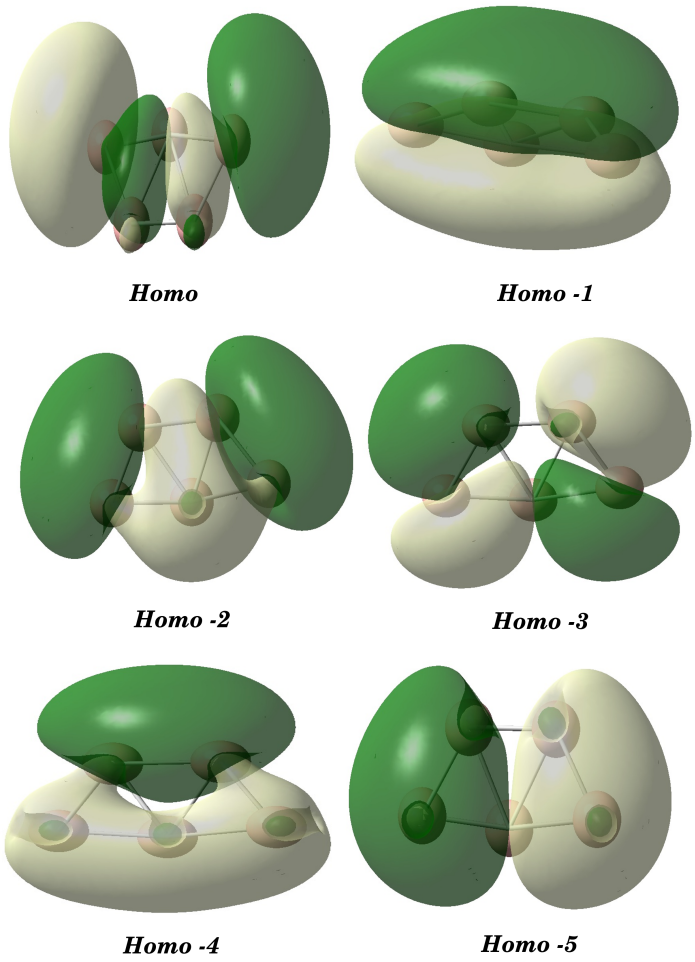

Figure 3.7: Schematic representation of the six valence type MOs of the electronic ground state of B_5^-.

Tai *et al.* [18] have reported the VDE to electronic ground $\widetilde{X}^2B_2$ state of B_5. They obtained a value of 2.64 and 2.47 eV at the G3/B3LYP and CBS/CCSD(T) level of theory, respectively, for this quantity. The VDE values obtained by the OVGF method are given in the last column of the table. In the latter case the VDE values for the $\widetilde{E}^2A_1$ state could not be obtained. This appears to be a shake-up state (as confirmed from the CASSCF-MRCI calculations) and originates from a two electrons transition. It can be seen from the table that energetic ordering of the first three electronic states is same in all the computed models (i.e RCCSD(T), MRCI and OVGF) and also they agree well with the experiment. Two genuine one electron process predicted by ROVGF are found at 5.37 and 5.79 eV. These correspond to detachment of electron from $1b_1$ and $6a_1$ orbitals, respectively. But for the fourth band (between 4.7-6.2 eV) it is anticipated that two or three shake-up states contribute to the spectrum [14]. It can be seen from the table that the energetic position for $\widetilde{D}^2B_1$ state remains nearly same in all the three

Table 3.10: The symmetry of vibrational mode and number of CSF'S for the ground $\widetilde{X}^1A_1$ of B_5^- and excited states $\widetilde{X}^2B_2$, $\widetilde{A}^2A_1$, $\widetilde{B}^2B_2$, $\widetilde{C}^2A_1$, $\widetilde{D}^2B_1$ and $\widetilde{E}^2A_1$ of B_5 neutral on distorting the anion geometry are tabulated here.

S.NO	CSFs						
	$\widetilde{X}^1A_1$	$\widetilde{X}^2B_2$	$\widetilde{A}^2A_1$	$\widetilde{B}^2B_2$	$\widetilde{C}^2A_1$	$\widetilde{D}^2B_1$	$\widetilde{E}^2A_1$
a_1	3564	6948	6968	6948	6968	6912	6968
a_2	6900	13860	13860	13860	13860	13860	13860
b_1	6980	13840	13880	13840	13880	13880	13880
b_2	900	1182	1182	1182	1182	1170	1182

Table 3.11: The VDEs of B_5^- are calculated with different active spaces are given below.

S.NO	Method	VDEs					
1	MRCI(8,8)	2.522 $\widetilde{X}$	4.008 $\widetilde{A}$	4.704 $\widetilde{B}$	5.250 $\widetilde{D}$	5.729 $\widetilde{C}$	5.926 $\widetilde{E}$
2	MRCI(8,9)	2.338 $\widetilde{X}$	3.784 $\widetilde{A}$	4.586 $\widetilde{B}$	5.234 $\widetilde{D}$	5.742 $\widetilde{C}$	5.809 $\widetilde{E}$
3	MRCI(10,8)	2.397 $\widetilde{X}$	3.982 $\widetilde{A}$	5.228 $\widetilde{D}$	5.871 $\widetilde{C}$	6.174 $\widetilde{C}$	7.293 $\widetilde{B}$
4	MRCI(10,10)	2.408 $\widetilde{X}$	3.920 $\widetilde{A}$	4.654 $\widetilde{B}$	5.236 $\widetilde{C}$	5.248 $\widetilde{D}$	5.827 $\widetilde{E}$
5	MRCI(12,10)	2.283 $\widetilde{X}$	3.529 $\widetilde{A}$	4.406 $\widetilde{B}$	4.957 $\widetilde{C}$	5.242 $\widetilde{D}$	5.638 $\widetilde{E}$

theoretical results presented in Table 3.9. However, energetic location of the $\widetilde{C}^2A_1$ state seems to be conflicting. The location of the state at 5.79 eV of A_1 symmetry found from the OVGF results may correspond to this state. We have carried-out extensive CASSCF(11, 10)-MRCI calculations and found that this state is located at $\sim$ 4.96 eV. It has been shown in (in Chapter 4) that experimental structure of the detachment band in this energy region reproduced only when this state is included in the dynamics. Similar to the study of B_4^-, the dependence of the VDEs on the active space and basis sets are also studied and are tabulated in Tables 3.10 to 3.12.

3.2.3 B_7^-

The spectral intensities in the photodetachment spectrum of B_7^- found to be altered by the source of boron cluster beam [15], indicating the contribution of more than one

Table 3.12: The VDEs of B_5^- are calculated with different basis sets are given below.

S.NO	Basis	$\widetilde{X}^2B_2$	$\widetilde{A}^2A_1$	$\widetilde{B}^2B_2$	$\widetilde{C}^2A_1$	$\widetilde{D}^2B_1$	$\widetilde{E}^2A_1$
1	cc-pVDZ	1.971	3.203	4.030	4.591	4.954	5.313
2	cc-pVTZ	2.187	3.429	4.301	4.856	5.141	5.337
3	cc-pVQZ	2.264	3.513	4.400	4.953	5.217	5.624
4	aug-cc-pVDZ	2.208	3.449	4.276	4.831	5.181	5.552
5	aug-cc-pVTZ	2.283	3.529	4.406	4.954	5.242	5.638

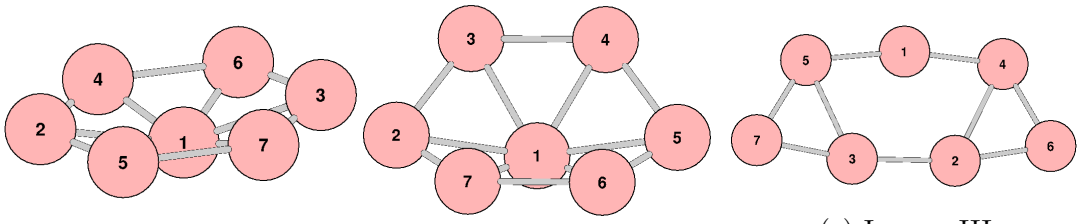

(a) Isomer I (b) Isomer II (c) Isomer III

Figure 3.8: Optimized structures of isomer I, II and III of B_7^-, respectively.

low-lying isomers. Boldyrev *et al.* with his *ab initio* calculations confirmed that three isomers of B_7^- viz., a triplet hexagonal pyramidal (C_{6v}, $^3A_1$), a singlet pyramidal (C_{2v}, $^1A_1$) and a singlet planar (C_{2v}, $^1A_1$) contribute most to the recorded photodetachment band structure [15]. The above three isomers will be identified as I, II and III in the given order in the rest of this chapter. Geometry of the equilibrium minimum of the electronic ground state of the isomer I of B_7^- is optimized at the UMP2 level of theory using the aug-cc-pVDZ basis set [28]. It is well known that the wavefunction suffers from spin contamination in calculations with unrestricted spin orbitals. The spin contamination value in the ground electronic wavefunction of the C_{6v} ($^3A_1$) isomer I at the UMP2 level of theory is $\sim 2\%$. Therefore, for this isomer the optimized geometry at the UMP2 level can be safely utilized as a reference. The optimized geometry parameters of this isomer are given in Table 3.13 and compared with the available theoretical data from the literature [15, 16, 18]. The *ab initio* force constant matrix for the electronic ground state of the anion is obtained at the same level of theory and the harmonic frequencies (ω_i) and mass-weighted normal displacement coordinates (Q_i) of the fifteen vibrational modes of B_7^- are calculated. A similar exercise is repeated for the C_{2v} pyramidal (isomer II, $^1A_1$) and C_{2v} planar (isomer III, $^1A_1$) isomers of of B_7^-. As these are closed shell species, the calculations are carried out with MP2 method for them in contrast to isomer I. The calculated geometry parameters of these two isomers are also included in Table 3.13. The optimized equilibrium structure of three isomers of B_7^- are shown in Fig. 3.8.

The vibrational modes of B_7^- belong to the following IREPs of C_{6v} (I) and C_{2v} (II and III) symmetry point groups.

$$\begin{aligned} \text{I} : \Gamma_{vib} &= 2a_1 + 3e_2 + b_1 + 2b_2 + 2e_1 \\ \text{II} : \Gamma_{vib} &= 5a_1 + 3a_2 + 3b_1 + 4b_2 \\ \text{III} : \Gamma_{vib} &= 6a_1 + 2a_2 + 2b_1 + 5b_2 \end{aligned}$$

The harmonic frequencies of these fifteen vibrational modes are given in Table 3.14 and compared with the literature data [15, 18] for all three isomers discussed above.

The following MO sequence is obtained for the electronic ground state of the isomers

Table 3.13: Optimized equilibrium geometry parameters of the electronic ground state of isomer I, II and III of B_7^- (see text for details). Theoretical results available in the literature [15, 18] are also included in the table for comparison. Equilibrium minimum energy (E_{eq}), bond length (R) and bond angle (<) are given in hartree, angstrom and degree units, respectively.

parameters	B3LYP/6-311+G		[a]
	This work	Ref. [15]	Ref. [18]
Pyramidal C_{6v} Isomer; I			
E_{eq}	-173.1323	-173.8038	-173.3849
$R(B1-B2,3,4,5,6,7)$	1.689	1.655	1.626
$R(B2-B3)$	1.646	1.606	1.626
Pyramidal C_{2v} Isomer; II			
E_{eq}	-173.1320	-173.7975	-173.3748
$R(B1-B2,3,5,6)$	1.701	1.667	1.667
$R(B1-B4,7)$	1.797	1.738	1.747
$R(B2-B3)$	1.685	1.660	1.664
$R(B4-B3,5)$	1.604	1.558	1.563
Planar C_{2v} Isomer; III			
E_{eq}	-173.1149	-173.7861	-173.3701
$R(B1-B2,3)$	1.963	1.999	
$R(B1-B4,5)$	1.617	1.584	
$R(B1-B6,7)$	2.830	2.780	
$<(B2-B1-B3)$	50.70	48.96	
$<(B4-B1-B5)$	167.81	162.85	
$<(B6-B1-B7)$	115.98	113.82	

[a] While the bond lengths and angles were calculated at the B3LYP/6-31G(D) level of theory, the equilibrium minimum energy (E_{eq}) is reported at the CCSD(T)/CBS(DTQ) level of theory in Ref. [18].

of B_7^-

$$\text{I} : \begin{cases} \alpha\text{-MOs} & (1a_1)^1(1e_1)^2 \ldots\ldots\ldots\ldots (4a_1)^1(5a_1)^1(1b_1)^1(3e_1)^2(4e_1)^2 \\ \beta\text{-MOs} & (1a_1)^1(1e_1)^2 \ldots\ldots\ldots\ldots (4a_1)^1(1b_1)^1(5a_1)^1(3e_1)^2 \end{cases}$$

$$\text{II} : (1a_1)^2(1b_1)^2 \ldots\ldots\ldots\ldots (3b_1)^2(7a_1)^2(4b_2)^2(4b_1)^2(5b_2)^2$$

$$\text{III} : (1a_1)^2(1b_2)^2 \ldots\ldots\ldots\ldots (1b_1)^2(8a_1)^2(9a_1)^2(1a_2)^2(7b_2)^2$$

The important low-lying MOs of isomer I, II and III are plotted in figs. 3.9 to 3.11, respectively. The neutral isomer I of B_7 is formed in its electronic ground $\widetilde{X}^2E_1$, first $\widetilde{A}^4E_1$ and second $\widetilde{B}^2E_1$ excited states upon electron detachment from $4e_1$ (α orbital), $3e_1$ (β orbital) and $3e_1$ (α orbital) of B_7^-, respectively. Similarly, the ground $\widetilde{X}^2B_2$, first $\widetilde{A}^2B_1$, second $\widetilde{B}^2B_2$, third $\widetilde{C}^2A_1$ and fourth $\widetilde{D}^2B_1$ excited electronic states of the

Table 3.14: Harmonic frequencies (in cm^{-1}) of the fifteen vibrational modes of three isomers of B_7^- (see text for details). The present theoretical results are compared with the literature data and included in the table.

Symmetry	Mode	Frequency		
		MP2/aug-cc-pVDZ	B3LYP/6-311+G	MP2/aug-cc-pVDZ
		This work	Ref. [15]	Ref. [18]
Pyramidal C_{6v} Isomer I				
a_1	ω_1	893.6	917.7	893.6
	ω_2	283.5	293.0	283.5
b_1	ω_3	1158.6	1056.5	1158.6
b_2	ω_4	1247.7	756.2	1247.7
	ω_5	660.7	352.3	660.8
e_1	ω_6	1154.4	1120.8	1154.5
	ω_7	715.0	756.2	715.0
e_2	ω_8	1073.9	1111.3	1073.9
	ω_9	665.8	685.4	665.8
	ω_{10}	412.0	355.6	411.9
Pyramidal C_{2v} Isomer II				
a_1	ω_1	1087.6	1129.7	1087.2
	ω_2	923.9	931.6	924.5
	ω_3	636.1	652.2	636.3
	ω_4	407.0	440.5	406.9
	ω_5	244.5	239.8	244.8
a_2	ω_6	1070.3	1104.2	1069.3
	ω_7	627.8	647.7	628.5
	ω_8	397.2	422.8	397.2
b_1	ω_9	1159.7	1183.0	1159.1
	ω_{10}	1050.6	1091.3	1051.7
	ω_{11}	661.1	694.8	661.0
b_2	ω_{12}	1102.0	1094.3	1102.1
	ω_{13}	780.6	796.7	781.4
	ω_{14}	532.9	570.3	532.9
	ω_{15}	360.1	409.2	360.1
Planar C_{2v} Isomer III				
a_1	ω_1	1276.4	1303.0	1275.9
	ω_2	1200.5	1207.4	1200.3
	ω_3	786.9	816.9	786.1
	ω_4	619.4	664.7	618.7
	ω_5	478.0	566.4	478.3
	ω_6	361.0	435.1	361.3
a_2	ω_7	448.0	472.2	449.0
	ω_8	385.4	245.7	385.9
b_1	ω_9	441.1	415.9	440.8
	ω_{10}	195.8	183.4	196.7
b_2	ω_{11}	1370.9	1272.6	1372.3
	ω_{12}	1204.2	1125.8	1203.5
	ω_{13}	991.7	885.9	991.8
	ω_{14}	733.7	671.3	732.8
	ω_{15}	472.1	534.0	472.5

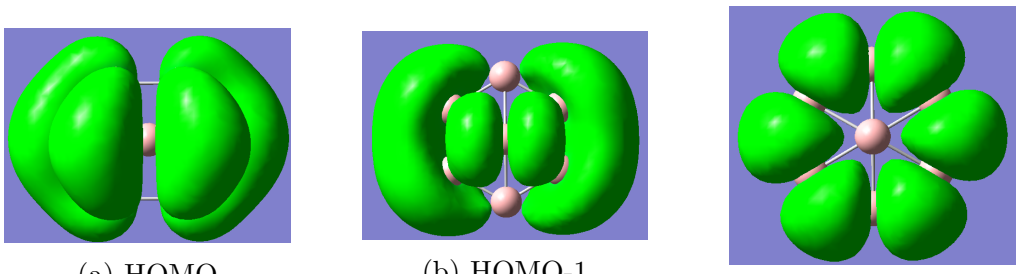

(a) HOMO (b) HOMO-1 (c) HOMO-2

Figure 3.9: Low-lying MOs of isomer I of B_7^-

neutral isomer II result from electron detachment from $5b_2$, $4b_1$, $4b_2$, $7a_1$ and $3b_1$ MOs of the anion, respectively. The electronic states $^2A_2$, $^2B_2$, $\widetilde{B'}^2B_1$, $\widetilde{C'}^2A_1$ and $\widetilde{D'}^2A_1$ of the neutral isomer III result from detachment of an electron out of $1a_2$, $7b_2$, $1b_1$, $9a_1$ and $8a_1$ MOs of the B_7^-, respectively. The VDEs of all three isomers are calculated at the U(R)OVGF/aug-cc-pVDZ level of theory and for the isomers II and III the VDEs are also calculated by MRCI method by using CASSCF orbitals using the same basis set. In the latter method the VDEs are extracted from the difference of the calculated energies of the electronic ground state of the anion B_7^- with the ground and excited states of neutral B_7. All geometry optimizations, vibrational frequency and U(R)OVGF calculations are performed using Gaussian-03 program [29] modules. On the other hand, CASSCF-MRCI calculations are carried out by using MOLPRO suite of programs [42]. The adiabatic energies of the mentioned electronic states of neutral isomers are calculated *ab initio* along the dimensionless normal displacement coordinates of the 15 vibrational degrees of freedom. These energies are calculated for $Q_i = \pm 0.10$ and in the range -1.50 to $+1.50$ with an increment of 0.25, along i^{th} vibrational mode (keeping others at their equilibrium value at $\mathbf{Q}$=0). While the electronic energies of the neutral isomer I are calculated from the VDEs calculated by the OVGF method, those of isomer II and III are calculated from the CASSCF-MRCI data.

To calculate the electronic ground state energies of isomer II of B_7^- by the CASSCF-MRCI method, the active space is designed to consist of $3a_1$, $3b_1$, $3b_2$ and $1a_2$ MOs pertinent to the C_{2v} point group symmetry designation. This includes 1, 2, 2, 0 occupied and 2, 1, 1, 1 virtual orbitals and corresponds to a distribution of 10 electrons in 10 orbitals. The core orbitals $5b_1$, $2b_1$, $3b_2$, $1a_2$ were frozen in the MRCI calculations to reduce the CPU time. The energies of the ground and excited electronic states of corresponding neutral B_7 are calculated by correlating 9 electrons in 10 orbitals as described above. This is a sufficiently large active space and expected to offer an accurate description of the electron correlation effects in B_7. The state symmetries and VDEs computed at the C_{2v} symmetry configuration are given in Table 3.15. It can be seen from the table that the VDEs obtained by the present MRCI calculations using the CAS (10,10/9,10) are in good accord with the available theoretical and experimental data [15]. The VDE of the $\widetilde{X}^2B_2$ electronic state of B_7 isomer II calculated by Nguyen *et al.* by the CCSD(T) including CBS extrapolation is 2.87 eV [18]. In the last column

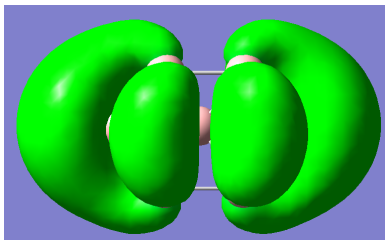

(a) HOMO

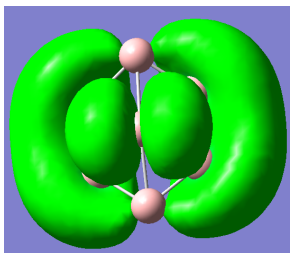

(b) HOMO-1

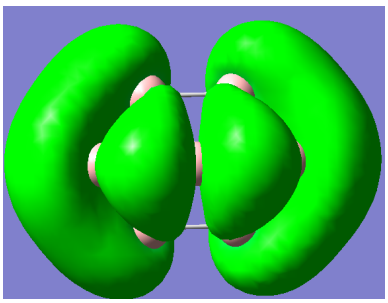

(c) HOMO-2

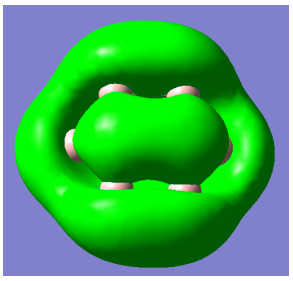

(d) HOMO-3

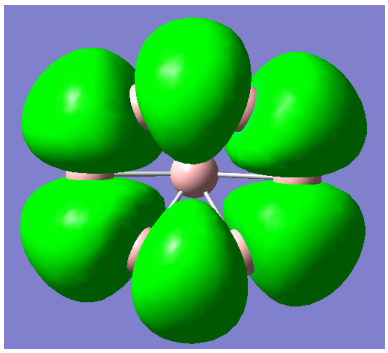

(e) HOMO-4

Figure 3.10: Low-lying MOs of isomer II of B_7^-

of Table 3.15 the VDEs obtained at the OVGF/aug-cc-pVDZ level of theory are also included. We also studied the dependence of these VDEs on the size of the CAS space as well as the choice of a basis set. The CAS (10,10/9,10) and the aug-cc-pVDZ basis set yield fairly accurate results within the affordable computational cost.

A similar study (*vide supra*) has been carried out in order to calculate electronic ground and energetically low-lying excited states of the neutral isomer III of B_7 cluster. A CAS space is constructed in terms of the a_1, b_1, b_2 and a_2 MOs of the C_{2v} symmetry point group. In this case the CAS space includes 2, 1, 1, 1 occupied and 2, 0, 2, 0 virtual orbitals in that order. A set of 10 electrons are correlated in 9 orbitals for B_7^- isomer III and 9 electrons are correlated in 9 orbitals for electronic states of neutral B_7 isomer III. The state symmetries of B_7 isomer III and VDE values are given in Table 3.15. The experimental and theoretical VDE results from the literature as well as those obtained at the OVGF/aug-cc-pVDZ level of theory are given in the table. Eventhough

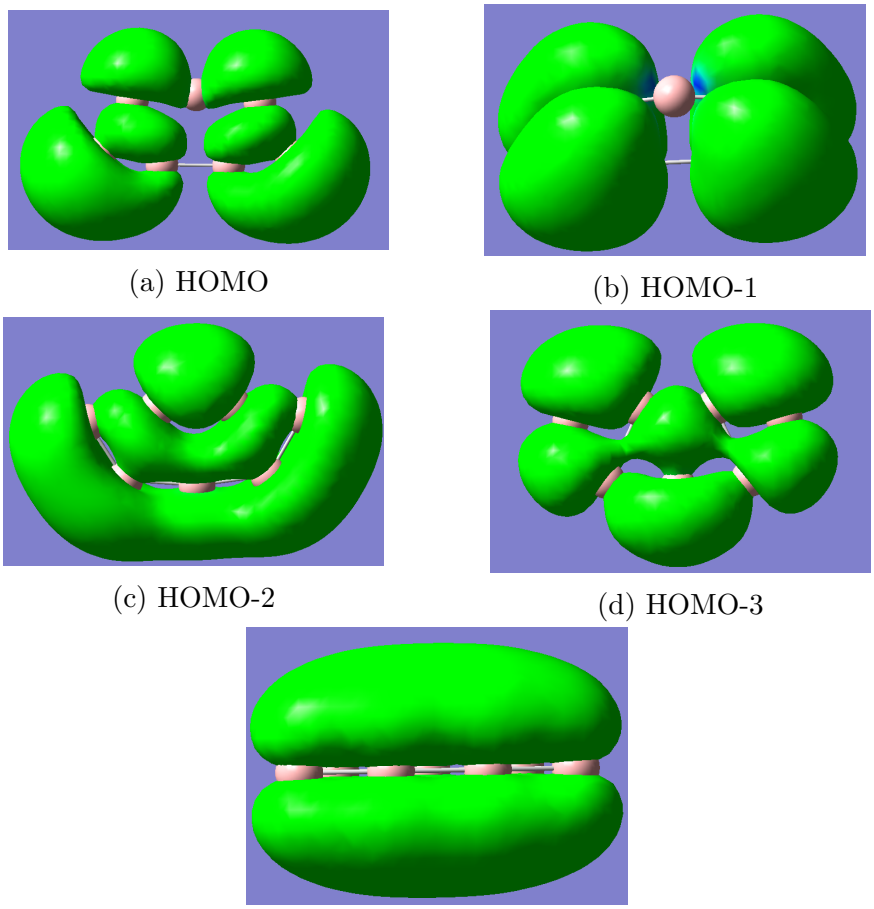

(a) HOMO

(b) HOMO-1

(c) HOMO-2

(d) HOMO-3

(e) HOMO-4

Figure 3.11: Low-lying MOs of isomer III of B_7^-

VDEs calculated by MRCI method generally agree well with the experimental and other theoretical [15] estimates, a reversal of energetic ordering of the $^2A_2$ and $^2B_2$ can be seen when compared to ROVGF calculations (cf. Table 3.15). While in the MRCI/CASSCF method, the first excited electronic state of neutral planar isomer has A_2 symmetry, in the ROVGF results it is found to have the B_2 symmetry. As explained in Section 4.2.3, the experimental observations for the second band (short vibrational progression and the peak maximum) can only be explained if the electronic ground state of neutral planar isomer belongs to B_2 symmetry. We checked this result by varying the active space in all possible ways and found that the A_2 state is lower in energy than the B_2 state in the CASSCF-MRCI results. This may be attributed to the strong correlation (relaxation) effects present in $^2A_2$ state. The state B_1 is a shakeup state, which is resulted from two electron transition located at $\sim$ 4.14 eV.

Table 3.15: Comparison of the calculated VDEs (in eV) of isomers I, II and III of B_7^- (see text for details) with the experimental and theoretical literature data [15].

Isomer of B_7^-	Electronic state of B_7^-	This study MRCI	This study OVGF	Experiment Ref. [15]	ROVGF Ref. [15]	Assignment (*cf.* Fig. 4.20)
I: C_{6v} $^3A_1$	$\widetilde{X}^2E_1$	-	2.90	2.85	2.74	X
	$\widetilde{A}^4E_1$	-	4.10	4.05	4.14	D
	$\widetilde{B}^2E_1$	-	4.34		4.28	
II: C_{2v} $^1A_1$	$\widetilde{X}^2B_2$	2.65	2.68	2.85	2.70	X
	$\widetilde{A}^2B_1$	4.25	4.10	4.21	4.07	E
	$\widetilde{B}^2B_2$	4.39	4.32	4.35	4.29	F
	$\widetilde{C}^2A_1$	5.18	5.27	5.32	5.31	H
	$\widetilde{D}^2B_1$	5.88	5.68	5.64	5.66	I
III: C_{2v} $^1A_1$	$^2A_2$	3.28	3.53	3.71	3.67	B
	$^2B_2$	3.76	3.30	3.44	3.40	A
	$\widetilde{B'}^2B_1$	4.14	-	-	-	-
	$\widetilde{C'}^2A_1$	4.77	4.83	4.60	4.92	G
	$\widetilde{D'}^2A_1$	4.92	4.88	-	4.97	-

3.3 Multistate Hamiltonian

To study the photodetachment spectrum of B_4^-, B_5^- and B_7^- cluster anions, suitable vibronic Hamiltonians of the low- lying electronic states of neutral B_4, B_5 and B_7 are constructed here using the *ab initio* electronic structure data calculated above. The Hamiltonians are constructed in terms of the normal coordinates of the vibrational modes (**Q**) of the reference electronic ground state of the anions, utilizing a diabatic electronic basis and symmetry selection rules. While the coupling between the states of same spin multiplicity is caused by the vibrational modes of appropriate symmetry and governed by the vibronic selection rules [44], the same between the states of different spin multiplicity results from more involved spin vibronic selection rules [45]. The singlet spin function $^1\Psi$ always belongs to the totally symmetric representation of the molecular point group. The three sub levels of the triplet spin function ($^3\psi_x$, $^3\psi_y$ and $^3\psi_z$) on the other hand transform as the three components of the rotational angular momentum (R_x, R_y and R_z) operator. As a result, the components of the triplet state would belong to $\Gamma_{^3\Psi_k} \otimes \Gamma_{R_k}$; k ∈x, y, z, symmetry species of the molecular symmetry point group. A non-vanishing element of the spin-orbit coupling matrix $\langle ^3\psi | H_{SO} | ^1\psi \rangle$ (H_{SO} being spin-orbit coupling operator) should therefore satisfy

$$\Gamma_{^3\Psi_k} \otimes \Gamma_{R_k} \otimes \Gamma_{^1\Psi} \supset \Gamma_{A_1} \quad , \tag{3.6a}$$

(Γ_{A_1} is totally symmetric IREP) symmetry selection rule. Otherwise, a finite distortion along suitable vibrational modes ($\mathbf{Q}$) which satisfy,

$$\Gamma_{^3\Psi_k} \otimes \Gamma_{R_k} \otimes \Gamma_{^1\Psi} \otimes \Gamma_Q \supset \Gamma_{A_1} \quad , \tag{3.6b}$$

can cause the coupling between singlet and triplet states [46].

3.3.1 Singlet and triplet states of B_4

The symmetry rule allows a coupling (in first-order) of the electronic ground $\widetilde{X}^1A_g$ state of B_4 with its excited $\widetilde{A}^1B_{2u}$ and $\widetilde{B}^1B_{2g}$ states through the vibrational modes of b_{2u} and b_{2g} symmetry, respectively, in the D_{2h} symmetry point group. Likewise, the $\widetilde{A}^1B_{2u}$ state can be coupled to the $\widetilde{B}^1B_{2g}$ state via the vibrational modes of a_u symmetry. The vibrational modes of b_{3g} and a_u symmetry can couple the triplet $\widetilde{a}^3B_{2u}$, $\widetilde{b}^3B_{1u}$ and $\widetilde{a}^3B_{2u}$, $\widetilde{c}^3B_{2g}$ states, respectively. The $\widetilde{b}^3B_{1u}$-$\widetilde{c}^3B_{2g}$ states can be coupled through the vibrational modes of b_{3u}. symmetry.

As stated above, the intersystem crossing between the singlet and triplet states is governed by the spin vibronic selection rules of Eq. 3.6. The static and dynamic components of the spin-orbit coupling are described by Eqs. 3.6a and 3.6b, respectively. The rotational angular momentum operator R_k in these equations transforms to the b_{1g}, b_{2g} and b_{3g} IREPs of the D_{2h} symmetry point group along z, y and x directions, respectively. It can be trivially analyzed in accordance with Eq. 3.6a that the static spin-orbit coupling is allowed between the $\widetilde{X}^1A_g$-$\widetilde{c}^3B_{2g}$, $\widetilde{A}^1B_{2u}$-$\widetilde{b}^3B_{1u}$ and $\widetilde{C}^1B_{1u}$-$\widetilde{a}^3B_{2u}$ electronic states of B_4 only. The direct product of the IREP's of these states yields b_{2g}, b_{3g} and b_{3g} IREPs of the rotational angular momentum operator in that order. The strength of these static spin-orbit coupling is estimated using the Briet-Pauli operator [47] within MRCI(11,10)/aug-cc-pVTZ level of theory using the MOLPRO suite of programs. Coupling strengths of $\sim$ -0.64, $\sim$ 1.15 and $\sim$ 1.46 cm^{-1} are obtained between the three pairs of states mentioned above, respectively.

For the distorted (from equilibrium) configurations of B_4, the dynamic spin-orbit coupling (in first-order) can be caused by a vibrational mode of suitable symmetry in accordance with Eq. 3.6b. Many possibilities exist in this situation. For example, the coupling between states can be caused by any component (x, y, z) of the rotational angular momentum operator provided a vibrational mode of appropriate symmetry exists. Various possibilities emerged in accordance of the selection rules of Eq. 3.6 are presented in Table 3.16. In this table the IREP of the x, y and z component of the rotational angular momentum operator is given in the second row. The symmetry of the electronic states are given in the first row and first column. The symmetry of the vibrational mode which can induce spin-orbit coupling in the distorted nuclear geometry is given in the rest of the table. For example, for a coupling between the $\widetilde{X}$ and $\widetilde{a}$ states along the Z component of the rotational angular momentum operator, the selection rule reads, $[A_g \otimes b_{1g} \otimes B_{2u}] \otimes b_{3u} \supset A_g$ in the D_{2h} symmetry point group. The remaining coupling vibrational modes given in the table can be determined in a similar way. A

Table 3.16: Selection rules for the dynamic spin vibronic coupling for the singlet and triplet electronic states of B_4.

	$\widetilde{a}^3B_{2u}$			$\widetilde{b}^3B_{1u}$			$\widetilde{c}^3B_{2g}$		
	$b_{1g}(z)$	$b_{2g}(y)$	$b_{3g}(x)$	b_{1g}(z)	b_{2g}(y)	b_{3g}(x)	b_{1g}(z)	b_{2g}(y)	b_{3g}(x)
$\widetilde{X}^1A_g$	b_{3u}	a_u	b_{1u}	a_u	b_{3u}	b_{2u}	b_{3g}	a_g	b_{1g}
$\widetilde{A}^1B_{2u}$	b_{1g}	b_{2g}	b_{3g}	b_{2g}	b_{1g}	a_g	b_{1u}	b_{2u}	b_{3u}
$\widetilde{B}^1B_{2g}$	b_{1u}	b_{2u}	b_{3u}	b_{2u}	b_{1u}	a_u	b_{1g}	b_{2g}	b_{3g}
$\widetilde{C}^1B_{1u}$	b_{2g}	b_{1g}	a_g	b_{1g}	b_{2g}	b_{3g}	b_{2u}	b_{1u}	a_u

calculation of all the spin-vibronic coupling parameters is out of the scope of the present investigations and will be taken up separately in a forthcoming publication.

Given the very small magnitude of the static spin-orbit couplings and proposed future work (which is much involved as regard to the calculation of parameters of various order and fitting of the Hamiltonian) on the dynamic spin-orbit coupling elements, we consider here to understand the nonadiabatic electronic coupling effects only. The vibronic Hamiltonian of the low-lying six electronic states of B_4 in such a situation can be expressed in a block diagonal form as

$$\mathcal{H} = (\mathcal{T}_N + \mathcal{V}_0)\mathbf{1_6} + \begin{pmatrix} u_{\widetilde{X}} & u_{\widetilde{X}\widetilde{A}} & u_{\widetilde{X}\widetilde{B}} & 0 & 0 & 0 \\ & u_{\widetilde{A}} & u_{\widetilde{A}\widetilde{B}} & 0 & 0 & 0 \\ h.c & & u_{\widetilde{B}} & 0 & 0 & 0 \\ 0 & 0 & 0 & u_{\widetilde{a}} & u_{\widetilde{a}\widetilde{b}} & u_{\widetilde{a}\widetilde{c}} \\ 0 & 0 & 0 & & u_{\widetilde{b}} & u_{\widetilde{b}\widetilde{c}} \\ 0 & 0 & 0 & h.c & & u_{\widetilde{c}} \end{pmatrix}, \tag{3.7a}$$

where, $(\mathcal{T}_N + \mathcal{V}_0)$, represents the unperturbed Hamiltonian of the reference state ($\widetilde{X}^2B_{1u}$ state of B_4^-), treated as harmonic with

$$\mathcal{T}_N = -\frac{1}{2}\sum_{i=1}^{6}\omega_i\left(\frac{\partial^2}{\partial Q_i^2}\right), \tag{3.7b}$$

$$\mathcal{V}_0 = \frac{1}{2}\sum_{i=1}^{6}\omega_i Q_i^2 \tag{3.7c}$$

$\mathbf{I}_6$ is a 6×6 Unit matrix. The elements of the electronic (matrix) Hamiltonian in equation 3.7a represent the energies of the diabatic electronic states (diagonal) and their coupling potentials (off-diagonal) of B_4. These elements are expressed in terms of a standard Taylor series expansion around the reference equilibrium configuration (at

Table 3.17: Linear intrastate coupling parameter (κ) for the $\widetilde{X}^1A_g$, $\widetilde{a}^3B_{2u}$, $\widetilde{b}^3B_{1u}$, $\widetilde{A}^1B_{2u}$, $\widetilde{c}^3B_{2g}$ and $\widetilde{B}^1B_{2g}$ electronic states of B_4 derived from the CASSCF-MRCI potential energy data. All quantities are given in eV.

modes	frequency	κ					
(symmetry)	(eV)	$\widetilde{X}^1A_g$	$\widetilde{a}^3B_{2u}$	$\widetilde{b}^3B_{1u}$	$\widetilde{A}^1B_{2u}$	$\widetilde{c}^3B_{2g}$	$\widetilde{B}^1B_{2g}$
$\nu_1(a_g)$	0.1414	-0.0147	0.0169	-0.0568	0.0132	-0.1907	-0.1863
$\nu_2(a_g)$	0.0997	0.1737	-0.1736	-0.0114	-0.1634	0.0115	0.0048

Q=0) as

$$u_k = E_0^{(k)} + \sum_{i=1}^{2} \kappa_i^{(k)} Q_i + \frac{1}{2}\sum_{i=1}^{6} \gamma_i^{(k)} Q_i^2 + \frac{1}{2}\gamma_{12}^{(k)} Q_1 Q_2, k \in X, A, B, a, b, c \quad (3.7d)$$

$$u_{kl} = \sum_i \lambda_i^{kl} Q_i + \sum_m \sum_n \lambda_{mn}^{kl} Q_m Q_n, \quad (3.7e)$$

where $kl \in (\widetilde{X}\widetilde{A},\ \widetilde{X}\widetilde{B},\ \widetilde{A}\widetilde{B},\ \widetilde{a}\widetilde{b},\ \widetilde{a}\widetilde{c},\ \widetilde{b}\widetilde{c})$ and $i,\ m,\ n \in$ relevant coupling vibrational modes. In the above equations the quantity $E_0^{(k)}$ represents the VDE of the k^{th} electronic state. $\kappa_i^{(k)}$ and $\gamma_i^{(k)}$ are the linear and second-order coupling parameters of the i^{th} vibrational mode in the k^{th} electronic state. The quantity $\gamma_{12}^{(k)}$ is bilinear coupling parameter along the two symmetric vibrational modes. The quantity $\lambda_i^{(kl)}$ is the linear vibronic coupling parameter between the k and l electronic states along the i^{th} vibrational mode. The quantity $\lambda_{mn}^{(kl)}$ is the interstate bilinear vibronic coupling parameter between the k and l electronic states along the m^{th} and n^{th} vibrational mode. After some algebra, this coupling parameter in a second-order coupling model can be expressed as :

$$\lambda_{i,j}^{1,2} = \frac{1}{4}\sqrt{\frac{\partial^2}{\partial Q_i^2}\frac{\partial^2}{\partial Q_j^2}(V_2 - V_1)^2 - 2(\gamma_i^2 - \gamma_i^1)(\gamma_j^2 - \gamma_j^1)} \quad . \quad (3.8)$$

All the coupling parameters defined above are estimated by performing extensive *ab initio* calculations of electronic energies as discussed in Sec. 3.2.1. The calculated adiabatic electronic energies are fitted to the adiabatic form of the diabatic electronic Hamiltonian of Eq. 3.7a to estimate these parameters. We note that the interstate bilinear parameter as defined in Eq. 3.8 above are estimated both by a two-dimensional fit (using MATHEMATICA [48]) as well as a suitable finite difference of the electronic energies. The linear intrastate and interstate coupling parameters are given in Tables 3.17, 3.18. The interstate bilinear coupling parameters are given in Table 3.19.

The coupling parameters of Table 3.17 reveal that the symmetric vibrational mode ν_1 is active in the $\widetilde{c}^3B_{2g}$ and $\widetilde{B}^1B_{2g}$ electronic states only. The vibrational mode ν_2 on the

Table 3.18: Linear interstate coupling parameters (λ^{kl}) for the electronic states of B_4 estimated from the CASSCF-MRCI potential energy data. All quantities are given in eV.

	Coupled states	b_{1u}	b_{2u}	b_{3u}	b_{3g}
$\lambda^{X,A}$	$\widetilde{X}^1A_g$-$\widetilde{A}^1B_{2u}$	-	-	-	-
$\lambda^{X,B}$	$\widetilde{X}^1A_g$-$\widetilde{B}^1B_{2g}$	-	-	-	-
$\lambda^{A,B}$	$\widetilde{A}^1B_{2u}$-$\widetilde{B}^1B_{2g}$	-	-	-	-
$\lambda^{a,b}$	$\widetilde{a}^3B_{2u}$-$\widetilde{b}^3B_{1u}$	-	-	-	0.1759
$\lambda^{a,c}$	$\widetilde{a}^3B_{2u}$-$\widetilde{c}^3B_{2g}$	-	-	-	-
$\lambda^{b,c}$	$\widetilde{b}^3B_{1u}$-$\widetilde{c}^3B_{2g}$	-	-	0.0794	-

Table 3.19: Interstate bilinear coupling parameter (in eV) for the electronic states of B_4

States	Symmetry of coupling mode	coupled modes	λ
$\widetilde{X}^1A_g$-$\widetilde{A}^1B_{2u}$	b_{2u}	$a_g(\nu_1)$,$b_{2u}(\nu_4)$	-
		$a_g(\nu_2)$,$b_{2u}(\nu_4)$	-
		$b_{1u}(\nu_3)$,$b_{3g}(\nu_6)$	0.0692
$\widetilde{A}^1B_{2u}$-$\widetilde{B}^1B_{2g}$	a_u	$b_{3u}(\nu_5)$,$b_{3g}(\nu_6)$	-
$\widetilde{a}^3B_{2u}$-$\widetilde{b}^3B_{1u}$	b_{3g}	$a_g(\nu_1)$,$b_{3g}(\nu_6)$	-
		$a_g(\nu_1)$,$b_{3g}(\nu_6)$	-
		$b_{1u}(\nu_3)$,$b_{2u}(\nu_4)$	0.0141
$\widetilde{a}^3B_{2u}$-$\widetilde{c}^3B_{2g}$	a_u	$b_{3u}(\nu_5)$,$b_{3g}(\nu_6)$	-
$\widetilde{b}^3B_{1u}$-$\widetilde{c}^3B_{2g}$	b_{3u}	$a_g(\nu_1)$, $b_{3u}(\nu_5)$	-
		$a_g(\nu_2)$, $b_{3u}(\nu_5)$	-

other hand is expected to be significantly excited in the $\widetilde{X}^1A_g$, $\widetilde{a}^3B_{2u}$ and $\widetilde{A}^1B_{2u}$ electronic states of B_4. It can be seen from Table 3.18 that the coupling between the singlet states is insignificant (in first-order). The $\widetilde{a}^3B_{2u}$-$\widetilde{b}^3B_{1u}$ and $\widetilde{b}^3B_{1u}$-$\widetilde{c}^3B_{2g}$ electronic states are however coupled, along the ν_6 and ν_5 vibrational modes, respectively. Simultaneous displacements along ν_5 and ν_6 vibrational modes can cause a coupling between the $\widetilde{X}^1A_g$ and $\widetilde{A}^1B_{2u}$ electronic states. Coupling between $\widetilde{a}^3B_{2u}$-$\widetilde{b}^3B_{1u}$ electronic states can also be caused by a simultaneous displacement along the ν_3 and ν_5 vibrational modes. The diagonal second-order and the bilinear coupling parameters given in Table 3.20 are also significant.

In order to confirm that the coupling parameters presented above do not suffer from any spin contamination (although we have confirmed above that the spin contamination is negligible in the calculated UB3LYP results), we have calculated them again using the vibrational coordinates derived from the ROMP2 calculations. The electronic energies and the parameters of the Hamiltonian of Eq. 3.7a are calculated with the similar approach as mentioned above. The calculated Hamiltonian parameters are given in Tables 3.21-3.24. It can be seen in comparison with the data in Tables 3.17-3.20 that

Table 3.20: The diagonal second-order (γ) and bilinear (γ_{12}) coupling parameters (in eV) for the $\widetilde{X}^1A_g$, $\widetilde{a}^3B_{2u}$, $\widetilde{b}^3B_{1u}$, $\widetilde{A}^1B_{2u}$, $\widetilde{c}^3B_{2g}$ and $\widetilde{B}^1B_{2g}$ electronic states of B_4.

modes	γ					
(symmetry)	$\widetilde{X}^1A_g$	$\widetilde{a}^3B_{2u}$	$\widetilde{b}^3B_{1u}$	$\widetilde{A}^1B_{2u}$	$\widetilde{c}^3B_{2g}$	$\widetilde{B}^1B_{2g}$
$\nu_1(a_g)$	0.0038	-0.0106	0.0012	-0.0098	0.0116	0.0120
$\nu_2(a_g)$	-0.0354	-0.0078	0.0152	-0.0044	0.0098	0.0088
$\nu_3(b_{1u})$	0.0938	-0.0446	0.0532	-0.1214	0.0012	0.0058
$\nu_4(b_{2u})$	0.0126	-0.0274	-0.0110	-0.0194	-0.0028	-0.0010
$\nu_5(b_{3u})$	0.0324	-0.0518	-0.0072	-0.0512	0.0142	-0.0480
$\nu_6(b_{3g})$	-0.0098	-0.0054	0.0046	0.0140	0.0068	0.0094
bilinear ν_1-ν_2	-0.0127	0.0146	-0.0013	0.0143	0.0000	0.0013

Table 3.21: Linear intrastate coupling parameter (κ) for the $\widetilde{X}^1A_g$, $\widetilde{a}^3B_{2u}$, $\widetilde{b}^3B_{1u}$, $\widetilde{A}^1B_{2u}$, $\widetilde{c}^3B_{2g}$ and $\widetilde{B}^1B_{2g}$ electronic states of B_4 derived from the CASSCF-MRCI potential energy data calculated using the ROMP2 optimized geometry of B_4^-. All quantities are given in eV.

modes	frequency	κ					
(symmetry)	(eV)	$\widetilde{X}^1A_g$	$\widetilde{a}^3B_{2u}$	$\widetilde{b}^3B_{1u}$	$\widetilde{A}^1B_{2u}$	$\widetilde{c}^3B_{2g}$	$\widetilde{B}^1B_{2g}$
$\nu_1(a_g)$	0.1449	-0.0195	0.0321	-0.0526	0.0297	-0.1951	-0.1891
$\nu_2(a_g)$	0.0993	0.1592	-0.1732	-0.0145	-0.1647	0.0022	-0.0072

the two sets of parameters are in very good accord with each other. The coupling strength between the $\widetilde{b}$ and $\widetilde{c}$ electronic states along the ν_5 vibrational mode is about a factor of the two lower in the results of Table 3.22. The importance of the above coupling parameters in the photodetachment spectrum of B_4^- is examined in detail in Chapter 4.

Table 3.22: Linear interstate coupling parameters (λ^{kl}) for the electronic states of B_4 estimated from the CASSCF-MRCI potential energy data calculated using the ROMP2 optimized geometry of B_4^-. All quantities are given in eV.

	Coupled states	b_{1u}	b_{2u}	b_{3u}	b_{3g}
$\lambda^{X,A}$	$\widetilde{X}^1A_g$-$\widetilde{A}^1B_{2u}$	-	-	-	-
$\lambda^{X,B}$	$\widetilde{X}^1A_g$-$\widetilde{B}^1B_{2g}$	-	-	-	-
$\lambda^{A,B}$	$\widetilde{A}^1B_{2u}$-$\widetilde{B}^1B_{2g}$	-	-	-	-
$\lambda^{a,b}$	$\widetilde{a}^3B_{2u}$-$\widetilde{b}^3B_{1u}$	-	-	-	0.1732
$\lambda^{a,c}$	$\widetilde{a}^3B_{2u}$-$\widetilde{c}^3B_{2g}$	-	-	-	-
$\lambda^{b,c}$	$\widetilde{b}^3B_{1u}$-$\widetilde{c}^3B_{2g}$	-	-	0.0362	-

Table 3.23: Interstate bilinear coupling parameter (in eV) for the electronic states of B_4 calculated using the ROMP2 optimized geometry of B_4^-

States	Symmetry of coupling mode	coupled modes	λ
$\widetilde{X}^1A_g$-$\widetilde{A}^1B_{2u}$	b_{2u}	$a_g(\nu_1)$,$b_{2u}(\nu_4)$	-
		$a_g(\nu_2)$,$b_{2u}(\nu_4)$	-
		$b_{1u}(\nu_3)$,$b_{3g}(\nu_6)$	0.2165
$\widetilde{A}^1B_{2u}$-$\widetilde{B}^1B_{2g}$	a_u	$b_{3u}(\nu_5)$,$b_{3g}(\nu_6)$	0.0840
$\widetilde{a}^3B_{2u}$-$\widetilde{b}^3B_{1u}$	b_{3g}	$a_g(\nu_1)$,$b_{3g}(\nu_6)$	-0.0079
		$a_g(\nu_1)$,$b_{3g}(\nu_6)$	-0.0131
		$b_{1u}(\nu_3)$,$b_{2u}(\nu_4)$	-
$\widetilde{a}^3B_{2u}$-$\widetilde{c}^3B_{2g}$	a_u	$b_{3u}(\nu_5)$,$b_{3g}(\nu_6)$	-
$\widetilde{b}^3B_{1u}$-$\widetilde{c}^3B_{2g}$	b_{3u}	$a_g(\nu_1)$, $b_{3u}(\nu_5)$	
		$a_g(\nu_2)$, $b_{3u}(\nu_5)$	-

Table 3.24: The diagonal second-order (γ) and bilinear (γ_{12}) coupling parameters (in eV) for the $\widetilde{X}^1A_g$, $\widetilde{a}^3B_{2u}$, $\widetilde{b}^3B_{1u}$, $\widetilde{A}^1B_{2u}$, $\widetilde{c}^3B_{2g}$ and $\widetilde{B}^1B_{2g}$ electronic states of B_4 calculated using the ROMP2 optimized geometry of B_4^-

modes	γ					
(symmetry)	$\widetilde{X}^1A_g$	$\widetilde{a}^3B_{2u}$	$\widetilde{b}^3B_{1u}$	$\widetilde{A}^1B_{2u}$	$\widetilde{c}^3B_{2g}$	$\widetilde{B}^1B_{2g}$
$\nu_1(a_g)$	0.0045	-0.0117	0.0008	-0.0108	0.0110	0.0113
$\nu_2(a_g)$	-0.0262	-0.0059	0.0163	-0.0025	0.0091	0.0081
$\nu_3(b_{1u})$	0.0694	-0.0244	0.0869	-0.1064	-0.0415	0.0038
$\nu_5(b_{2u})$	0.0114	-0.0235	-0.0118	-0.0201	-0.0003	0.0001
$\nu_4(b_{3u})$	0.0310	-0.0542	-0.0061	-0.0558	-0.0027	-0.0396
$\nu_6(b_{3g})$	-0.0087	-0.0366	0.0578	0.0309	0.0005	0.0025
bilinear ν_1-ν_2	-0.0121	0.0134	-0.0024	0.0135	0.0000	0.0006

3.3.2 Doublet electronic states of B_5

While the symmetric vibrational modes are Condon active in the energetically low-lying six electronic states of B_5, the vibrational modes of b_2 symmetry can cause symmetry allowed coupling between its $\widetilde{X}$ and $\widetilde{A}$, $\widetilde{C}$ and $\widetilde{E}$ electronic states. Similarly, the $\widetilde{X}$-$\widetilde{D}$ coupling is allowed through the vibrational modes of a_2 symmetry. The vibrational modes of b_2 symmetry can couple $\widetilde{A}$-$\widetilde{B}$, $\widetilde{B}$-$\widetilde{C}$ and $\widetilde{B}$-$\widetilde{E}$ electronic states. Whereas, the vibrational modes of b_1 symmetry can couple $\widetilde{A}$-$\widetilde{D}$, $\widetilde{C}$-$\widetilde{D}$ and $\widetilde{D}$-$\widetilde{E}$ electronic states of B_5. The vibrational modes of a_2 symmetry can also cause a coupling between the $\widetilde{B}$ and $\widetilde{D}$ electronic states.

A diabatic vibronic Hamiltonian corresponding to this coupling scheme can be written as

$$\mathcal{H} = (\mathcal{T}_N + \mathcal{V}_0)\mathbf{1_6} + \begin{pmatrix} u_{\widetilde{X}} & u_{\widetilde{X}\widetilde{A}} & 0 & u_{\widetilde{X}\widetilde{C}} & u_{\widetilde{X}\widetilde{D}} & u_{\widetilde{X}\widetilde{E}} \\ & u_{\widetilde{A}} & u_{\widetilde{A}\widetilde{B}} & 0 & u_{\widetilde{A}\widetilde{D}} & 0 \\ & & u_{\widetilde{B}} & u_{\widetilde{B}\widetilde{C}} & u_{\widetilde{B}\widetilde{D}} & u_{\widetilde{B}\widetilde{E}} \\ & h.c & & u_{\widetilde{C}} & u_{\widetilde{C}\widetilde{D}} & 0 \\ & & & & u_{\widetilde{D}} & u_{\widetilde{D}\widetilde{E}} \\ & & & & & u_{\widetilde{E}} \end{pmatrix} \tag{3.9a}$$

The nuclear kinetic $\mathcal{T}_N$ and potential $\mathcal{V}_0$ energy terms of the reference electronic ground state of B_5^- are defined in the same way as in Eqs. 3.7a. In this case the index i runs from 1 to 9.

The computed *ab initio* potential energies of the electronic states of B_5 reveal considerable anharmonicity (see below) along the symmetric vibrational modes particularly along ν_3. While some of the potential functions could be represented very well by a second-order Taylor expansion, many of them required expansion upto fourth or even sixth-order terms for a satisfactory description. The u_k's in Eq. (3.9a) are therefore expressed in general as

$$u_k = E_0^{(k)} + \sum_{i=1}^{4} f_i^{(k)} + \frac{1}{2}\sum_{i=5}^{9} \gamma_i^{(k)} {Q_i}^2 + \frac{1}{2}\sum_{i=1}^{4}\sum_{j>i}^{4} \gamma_{ij}^{(k)} Q_i Q_j + \frac{1}{2}\sum_{i=7}^{9}\sum_{j>i}^{9} \gamma_{ij}^{(k)} Q_i Q_j \tag{3.9b}$$

The parameters of the above equation are defined in the same way as in Sec. 3.3.1. The function $f_i^{(k)}$ is defined as

$$f_i^{(k)} = \frac{1}{n!}\sum_{n=1}^{6} c_n^{(k)} Q_i^n. \tag{3.9c}$$

In the following a fourth-order polynomial is used to fit the energies of the $\widetilde{B}$ electronic state along ν_2, $\widetilde{D}$ and $\widetilde{E}$ electronic states along ν_1, ν_2 and ν_4 vibrational modes. The energies of the $\widetilde{C}$, $\widetilde{D}$ and $\widetilde{E}$ electronic states along ν_3 are fitted by a sixth-order polynomial function. A second-order function is found to be adequate for the remaining electronic states and vibrational modes. The elements u_{kl} of Eq. (3.9a) are represented as

$$u_{kl} = \sum_i \lambda_i^{kl} Q_i. \tag{3.9d}$$

Some of the fit parameters of the potential function of Eq. 3.9(b-c) along the symmetric vibrational modes are given in Table 3.25. The fourth and sixth-order polynomial fits of the *ab initio* VDEs of the electronic states are shown in Fig. 3.12. It can be seen from this figure that the *ab initio* energy points are very well represented by these higher-order polynomial functions. Strong anharmonicity of the electronic energies, particularly in the vicinity of the degeneracies [see later in Fig. 3.17], is revealed by the data of Table 3.25. The latter also reveal large coupling strength of ν_2 in the $\widetilde{D}$ state and ν_3 in the $\widetilde{X}$

Table 3.25: Fit parameters (in eV) of the potential energy function [Eq. (3.9c)] of the $\widetilde{X}^2B_2$, $\widetilde{A}^2A_1$, $\widetilde{B}^2B_2$, $\widetilde{C}^2A_1$, $\widetilde{D}^2B_1$ and $\widetilde{E}^2A_1$ electronic states of B_5^- are derived from the CASSCF-MRCI data.

State	Mode	C_1	C_2	C_3	C_4	C_5	C_6
$\widetilde{X}^2B_2$	ν_1	-0.0326	0.0012	-	-	-	-
	ν_2	-0.0340	-0.0019	-	-	-	-
	ν_3	0.1274	-0.0088	-	-	-	-
	ν_4	-0.0453	0.0074	-	-	-	-
$\widetilde{A}^2A_1$	ν_1	-0.0324	0.0050	-	-	-	-
	ν_2	-0.0431	-0.0095	-	-	-	-
	ν_3	-0.0123	-0.0330	-	-	-	-
	ν_4	-0.0376	-0.0086	-	-	-	-
$\widetilde{B}^2B_2$	ν_1	0.1428	0.0047	-0.0010	-0.0001	-	-
	ν_2	0.0850	-0.0032	-0.0003	-0.0022	-	-
	ν_3	-0.1348	0.0015	-0.0272	-0.0246	-	-
	ν_4	0.0738	-0.0269	-0.0085	-0.0012	-	-
$\widetilde{C}^2A_1$	ν_1	0.1353	-0.0070	-	-	-	-
	ν_2	-0.0301	-0.0014	-0.0026	0.0010	-	-
	ν_3	-0.0368	0.0139	-0.0042	-0.0135	-0.0047	0.0001
	ν_4	0.0749	-0.0130	-	-	-	-
$\widetilde{D}^2B_1$	ν_1	0.0290	-0.0014	-0.0039	-0.0003	-	-
	ν_2	-0.1806	0.0048	-0.0003	0.0006	-	-
	ν_3	-0.0632	0.0383	0.0326	-0.0411	-0.0033	0.0143
	ν_4	-0.0227	-0.0026	-0.0004	0.0000	-	-
$\widetilde{E}^2A_1$	ν_1	0.1483	0.0025	-0.0003	0.0011	-	-
	ν_2	0.0419	-0.0280	-0.0107	-0.0005	-	-
	ν_3	-0.1171	-0.0048	0.0068	0.0306	-0.0391	0.0130
	ν_4	0.0644	-0.0167	-0.0006	0.0005	-	-

Table 3.26: Linear interstate coupling parameters λ^{kl} [in eV] for the electronic states of the B_5 estimated from the CASSCF- MRCI data.

modes (symmetry)	$\lambda^{X,A}$ $\tilde{X}^2B_2$-$\tilde{A}^2A_1$	$\lambda^{X,C}$ $\tilde{X}^2B_2$ -$\tilde{C}^2A_1$	$\lambda^{X,E}$ $\tilde{X}^2B_2$-$\tilde{E}^2A_1$	$\lambda^{A,B}$ $\tilde{A}^2A_1$-$\tilde{B}^2B_2$	$\lambda^{B,C}$ $\tilde{B}^2B_2$-$\tilde{C}^2A_1$	$\lambda^{B,E}$ $\tilde{B}^2B_2$-$\tilde{E}^2A_1$	$\lambda^{D,E}$ $\tilde{D}^2B_1$-$\tilde{E}^2A_1$
$\nu_5(a_2)$	-	-	-	-	-	-	-
$\nu_6(b_1)$	-	-	-	-	-	-	0.0608
$\nu_7(b_2)$	0.1174	0.1279	0.2261	-	-	0.0819	-
$\nu_8(b_2)$	-	0.1545	-	0.0989	0.0394	-	-
$\nu_9(b_2)$	0.0753	0.2216	-	-	0.1643	0.1625	-

and $\widetilde{B}$ states. The coupling strengths of the remaining vibrational modes are moderate or weak.

The interstate coupling parameters of the Eq. 3.9(d) are given in Table 3.26. An analysis of the data presented in this table reveal that the coupling strength of vibrational mode ν_9 in the $\widetilde{X}$-$\widetilde{A}$, $\widetilde{X}$-$\widetilde{C}$, $\widetilde{B}$-$\widetilde{C}$ and $\widetilde{B}$-$\widetilde{E}$, ν_7 in the $\widetilde{X}$-$\widetilde{E}$, ν_8 in the $\widetilde{A}$-$\widetilde{B}$ and ν_6 in the $\widetilde{D}$-$\widetilde{E}$ electronic states is largest. The second-order and the bilinear coupling parameters of the remaining modes are given in Table 3.27.

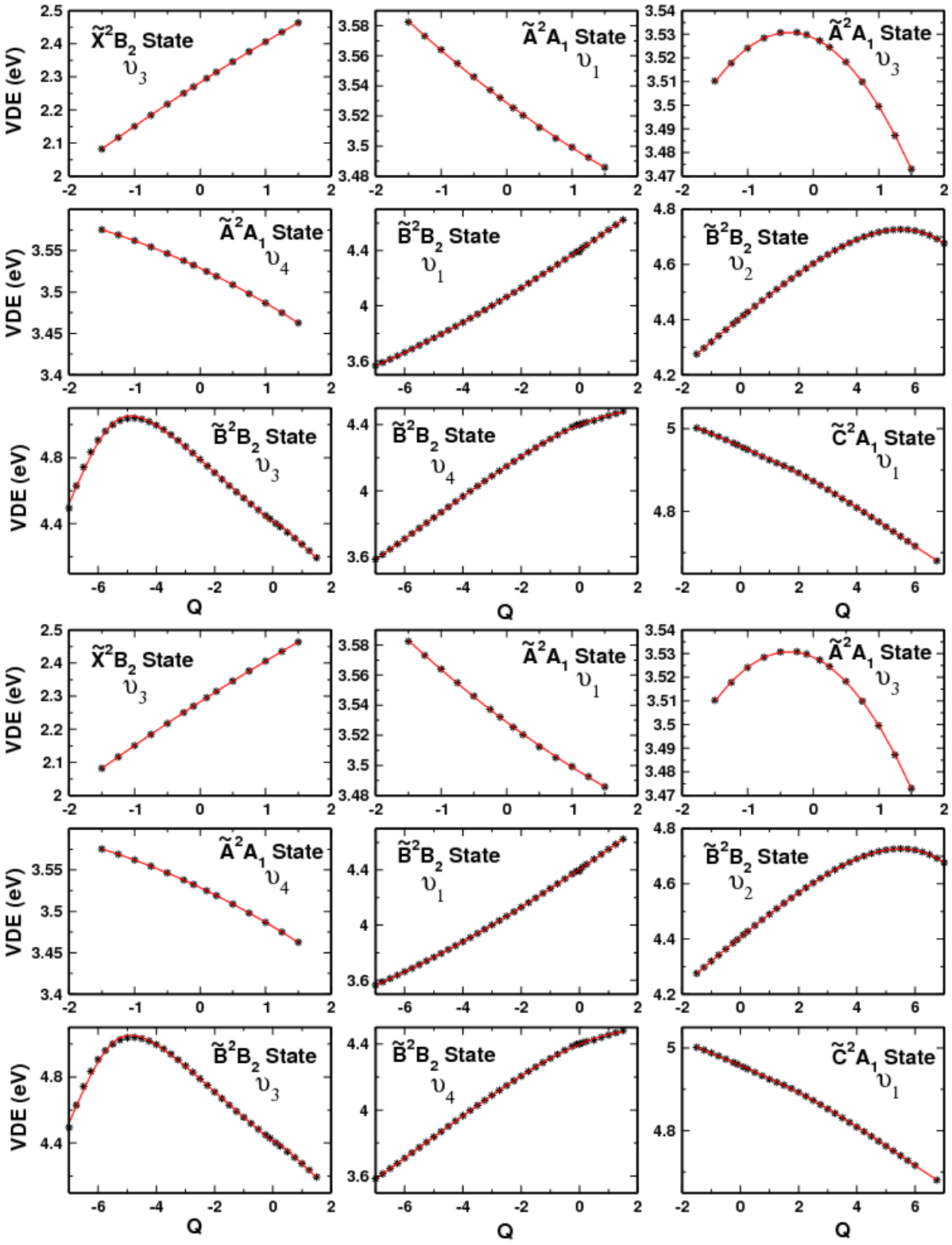

Figure 3.12: The higher order polynomial (fourth or sixth order) fit (solid line) of the calculated *ab initio* electronic energies (points) of B_5 along symmetric vibrational modes indicated in the panel. The parameters of the Table 3.25 are derived from the above fit.

Table 3.27: The diagonal second-order and bilinear coupling parameters of Eq. 3.9(b) of the vibronic Hamiltonian of B_5. The parameter values are given in eV.

modes	γ					
(symmetry)	$\widetilde{X}^2B_2$	$\widetilde{A}^2A_1$	$\widetilde{B}^2B_2$	$\widetilde{C}^2A_1$	$\widetilde{D}^2B_1$	$\widetilde{E}^2A_1$
$\nu_5(a_2)$	-0.0002	-0.0118	0.0086	-0.0360	-0.0120	-0.0464
$\nu_6(b_1)$	0.0212	-0.0030	-0.0288	-0.0122	-0.0264	-0.0130
$\nu_7(b_2)$	-0.0170	0.0288	0.0240	0.0062	-0.0114	0.0452
$\nu_8(b_2)$	-0.0078	-0.0382	0.0136	0.0240	-0.1206	-0.0206
$\nu_9(b_2)$	0.0064	0.0322	-0.0954	0.0670	-0.1360	-0.0148
Intrastate bilinear coupling constants						
$\nu_1\nu_2$	0.0060	0.0106	-0.0102	-0.0188	0.0215	-0.0449
$\nu_1\nu_3$	-0.0034	-0.0164	0.0050	0.0314	0.0060	0.0350
$\nu_1\nu_4$	0.0005	-0.0008	0.0000	-0.0051	-0.0028	-0.0284
$\nu_2\nu_3$	0.0026	0.0216	0.0019	0.0021	0.0003	0.0283
$\nu_2\nu_4$	0.0009	-0.0032	-0.0085	-0.0040	0.0005	-0.0166
$\nu_3\nu_4$	-0.0028	0.0017	-0.0032	0.0072	0.0003	0.0059
$\nu_7\nu_8$	0.0013	0.0434	-0.0200	-0.0038	0.0450	0.0092
$\nu_7\nu_9$	-0.0009	-0.0065	-0.0010	0.0034	0.0044	-0.0190
$\nu_8\nu_9$	0.0043	-0.0185	0.0372	-0.0816	0.0880	-0.0216

3.3.3 Electronic states of B_7

It is well established that coupling of electronic and nuclear motion is ubiquitous in polyatomic systems and such coupling leads to complex structure of electronic spectra and ultrafast nonradiative decay of electronically excited molecules [49,50]. Taking these facts into account, to study the photodetachment spectrum of B_7^- cluster anion, coupled vibronic Hamiltonians of the energetically low-lying electronic states of isomer I, II and III of neutral B_7 are constructed here using the *ab initio* electronic energy data calculated above. It is already discussed that the isomer I supports orbitally degenerate electronic states, where as electronic states of isomer II and III are nondegenerate. The electronic degeneracy of isomer I is symmetry enforced and undergoes JT splitting along suitable symmetry allowed nuclear coordinates. The resulting JT split electronic energy surfaces may further interact with the energetically close nondegenerate electronic states and can undergo PJT type of coupling. The coupling of the nondegenerate electronic states of isomer II and III can also be caused by suitable symmetry allowed vibrational modes. The discussions above reveal that this system quite unique in terms of rich variety of vibronic coupling mechanisms that could exist in a single molecular system and to the best of our knowledge, dynamics of such a complex system has not been treated in the literature so far.

The Hamiltonians of neutral B_7 originating from the three isomers of B_7^- are constructed separately here in terms of the normal displacement coordinates of the vibrational modes ($\mathbf{Q}$) of the reference electronic ground state of the anions, utilizing a diabatic electronic basis and symmetry selection rules [44]. The first-order coupling within

(intra) and between (inter) electronic states is governed by the symmetry selection rule; $\Gamma_i \otimes \Gamma_Q \otimes \Gamma_j \supset A_1$. The symbol, Γ represents the IREP, i and j are the electronic state indices, and Q represents the coupling vibrational mode.

While the totally symmetric a_1 vibrational modes are intrastate coupling modes, the e_2 modes are JT active in isomer I. The e_2 modes lift the degeneracy of $\widetilde{X}^2E_1$, $\widetilde{A}^4E_1$ and $\widetilde{B}^2E_1$ electronic states of this isomer. Therefore, all six JT split components of these electronic states are relevant for the nuclear dynamics of isomer I within the energy range considered here. The $\widetilde{X}^2E_1$ -$\widetilde{B}^2E_1$ electronic states can also be coupled by the vibrational modes of e_2 symmetry. The *ab initio* electronic structure data reveal negligible coupling in this case. The coupling between states $\widetilde{X}^2E_1$ -$\widetilde{A}^4E_1$ and $\widetilde{A}^4E_1$ -$\widetilde{B}^2E_1$ of different spin multiplicity is governed by the spin-orbit interactions. The spin-orbit coupling parameters are calculated by using Briet-Pauli operator method implemented in Molpro package [42]. The resulting data reveal that the spin-orbit splitting of $\widetilde{X}^2E_1$, $\widetilde{A}^4E_1$ and $\widetilde{B}^2E_1$ electronic states is 0.45, 6.0 and 3.0 cm^{-1}, respectively. The coupling strength between the components of $\widetilde{X}^2E_1$ and $\widetilde{A}^4E_1$ at C_{6v} symmetry configuration is 1.72 cm^{-1} (magnitude). Therefore, because of extremely small size of the spin-orbit coupling parameters as compared to the JT coupling parameters (discussed later in the text), the spin-orbit coupling is neglected in the present study. Neglect of spin-orbit interactions reduces the vibronic Hamiltonian for the $\widetilde{X}^2E_1$, $\widetilde{A}^4E_1$ and $\widetilde{B}^2E_1$ states of neutral isomer I into a block diagonal form consisting of three $2 \otimes 2$ blocks each representing the JT interactions within a degenerate electronic manifold. Such a Hamiltonian can be written as

$$\mathcal{H}_{\mathrm{I}} = (\mathcal{T}_N + \mathcal{V}_0)\mathbf{1_6} + \begin{pmatrix} v_{1x} & v_{1x-1y} & 0 & 0 & 0 & 0 \\ & v_{1y} & 0 & 0 & 0 & 0 \\ & & v_{2x} & v_{2x-2y} & 0 & 0 \\ h.c & & & v_{2y} & 0 & 0 \\ & & & & v_{3x} & v_{3x-3y} \\ & & & & & v_{3y} \end{pmatrix}, \tag{3.10a}$$

where

$$\mathcal{T}_N = -\frac{1}{2}\sum_{i \in a_1,\, b_1,\, b_2} \omega_i \frac{\partial^2}{\partial Q_i^2} - \frac{1}{2}\sum_{i \in e_1,\, e_2} \omega_i \left(\frac{\partial^2}{\partial Q_{ix}^2} + \frac{\partial^2}{\partial Q_{iy}^2}\right), \tag{3.10b}$$

and

$$\mathcal{V}_0 = \frac{1}{2}\sum_{i \in a_1,\, b_1,\, b_2} \omega_i Q_i^2 + \frac{1}{2}\sum_{i \in e_1,\, e_2} \omega_i \left(Q_{ix}^2 + Q_{iy}^2\right), \tag{3.10c}$$

$$
\begin{aligned}
v_{kx/ky} &= E_0^k + \sum_{i\,\in\,a_1}\kappa_i^k Q_i \pm \sum_{i\,\in\,e_2}\lambda_i^k Q_{ix} + \frac{1}{2}\sum_{i,j\,\in\,a_1}\gamma_{ij}^k Q_i Q_j + \frac{1}{2}\sum_{i\,\in\,b_1}\gamma_i^k Q_i^2 + \frac{1}{2}\sum_{i,j\,\in\,b_2}\gamma_{ij}^k Q_i Q_j \\
&\quad \frac{1}{2}\sum_{i,j\,\in\,e_1,\,e_2}[\gamma_{ij}^k(Q_{ix}Q_{jx}+Q_{iy}Q_{jy})] \pm \frac{1}{2}\sum_{i,j\,\in\,e_1,\,e_2}[\eta_{ij}^k(Q_{ix}Q_{jx}-Q_{iy}Q_{jy})] \\
&\quad \pm\frac{1}{2}\sum_{i\,\in\,a_1,j\,\in\,e_2}\gamma_{ij}^k Q_i Q_{jx}, \qquad (3.10d)
\end{aligned}
$$

$$
v_{kx-ky} = \sum_{i\in e_2}\lambda_i^k Q_{iy} + \sum_{i,j\,\in\,e_1,\,e_2}\eta_{ij}^k Q_{ix}Q_{jy} + \frac{1}{2}\sum_{i\,\in\,a_1,j\,\in\,e_2}\gamma_{ij}^k Q_i Q_{jy}. \qquad (3.10e)
$$

The electronic states $\widetilde{X}^2B_2$ and $\widetilde{A}^2B_1$ of the neutral isomer II of B_7^- are coupled by the vibrational modes of a_2 symmetry. The latter modes also couple $\widetilde{X}^2B_2$ -$\widetilde{D}^2B_1$, $\widetilde{A}^2B_1$ -$\widetilde{B}^2B_2$ and $\widetilde{B}^2B_2$ -$\widetilde{D}^2B_1$ electronic states. The vibrational modes of b_2 symmetry couples $\widetilde{X}^2B_2$ -$\widetilde{C}^2A_1$ and $\widetilde{B}^2B_2$ -$\widetilde{C}^2A_1$ electronic states. The electronic states $\widetilde{A}^2B_1$ -$\widetilde{C}^2A_1$ and $\widetilde{C}^2A_1$ -$\widetilde{D}^2B_1$ are coupled by vibrational modes of b_1 symmetry. Therefore, the vibronic Hamiltonian for the coupled manifold of electronic states of the neutral isomer II of B_7^- can be expressed as

$$
\mathcal{H}_{\rm II} = (\mathcal{T}_N+\mathcal{V}_0)\mathbf{1_5} + \begin{pmatrix}
u_{11} & \sum_{i\in a_2}\lambda_i^{1-2}Q_i & 0 & \sum_{i\in b_2}\lambda_i^{1-4}Q_i & \sum_{i\in a_2}\lambda_i^{1-5}Q_i \\
 & u_{22} & \sum_{i\in a_2}\lambda_i^{2-3}Q_i & \sum_{i\in b_1}\lambda_i^{2-4}Q_i & 0 \\
h.c & & u_{33} & \sum_{i\in b_2}\lambda_i^{3-4}Q_i & \sum_{i\in a_2}\lambda_i^{3-5}Q_i \\
 & & & u_{44} & \sum_{i\in b_1}\lambda_i^{4-5}Q_i \\
 & & & & u_{55}
\end{pmatrix}. \qquad (3.11a)
$$

The electronic ground $^2A_2$ state of neutral isomer III of B_7^- can be coupled to its $^2B_2$, $\widetilde{B'}^2B_1$, $\widetilde{C'}^2A_1$ and $\widetilde{D'}^2A_1$ states by the b_1, b_2, a_2 and a_2 vibrational modes, respectively. Similarly, the coupling of $^2B_2$ state to the $\widetilde{B'}^2B_1$, $\widetilde{C'}^2A_1$ and $\widetilde{D'}^2A_1$ states is allowed by vibrational modes of a_2, b_2 and b_2 symmetry, respectively. The vibrational modes of b_1 symmetry can couple the $\widetilde{B'}^2B_1$ state with the $\widetilde{C'}^2A_1$ and $\widetilde{D'}^2A_1$ states. The electronic states $\widetilde{C'}^2A_1$ -$\widetilde{D'}^2A_1$ coupled by vibrational modes of a_1 symmetry. With such a coupling scheme the vibronic Hamiltonian of isomer III can be written as

$$\mathcal{H}_{\rm III} = (\mathcal{T}_N + \mathcal{V}_0)\mathbf{1_5} + \begin{pmatrix} u_{11} & \sum_{i\in b_1}\lambda_i^{1-2}Q_i & \sum_{i\in b_2}\lambda_i^{1-3}Q_i & \sum_{i\in a_2}\lambda_i^{1-4}Q_i & \sum_{i\in a_2}\lambda_i^{1-5}Q_i \\ & u_{22} & \sum_{i\in a_2}\lambda_i^{2-3}Q_i & \sum_{i\in b_2}\lambda_i^{2-4}Q_i & \sum_{i\in b_2}\lambda_i^{2-5}Q_i \\ & & u_{33} & \sum_{i\in b_1}\lambda_i^{3-4}Q_i & \sum_{i\in b_1}\lambda_i^{3-5}Q_i \\ & h.c & & u_{44} & \sum_{i\in a_1}\lambda_i^{4-5}Q_i \\ & & & & u_{55} \end{pmatrix}. \quad (3.11b)$$

The elements of the vibronic Hamiltonians (3.11a) and (3.11b) are given by

$$\mathcal{T}_N = -\frac{1}{2}\sum_{i=1}^{15}\omega_i\left(\frac{\partial^2}{\partial Q_i^2}\right), \quad (3.11c)$$

$$\mathcal{V}_0 = \frac{1}{2}\sum_{i=1}^{15}\omega_i Q_i^2, \quad (3.11d)$$

In the above, $\mathcal{T}_N$ and $\mathcal{V}_0$ represent the kinetic and potential energy operators, respectively, of the reference electronic ground state of B_7^-. Vibrational modes are designated by the index i. The quantity ω_i represents the harmonic vibrational frequency of the mode i. The diagonal elements of the electronic Hamiltonians $\mathcal{H}_{\rm II}$ and $\mathcal{H}_{\rm III}$ are expanded in a Taylor series around the reference equilibrium geometry (occurring at $\mathbf{Q}$=0) as [44].

$$\begin{aligned} u_{kk} = {} & E_0^{(k)} + \sum_{i\in a_1}\kappa_i^{(k)}Q_i + \frac{1}{2}\sum_{i\in a_1,a_2,b_1,b_2}\gamma_i^{(k)}Q_i^2 + \frac{1}{2}\sum_{i\in a_1}\sum_{j\in a_1>i}\gamma_{ij}^{(k)}Q_iQ_j + \\ & \frac{1}{2}\sum_{i\in b_1}\sum_{j\in b_1>i}\gamma_{ij}^{(k)}Q_iQ_j + \frac{1}{2}\sum_{i\in b_2}\sum_{j\in b_2>i}\gamma_{ij}^{(k)}Q_iQ_j + \frac{1}{2}\sum_{i\in a_2}\sum_{j\in a_2>i}\gamma_{ij}^{(k)}Q_iQ_j + \\ & \frac{1}{3!}\sum_{i=1}^{15}\gamma_{3i}^{(k)}Q_i^3 + \frac{1}{4!}\sum_{i=1}^{15}\gamma_{4i}^{(k)}Q_i^4 \end{aligned} \quad (3.11e)$$

The symbols introduced in the Hamiltonian of all three isomers $\mathcal{H}_{\rm I}$, $\mathcal{H}_{\rm II}$ and $\mathcal{H}_{\rm III}$ have the following meaning. The notation $\mathbf{1}_m$ stands for a $m \times m$ unit matrix. The quantity E_0^k represents the VDE of the k^{th} electronic state. κ_i^k and γ_i^k are the linear and second-order coupling parameters of the i^{th} vibrational mode in the k^{th} electronic state. γ_{ij}^k is the intrastate bilinear coupling parameter between i^{th} and j^{th} modes. λ_i^k denotes the linear JT coupling parameter of the k^{th} state along the i^{th} vibrational mode. $\lambda_i^{(k-l)}$ is the LVC parameter between two electronic states, k and l of B_7. It can be seen from Eq. (3.11e) that higher order (up to quartic) Taylor expansion is necessary in order

to reproduce the strong anharmonicity of the potential energies along some vibrational modes (see, Tables 3.31 and 3.32). All coupling parameters discussed above are extracted by fitting the calculated *ab initio* electronic energies to the adiabatic form of the diabatic electronic Hamiltonians presented in Eqs. 3.10a-3.11b. The resulting parameters of all three isomers are given in Tables 3.28-3.33.

Table 3.28: Linear (κ or λ), quadratic (γ and η) and bilinear intrastate coupling parameters (in eV units) of the $\widetilde{X}^2E_1$, $\widetilde{A}^4E_1$ and $\widetilde{B}^2E_1$ electronic states of isomer I. The dimensionless coupling strengths are given in the parentheses.

		Isomer I		
Parameter	Modes	$\widetilde{X}^2E_1$	$\widetilde{A}^4E_1$	$\widetilde{B}^2E_1$
κ	ν_1	0.0247 (0.02)	0.0251 (0.03)	0.0311 (0.04)
	ν_2	-0.0684 (1.86)	0.0026 (0.00)	0.0016 (0.00)
λ	ν_8	0.1205 (0.41)	0.1321 (0.49)	0.1136 (0.36)
	ν_9	0.0467 (0.16)	0.0074 (0.00)	0.0058 (0.00)
	ν_{10}	0.0678 (0.88)	0.0229 (0.10)	0.0368 (0.26)
γ	ν_1	0.0021	-0.0001	0.0001
	ν_2	-0.0167	-0.0031	-0.0050
	ν_3	0.0204	0.0065	0.0070
	ν_4	-0.0005	-0.0176	-0.0163
	ν_5	0.0029	0.0036	0.0069
	ν_6	0.0081	-0.0097	-0.0123
	ν_7	0.0059	-0.0138	-0.0134
	ν_8	0.0067	-0.0009	0.0003
	ν_9	-0.0033	-0.0099	-0.0078
	ν_{10}	0.0034	-0.0079	-0.0041
η	ν_6	-0.0107	0.0015	-0.0031
	ν_7	0.0071	0.0015	-0.0019
	ν_8	-0.0023	-0.0059	0.0055
	ν_9	-0.0010	-0.0193	0.0165
	ν_{10}	0.0000	0.0000	0.0000
bilinear	$\nu_1\nu_2$	-0.0031	0.0026	0.0029
	$\nu_1\nu_8$	0.0134	-0.0050	0.0178
	$\nu_1\nu_9$	0.0006	-0.0114	-0.0022
	$\nu_1\nu_{10}$	-0.0124	-0.0396	-0.0278
	$\nu_2\nu_8$	0.0064	0.0057	0.0042
	$\nu_2\nu_9$	0.0173	0.0080	0.0018
	$\nu_2\nu_{10}$	0.0252	-0.0030	0.0072
	$\nu_4\nu_5$	0.0021	-0.0091	-0.0010
	$\nu_6\nu_7$	0.0013	-0.0078	-0.0146
	$\nu_8\nu_9$	0.0000	-0.0007	0.0015
	$\nu_8\nu_{10}$	-0.0013	-0.0083	0.0087
	$\nu_9\nu_{10}$	-0.0020	-0.0003	0.0078

Table 3.29: Linear (κ), quadratic (γ) and bilinear intrastate coupling parameters (in eV units) of the $\widetilde{X}^2B_2$, $\widetilde{A}^2B_1$, $\widetilde{B}^2B_2$, $\widetilde{C}^2A_1$ and $\widetilde{D}^2B_1$ electronic states of isomer II. The dimensionless coupling strengths are given in the parentheses.

Parameter	Modes	$\widetilde{X}^2B_2$	$\widetilde{A}^2B_1$	$\widetilde{B}^2B_2$	$\widetilde{C}^2A_1$	$\widetilde{D}^2B_1$
κ	ν_1	-0.0485 (0.07)	0.1148 (0.47)	-0.1382 (0.39)	-0.1930 (1.02)	0.0143 (0.01)
	ν_2	-0.0185 (0.02)	-0.0449 (0.15)	-0.0103 (0.03)	-0.0797 (0.24)	-0.0431 (0.07)
	ν_3	0.0959 (0.69)	0.0018 (0.00)	-0.0159 (0.02)	0.0139 (0.02)	-0.0667 (0.36)
	ν_4	0.0390 (0.22)	-0.0202 (0.13)	0.0009 (0.02)	0.0762 (1.14)	0.0007 (0.00)
	ν_5	0.1416 (9.35)	-0.0653 (1.11)	0.0506 (2.10)	-0.0113 (0.69)	-0.0688 (2.58)
γ	ν_1	0.0133	-0.0096	0.0072	-0.0027	0.0155
	ν_2	-0.0001	-0.0011	-0.0003	-0.0036	-0.0006
	ν_3	-0.0094	-0.0234	0.0153	-0.0110	0.0118
	ν_4	0.0033	-0.0064	-0.0053	-0.0186	-0.0058
	ν_5	0.0116	-0.0227	-0.0024	0.0134	-0.0169
	ν_6	0.0135	-0.0571	0.0589	0.0008	0.0061
	ν_7	-0.0053	0.0114	-0.0342	-0.0053	0.0227
	ν_8	-0.0086	-0.0078	-0.0023	-0.0148	-0.0081
	ν_9	0.0040	-0.0053	0.0151	-0.0279	0.0096
	ν_{10}	0.0108	-0.0091	0.0353	0.0056	0.0385
	ν_{11}	0.0012	-0.0152	-0.0062	0.0000	-0.0079
	ν_{12}	-0.0183	-0.0023	0.0943	-0.0118	0.0222
	ν_{13}	0.0002	-0.0321	-0.0532	0.0237	-0.0281
	ν_{14}	0.0037	-0.0484	0.0019	0.0256	-0.0347
	ν_{15}	0.0106	-0.0200	-0.0471	0.0352	-0.0062
γ_{ij}	$\nu_1\nu_2$	0.0045	-0.0105	0.0033	0.0003	-
	$\nu_1\nu_3$	0.0068	0.0141	-0.0052	0.0000	-
	$\nu_1\nu_4$	0.0063	-0.0028	-0.0081	0.0000	-
	$\nu_1\nu_5$	0.0139	0.0000	-0.0064	0.0017	-
	$\nu_2\nu_3$	0.0225	0.0270	0.0137	0.0000	-
	$\nu_2\nu_4$	-0.0022	0.0011	0.0067	-0.0003	-
	$\nu_2\nu_5$	-0.0021	-0.0080	-0.0029	0.0003	-
	$\nu_3\nu_4$	0.0039	0.0104	-0.0092	0.0005	-
	$\nu_3\nu_5$	0.0079	0.0065	-0.0071	-0.0001	-
	$\nu_4\nu_5$	-0.0014	0.0049	0.0001	-0.0007	-
	$\nu_6\nu_7$	-0.0058	0.0125	0.0118	0.0140	-
	$\nu_6\nu_8$	0.0050	-0.0050	-0.0084	-0.0266	-
	$\nu_7\nu_8$	-0.0042	-0.0113	0.0132	-0.0185	-
	$\nu_9\nu_{10}$	-0.0026	-0.0241	0.0048	0.0215	-
	$\nu_9\nu_{11}$	0.0018	-0.0261	-0.0030	0.0546	-
	$\nu_{10}\nu_{11}$	-0.0012	-0.0718	-0.0143	-0.0053	-
	$\nu_{12}\nu_{13}$	-0.0210	-0.0340	-0.0322	0.0145	-
	$\nu_{12}\nu_{14}$	0.0182	0.0333	0.0105	-0.0316	-
	$\nu_{12}\nu_{15}$	-0.0009	-0.0196	0.0037	-0.0018	-
	$\nu_{13}\nu_{14}$	-0.0058	0.0308	0.0119	-0.0090	-
	$\nu_{13}\nu_{15}$	0.0055	0.0128	0.0228	0.0008	-
	$\nu_{14}\nu_{16}$	0.0013	-0.0196	-0.0004	0.0177	-

Table 3.30: Linear (κ), quadratic (γ) and bilinear intrastate coupling parameters (in eV units) of the $^2A_2$, $^2B_2$, $\widetilde{B'}^2B_1$, $\widetilde{C'}^2A_1$ and $\widetilde{D'}^2A_1$ electronic states of isomer III. The dimensionless coupling strengths are given in the parentheses.

Parameter	Modes	$^2A_2$	$^2B_2$	$\widetilde{B'}^2B_1$	$\widetilde{C'}^2A_1$	$\widetilde{D'}^2A_1$
κ	ν_1	-0.1604 (0.51)	0.0036 (0.00)	-0.3367 (2.27)	-0.1409 (0.39)	-0.3149 (1.98)
	ν_2	0.0230 (0.01)	0.0779 (0.14)	0.1401 (0.44)	0.0670 (0.10)	-0.0012 (0.00)
	ν_3	-0.0448 (0.10)	-0.0193 (0.02)	-0.0184 (0.02)	-0.0311 (0.05)	-0.0817 (0.35)
	ν_4	0.0325 (0.09)	0.0412 (0.14)	0.0134 (0.01)	-0.0138 (0.01)	0.0028 (0.00)
	ν_5	0.0229 (0.07)	0.0231 (0.07)	0.0145 (0.03)	0.0058 (0.00)	0.0214 (0.06)
	ν_6	-0.0549 (0.75)	0.0256 (0.16)	0.0803 (1.60)	0.1189 (3.52)	-0.0699 (1.21)
γ	ν_1	0.0070	0.0339	0.0350	0.0078	0.0694
	ν_2	0.0067	0.0405	0.0330	0.0025	0.0385
	ν_3	0.0001	0.0059	-0.0029	-0.0190	0.0152
	ν_4	-0.0012	-0.0051	0.0043	-0.0024	-0.0012
	ν_5	-0.0047	-0.0031	-0.0138	-0.0093	-0.0101
	ν_6	0.0003	-0.0125	0.0066	-0.0202	0.0244
	ν_7	0.0061	-0.0023	-0.0097	-0.0030	0.0069
	ν_8	-0.0198	0.0047	-0.0229	-0.0013	-0.0460
	ν_9	-0.0348	0.0258	-0.0344	0.0042	-0.0031
	ν_{10}	-0.0228	-0.0011	-0.0524	-0.0221	-0.0405
	ν_{11}	0.0079	-0.0523	-0.0001	-0.0138	0.0619
	ν_{12}	-0.0111	-0.0209	-0.0088	-0.0177	-0.0381
	ν_{13}	0.0035	-0.0747	-0.0021	-0.1132	-0.0025
	ν_{14}	0.0022	-0.0329	0.0008	-0.0517	0.0202
	ν_{15}	-0.0042	0.0460	-0.0194	-0.0057	-0.0302
Bilinear	$\nu_1\nu_2$	0.0005	-0.0182	-0.0051	-0.0396	0.0137
	$\nu_1\nu_3$	0.0038	-0.0124	-0.0081	-0.0488	0.0368
	$\nu_1\nu_4$	-0.0002	0.0018	0.0078	0.0276	-0.0137
	$\nu_1\nu_5$	-0.0034	-0.0138	-0.0101	0.0129	-0.0074
	$\nu_1\nu_6$	-0.0004	0.0012	-0.0021	-0.0822	0.0717
	$\nu_2\nu_3$	- 0.0005	0.0010	0.0168	0.0112	0.0285
	$\nu_2\nu_4$	-0.0013	-0.0099	-0.0140	-0.0057	0.0057
	$\nu_2\nu_5$	0.0046	0.0236	0.0136	0.0087	0.0041
	$\nu_2\nu_6$	-0.0013	0.0290	0.0097	-0.0043	0.0328
	$\nu_3\nu_4$	0.0010	-0.0005	-0.0010	0.0059	-0.0023
	$\nu_3\nu_5$	-0.0038	0.0108	0.0008	0.0060	-0.0080
	$\nu_3\nu_6$	0.0046	0.0009	0.0075	-0.0203	0.0435
	$\nu_4\nu_5$	0.0031	-0.0066	0.0043	-0.0008	-0.0115
	$\nu_4\nu_6$	-0.0011	0.0012	-0.0021	0.0007	-0.0274
	$\nu_5\nu_6$	0.0077	0.0108	0.0043	0.0051	-0.0202
	$\nu_7\nu_8$	-0.0055	-0.0110	-0.0217	-0.0217	-0.0142
	$\nu_9\nu_{10}$	0.0012	0.0012	0.0012	0.0012	0.0012
	$\nu_{11}\nu_{12}$	-0.0097	-0.0305	-0.0183	0.0463	0.0202
	$\nu_{11}\nu_{13}$	0.0053	-0.0254	-0.0168	-0.0321	0.0318
	$\nu_{11}\nu_{14}$	-0.0049	0.0091	-0.0075	-0.0308	0.0027
	$\nu_{11}\nu_{15}$	0.0012	-0.0214	0.0038	0.0044	-0.0073
	$\nu_{12}\nu_{13}$	0.0111	-0.0451	-0.0050	-0.0226	0.0300
	$\nu_{12}\nu_{14}$	-0.0029	0.0025	0.0055	0.0032	0.0042
	$\nu_{12}\nu_{15}$	-0.0044	-0.0265	-0.0226	0.0482	0.0222
	$\nu_{13}\nu_{14}$	0.0037	0.0309	0.0284	0.0392	0.0009
	$\nu_{13}\nu_{15}$	0.0065	-0.0188	-0.0063	-0.0099	0.0753
	$\nu_{14}\nu_{16}$	-0.0042	-0.0343	-0.0311	-0.0387	0.0050

Table 3.31: Higher order coupling parameters (in eV units) of the Taylor expansion of the electronic Hamiltonian [*cf.* Eq. (3.11e)] of isomer II.

Parameter	Modes	$\widetilde{X}^2B_2$	$\widetilde{A}^2B_1$	$\widetilde{B}^2B_2$	$\widetilde{C}^2A_1$
γ_3	ν_1	-	-0.0080	0.0005	0.0104
	ν_2	0.0001	-	-	0.0000
	ν_3	-0.0013	-0.0013	0.0028	-0.0021
	ν_4	-	0.0015	-0.0002	-0.0013
	ν_5	-0.0034	-	0.0021	-0.0010
γ_4	ν_1	-0.0006	-0.0020	-0.0002	-0.0037
	ν_2	-	-	-	0.0000
	ν_3	-	0.0007	-0.0008	-0.0007
	ν_4	0.0004	0.0002	0.0002	0.0009
	ν_5	-0.0007	-	0.0006	-0.0035
	ν_{10}	-0.0253	0.0207	-0.1057	
	ν_{12}	-	-	0.1718	
	ν_{13}	0.0169	-	-	
	ν_{14}	0.0015	-0.0073	0.0014	
	ν_{15}	-	-	0.0126	

Table 3.32: Same as in Table 3.31 for isomer III.

Parameter	Modes	$^2A_2$	$^2B_2$	$\widetilde{B'}^2B_1$	$\widetilde{C'}^2A_1$	$\widetilde{D'}^2A_1$
γ_3	ν_1	-	0.0073	-	-0.0247	0.0317
	ν_2	-	0.0188	0.0100	-0.0036	0.0032
	ν_3	-	0.0009	0.0005	-0.0129	0.0119
	ν_4	-	-	-0.0011	0.0012	-0.0002
	ν_5	-	-	-	0.0002	0.0002
	ν_6	-	-	-0.0077	-0.0045	0.0009
γ_4	ν_1	-	0.0007	-	-0.0156	0.0146
	ν_2	-	0.0113	0.0016	0.0091	-0.0025
	ν_3	-	0.0002	0.0002	0.0074	-0.0066
	ν_4	-	-	0.0003	0.0002	0.0002
	ν_5	-	-	-	0.0001	0.0003
	ν_6	-	-0.0009	-0.0002	-0.0039	0.0015

Table 3.33: Linear interstate coupling parameters (λ in eV units) between the given electronic states of isomer II and III. Numbers (dimensionless) in the parenthesis denote the excitation strength of the given vibrational mode.

	Isomer II								
Mode (Symmetry)	$\widetilde{X}^2B_2$ -$\widetilde{A}^2B_1$	$\widetilde{X}^2B_2$ -$\widetilde{C}^2A_1$	$\widetilde{X}^2B_2$ -$\widetilde{D}^2B_1$	$\widetilde{A}^2B_1$ -$\widetilde{B}^2B_2$	$\widetilde{A}^2B_1$ -$\widetilde{C}^2A_1$	$\widetilde{B}^2B_2$ -$\widetilde{C}^2A_1$	$\widetilde{B}^2B_2$ -$\widetilde{D}^2B_1$	$\widetilde{C}^2A_1$ -$\widetilde{D}^2B_1$	
$\nu_6(a_2)$	-	-	-	0.0164 (0.01)	-	-	-	-	
$\nu_7(a_2)$	0.0864 (0.62)	-	0.1518 (1.90)	-	-	-	0.1395 (1.61)	-	
$\nu_8(a_2)$	0.0297 (0.18)	-	0.0413 (0.35)	0.0785 (1.27)	-	-	-	-	
$\nu_9(b_1)$	-	-	-	-	-	-	-	0.0728 (0.13)	
$\nu_{10}(b_1)$	-	-	-	-	-	-	-	0.0741 (0.16)	
$\nu_{11}(b_1)$	-	-	-	-	0.0615 (0.28)	-	-	-	
$\nu_{12}(b_2)$	-	0.1013 (0.27)	-	-	-	-	-	-	
$\nu_{13}(b_2)$	-	0.1179 (0.74)	-	-	-	0.0905 (0.44)	-	-	
$\nu_{14}(b_2)$	-	0.1112 (1.42)	-	-	-	0.0472 (0.25)	-	-	
$\nu_{15}(b_2)$	-	0.1825 (8.37)	-	-	-	0.1067 (2.86)	-	-	
	Isomer III								
Mode (Symmetry)	$^2A_2$ -$^2B_2$	$^2A_2$ -$\widetilde{B'}^2B_1$	$^2A_2$ -$\widetilde{C'}^2A_1$	$^2A_2$ -$\widetilde{D'}^2A_1$	$^2B_2$ -$\widetilde{C'}^2A_1$	$^2B_2$ -$\widetilde{D'}^2A_1$	$\widetilde{B'}^2B_1$ -$\widetilde{C'}^2A_1$	$\widetilde{B'}^2B_1$ -$\widetilde{D'}^2A_1$	$\widetilde{C'}^2A_1$ -$\widetilde{D'}^2A_1$
ν_1 (a_1)	-	-	-	-	-	-	-	-	0.1314 (0.34)
ν_2 (a_1)	-	-	-	-	-	-	-	-	-
ν_3 (a_1)	-	-	-	-	-	-	-	-	-
ν_4 (a_1)	-	-	-	-	-	-	-	-	0.0136 (0.02)
ν_5 (a_1)	-	-	-	-	-	-	-	-	-
ν_6 (a_1)	-	-	-	-	-	-	-	-	0.0289 (0.21)
ν_7 (a_2)	-	-	0.0778 (1.3)	0.0116 (0.0)	-	-	-	-	
ν_8 (a_2)	-	-	-	-	-	-	-	-	
ν_9 (b_1)	0.0636 (0.6)	-	-	-	-	-	0.0606 (0.6)	0.0818 (1.1)	
ν_{10} (b_1)	0.0476 (1.9)	-	-	-	-	-	0.0519 (2.2)	0.0437 (1.6)	
ν_{11} (b_2)	-	-	-	-	0.0942 (0.2)	0.1788 (0.6)	-	-	
ν_{12} (b_2)	-	0.0180 (0.0)	-	-	0.0662 (0.1)	-	-	-	
ν_{13} (b_2)	-	-	-	-	-	0.1295 (0.6)	-	-	
ν_{14} (b_2)	-	-	-	-	-	0.1270 (1.0)	-	-	
ν_{15} (b_2)	-	-	-	-	-	-	-	-	

3.4 Adiabatic potential energy surfaces

3.4.1 Singlet and triplet electronic states of B_4

The adiabatic PESs of the singlet $\widetilde{X}$, $\widetilde{A}$, $\widetilde{B}$ and triplet $\widetilde{a}$, $\widetilde{b}$, $\widetilde{c}$ electronic states of B_4 are obtained by diagonalizing the diabatic electronic Hamiltonian $(\mathcal{H} - T_N I_6)$ introduced in Eq. (3.7a). One dimensional cuts of the resulting adiabatic PESs are shown in Figures 3.13 and 3.14. In Fig. 3.13 cuts of singlet $\widetilde{X}^1A_g$, $\widetilde{A}^1B_{2u}$ and $\widetilde{B}^1B_{2g}$ electronic states are shown along the normal displacement coordinates of the totally symmetric vibrational modes ν_1 and ν_2. In these plots the lines indicate the potential energies derived from the model using the parameters of Tables 3.17 to 3.20. The points superimposed on them represent the CASSCF-MRCI data obtained by using UB3LYP optimized (squares in blue color) and ROMP2 optimized (circles in red color) reference geometry. It can be seen from Table 3.3 that the calculated VDEs obtained with the two reference geometries differ (within the error limit of $\sim$ 0.3 eV). In the plots given in Figures 3.13 and 3.14 we have adjusted the VDE values obtained with the ROMP2 geometry to those obtained with the UB3LYP reference geometry. With this constant adjustment, the two sets of *ab initio* data can be seen to be in excellent agreement with each other and also with the model potential energy curves. It is intriguing to note that the slopes and curvatures of the PESs around the reference equilibrium geometry ($\mathbf{Q}$=0) are in perfect accord with each other. These are the most important quantities required for the theoretical models developed here. The $\widetilde{X}^1A_g$ state is vertically well separated (by $\sim$ 2.0 eV or more, cf., Table 3.3) from the other two singlet states and the coupling of this state with them is not found from the calculated energy data. However, it can be seen that the equilibrium minimum of the $\widetilde{X}$ state significantly shifts from $\mathbf{Q}$=0, alarming a significant condon activity of the ν_1 vibrational mode in the nuclear dynamics of the $\widetilde{X}$ state. A similar situation arises for the $\widetilde{A}^1B_{2u}$ state along the ν_1 vibrational mode. Considering the same argument, the condon activity of ν_2 vibrational mode is expected to be significant in the dynamics of the $\widetilde{B}^1B_{2g}$ state, however the effect is expected to be significantly smaller in this case.

As stated above, that a coupling in first-order between the $\widetilde{X}$ and $\widetilde{A}$ electronic state requires a vibrational mode of b_{2u} symmetry. Since the coupling parameter of the single b_{2u} mode of B_4 between the $\widetilde{X}$-$\widetilde{A}$ electronic states is zero (in first-order), we looked for the possible bilinear combinations of vibrational modes that transform to the b_{2u} symmetry description of the D_{2h} point group. The possible combinations are $\nu_1 \otimes \nu_4$, $\nu_2 \otimes \nu_4$ and $\nu_3 \otimes \nu_6$. Out of these three combinations the third one is only found to yield a bilinear interstate coupling parameter of $\sim$ 0.069 eV. Similar possible combination of modes are examined between all pairs of electronic states of B_4. Detailed analysis yields that the triplet pair of states $\widetilde{a}$ and $\widetilde{b}$ can be coupled via the $\nu_3 \otimes \nu_4$ combination which transforms to the b_{3g} symmetry representation. The coupling parameter in this case is found to be $\sim$ 0.014 eV. Despite the fact that the $\widetilde{A}$-$\widetilde{B}$ electronic states are vertically only $\sim$ 0.5 eV apart, a coupling between these states (which requires a vibrational mode of a_u symmetry) could not be established.

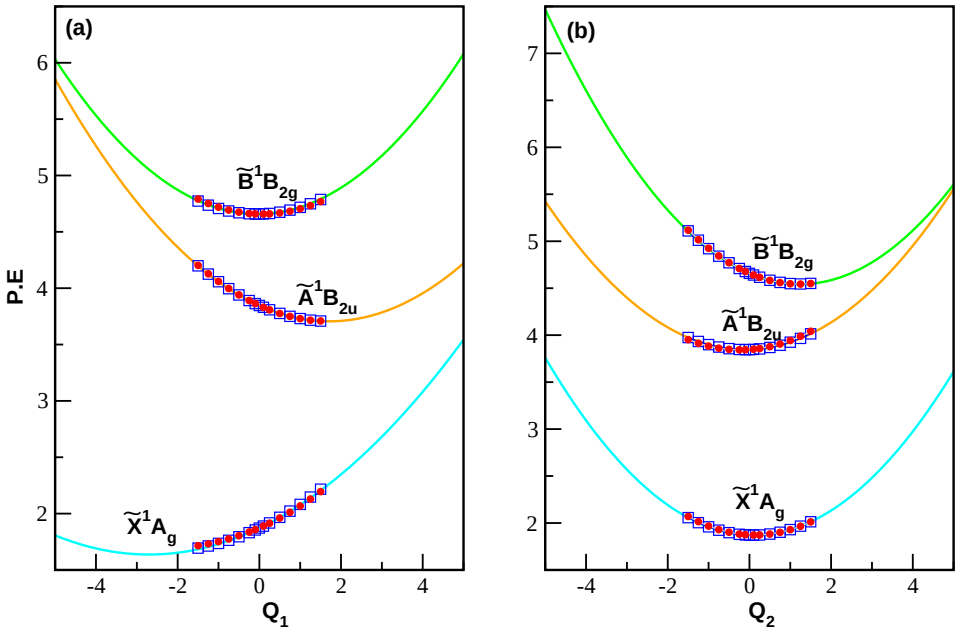

Figure 3.13: One dimensional plot of the adiabatic PESs of the $\widetilde{X}^1A_g$, $\widetilde{A}^1B_{2u}$ and $\widetilde{B}^1B_{2g}$ electronic states of B_4 as a function of the dimensionless normal coordinates of the totally symmetric vibrational modes. The potential energies obtained from the vibronic model are shown by the lines. The potentials energy points calculated by using the UB3LYP optimized reference state are shown by square (blue color) symbol. The same calculated by using the ROMP2 optimized reference state are shown in circle (red) symbol.

The energetic minimum of the seam of CIs between the $\widetilde{X}$-$\widetilde{A}$ states is estimated to occur at $\sim$ 8.18 eV. This is $\sim$ 4.38 eV above the minimum of the $\widetilde{A}$ state. Similarly, an intersection minimum between the $\widetilde{A}$-$\widetilde{B}$ states at $\sim$ 5.10 eV, lying $\sim$ 0.81 eV above the $\widetilde{B}$ state minimum is estimated, from the electronic structure data.

For the triplet electronic states of B_4 the low-energy curve crossings between the $\widetilde{a}$-$\widetilde{b}$ states can be immediately seen from Fig. 3.14. These states are indeed coupled via the vibrational mode ν_6 of b_{3g} symmetry (cf, Table 3.18). Also, a nonzero bilinear interstate coupling has been found between these states as described in the previous paragraph. The triplet $\widetilde{c}$ state of B_4 is vertically $\sim$ 1.0 eV above its triplet $\widetilde{b}$ state. Despite this, a very strong coupling between these states along the ν_5 vibrational mode of b_{3u} symmetry can be found from the data of Table 3.18. The coupling between the $\widetilde{a}$-$\widetilde{c}$ states of B_4 is found to be insignificant. The intersections between the $\widetilde{a}$-$\widetilde{b}$ states yield an energetic minimum of $\sim$ 3.34 eV, on its seam which almost coincides with the energetic minimum of the $\widetilde{b}$ state ($\sim$ 3.27 eV). Similarly, the minimum of the seam of CIs between the $\widetilde{b}$-$\widetilde{c}$ states occurs at $\sim$ 11.33 eV which is $\sim$ 7.24 eV above the energetic minimum of the $\widetilde{c}$ state. It emerges from the above discussion that the $\widetilde{a}$-$\widetilde{b}$ CIs expected to have profound impact on the dynamics of these electronic states. Despite a very strong coupling of the $\widetilde{b}$ and $\widetilde{c}$ states along ν_5 (cf., Table 3.18), the $\widetilde{b}$-$\widetilde{c}$ CIs occur at very high energy and not

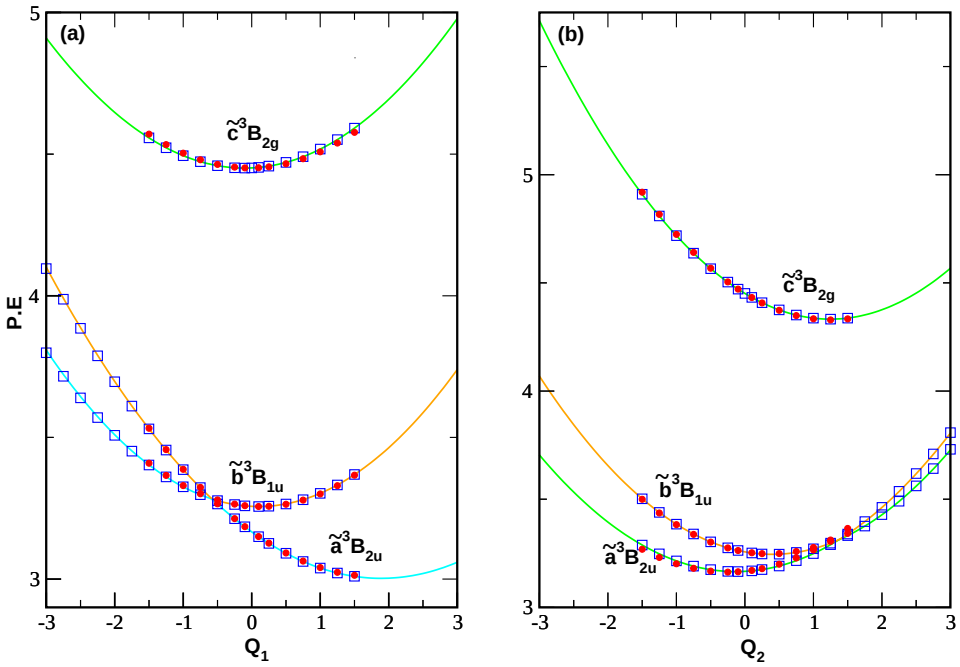

Figure 3.14: Same as in Fig. 3.13 for the $\widetilde{a}^3B_{2u}$, $\widetilde{b}^3B_{1u}$ and $\widetilde{c}^3B_{2g}$ electronic states of B_4.

expected to have any impact on the dynamics of these states. Since the VDEs calculated with the UB3LYP and ROMP2 reference geometries slightly differ from each other, this difference is expected to have some effects on the stationary points of the PESs discussed above. We estimated these stationary points using energies obtained with the ROMP2 optimized reference geometry and an account of this estimate is the following. The minimum of the $\widetilde{X}$-$\widetilde{A}$ CIs estimated to occur at $\sim$ 1.7 eV above the minimum of the $\widetilde{A}$ state. The minimum of the $\widetilde{A}$-$\widetilde{B}$ CIs is located at $\sim$ 1.4 and $\sim$ 0.84 eV above the minimum of the $\widetilde{A}$ and $\widetilde{B}$ states, respectively. As regard to the $\widetilde{a}$-$\widetilde{b}$, $\widetilde{b}$-$\widetilde{c}$ and $\widetilde{a}$-$\widetilde{c}$ CIs similar results are found. The coupling between the $\widetilde{a}$-$\widetilde{c}$ states is insignificant and the minimum of $\widetilde{b}$-$\widetilde{c}$ CIs occurs at high energy. The $\widetilde{a}$-$\widetilde{b}$ CIs occurring at $\sim$ 3.30 eV is found to be quasi-degenerate with the minimum of $\widetilde{b}$ state at $\sim$ 3.25 eV.

The details of the effect of these energetic minima on the nuclear dynamics is presented in Chapter 4. A perspective drawing of the most important $\widetilde{a}$-$\widetilde{b}$ CIs of B_4 is presented in Fig. 3.15. It can be seen from this drawing that the degeneracy of the surfaces is retained along the symmetric vibrational mode, whereas the lower adiabatic surface develops new minima at broken (from equilibrium D_{2h}) symmetry configuration along the coupling mode ν_6.

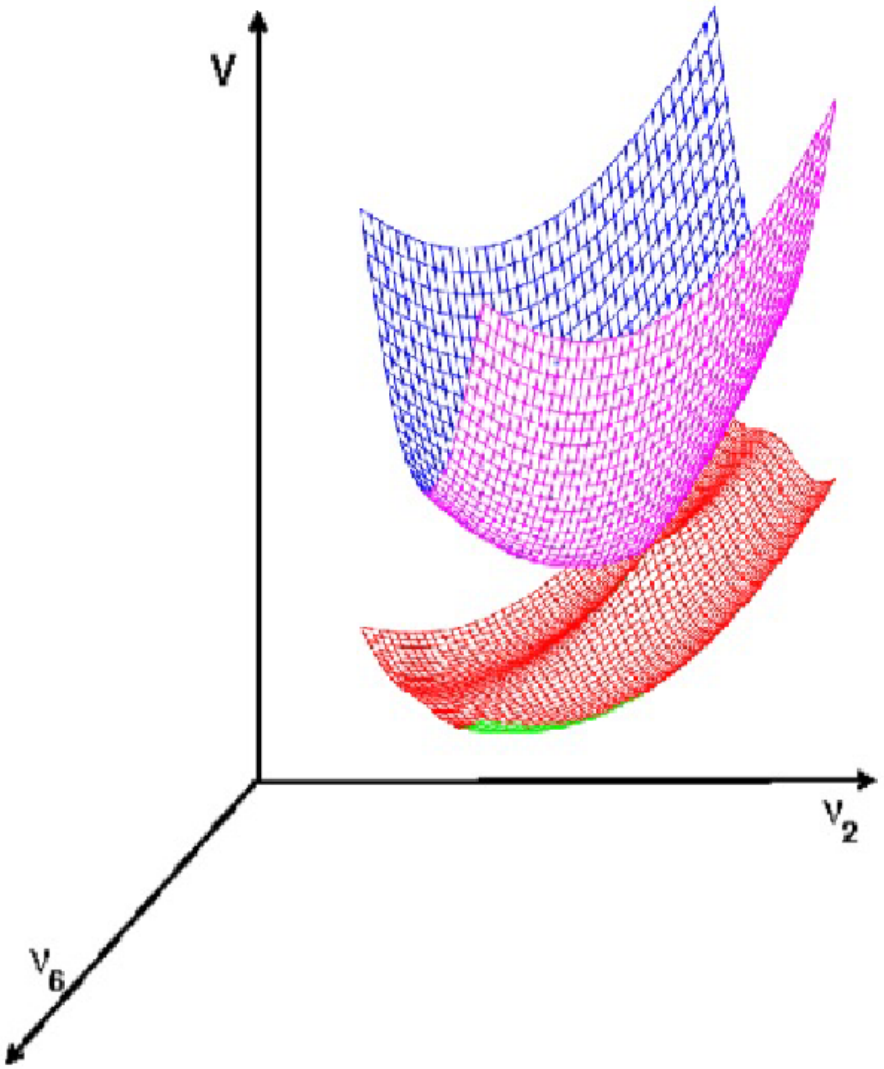

Figure 3.15: Three dimensional perspective view of the $\widetilde{a}^3B_{2u}$-$\widetilde{b}^3B_{1u}$ CIs of B_4 (see text for details)

3.4.2 Doublet electronic states of B_5

By diagonalizing the diabatic electronic Hamiltonian of Eq. 3.9a, the adiabatic potential energy functions for the $\widetilde{X}$, $\widetilde{A}$, $\widetilde{B}$, $\widetilde{C}$, $\widetilde{D}$ and $\widetilde{E}$ states of B_5^- are obtained. These are presented in Fig. 3.16 plotted along the totally symmetric vibrational modes. Crossing of different electronic states can be immediately seen from the figure. As in case of B_4, the energetic minimum of the seam of various CIs and the minimum of the upper adiabatic electronic states are also estimated in this case. The resulting data are collected in Table 3.34. The diagonal entries in this table are the energy at the minimum of a state. Whereas the off-diagonal entries represent the minimum of the seam of various CIs. It is generally observed that inclusion of the second-order coupling terms lowers

Table 3.34: Estimated equilibrium minimum (diagonal entries) and minimum of the seam of various CIs (off-diagonal entries) of the electronic states of B_5 within a quadratic coupling model. All quantities are given in eV.

	$\widetilde{X}^2B_2$	$\widetilde{A}^2A_1$	$\widetilde{B}^2B_2$	$\widetilde{C}^2A_1$	$\widetilde{D}^2B_1$	$\widetilde{E}^2A_1$
$\widetilde{X}^2B_2$	-	4.10	-	7.10	16.67	7.45
$\widetilde{A}^2A_1$	-	3.50	4.21	-	14.75	-
$\widetilde{B}^2B_2$	-	-	4.15	5.73	5.26	9.05
$\widetilde{C}^2A_1$	-	-	-	4.83	5.52	-
$\widetilde{D}^2B_1$	-	-	-	-	5.09	5.44
$\widetilde{E}^2A_1$	-	-	-	-	-	5.44

the energy of the minimum of the seam of CIs as compared to their value obtained in a linear coupling model (excluding the γ terms in the Hamiltonian). This lowering is quite significant (~ 2.38 eV) in case of the $\widetilde{X}$-$\widetilde{A}$ CIs, which puts the energetic minimum of its seam at ~ 0.6 eV above the minimum of the $\widetilde{A}$ state. The CIs of the $\widetilde{X}$ state with the remaining states occur at much higher energies and are not expected to have any role on the nuclear motion on these states in the time scale of the present investigations. Except the minimum of the $\widetilde{A}$-$\widetilde{B}$ CIs which occurs ~ 0.71 and ~ 0.06 eV above the minimum of the $\widetilde{A}$ and $\widetilde{B}$ state, respectively, all the other CIs with the $\widetilde{A}$ state occur at higher energies (cf, Table 3.34). Similarly, the minimum of the CIs of $\widetilde{B}$ state with others occurs much above its energetic minimum at ~ 4.15 eV. The energetic minimum of the CIs of $\widetilde{C}$ state with $\widetilde{B}$, $\widetilde{D}$ and $\widetilde{E}$ states occurs within ~ 1.0 eV above its energetic minimum and expected to be important in the nuclear dynamics on this state. The estimated minimum of the $\widetilde{C}$ state is also very close to the minimum of the $\widetilde{B}$-$\widetilde{C}$, $\widetilde{C}$-$\widetilde{D}$ and $\widetilde{D}$-$\widetilde{E}$ CIs (~ 0.15, ~ 0.43 and ~ 0.35 eV, respectively, in that order). The minimum of the $\widetilde{E}$ state is quasi-degenerate with the minimum of the $\widetilde{D}$-$\widetilde{E}$ CIs and lies only ~ 0.08 eV above the $\widetilde{C}$-$\widetilde{D}$ CIs. The dynamical consequences of all these findings are examined in detail in Chapter 4.

3.4.3 $\widetilde{X}^2E_1$, $\widetilde{A}^4E_1$ and $\widetilde{B}^2E_1$ electronic states of isomer I of B_7

It is mentioned above that the isomer I of B_7 possesses C_{6v} point group symmetry at the equilibrium geometry of the reference B_7^-. The first three electronic states of the B_7 (considered here) are orbitally degenerate at this geometry. The electronic degeneracy is restored upon distortions along the totally symmetric vibrational modes ν_1 and ν_2. The cuts of the adiabatic electronic PESs along the coordinates of these vibrational modes are shown in Figs. 3.18(a-b), respectively. In these figures the solid curves represent the adiabatic electronic energies obtained by diagonalizing the model diabatic electronic Hamiltonian, $\mathcal{H}_I - \mathcal{T}_N I_6$, using the parameters given in Table 3.28. The points superimposed on these curves represent the *ab initio* calculated adiabatic electronic energies. It can be seen from these figures that the degeneracy of the electronic states

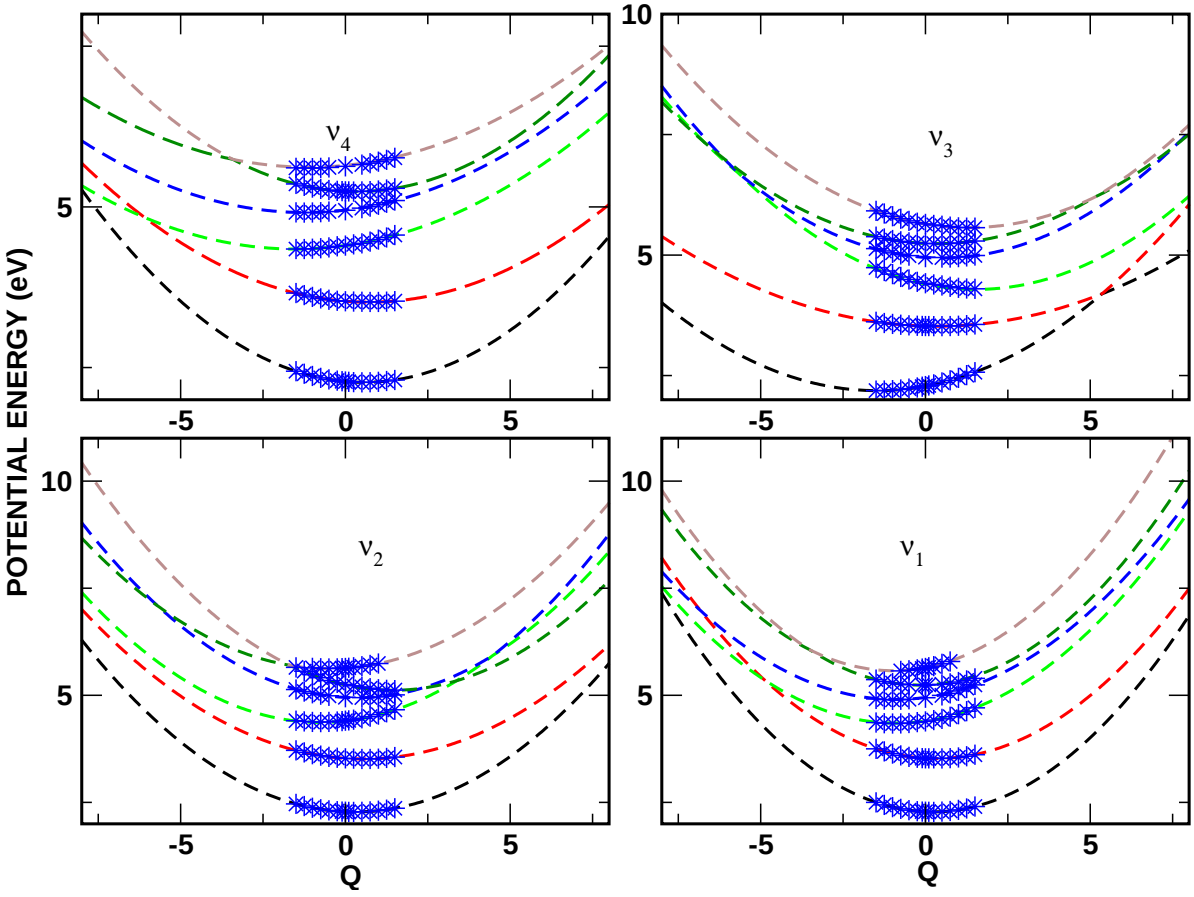

Figure 3.16: Same as in Fig 3.13 for the $\widetilde{X}^2B_2$, $\widetilde{A}^2A_1$, $\widetilde{B}^2B_2$, $\widetilde{C}^2A_1$, $\widetilde{D}^2B_1$ and $\widetilde{E}^2A_1$ electronic states of B_5 along the totally symmetric vibrational modes.

is not lifted along these modes and the calculated *ab initio* electronic energies are in very good accord with those obtained from the constructed vibronic model. It can be seen from Fig. 3.18(b) that the vibrational mode ν_2 is strongly condon active in the $\widetilde{X}^2E_1$ state of the isomer I of B_7. The equilibrium minimum of this state shifts considerably away from the equilibrium minimum of the reference state occurring at **Q**=0. The condon activity of both the modes in the remaining electronic states is very weak as can also be seen from the coupling strength data given in Table 3.28.

In contrast to the symmetric modes, distortion along the degenerate JT active e_2 vibrational modes split the electronic degeneracy of the above electronic states. One dimensional cuts of the degenerate $\widetilde{X}$, $\widetilde{A}$ and $\widetilde{B}$ electronic states of B_7 along the coordinates of one component of the e_2 vibrational modes are shown in Figs. 3.19(a-c), respectively. As in Fig. 3.18, the calculated *ab initio* energies and those obtained from the vibronic model are shown by the points and solid curves, respectively. It can be

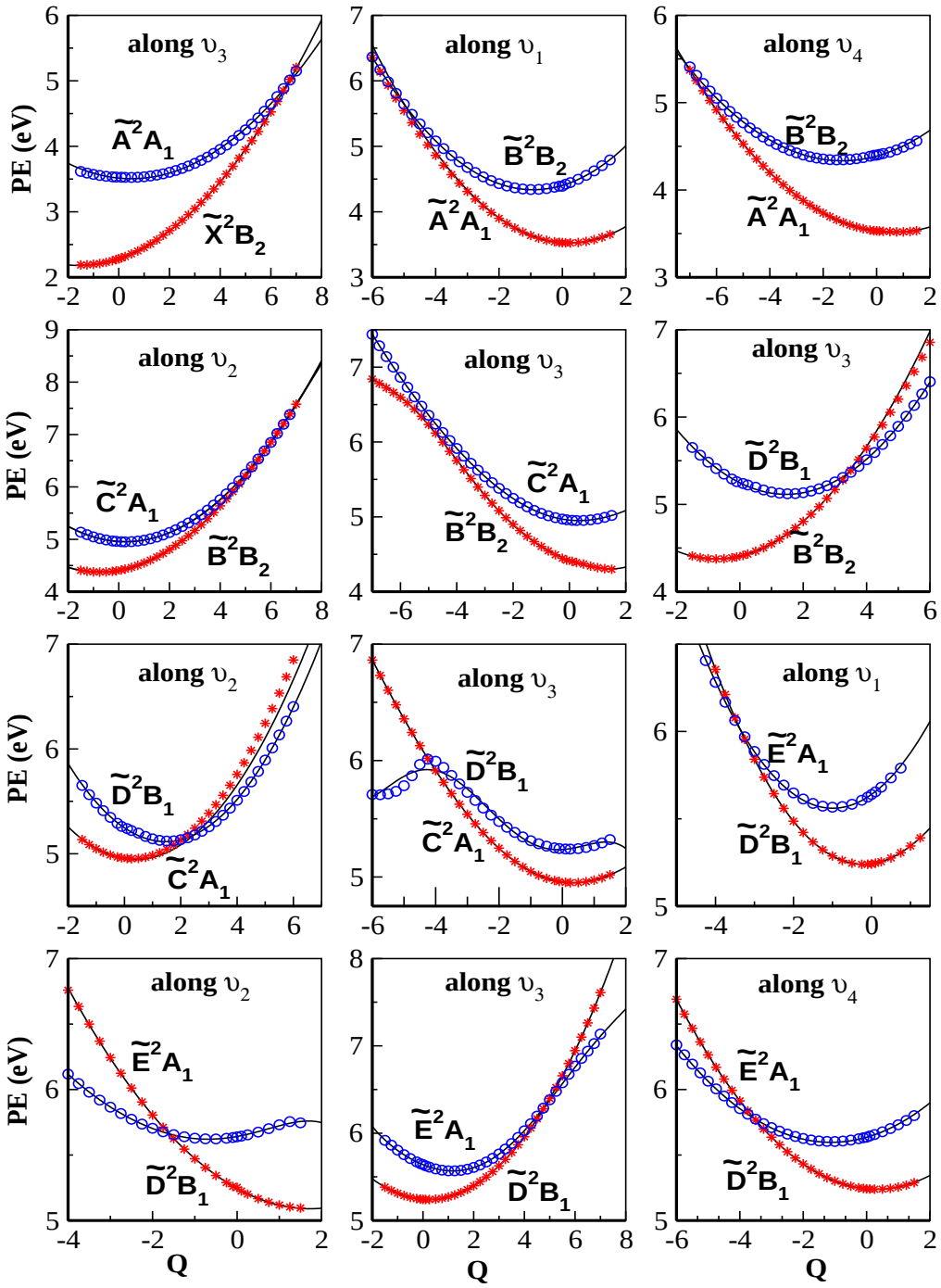

Figure 3.17: Potential energy functions (derived from higher order polynomial fit) of the electronic states of B_5 in the vicinity of crossings. The calculated *ab initio* energies are given by points.

seen that the vibronic model reproduces the *ab initio* energies extremely well also for geometries significantly away from the Franc-Condon zone. From the splitting pattern, it can be seen that the JT activity of the vibrational mode ν_8 is almost similar in all three states. The JT activity of the vibrational mode ν_{10} is the strongest in the $\widetilde{X}$ state and that of ν_9 is weakest in the $\widetilde{A}$ and $\widetilde{B}$ electronic states. It is well known that the JT splitting causes a symmetry breaking and as a result new minima (of lower symmetry) and saddle points develop on the lower adiabatic sheet of the JT split PESs [44]. The seam of CIs of the JT split PESs, on the other hand, occurs at the C_{6v} symmetry configurations and each point on this seam represents a 'cusp' in an adiabatic electronic basis. Using the linear and diagonal second order coupling parameters given in Table 3.28, the energetic minimum on this seam is calculated for all three degenerate electronic states. Energetic minima at $\sim$ 2.769, $\sim$4.096 and $\sim$4.339 eV are found, respectively, on the JT interaction seam of the $\widetilde{X}$, $\widetilde{A}$ and $\widetilde{B}$ electronic states. The new energetic minima on the lower adiabatic sheet of the JT split PESs of the $\widetilde{X}$, $\widetilde{A}$ and $\widetilde{B}$ states occur at $\sim$2.661, $\sim$4.024 and $\sim$4.276 eV, respectively. Therefore, the JT stabilization energy amounts to $\sim$0.11, $\sim$0.07 and $\sim$0.06 eV of these three states in that order.

3.4.4 $\widetilde{X}^2B_2$, $\widetilde{A}^2B_1$, $\widetilde{B}^2B_2$, $\widetilde{C}^2A_1$ and $\widetilde{D}^2B_1$ electronic states of isomer II of B_7

One dimensional cuts of the adiabatic PESs of the $\widetilde{X}$, $\widetilde{A}$, $\widetilde{B}$, $\widetilde{C}$ and $\widetilde{D}$ electronic states of the isomer II of B_7 are plotted along the coordinates of the symmetric vibrational modes ν_1-ν_5 in Figs. 3.20 (a-e), respectively. As in Figs. 3.18- 3.19, the potential energies obtained from the present theoretical model and computed *ab initio* are shown by the lines and points, respectively. In contrast to Fig. 3.18 of isomer I, where a second-order model was adequate to fit the *ab initio* data, a higher-order model had to be used for the same in case of isomer II. It can be seen from Fig. 3.20 that the *ab initio* points reveal substantial anharmonicity of the underlying PESs. It can be seen from Table 3.31 that third and fourth order terms contribute (along the given vibrational modes) to the Taylor expansion [*cf.* Eq. 3.11e] of the potential energy of this isomer. With such higher order expansion, it can be seen from Fig. 3.20 that the *ab initio* energies are very well reproduced by the model.

The energetic minimum of the seam of various CIs and the minimum of the upper adiabatic electronic states are estimated. The resulting data are collected in Table 3.35. The diagonal entries in this table are the energy at the minimum of a state. Whereas, the off-diagonal entries represent the minimum of the seam of CIs. Although the electronic state $\widetilde{X}^2B_2$ is energetically well separated from $\widetilde{A}^2B_1$ state (*cf.* Table 3.15) the energetic minimum of the seam of $\widetilde{X}^2B_2$ -$\widetilde{A}^2B_1$ CIs is located at $\sim$3.91 eV (*cf.* Table 3.35) and only $\sim$0.05 eV above the $\widetilde{A}$ state minimum. As the coupling strength of a_2 vibrational modes between these states is moderate (see Table 3.33), the CIs can act as a funnel for the nonradiative transfer of electronic population of $\widetilde{A}^2B_1$ state to the $\widetilde{X}^2B_2$ state. The minimum of $\widetilde{X}^2B_2$ -$\widetilde{B}^2B_2$ and $\widetilde{X}^2B_2$ -$\widetilde{C}^2A_1$ CIs occurs at $\sim$ 6.09 and $\sim$6.10 eV, respectively. These are $\sim$ 1.76 and $\sim$1.19 eV above the minimum of the

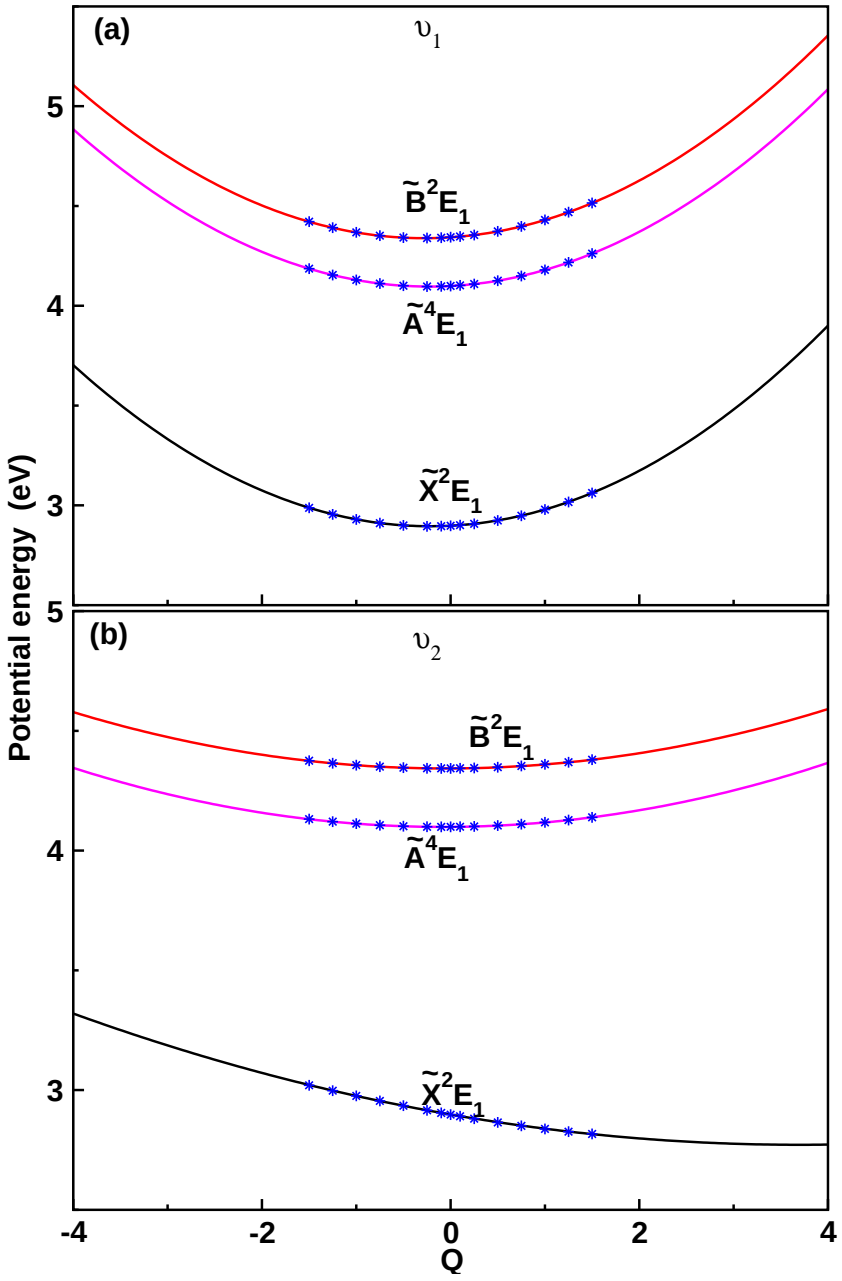

Figure 3.18: One dimensional plots of multidimensional adiabatic PESs of $\widetilde{X}^2E_1$, $\widetilde{A}^4E_1$ and $\widetilde{B}^2E_1$ electronic states of isomer I of B_7 as a function of the dimensionless normal displacement coordinates of the totally symmetric a_1 vibrational modes, ν_1-ν_2. The electronic energies are plotted along the coordinate of the given vibrational mode keeping others at their equilibrium reference configuration. The energies obtained from the constructed model and calculated *ab initio* are shown by the lines and points, respectively.

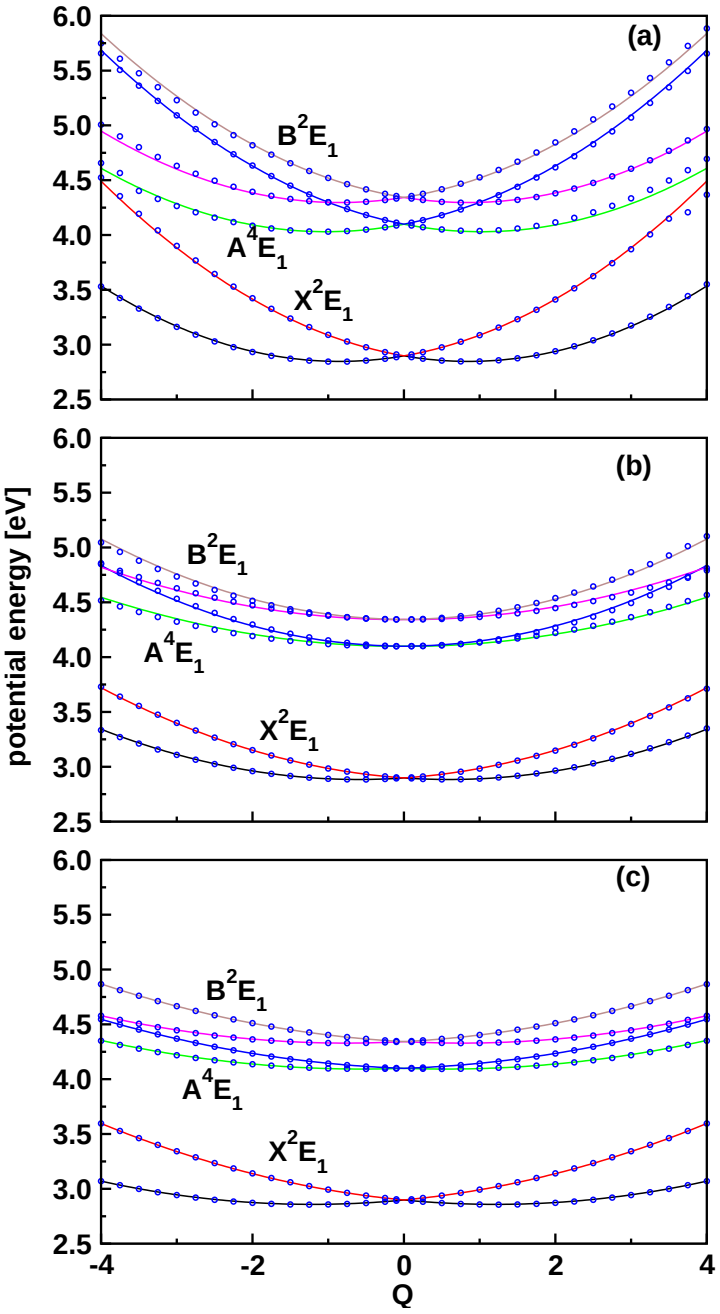

Figure 3.19: Same as in Fig. 3.18, plotted along the normal displacement coordinate of the x component of the JT active degenerate vibrational modes ν_8, ν_9 and ν_{10} in panel a, b and c, respectively.

$\widetilde{B}^2B_2$ and $\widetilde{C}^2A_1$ state, respectively. The minimum of $\widetilde{X}^2B_2$ -$\widetilde{D}^2B_1$ CIs occurs at ∼5.69 eV, which is just ∼0.10 eV above the minimum of $\widetilde{D}^2B_1$ electronic state. Similarly, the minimum of $\widetilde{A}$-$\widetilde{B}$ CIs occurs at ∼ 4.35 eV, which is only ∼ 0.02 eV above the minimum of $\widetilde{B}$ state. Furthermore the coupling of these two states via vibrational modes of a_2 symmetry is stronger [*cf.* Table 3.33]. Therefore, the vibronic structures of the $\widetilde{A}$ and $\widetilde{B}$ electronic states is expected to be strongly perturbed by the associated nonadiabatic effects. Eventhough the $\widetilde{A}^2B_1$ -$\widetilde{C}^2A_1$ CI occurs at ∼4.93 eV and located only ∼0.02 eV above the minimum of $\widetilde{C}^2A_1$ state, the coupling between these states via ν_{11} vibrational mode (*cf.* Table 3.33) is much weaker compared to $\widetilde{A}$-$\widetilde{B}$ coupling. Finally, the minimum of $\widetilde{B}^2B_2$ -$\widetilde{C}^2A_1$ CIs occurs at ∼5.00 eV and located ∼0.09 eV above the minimum of the $\widetilde{C}^2A_1$ state. The coupling strength of ν_{15} vibrational mode is also quite large between these states. Impact of these electronic state couplings on the nuclear dynamics is discussed in section 4.2.3.

3.4.5 $^2A_2$, $^2B_2$, $\widetilde{B'}^2B_1$, $\widetilde{C'}^2A_1$ and $\widetilde{D'}^2A_1$ electronic states of isomer III of B_7

Adiabatic potential energies of the $\widetilde{X'}$, $\widetilde{A'}$, $\widetilde{B'}$, $\widetilde{C'}$ and $\widetilde{D'}$ electronic states of the neutral isomer III are plotted as a function of the normal displacement coordinates of the totally symmetric vibrational modes (ν_1-ν_6) in Figs. 3.21(a-f). As in the case of isomer I and II, the calculated *ab initio* energies are in excellent accord with those obtained from the vibronic model in this case also. It can be seen from Fig. 3.21, in particular, from panel a and f that electronic states of isomer III exhibit a rich variety of curve crossings-all five states are entangled together. As in case of isomer II, the energetic minimum of various CIs and also the minimum of the states are estimated in this case. The results are collected in Table 3.35. It can be seen from the latter that the minimum of $\widetilde{X'}$-$\widetilde{A'}$ CIs is ∼0.73 and ∼0.16 eV above the minimum of the $\widetilde{X'}$ and $\widetilde{A'}$ states, respectively. The minimum of the $\widetilde{X'}$-$\widetilde{B'}$ CIs is quasi-degenerate with the minimum of the $\widetilde{B'}$ state and occurs ∼0.42 eV above the minimum of the $\widetilde{X'}$ state. Similarly, the minimum of $\widetilde{X'}$-$\widetilde{C'}$ CIs occurs nearly at the equilibrium minimum of the $\widetilde{C'}$ state. While the coupling of the $\widetilde{X'}$-$\widetilde{B'}$ state is not revealed by the electronic structure results, that of the $\widetilde{X'}$-$\widetilde{A'}$ and $\widetilde{X'}$-$\widetilde{C'}$ is expected to have noticeable impact on the nuclear dynamics (*cf.* Table 3.33). The intersection minimum of $\widetilde{B'}$ and $\widetilde{C'}$ state occurs ∼0.25 eV above the minimum of the $\widetilde{C'}$ state. These two states are strongly coupled through ν_{10} vibrational mode of b_1 symmetry. The $\widetilde{B'}$ and $\widetilde{D'}$ states are also fairly strongly coupled through ν_9 and ν_{10} vibrational modes. The intersection minimum of these states occurs ∼0.73 eV above the minimum of the $\widetilde{D'}$ state. The intersections between the remaining states occur at higher energies and are not expected to have any noticeable impact on the nuclear dynamics.

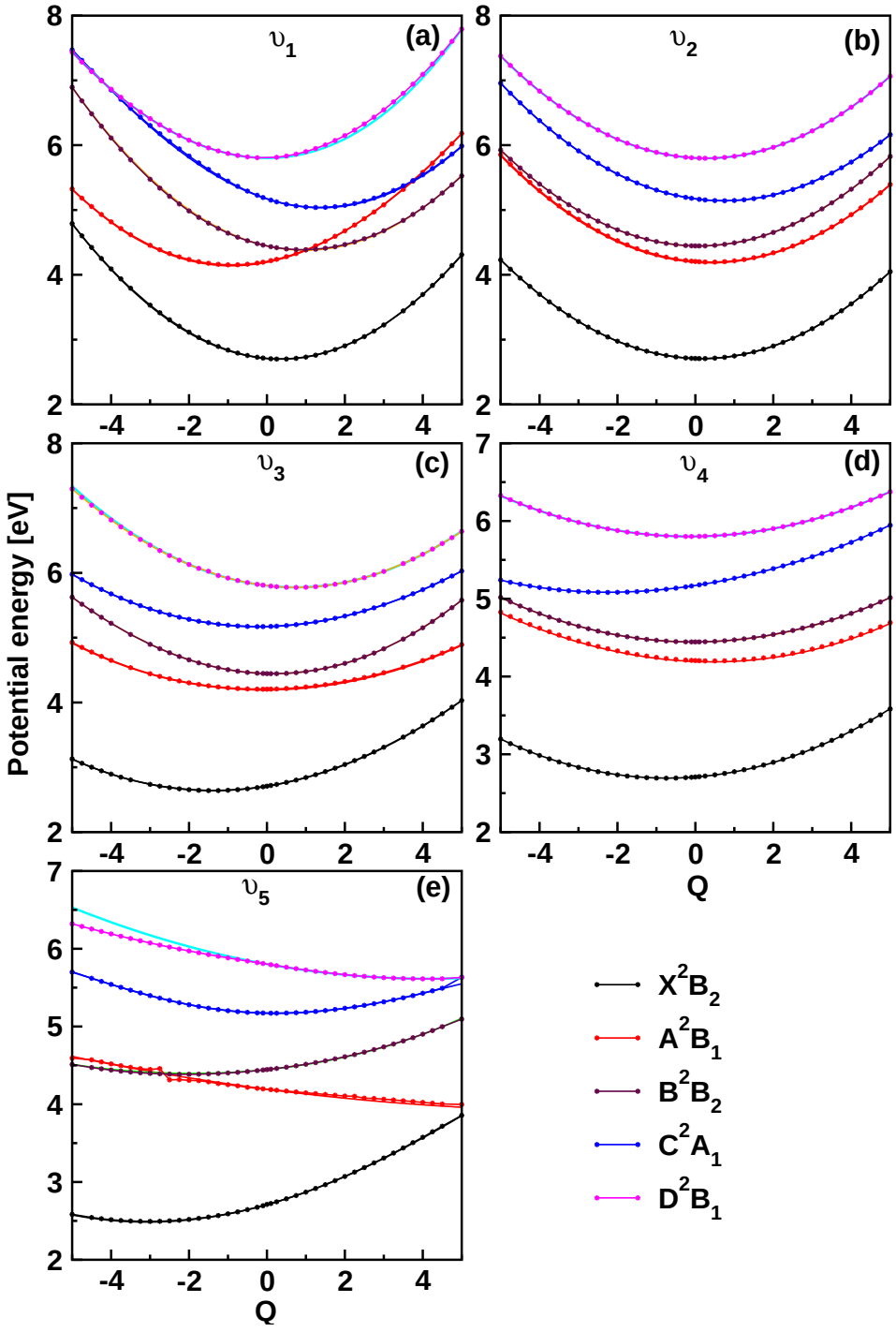

Figure 3.20: Same as in Fig. 3.18 for the $\widetilde{X}^2B_2$, $\widetilde{A}^2B_1$, $\widetilde{B}^2B_2$, $\widetilde{C}^2A_1$ and $\widetilde{D}^2B_1$ electronic states of neutral B_7 originating from the isomer II of B_7^-.

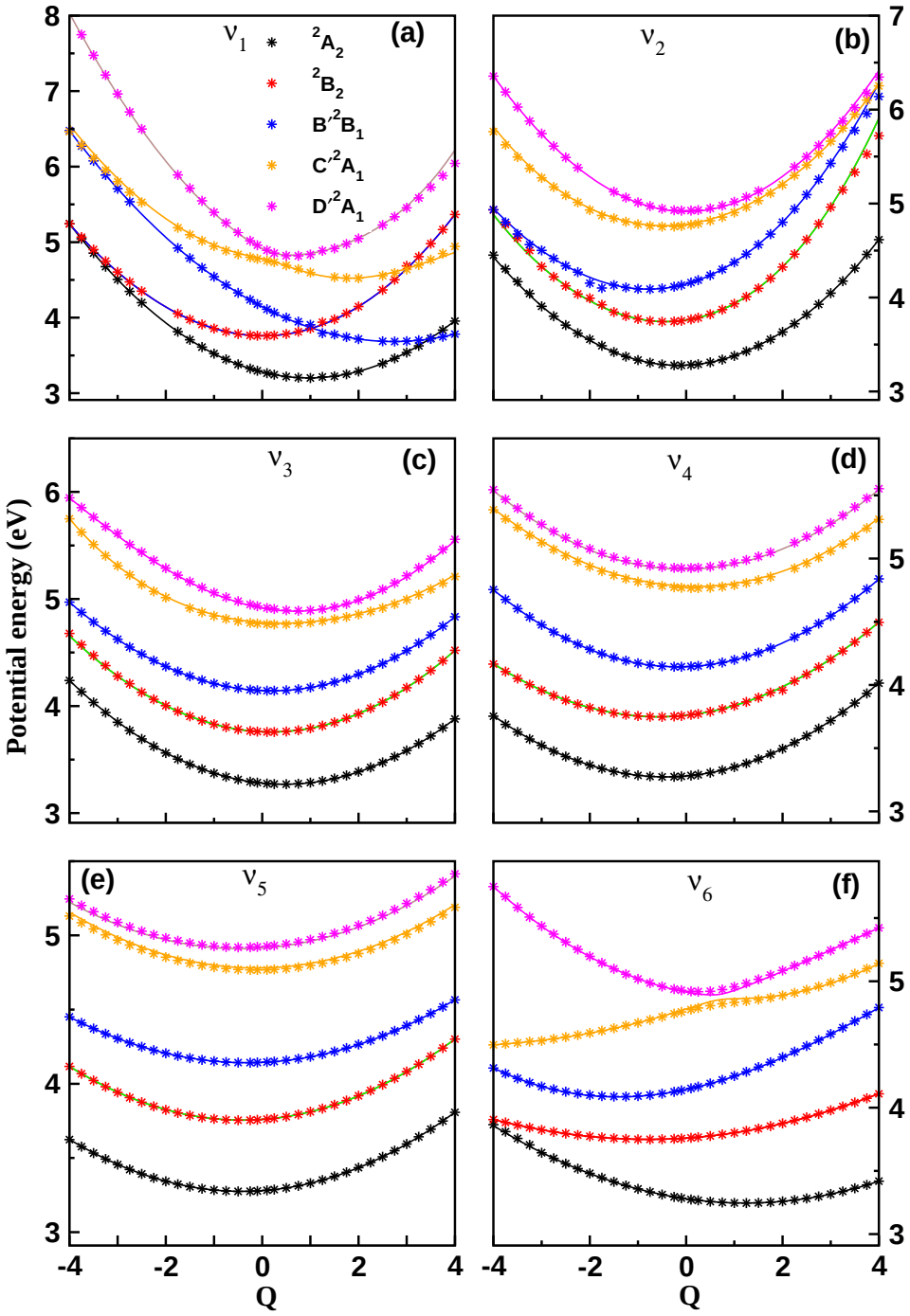

Figure 3.21: Same as in Fig. 3.18 for the ${}^2A_2$, ${}^2B_2$, $\widetilde{B'}^2B_1$, $\widetilde{C'}^2A_1$ and $\widetilde{D'}^2A_1$ electronic states of neutral B_7 originating from the isomer III of B_7^-.

Table 3.35: Estimated equilibrium minimum (diagonal entries) and minimum of the seam of various CIs (off-diagonal entries) of the electronic states of neutral isomer II and III within a quadratic coupling model. All quantities are given in eV.

	Isomer II						Isomer III				
	$\widetilde{X}$	$\widetilde{A}$	$\widetilde{B}$	$\widetilde{C}$	$\widetilde{D}$		$\widetilde{X'}$	$\widetilde{A'}$	$\widetilde{B'}$	$\widetilde{C'}$	$\widetilde{D'}$
$\widetilde{X}$	2.32	3.91	6.09	6.10	5.69	$\widetilde{X'}$	3.14	3.87	3.56	4.43	16.93
$\widetilde{A}$		3.86	4.35	4.93	-	$\widetilde{A'}$		3.71	3.79	4.47	5.28
$\widetilde{B}$			4.33	5.00	5.62	$\widetilde{B'}$			3.56	4.66	5.37
$\widetilde{C}$				4.91	5.59	$\widetilde{C'}$				4.41	6.70
$\widetilde{D}$					5.59	$\widetilde{D'}$					4.64

3.5 Summary

Structures of the low-lying electronic states of neutral B_4, B_5 and B_7 clusters have been investigated here as a prerequisite for the dynamics study (presented in Chapter 4) to examine the photodetachment spectrum of the corresponding anions. The electronic energies are calculated by the CASSCF-MRCI method along the normal coordinates of the reference equilibrium geometry of the corresponding anionic clusters. The possibilities of curve crossings and CIs among various electronic states of B_4 and B_5 are thoroughly examined. In case of B_4 the possibility of intersystem crossings between its singlet and triplet electronic states is also analyzed. The possible spin contamination issue in B_4^- is examined in detail using different electronic structure methods. With the aid of the calculated *ab initio* energies, model vibronic Hamiltonians are developed in terms of normal coordinates of vibrational modes and employing a diabatic electronic basis. It is found that the model required terms upto sixth order in the Taylor expansion of the elements of the electronic Hamiltonian matrix for a satisfactory representation of the calculated *ab initio* data for B_5 along same vibrational modes. Various stationary points of the multidimensional PESs, e.g., the energetic minimum of the seam of CIs and the equilibrium minimum of a state, are estimated. The static aspects of neutral B_7 clusters originating from electron detachment of three isomers (C_{6v} hexagonal pyramidal, C_{2v} pyramidal and C_{2v} planar) of anionic B_7^- cluster are examined. All three neutral B_7 clusters originating from the three isomers of B_7^- exhibit rich vibronic coupling mechanisms in their energetically low-lying electronic states. While the latter of the neutral cluster corresponding to the C_{6v} isomer are JT active, those corresponding to the C_{2v} isomers form symmetry allowed CIs. To the best of our knowledge, B_7 represents a unique system for which the complex vibronic structure of the energetically low-lying electronic state arise from anion precursors of different symmetry and a rich variety of VC mechanism. The expected impact of these energy data on the nuclear dynamics of B_4, B_5 and B_7 electronic states (studied in detail in Chapter 4) is discussed.

References

[1] H. Kato and K. Yamashita, Chem. Phys. Lett. **190**, 361 (1992).

[2] I. Boustani, Int. J. Quantum Chem. **52**, 1081 (1994).

[3] A. Ricca and C.W. Bauschlicher Jr., Chem. Phys. **208**, 233 (1996).

[4] I. Boustani, Phys. Rev. B. **55**, 16426 (1997).

[5] L. Hanley, J. L. Whitten, and S. L. Anderson, J. Phys. Chem. **92**, 5803 (1988).

[6] L. Hanley and S. L. Anderson, J. Phys. Chem. **91**, 5161 (1987).

[7] S. A. Ruatta, P. A. Hintz, and S. L. Anderson, J. Chem. Phys. **94**, 2833 (1991).

[8] P. A. Hintz, S. A. Ruatta, and S. L. Anderson, J. Chem. Phys. **92**, 292 (1992).

[9] M. Kobayashi, I. Higashi, and M. Takami, J. Solid State Chem. **133**, 211 (1997).

[10] R. N. Grimes, J. Chem. Educ. **81**, 657 (2004).

[11] A. N. Alexandrova, A. I. Boldyrev, H. J. Zhai, and L. S. Wang, Coord. Chem. Rev. **250**, 2811 (2006).

[12] B. Kiran, S. Bulusu, H.J Zhai, S. Yoo, X. C. Zeng and L. S. Wang. Proc. Natl. Acad. Sci. USA. **102**, 961 (2005).

[13] H. J. Zhai, L. S. Wang, A. N. Alexandrova, A. I. Boldyrev, and V. G. Zakrzewski, J. Phys. Chem. A **107**, 9319 (2003).

[14] H. J. Zhai, L. S. Wang, A. N. Alexandrova, and A. I. Boldyrev, J. Chem. Phys. **117**, 7917 (2002).

[15] H-J Zhai, L-S Wang, A. N. Alexandrova and A. I. Boldyrev, J. Phys. Chem. A **108**, 3509 (2004).

[16] Q-S Li, L-F Gong, and Z-M Gao, Chem. Phys. Lett. **390**, 220, (2004)

[17] M. T. Nguyen, M. H. Matus, V. T. Ngan, D. J. Grant, and D. A. Dixon, J. Phys. Chem. A **113**, 4895, (2009)

[18] T. B. Tai, D. J. Grant, M. T. Nguyen, and D. A. Dixon, J. Phys. Chem. A **114**, 994, (2010)

[19] D. C. Young, Computational Chemistry: A Practical Guide for Applying Techniques to Real World Problems, John Wiley & Sons, Inc., New York, USA, 2002, p. 227.

[20] A. N. Alexandrova, A. I. Boldyrev, Y. J. Fu, X. Yang, X. B. Wang, and L. S. Wang, J. Chem. Phys. **121**, 5709 (2004).

[21] A. N. Alexandrova and A.I. Boldyrev, J. Chem. Theory Comput. **1**, 566 (2005).

[22] J. V. Ortiz, J. Chem. Phys. **89**, 6348 (1988).

[23] L. S. Cederbaum, J. Phys.B **8**, 290 (1975).

[24] W. von Niessen, J. Schirmer, and L. S. Cederbaum, Comp. Phys. Rep. **1**, 57 (1984).

[25] T. S. Venkatesan, K. Deepika, and S. Mahapatra, J. Comput. Chem. **27**, 1093 (2006).

[26] A. D. Becke, J. Chem. Phys. **98**, 5648 (1993).

[27] R. A. Kendall, T. H. Dunning Jr., and R. J. Harrison, J. Chem. Phys. **96**, 6796 (1992).

[28] T. H. Dunning, Jr., J. Chem. Phys. **90**, 1007 (1989).

[29] M. J. Frisch, *et al.* Gaussian 03, Revision B. 05, Gaussian, Inc., Pittsburgh, PA, 2003.

[30] M. Head-Gordon, J. A. Pople, and M. J. Frisch, Chem. Phys. Lett. **153**, 503 (1988).

[31] M. J. Frisch, M. Head-Gordon, and J. A. Pople, Chem. Phys. Lett. **166**, 275 (1990).

[32] M. J. Frisch, M. Head-Gordon, and J. A. Pople, Chem. Phys. Lett. **166**, 281 (1990).

[33] J. Cizek, Adv. Chem. Phys. **14**, 35 (1969).

[34] G. D. Purvis and R. J. Bartlett, J. Chem. Phys. **76**, 1910 (1982).

[35] G. E. Scuseria, C. L. Janssen, and H. F. Schaefer III, J. Chem. Phys. **89**, 7382 (1988).

[36] G. E. Scuseria and H. F. Schaefer III, J. Chem. Phys. **90**, 3700 (1989).

[37] J. A. Pople, M. Head-Gordon, and K. Raghavachari, J. Chem. Phys. **87**, 5968 (1987).

[38] E. B. Wilson Jr., J. C. Decius, and P. C. Cross, Molecular vibrations (McGraw-Hill, New York, 1955).

[39] H. -J. Werner and P. J. Knowles, J. Chem. Phys. **89**, 5803 (1988).

[40] P. J. Knowles and H. -J. Werner, Chem. Phys. Lett. **145**, 514 (1988).

[41] P. J. Knowles and H. -J. Werner, Theor. Chim. Acta. **84**, 95 (1992).

[42] H. -J. Werner, P. J. Knowles, R. D. Amos, A. Bernhardsson, and others, MOLPRO-2010.2, a package of ab initio programs; Universitat Stuttgart: Stuttgart, Germany; University of Birmingham:Birmingham, United Kingdom, 2010.2.

[43] T. Koopmans. Physica. **1**, 104 (1933).

[44] H. Köppel, W. Domcke, and L. S. Cederbaum, Adv. Chem. Phys. **57**, 59 (1984).

[45] S. S. Shaik, J. Am. Chem. Soc. **101**, 3184 (1979)

[46] S. P. McGlynn, T. Azumi, and M, Kinoshita, The Triplet State, (Prentice-Hall, Engiewood Cliffs, N.J., 1969).

[47] A. Berning, M. Schweizer, H. -J. Werner, P. J. Knowles, and P. Palmieri, Mol. Phys. **98**, 1823 (2000).

[48] Mathematica, Version 5.0, Wolfram Research Inc., Champaign, IL (2003).

[49] *Conical Intersections: Electronic Structure, Dynamics and Spectroscopy*, W. Domcke, D. R. Yarkony, H. Köppel, Eds., World Scientific: Singapore, 2004.

[50] *Conical Intersections: Theory, Computation and Experiment*, W. Domcke, D. R. Yarkony, H. Köppel, Eds., World Scientific: Singapore, 2011.

4 Theoretical study of photodetachment spectra of anionic boron clusters. Nuclear dynamics

4.1 Introduction

The nuclear dynamics of boron clusters has not been studied in the literature except for B_3 [1] from our group. In this chapter we investigate how the complex structural properties of boron clusters detailed in Chapter 3 contribute to the nuclear dynamics underlying the observed photodetachment bands [2,3]. The crossings of various electronic states leading to CIs [7,8] often control the nuclear motion primarily on the participating electronic states and contribute to their overall band structures and time-dependent properties. The most critical consequence of CIs of electronic PESs is a break-down of the adiabatic BO theoretical formalism [9, 10]. In such circumstances it is therefore necessary to go beyond and examine nuclear motion concurrently with the electronic motion [7, 11–13]. The present study (wherever relevant) considers such a requirement. Moreover, the study here relies on a full quantum mechanical treatment including most of the relevant electronic and nuclear DOF.

The photodetachment spectrum of B_4^-, B_5^- and B_7^- considered here has been experimentally recorded by Wang and coworkers at three different (355, 266 and 193 nm) wavelengths of the probe laser photon [2, 3]. Depending on the energy of the probe photon at these wavelengths (3.496, 4.661 and 6.424 eV, respectively, in that order) the recorded vibronic bands reveal varied degree of energy resolution of the underlying peaks that could be attributed to the excitation of specific vibrational quanta. In the theoretical study detailed below, we tried to identify and assign the specific vibrational modes that contribute to a given spectral envelope predominantly.

The experimental photodetachment spectrum of B_4^- recorded by Wang and coworkers [2] reveals four broad bands in the 1.0-5.0 eV energy range. The recording at 355 nm photon wavelength revealed partially resolved structure of the $\widetilde{a}$ band whereas the $\widetilde{X}$ band revealed broad structure consistently at all three wavelengths of the photon used in the measurements. The latter is interpreted (through *ab initio* electronic structure calculations) to be due to a large geometry change of the neutral B_4 in its electronic ground state compared to that of B_4^- [2]. The detachment spectrum recorded at 266 nm revealed interesting and complex overlapping structures of the triplet $\widetilde{a}$ and $\widetilde{b}$ electronic states of B_4 [2]. While the origin of $\widetilde{X}$, $\widetilde{a}$ and $\widetilde{b}$ bands could be successfully predicted, the C band (as marked in the experiment [2]) that shows up in the 193 nm spectrum

could not be given a clear interpretation of its origin! In the present chapter, in addition to describing the detailed structure of the $\widetilde{X}$, $\widetilde{a}$ and $\widetilde{b}$ bands, we attempt to resolve this issue also.

The photodetachment spectrum of B_5^- recorded using same laser photons (as in case of B_4^-) revealed four bands in the 1.5-6.4 eV binding energy range [3]. While the three bands observed at lower energies are attributed to the $\widetilde{X}$, $\widetilde{A}$ and $\widetilde{B}$ doublet electronic states of B_5, the fourth one revealed much complex pattern observed at higher electron binding energies [3]. Resolved vibrational structures of the $\widetilde{X}$ and $\widetilde{A}$ bands are reported at 355 nm and 266 nm photon wavelengths, respectively. An adiabatic ionization energy of $\sim$ 2.33 eV is estimated from the resolved vibronic structure of the $\widetilde{X}$ state in which the 550 cm^{-1} vibrational mode is reported to make major progressions [3]. An average spacing of $\sim$ 530 cm^{-1} is estimated from the resolved vibronic structure of the $\widetilde{A}$ band observed in the 266 nm spectrum [3]. The $\widetilde{B}$ band, distinctly appeared in the 193 nm spectrum, is very broad and no vibrational progressions could be resolved. The complex features of the C band observed in the 193 nm spectrum is reported to originate from two one electron and several multielectron transitions. Inadequate energy resolution is one of the major shortcoming of the detachment spectrum of these small boron clusters. As pointed out by Wang and co-workers [2] that this is primarily due to low photodetachment cross sections of the light clusters and difficulty to produce them in cold conditions. The VDEs of B_5^- has been computed by the ROVGF as well as RCCSD(T) methods and excellent agreement with the experimental results has been reported [3]. The electron affinities of neutral B_4 and B_5 clusters and VDEs of their anions are calculated at CCSD(T) level and extrapolated upto CBS level [5, 6]. These reported results are in good accord with ours presented in Chapter 3.

The photodetachment spectrum of B_7^- recorded by Wang and co-workers reveals very complicated and congested band structure [4]. The spectrum recorded at 193 nm is reproduced in panel a of Fig. 4.20. A broad feature (X) at $\sim$2.85 eV and a very sharp and intense band (A) at $\sim$3.44 eV with a short vibrational progression with a spacing 480 (40) cm^{-1} are observed with the 355 nm laser photon. The adiabatic detachment energies $\sim$ 2.55 and 3.44 eV for X and A bands are observed in the experiment [4]. Four more bands B (3.71 eV), C (3.84 eV), D (4.05 eV) and E (4.21 eV) are observed at 266 laser energy. In 199 nm spectrum five more states appeared in a congested and narrow energy range of $\sim$ 0.7 eV. Overall total 11 distinct features are discernible in the 193 nm spectrum. The spectral intensities in the photodetachment spectrum of B_7^- found to be altered by the source of boron cluster beam [4], indicating the contribution of more than one low-lying isomers. Boldyrev *et al.* with his *ab initio* calculations confirmed that three isomers of B_7^- viz., a triplet hexagonal pyramidal (C_{6v}, $^3A_1$), a singlet pyramidal (C_{2v}, $^1A_1$) and a singlet planar (C_{2v}, $^1A_1$) contribute most to the recorded photodetachment band structure [4]. The above three isomers will be identified as I, II and III in the given order in the rest of this chapter.

In the present chapter we set out to investigate the detailed structure of each of the observed photodetachment bands of B_4^-, B_5^- and B_7^- by studying the underlying nuclear dynamics quantum mechanically using the techniques developed in 2 and employing the

Hamiltonians developed in Chapter 3. The excitations of vibrational modes, electronic nonadiabatic coupling effects and decay of the excited electronic states are examined and discussed in relation with the experimental observations mentioned above.

4.2 Results and Discussions

In this section we first report the complete broad band spectral envelopes of the electronic states of B_4, B_5 and B_7. These broad band envelopes are calculated by propagating WPs using the MCTDH program modules [14–17] and considering the complete Hamiltonians developed in Chapter 3. The *ab initio* electronic structure parameters reported therein are used (as are) without any adjustments. The theoretical results are compared with the reported experimental band structures [2, 3]. Subsequently, each of the broad spectral envelopes is critically examined at higher energy resolution. In this case the precise location of the vibronic levels is calculated by a time- independent matrix diagonalization approach employing the Lanczos algorithm [18] as stated above. The resolved band structures are also compared with resolved experimental results whenever available. Importantly, this exercise enabled us to identify the excitations of the vibrational modes underlying the broad experimental bands and assess the impact of electronic nonadiabatic effects on their overall structure. Finally, the decay of excited electronic states is examined and discussed.

4.2.1 Photodetachment bands of B_4^-

Broad band spectral envelope

The broad band spectrum of the low-lying electronic states of B_4 is shown in Fig. 4.1 along with the recorded 193 nm detachment spectrum of Wang and coworkers [2]. The theoretical results are obtained by using the six states diabatic Hamiltonian given in Eq. (3.7a) of Chapter 3 including all six vibrational degrees of freedom. Six separate WP propagations are carried out by preparing the WP initially in each of these electronic states and by numerically solving the time-dependent Schrödinger equation with the aid of the MCTDH program modules [14–17]. The technical details of the MCTDH WP propagations are given in Table 4.1. The time autocorrelation function data obtained from six calculations are combined in 1:1 statistical ratio, damped with an exponential function, $e^{-\frac{t}{\tau}}$ (with a damping time τ= 11 fs) and finally Fourier transformed to generate the spectral envelopes shown in the panel a and b of Fig. 4.1. While the set of Hamiltonian parameters (cf. Tables 3.17 to 3.20 of Chapter 3) obtained with the UB3LYP optimized equilibrium geometry of B_4^- used to calculate the spectrum in panel a, the same (cf. Tables 3.21 to 3.24 of Chapter 3) obtained with the ROMP2 optimized equilibrium geometry are used to calculate the spectrum in panel b. It can be seen that both the results agree extremely well with each other. This additionally demonstrates negligible spin contamination in the theoretical results presented here. Although the theoretical results in Figs. 4.1(a-b) obtained by using reference geometry optimized by two different methods agree extremely well with each other, the VDEs obtained from the

Table 4.1: The normal mode combinations, sizes of the primitive and single particle bases used in the WP propagation (using the MCTDH program modules [14–17]) on the $\widetilde{X}$-$\widetilde{a}$-$\widetilde{b}$-$\widetilde{A}$-$\widetilde{c}$-$\widetilde{B}$ electronic manifold of B_4^- using the Hamiltonian of Eq. (3.7a) of Chapter 3.

S.No	Normal modes	Primitive basis	SPF basis
1	ν_1,ν_3	(10,8)	[6,4,4,6,10,15]
2	ν_2,ν_5	(12,4)	[10,10,4,10,4,4]
3	ν_4,ν_6	(4,8)	[6,8,8,6,4,4]

ROMP2 optimized reference geometry seem to reproduce the experiment slightly better (cf., Table 3.3 of Chapter 3) , Therefore, we have adjusted the VDE values obtained with the UB3LYP optimized geometry to those of the ROMP2 reference values in calculating the band structure presented in panel a.

It can be seen that the experimental features of the recorded detachment spectrum (reproduced from ref. [2] in panel c) are reproduced very well by both sets of theoretical results presented in Fig. 4.1. We reiterate that the $\widetilde{X}$ band has been found to be broad and diffuse in all three different wavelengths of the probe laser photon used in the experiment [2]. The broad structure of the $\widetilde{X}$ band is attributed to a large geometry change of the equilibrium minimum configuration of the electronic ground state of B_4^- and B_4 [2].

The second broad band has been attributed to the vibronic structure of the $\widetilde{a}^3B_{2u}$ and $\widetilde{b}^3B_{1u}$ electronic states of B_4 based on their VDEs. It can be seen from Table 3.18 of Chapter 3 that these two states are coupled through the ν_6 vibrational mode of b_{3g} symmetry. Also, the bilinear interstate coupling parameter along $\nu_3\nu_4$ vibrational modes is nonzero for these states. It is discussed in Chapter 3 that the energetic minimum of the $\widetilde{a}$-$\widetilde{b}$ CIs occurs at $\sim$ 3.34 eV, which is quasi-degenerate with the minimum of the $\widetilde{b}$ state. This results into the highly overlapping and diffuse structure of the second detachment band of B_4^-. It can be seen that the observed asymmetry of this band is very well reproduced by the present theoretical results.

The third detachment band of B_4^- has been found to be formed by the $\widetilde{A}$, $\widetilde{c}$ and $\widetilde{B}$ electronic states of B_4. All these three states are located vertically within $\sim$1.0 eV of energy (cf., Table 3.3 of Chapter 3). The coupling of the singlet $\widetilde{A}$ and $\widetilde{B}$ states is not found from the electronic structure data. The triplet $\widetilde{c}$ state is however, strongly coupled to the $\widetilde{b}$ state through the ν_5 vibrational mode (cf., Table 3.18 of Chapter 3). Despite this, the energetic minimum of the $\widetilde{b}$-$\widetilde{c}$ CIs occurs at $\sim$ 11.33 eV which is $\sim$ 7.24 eV above the $\widetilde{c}$ state minimum. It is therefore very unlikely to expect any impact of the $\widetilde{b}$-$\widetilde{c}$ CIs on the overall structure of the third detachment band. Although the theoretical structure of this band in Fig. 4.1 reveals an overall agreement with the experiment, there remains several discrepancies:
(i) the structures above $\sim$ 3.7 eV and below $\sim$ 4.25 eV seen in the theoretical spectrum are missing in the experimental band,
(ii) the theoretical band reveals distinct peak structure, whereas the experimental band

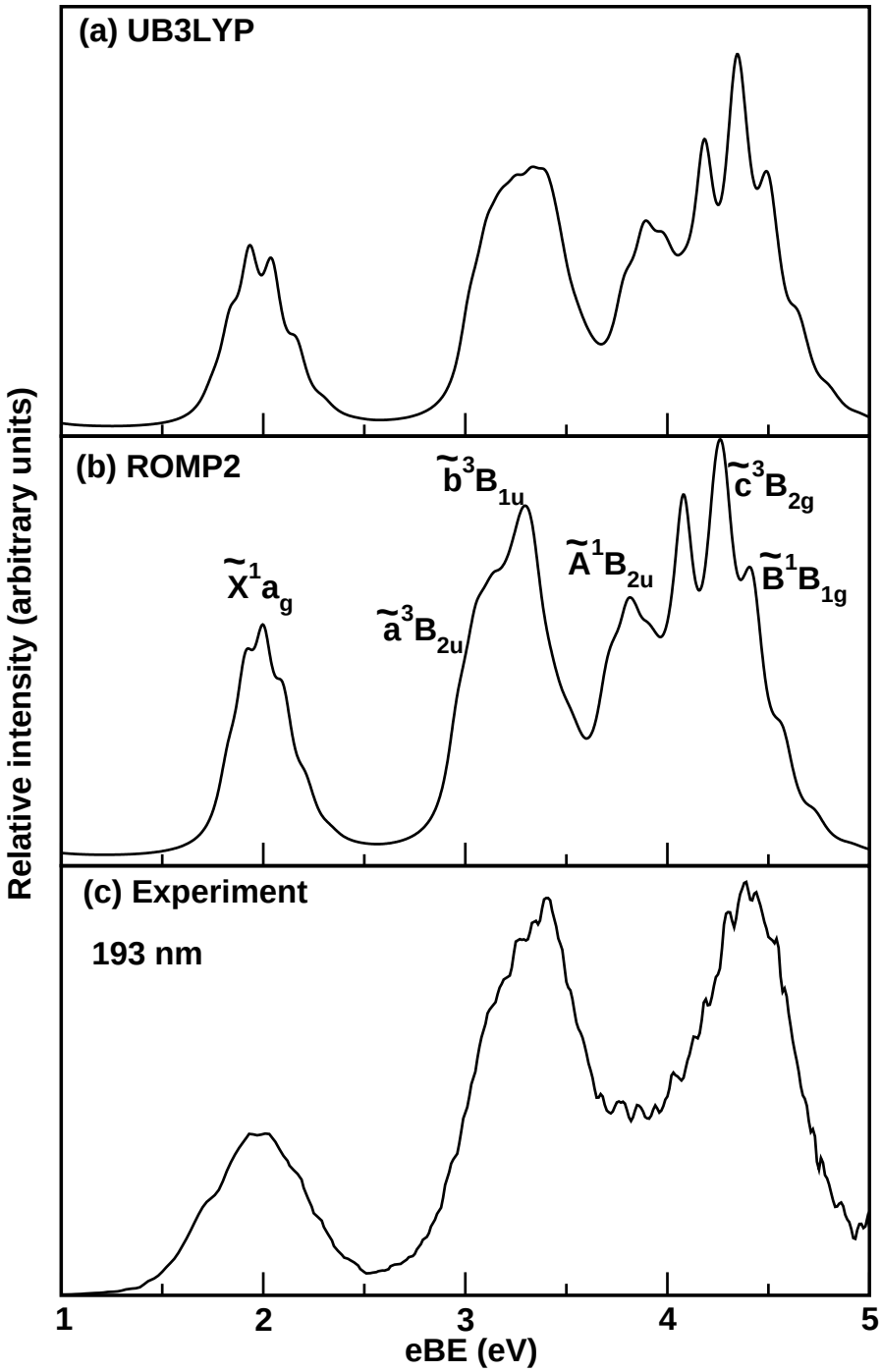

Figure 4.1: The photodetachment bands of B_4^- obtained by the time-dependent WP propagation approach (see text for details) and employing the complete vibronic Hamiltonian of Eq. 3.7a of Chapter 3. The theoretical results obtained by using the UB3LYP and ROMP2 reference geometries are shown in panel a and b, respectively. The symmetry of the final electronic states (of neutral B_4) at the reference equilibrium configuration is indicated in panel a. The 193 nm experimental recording of Wang and coworkers is reproduced from Ref. [2] and shown in panel b.

Table 4.2: The number of harmonic oscillator basis function used in the calculation of the stick vibronic spectrum of the mentioned electronic states of B_4.

S.NO	State(s)	No. of HO basis along ν_1,ν_2,ν_3,ν_4,ν_5,ν_6
1	$\widetilde{X}^1A_g$	9,100,2,2,2,2
2	$\widetilde{a}^3B_{2u}$	10,200,2,2,2,2
3	$\widetilde{b}^3B_{1u}$	80,4,2,2,2,2
4	$\widetilde{A}^1B_{2u}$	5,125,2,2,2,2
5	$\widetilde{c}^3B_{2g}$	320,6,2,2,2,2
6	$\widetilde{B}^1B_{2g}$	250,6,2,2,2,02
7	$\widetilde{X}^1A_g$-$\widetilde{A}^1B_{2u}$	30,300,10,10,2,2
8	$\widetilde{a}^3B_{2u}$-$\widetilde{b}^3B_{1u}$	10,150,6,6,45,2

is almost structureless.

Small detachment cross sections obtained in the experimental measurements [2] and the neglect of probable contribution from dynamic spin- orbit interactions of the triplet $\widetilde{c}$ state with the participating singlet states may be the reasons for the observed discrepancy. The latter issue is presently being examined in our group.

Interpretation of the structure of the detachment bands

The photodetachment bands of B_4^- presented in Fig. 4.1(a) are examined here in detail to reveal the contributions of the vibrational modes to the broad envelopes. A time-independent matrix diagonalization method (as discussed in Sec. 2.4.1) of Chapter 2 is employed for this purpose. This method yields the precise location of the vibronic lines within the accuracy of the present theoretical model. The technical details of the calculation of all the stick vibronic spectra presented in this section are given in Table 4.2. The calculated stick spectrum of a given state is convoluted with a Lorentzian function with 15 meV FWHM to generate the corresponding envelope. All theoretical calculations are carried out with the Hamiltonian parameters presented in Chapter 3 (cf., Tables 3.17 to 3.20 of Chapter 3) without any adjustments.

The vibrational structure of the $\widetilde{X}^1A_g$ electronic state of B_4 without including its coupling with the neighboring states is shown in panel a of Fig. 4.2. Both the symmetric vibrational modes ν_1 and ν_2 form progressions in this band. The dominant progression is formed by the ν_2 vibrational mode. The peaks are 1590 and 423 cm^{-1} spaced corresponding to the frequency of combination (ν_1+ν_2) and ν_2 vibrational modes, respectively. As stated above that a very broad structure of this band is observed in the experiment. The best, resolved band structure obtained in the 355 nm recording is given in panel b of Fig. 4.2. It can be seen that the overall width of the experimental band is in good accord with the theoretical results. The theoretical VDEs of $\sim$ 1.903 eV (cf., Table 3.3 of Chapter 3) is also in good agreement with the experimental estimate of $\sim$ 1.99 $\pm$ 0.05 eV [2]. This estimate is slightly in better agreement with the results obtained

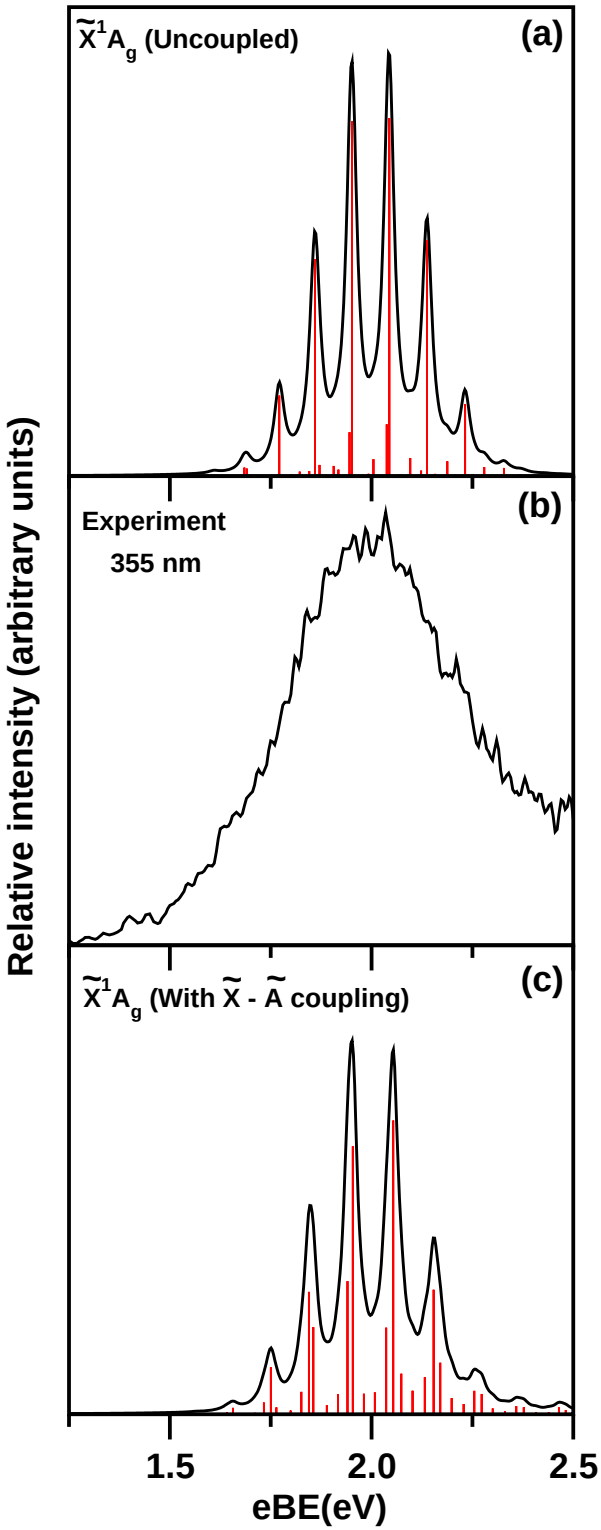

Figure 4.2: The stick vibronic spectrum of the $\widetilde{X}^1A_g$ electronic state of B_4 along with the convoluted spectral envelope. The spectrum obtained by excluding all couplings with the neighboring states is given in panel a. The best resolved 355 nm experimental recording is reproduced from Ref. [2] and shown in panel b. The spectrum obtained by including the coupling with the $\widetilde{A}$ electronic state is shown in panel c.

Table 4.3: Optimized equilibrium geometry parameters of the electronic ground state of B_4. The results available in the literature [2] are also included in the table for comparison.

S.No	Equilibrium parameters for B_4 in the $\widetilde{X}^1A_g$ state	Ref. [2]	Ref. [5][a]	This work B3LYP/aug-cc-pVTZ
1	E_{total}/hatree	-99.156	-98.919	-99.137
2	R(B1-B2)/angstrom	1.523	1.5754	1.519
3	R(B1-B3)/angstrom	-	1.9334	1.889
4	R(B2-B4)/angstrom	-	-	2.399
5	$\angle B1-B2-B3$ /degrees	76.50	75.7	76.5
6	$\angle B2-B1-B4$ /degrees	-	104.3	103.5

[a] The total electronic energy calculated at CCSD(T) and extrapolated to complete basis set upto doubles, triples and quadrapole zeta (CBS(DTQ)) approximation. The geometry parameters reported at CCSD(T)/aug-cc-pVTZ level of theory.

from ROMP2 and UCCSD(T) optimized reference geometry. It is discussed in Chapter 3 that the $\widetilde{X}^1A_g$ state is not coupled (in first-order) with the other two singlet states $\widetilde{A}$ and $\widetilde{B}$. A non-zero bilinear interstate $\widetilde{X}$-$\widetilde{A}$ coupling along $\nu_3\nu_6$ combination modes has been found (cf., Tables 3.19 and 3.23 of Chapter 3). However, no noticeable impact of this coupling on the structure of the $\widetilde{X}$ band is observed. The $\widetilde{X}$ band obtained by including the $\widetilde{X}$-$\widetilde{A}$ coupling is shown in panel c. The significant geometry change (along the B-B-B angle) from the anion to the neutral ground electronic state is obvious from the structure of $\widetilde{X}$ band. The intensity of the origin (0-0) peak is very small and the maximum shifts to the $4^{th}/5^{th}$ quantum of excitation of the ν_2 vibrational mode. We also optimized the equilibrium geometry of B_4 in the $\widetilde{X}$ state, at the B3LYP/aug-cc-pVTZ level of theory. The optimized geometry parameters are given in Table 4.3 and compared with the available literature data [3,5]. It can be seen in comparison with the optimized geometry parameters of the anionic $\widetilde{X}^2B_{1u}$ state (cf., Table 3.1 of Chapter 3) that all the adjacent B-B bonds are shortened by 0.04 angstrom[1] and the B-B-B angles are reduced by $\sim 13^\circ$ in the neutral ground state. The bond between the diagonally opposite B atoms elongates by ~ 0.24 angstroms in the neutral ground state.

The vibrational structures of the uncoupled $\widetilde{a}^3B_{2u}$ and $\widetilde{b}^3B_{1u}$ electronic states of B_4 are shown in panel a and b of Fig. 4.3, respectively. It can be seen from Table 3.18 of Chapter 3 that the coupling strength of both the symmetric vibrational modes is very small in the $\widetilde{b}$ state whereas, the vibrational mode ν_2 has a large coupling strength in the $\widetilde{a}$ state. The bilinear $\nu_1\nu_2$ coupling parameter in the $\widetilde{a}$ state is $\sim$10 times larger than that in the $\widetilde{b}$ state (Table 3.19 of Chapter 3). As a result distinct progression of the ν_2 vibrational mode can be observed in the spectrum of the $\widetilde{a}$ state (panel a). The peaks are $\sim 741\ cm^{-1}$ spaced, corresponding to the frequency of the ν_2 vibrational mode in the $\widetilde{a}$ state. In contrast, the spectrum of the $\widetilde{b}$ state (panel b) shows only weak

[1]Due to some conflict in latex packages, I am unable to write the symbol of angstrom.

structures. Very weak excitation of ν_1 vibrational modes at an energy spacing (from 0-0 peak) of $\sim$ 1150 cm^{-1} can be seen from the spectrum of panel b of Fig. 4.3. The band structure of the $\widetilde{a}$ and $\widetilde{b}$ electronic states, is found to be very broad and overlapping in the experimental recording [2]. As already discussed that the $\widetilde{a}$ and $\widetilde{b}$ states are coupled through the ν_6 (Table 3.18 of Chapter 3) and $\nu_3\nu_4$ (Table 3.19 of Chapter 3) vibrational modes, and the energetic minimum of $\widetilde{a}$-$\widetilde{b}$ CIs is quasi-degenerate with the minimum of the $\widetilde{b}$ state. Strong nonadiabatic mixing of the $\widetilde{a}$ and $\widetilde{b}$ electronic states therefore causes a blurring of the distinct weak vibrational structure of the uncoupled $\widetilde{b}$ state. The coupling strength of the $\widetilde{b}$ with the $\widetilde{c}$ state is also very large (Table 3.18 of Chapter 3), however, these two states are vertically $\sim$ 1.0 eV apart (cf. Table 3.3 of Chapter 3). Also the minimum of the $\widetilde{b}$-$\widetilde{c}$ CIs occurs at much high energy, $\sim$ 7.24 eV above the minimum of the $\widetilde{b}$ state and does not have any impact on the spectrum. The $\widetilde{a}$-$\widetilde{b}$ coupled states spectrum is plotted in panel c of Fig. 4.3. Some increase of the spectral line density can be immediately seen from the spectrum of panel c. The excitation of non totally symmetric mode ν_6 with an energy spacing of $\sim$ 1004 cm^{-1} is estimated from the irregular spectral progression.

It is shown in Fig. 4.1 and discussed therein that the third detachment band of B_4^- is formed by three energetically close-lying ($\widetilde{A}^1B_{2u}$, $\widetilde{c}^3B_{2g}$ and $\widetilde{B}^1B_{2g}$) electronic states of B_4. These states are found to be decoupled from each other (except the possible dynamic spin-orbit coupling which is not explored in this chapter) or coupling of any of these states (if exists) with a lower one occurs at very high energies (for example, the $\widetilde{b}$-$\widetilde{c}$ coupling, see Chapter 3 for details) and does not play any role in the energy range of the detachment bands studied here. The composite third detachment band of B_4 obtained by combining the stick spectrum of the $\widetilde{A}$, $\widetilde{c}$ and $\widetilde{B}$ electronic states is shown in the panel a of Fig. 4.4. The 193 nm and 266 nm experimental bands of Ref [2] are shown in panel b of Fig. 4.4. It can be seen in comparison that in the 193 nm spectrum the detachment cross section of the $\widetilde{A}$ state is very small. Whereas, distinct vibrational structure of the $\widetilde{A}$ band is obtained in the theoretical results. The 266 nm experimental spectrum, however reveals some structure in this region. At high energies the broad band experimental envelope agrees fairly well with the overall composite spectrum of the $\widetilde{c}$ and $\widetilde{B}$ electronic states of B_4. The vibrational mode ν_2 in the $\widetilde{A}$ and ν_1 in the $\widetilde{c}$ and $\widetilde{B}$ electronic states from dominant progressions. Peak spacings of $\sim$ 767, $\sim$ 1234 and $\sim$ 1237 cm^{-1} are found corresponding to the frequency of these modes in the mentioned electronic states, respectively.

Internal conversion dynamics

Dynamics of the electronic excited states of B_4 cluster is examined in terms of time-dependence of adiabatic electronic populations recorded in the WP calculations. The time dependence of the adiabatic populations when the WP prepared on $\widetilde{X}$, $\widetilde{a}$, $\widetilde{b}$, $\widetilde{A}$, $\widetilde{c}$ and $\widetilde{B}$ electronic states is shown in panel a-f of Fig. 4.5. Except for the $\widetilde{a}^3B_{2u}$ and $\widetilde{b}^3B_{1u}$ electronic states the nonadiabatic coupling effects are found not very insignificant in B_4. The coupling between the $\widetilde{A}^1B_{2u}$ and $\widetilde{X}^1A_g$ states through the intermode bilinear ($\nu_3\nu_6$)

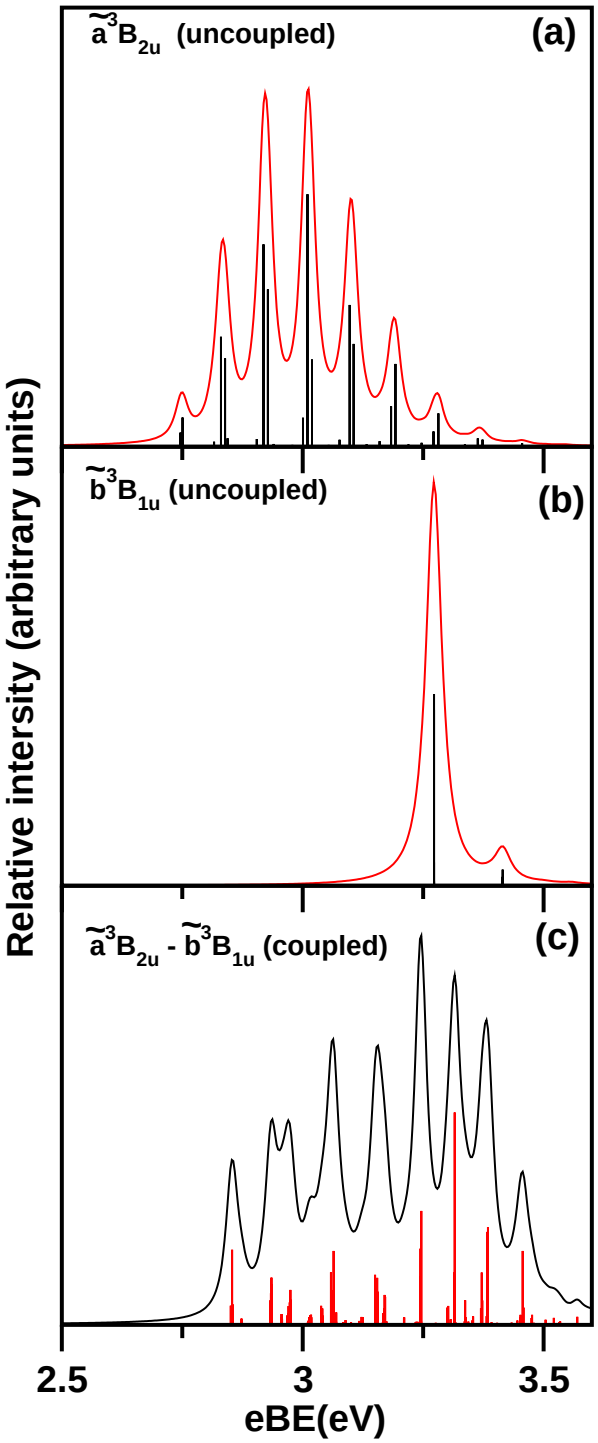

Figure 4.3: Stick vibronic spectrum and the corresponding convoluted envelope. The spectra of uncoupled $\widetilde{a}$ and $\widetilde{b}$ states are shown in panels a and b, respectively. The entire $\widetilde{a}$-$\widetilde{b}$ spectrum obtained by including nonadiabatic coupling between them is shown in panel c.

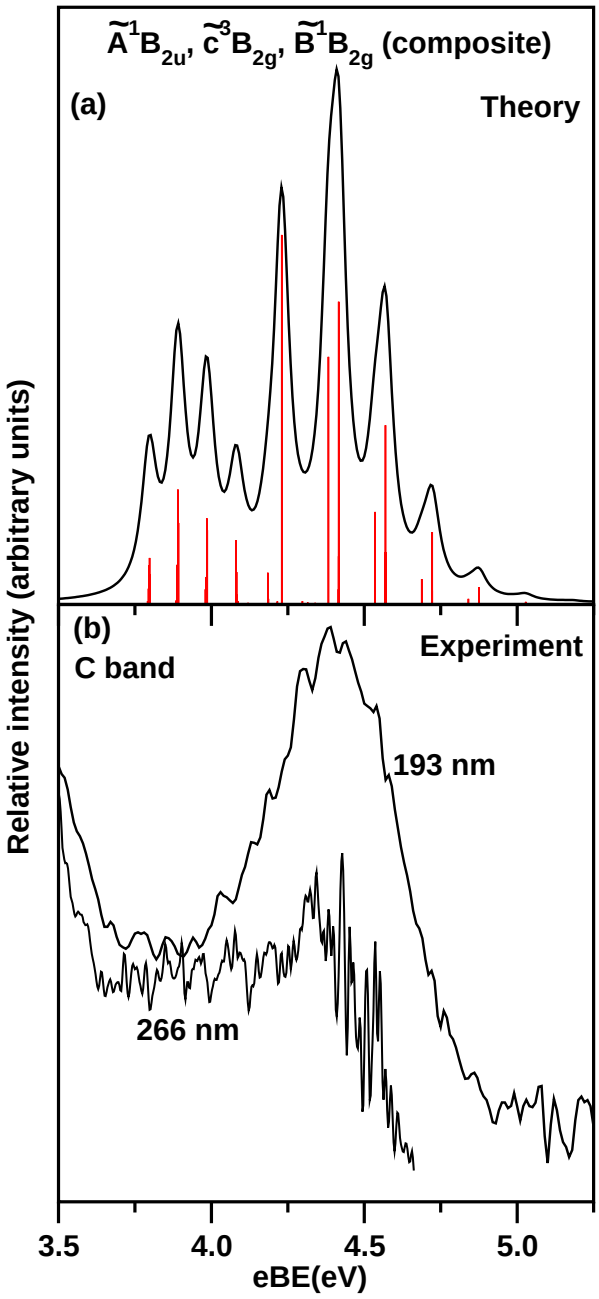

Figure 4.4: Composite stick vibronic spectrum and the convoluted envelope (panel a) of the $\widetilde{A}$, $\widetilde{c}$ and $\widetilde{B}$ electronic states of B_4. The 193 and 266 nm experimental recordings of Ref. [2] are shown in panel b for comparison.

coupling term (cf., Table 3.19 of Chapter 3) has been found to have very mild effects on the vibronic energy level structure of these electronic states only. Less than 1 % of the electronic population flows to the $\widetilde{X}$ state when the WP is initially prepared on the $\widetilde{A}$ state in this case.

In contrast to the above scenario, the nonadiabatic coupling appears to have significant effect on the dynamics of the $\widetilde{a}^3B_{2u}$ and $\widetilde{b}^3B_{1u}$ electronic states. To assess these coupling effects on the nonradiative internal conversion dynamics we show the time-dependence of the adiabatic and diabatic electronic populations in Fig. 4.6. The adiabatic (thick solid line) and diabatic (thin dashed line) electronic populations for an initial location of the WP on the $\widetilde{a}$ and $\widetilde{b}$ diabatic states are shown in panel a and b of Fig. 4.6, respectively. It can be seen from panel a of Fig. 4.6(a) that the diabatic population of the $\widetilde{a}$ state starts from 1.0 and that of the $\widetilde{b}$ state from 0.0 at t=0. The population of the $\widetilde{a}$ state flows to the $\widetilde{b}$ state in time and fluctuates around 0.8 at longer times. The recurrences in the diabatic population curves indicate WP moves back and forth between the two states in a time scale of $\sim$ 49 fs which nearly corresponds to the period of the ν_2 vibrational mode. It can be seen from the Table 3.18 of Chapter 3 that the latter mode is strongly active in the $\widetilde{a}$ state of B_4. Since a diabatic state is an admixture of the two (lower and upper) adiabatic states, the initial location of the WP on the diabatic state corresponds to 70 % and 30 % population of the two adiabatic states. The upper and lower adiabatic population curves in panel b correlates to the $\widetilde{a}$ and $\widetilde{b}$ states of B_4, respectively. The oscillations in the adiabatic population curves are much smaller in magnitude compared to those in the diabatic population curves, and relatively less significant population flows to the adiabatic states in this situation.

The adiabatic and diabatic electronic populations for an initial location of the WP on the $\widetilde{b}^3B_{1u}$ electronic state (diabatic) are plotted in panel b of Fig. 4.6. The lower thin dashed and thick solid curves represent diabatic and adiabatic population, respectively, of the $\widetilde{b}$ state whereas the same for the $\widetilde{a}$ state are represented by the same two curves in the upper part of panel b. In contrast to the population curves of panel a, a large fraction of population flows to both the electronic states in this case. This is because the equilibrium minimum of the $\widetilde{b}$ state is near degenerate to the minimum of the $\widetilde{a}$-$\widetilde{b}$ CIs (cf., Chapter 3). The diabatic population of the $\widetilde{b}$ state starts from 1.0 at t=0. The corresponding adiabatic population is $\sim$ 0.7 at t=0. A sharp decay of population occurs within $\sim$ 10 fs followed by the quasi-periodic recurrences. The diabatic population of the $\widetilde{a}$ state on the other hand starts from zero at t=0 and exhibits quasi-periodic recurrences at longer times. The corresponding adiabatic population also exhibits oscillatory pattern starting at $\sim$ 0.3 at t=0. The initial sharp decrease of population relates to a decay rate of the $\widetilde{b}$ state of $\sim$ 14 fs ($\sim$ 7 fs) in the diabatic (adiabatic) picture.

We note that the coupling parameters of the Hamiltonian derived from the ROMP2 optimized reference geometry (cf., Tables 3.21 to 3.24 of Chapter 3) are almost identical to those obtained from the UB3LYP optimized reference geometry (cf., Tables 3.17 to 3.20 of Chapter 3). The stationary points of the $\widetilde{a}$-$\widetilde{b}$ are also nearly identical in the two sets of results (cf., Chapter 3). The electronic population dynamics discussed above also remains same when calculated with the parameters of (cf., Tables 3.17 to 3.20).

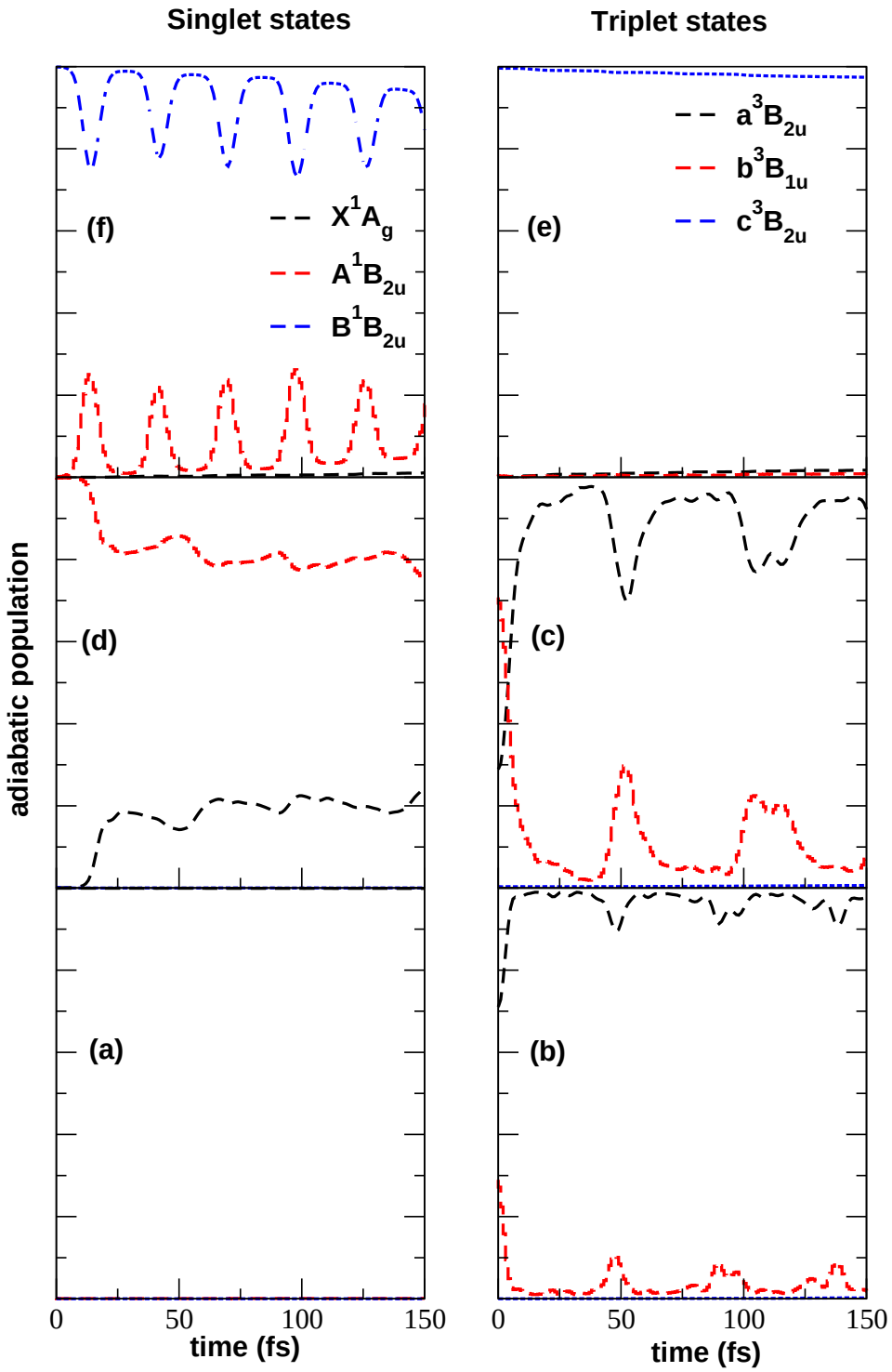

Figure 4.5: Time-dependence of the adiabatic electronic populations in the coupled surface dynamics of B_4. The electronic populations for an initial preparation of the WP on the $\widetilde{X}$, $\widetilde{a}$, $\widetilde{b}$, $\widetilde{A}$, $\widetilde{c}$ and $\widetilde{B}$ electronic states are shown in panel a-e, respectively (see text for details).

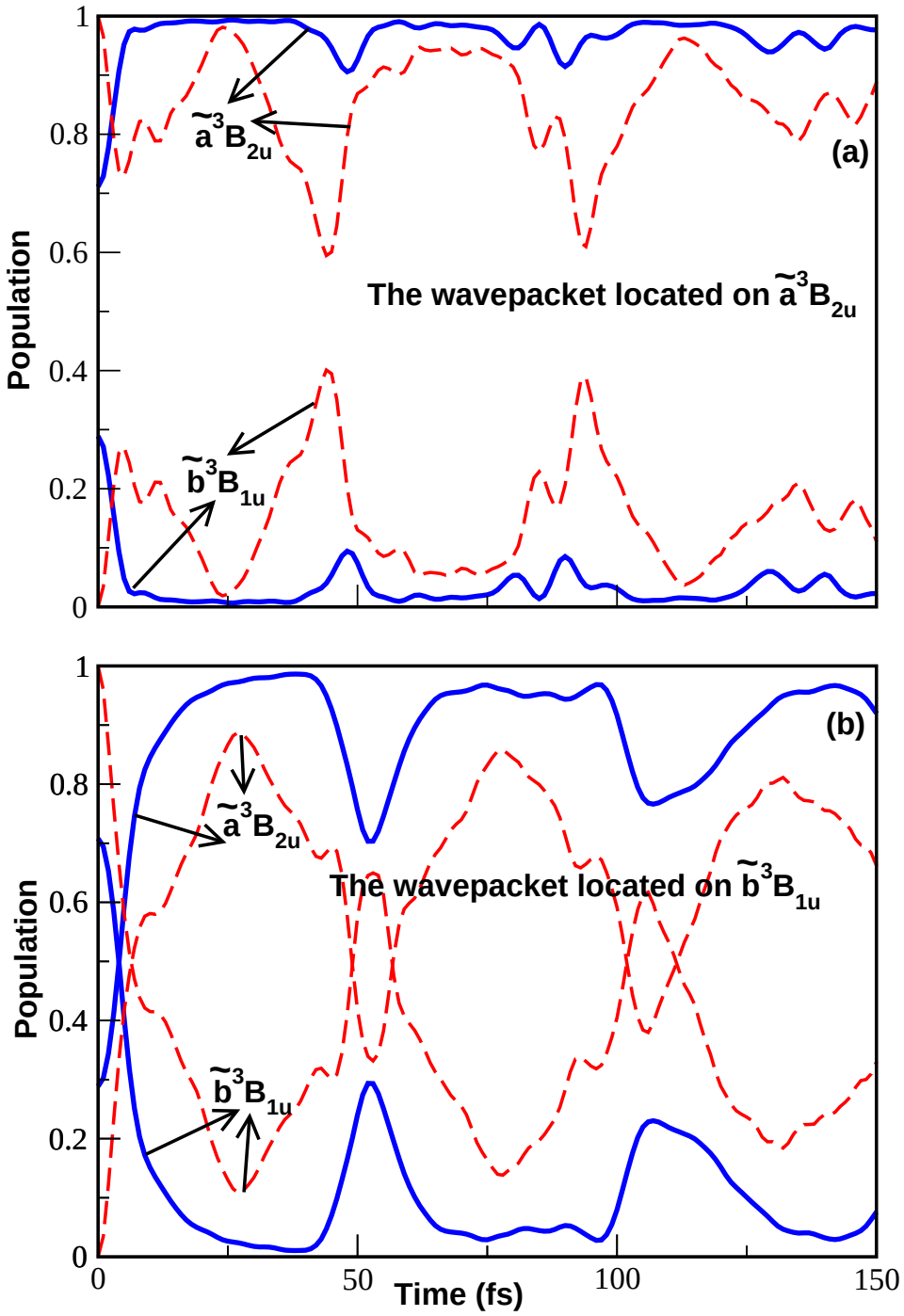

Figure 4.6: Time-dependence of the diabatic (dashed lines) and adiabatic (solid lines) electronic populations in the coupled surface dynamics of B_4. The electronic populations for an initial preparation of the WP on the $\widetilde{a}$ and $\widetilde{b}$ electronic states are shown in panel a and b, respectively (see text for details).

Table 4.4: The normal mode combinations, sizes of the primitive and single particle bases used in the WP propagation (using the MCTDH program modules [14–17]) on the $\widetilde{X}$-$\widetilde{A}$-$\widetilde{B}$-$\widetilde{C}$-$\widetilde{D}$-$\widetilde{E}$ electronic states of B_5 using Hamiltonian of Eq. (3.9) of 3.

S.No	Normal modes	Primitive basis	SPF basis
1	ν_1,ν_3,ν_7	(6,10,8)	[8,8,10,10,4,10]
2	ν_2,ν_6,ν_8	(10,6,6)	[10,8,10,8,4,8]
3	ν_4,ν_5,ν_9	(8,4,8)	[4,10,8,8,10,10]

4.2.2 Photodetachment bands of B_5^-

Broad band spectral envelope

The broad band spectral envelope of B_5 obtained by WP propagations using the MCTDH method [14–17] is shown in the panel a of Fig. 4.7. The 193 nm experimental recording of Ref. [2] is shown in the panel b of Fig. 4.7. Six separate WP calculations are carried out with six different choices of initial state, the time autocorrelation functions derived from these calculations are then combined, damped with an exponential function ($e^{-\frac{t}{\tau}}$, with τ_r=11 fs) and Fourier transformed to generate the spectral envelopes shown in panel a. The full Hamiltonian and its parameters given in Eq. 3.9 and Tables 3.25 to 3.27 respectively of Chapter 3, are used in the WP calculations. The technical details of the WP calculations using MCTDH program modules [14–17] are given in Table 4.4. It can be seen from Fig. 4.7 that the broad band theoretical spectrum agrees fairly well with the experimental band structures.

While the 193 nm experimental spectrum [3] reveals broad structures of all detachment bands (with a partial resolution of the C band), resolved vibronic structures of the $\widetilde{X}$ and $\widetilde{A}$ states are reported in the 355 nm and 266 nm recordings, respectively. The individual band structures at higher energy resolutions are discussed later in the text. The first band is found to originate from photodetachment of B_5^- to the $\widetilde{X}^2B_2$ electronic state of B_5. An adiabatic detachment energy of $\sim$ 2.33 eV is reported for this band [3]. The second and third bands are found to represent the vibronic structures of the $\widetilde{A}^2A_1$ and $\widetilde{B}^2B_2$ electronic states of B_5. The third band marked C in the energy range between 4.7-6.2 eV seems to reveal features originating from both one electron detachment channels as well as multi-electron transitions [3]. No assignment of these features are available from an analysis of the experimental spectrum [3]. We have found two one-electron detachment channels leading to $\widetilde{C}^2A_1$ and $\widetilde{D}^2B_1$ electronic states of B_5 and several shake-up states (electron detachment followed by electron reorganization) exist in this energy range. A careful examination of the details of these shake-up states is out of the scope of the present chapter and is left to a future work. We however mention that along with one electron detachment states $\widetilde{C}$ and $\widetilde{D}$ we considered the shake-up state $\widetilde{E}$ in the theoretical calculations of the C band. The latter state is found to have some contribution in the observed structure of the C band between $\sim$ 5.4-6.0 eV. The structures between $\sim$ 4.7-5.4 eV are found to be formed by the $\widetilde{C}$ and $\widetilde{D}$ electronic states

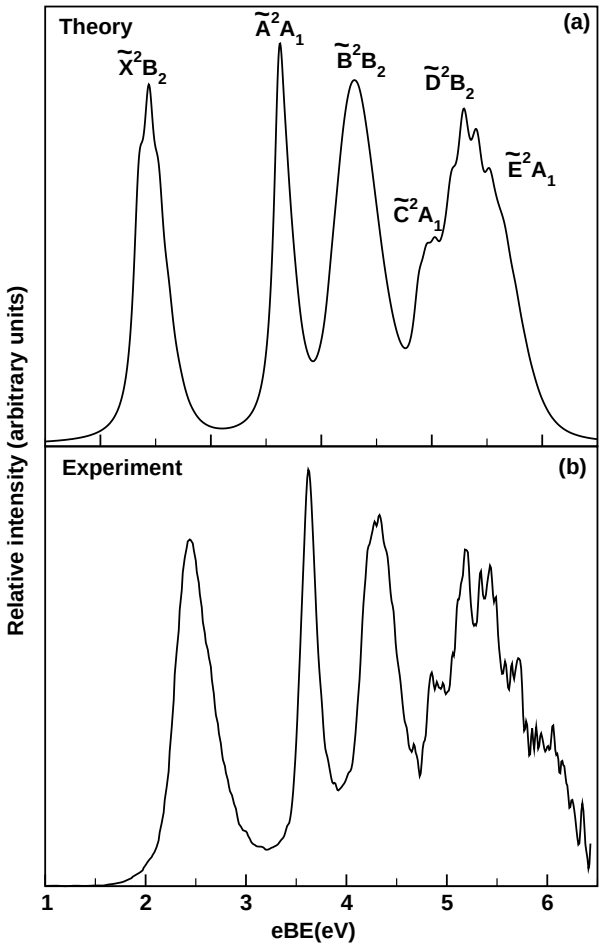

Figure 4.7: Broad band spectral envelope (panel a) of the low-lying six electronic states of B_5 cluster obtained by the WP propagations using the complete Hamiltonian of Eq. 3.9 of Chapter 3 (see text for details). The symmetry designation of the electronic states at the reference C_{2v} configuration is given in the panel. The 193 nm experimental recording of Ref. [3] is shown in panel b. The relative heights of the theoretical envelopes are adjusted to the maximum relative to the electron detachment probabilities extracted from the experimental spectrum.

of B_5.

As discussed in Chapter 3 that the existence of the $\widetilde{C}^2A_1$ state does not have any clear evidence in the literature. In our CASSCF(11,10)-MRCI calculations we found this state at $\sim$ 4.96 eV of VDE. Now, the hump in the experimental results, between $\sim$ 4.5-5.0 eV can only be obtained with the CASSCF(11, 10)-MRCI results, as shown in Fig. 4.7. We therefore strongly believe (as confirmed by more test calculations) the existence of the $\widetilde{C}^2A_1$ state in this energy region. The OVGF calculations clearly overestimate the energy of this state and lead to a conflicting energetic ordering.

Table 4.5: The number of harmonic oscillator basis function used in the calculation of the stick vibronic spectrum of the mentioned electronic states of B_5.

S.NO	State	No of HO basis along ν_1,ν_2,ν_3,ν_4,ν_6,ν_7,ν_8,ν_9
1	$\widetilde{X}^2B_2$	5,5,76,19,2,3,3,3
2	$\widetilde{A}^2A_1$	3,8,3,16,2,3,3,3
3	$\widetilde{B}^2B_2$	15,7,26,12,2,3,3,3
4	$\widetilde{C}^2A_1$	50,4,7,60,2,3,3,3
5	$\widetilde{D}^2B_1$	3,100,6,10,2,3,3,3
6	$\widetilde{E}^2A_1$	15,3,22,11,2,3,3,3
7	$\widetilde{X}^2B_2$-$\widetilde{A}^2A_1$	4,3,25,12,2,10,3,15
8	$\widetilde{X}^2B_2$-$\widetilde{C}^2A_1$	4,3,12,6,2,4,9,54
9	$\widetilde{X}^2B_2$-$\widetilde{E}^2A_1$	18,3,26,12,2,3,3,34
10	$\widetilde{A}^2A_1$-$\widetilde{B}^2B_2$	12,8,32,18,2,3,10,3
11	$\widetilde{B}^2B_2$-$\widetilde{C}^2A_1$	8,6,20,12,2,3,3,40
12	$\widetilde{B}^2B_2$-$\widetilde{E}^2A_1$	6,4,16,9,2,2,2,36
13	$\widetilde{D}^2B_1$-$\widetilde{E}^2A_1$	10,20,30,15,40,2,2,2

Interpretation of the structure of the detachment bands

The vibrational fine structures underlying the broad detachment bands of B_5^- shown in Fig. 4.7 are examined here. The time-independent matrix diagonalization approach is employed to calculate the stick line spectrum underlying the broad spectral envelopes. In Table 4.5, the technical details of the calculation of each spectrum shown below are given. Each spectrum is converged with respect to the parameters given in this table. The stick spectra presented below are convoluted with a Lorentzian function of 15 meV FWHM to generate the respective spectral envelopes.

The vibrational structure of the $\widetilde{X}$ state of B_5 in absence of coupling with its neighboring states is shown in panel a and the resolved 355 nm experimental recording of Ref [3] is shown in panel b of Fig. 4.8. It can be seen in comparison that the theoretical results are in very good agreement with the experimental band structure of the $\widetilde{X}$ state. The weak feature observed at $\sim$ 2.24 eV in the experiment and attributed to a hot band understandably cannot be seen in the theoretical results. From the data given in Table 3.25 of Chapter 3, the excitation of vibrational modes ν_3 and ν_4 can be expected in this band. The excitation of the ν_3 mode is stronger than that of ν_4. Line spacings of $\sim$ 724 and $\sim$ 658 cm^{-1} corresponding to the frequency of these modes, respectively, can be extracted from the theoretical spectrum. A vibrational progression of $\sim$ 550 cm^{-1} has been estimated from the experimental band structure [3] of the $\widetilde{X}$ state.

It can be seen from the data given in Table 3.26 that $\widetilde{X}$ state is coupled (in first-order) with the $\widetilde{A}^2A_1$ state via ν_7 and ν_9 vibrational modes, with the $\widetilde{C}^2A_1$ state via the ν_7, ν_8 and ν_9 vibrational modes and with $\widetilde{E}^2A_1$ state via the ν_7 vibrational mode of b_2

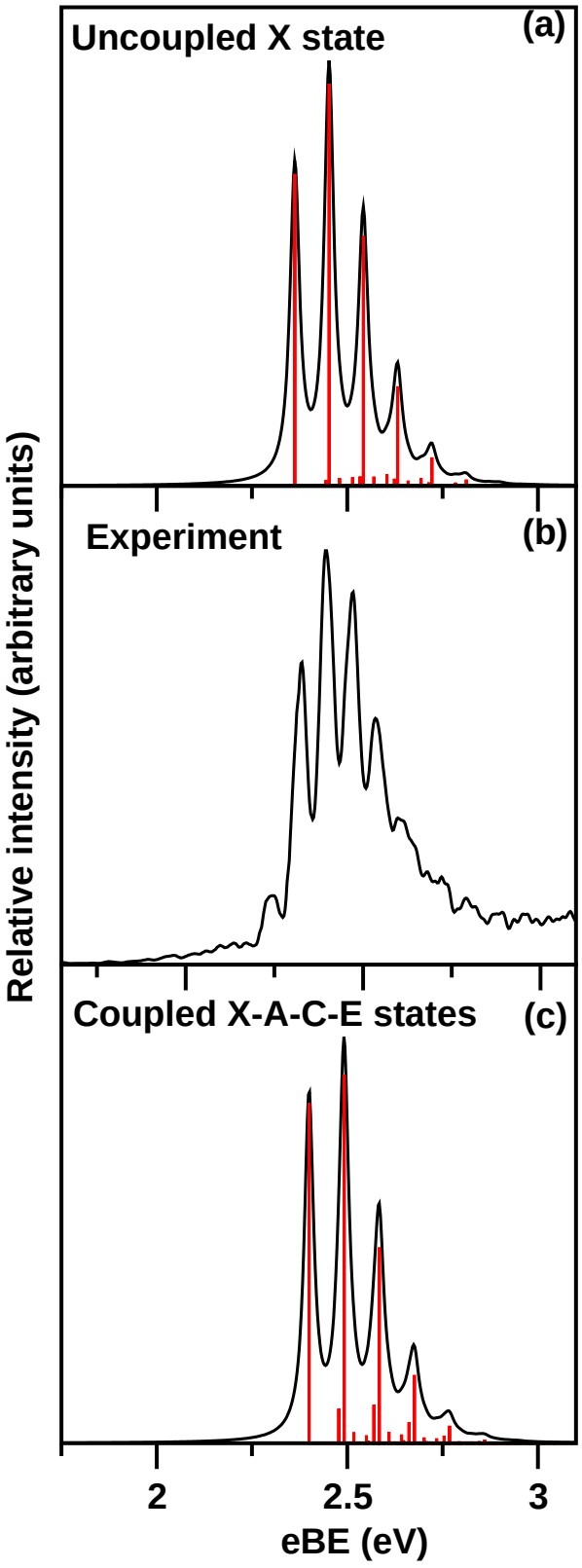

Figure 4.8: Stick vibronic spectrum and convoluted envelope of the $\widetilde{X}^2B_2$ electronic state of B_5 in the uncoupled (panel a) and $\widetilde{X}$-$\widetilde{A}$-$\widetilde{C}$-$\widetilde{E}$ coupled (panel c) states situation. The 355 nm experimental recording reproduced from Ref. [3] and shown in panel b.

symmetry. The coupling strength is strongest between the $\widetilde{X}$ and $\widetilde{C}$ states through the ν_9 vibrational mode. Now considering the data presented in Table 3.34 of Chapter 3 and discussions therein, it is expected that only the $\widetilde{X}$-$\widetilde{A}$ coupling will have some impact on the vibrational structure of the $\widetilde{X}$ band, the intersections of the $\widetilde{X}$ state with the others occur at much higher energies. The coupling effect of each of the above states on the $\widetilde{X}$ band is examined in detail. To save space we do not show the calculated band structures obtained by including each of these couplings. The coupling of the $\widetilde{X}$ state with the rest of the states does not have any major impact on its vibronic structure. The final structure of the $\widetilde{X}$ band including all couplings mentioned above is shown in the panel c of Fig. 4.8. It can be seen that the resolved experimental band structure (panel b) is indeed in good agreement with the theoretical results of panel c and nonadiabatic coupling causes some increase of the vibronic line density. Weak excitations of the nontotally symmetric coupling vibrational modes ν_7, ν_8 and ν_9 are extracted from the stick vibronic spectrum of panel c.

The vibrational structure of the uncoupled $\widetilde{A}$ state of B_5 is presented in panel a along with the better resolved 266 nm experimental recording [3] in panel b of Fig. 4.9. It can be seen that the overall structure of the theoretical band is already in good agreement with the experimental results. All symmetric vibrational modes are very weakly active (cf., Table 3.25 of Chapter 3) in this electronic state. The excitation strength of the ν_4 vibrational mode is highest among them. We indeed find the progression of ν_4 vibrational mode with an energy spacings of ~ 530 cm^{-1} in theoretical stick spectrum of Fig 4.9(a). An energy spacing of ~ 530 cm^{-1} similar to that in the $\widetilde{X}$ band was reported in the experiment [3]. We note that we differ with the experiment [3] in terms of major progressions in the $\widetilde{X}$ and $\widetilde{A}$ bands of B_5. The theory predicts major progression of ν_3 in the $\widetilde{X}$ and ν_4 in the $\widetilde{A}$ state of B_5.

The equilibrium minimum of the $\widetilde{A}$ state occurs ~ 0.6 and ~ 0.7 eV below the minimum of the $\widetilde{X}$-$\widetilde{A}$ and $\widetilde{A}$-$\widetilde{B}$ CIs (see Chapter 3 for details). These two pairs of states are coupled by the vibrational modes ν_7, ν_9 and ν_7 (cf., Table 3.26 of Chapter 3), respectively. The vibronic structure of the $\widetilde{A}$ state obtained by including the coupling with the $\widetilde{X}$ and $\widetilde{B}$ states is shown in panel c of Fig. 4.9. It can be seen from the latter that the nonadiabatic coupling causes an increase of the spectral line density although the intensity of the lines is very small. As a result the spectral envelope becomes broad and diffuse and agrees more closely to the experiment. Weak excitation of ν_9 vibrational mode is found in this case.

Although a partially structured $\widetilde{B}$ band with extremely low intensity was obtained in the 266 nm recording it appeared to be very broad and diffuse in the 193 nm recording [3]. No vibrational progressions could be resolved from these experimental band structures. The data of Table 3.26 of Chapter 3 reveal that the $\widetilde{B}$ state is coupled (in first-order) with $\widetilde{A}$, $\widetilde{C}$ and $\widetilde{E}$ electronic states via the vibrational modes ν_8; ν_8, ν_9 and ν_7, ν_9, respectively, of b_2 symmetry. The equilibrium minimum of the $\widetilde{B}$ state occurs ~ 0.06, ~ 1.58 and ~ 4.90 eV below the minimum of the $\widetilde{A}$-$\widetilde{B}$, $\widetilde{B}$-$\widetilde{C}$ and $\widetilde{B}$-$\widetilde{E}$ CIs. It therefore appears to be interesting to critically investigate the impact of these couplings on the observed diffuse structure of the $\widetilde{B}$ band of B_5.

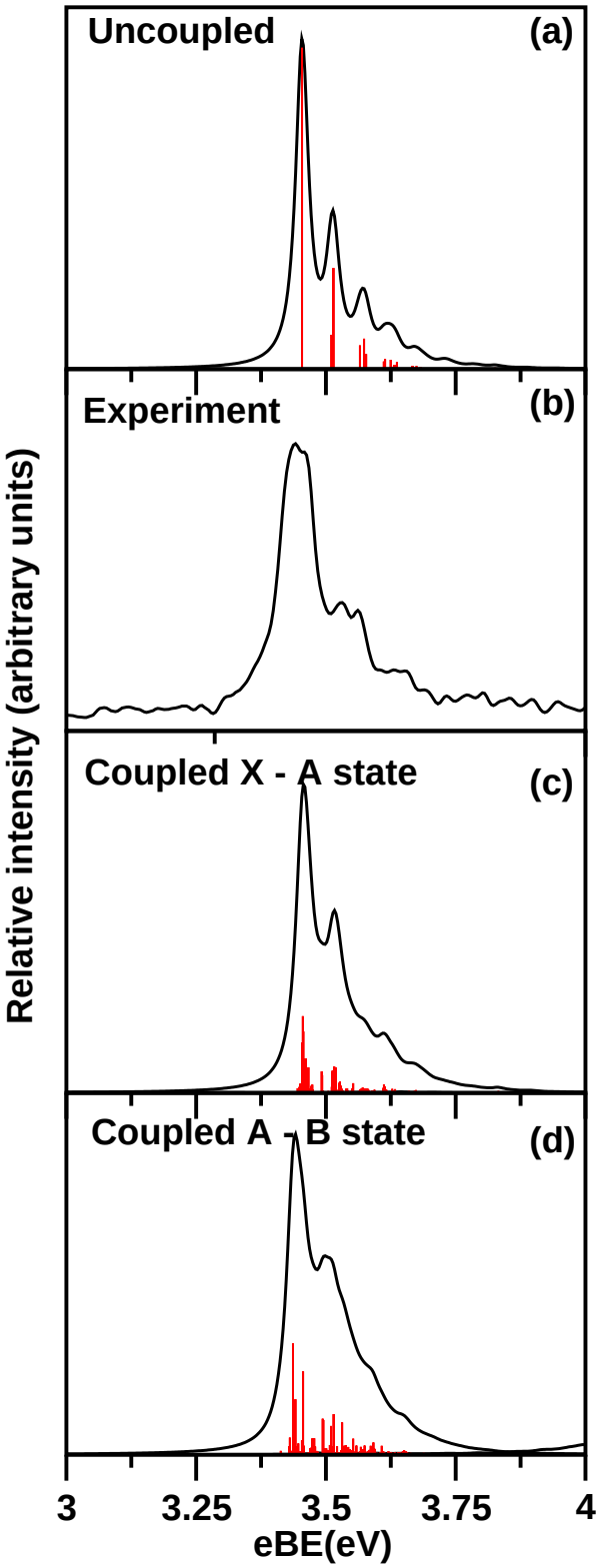

Figure 4.9: Same as in Fig. 4.8 for the $\widetilde{A}^2A_1$ electronic state of B_5 in the uncoupled (panel a) and coupled (panel c) states situations. The 266 nm experimental recording of Ref. [3] is reproduced in panel b.

The vibrational structure of the uncoupled $\widetilde{B}$ state is presented in panel a of Fig. 4.10. All four totally symmetric vibrational modes are excited in this band. The excitation of the mode ν_3 is strongest. Peak spacings of 1242, 901, 723 and 337 cm^{-1} corresponding to the modified frequency of ν_1, ν_2, ν_3 and ν_4 vibrational modes, respectively, in the $\widetilde{B}$ state are extracted from the stick line spectrum of Fig. 4.10(a). The $\widetilde{B}$ band is examined by including the $\widetilde{A}$-$\widetilde{B}$, $\widetilde{B}$-$\widetilde{C}$ and $\widetilde{B}$-$\widetilde{E}$ couplings. The effect of $\widetilde{A}$-$\widetilde{B}$ coupling on the structure of the $\widetilde{B}$ band is found to be the strongest. It causes a huge increase in the vibronic line density. As mentioned above that the $\widetilde{B}$ state minimum occurs only ~ 0.06 eV below the minimum of the $\widetilde{A}$-$\widetilde{B}$ CIs and therefore the entire $\widetilde{B}$ band is perturbed by the associated nonadiabatic coupling. In contrast, the effect of coupling with the $\widetilde{C}$ and $\widetilde{E}$ states on the structure of the $\widetilde{B}$ band is far less. The $\widetilde{B}$ band obtained by including the above couplings is shown in panel c of Fig. 4.10. It can be seen that observed diffuse structure of this band [3] is much better reproduced by the spectrum of panel c.

The vibrational energy level spectrum of the uncoupled $\widetilde{C}$, $\widetilde{D}$ and $\widetilde{E}$ electronic states are shown in panel a, b and c, respectively, of Fig. 4.11. The vibrational modes ν_1 and ν_4 form detectable progression in the $\widetilde{C}$ state. Line spacings of ~ 1191 and ~ 474 cm^{-1}, respectively, are extracted from the spectrum of the $\widetilde{C}$ state. The vibrational mode ν_2 form extended progression in the $\widetilde{D}$ state. Line spacing of ~ 964 cm^{-1} has been found from its spectrum shown in panel b. The vibrational modes ν_1, ν_3 and ν_4 from detectable progression in the spectrum of the $\widetilde{E}$ state shown in Fig. 4.11(c). Peak spacings of 1239, 723 and 471 cm^{-1} corresponding to the excitation of these modes, respectively, are extracted from this spectrum.

It is discussed in Chapter 3 that the $\widetilde{C}$ state is coupled with the $\widetilde{X}$ and $\widetilde{B}$ states, the $\widetilde{D}$ state is coupled with the $\widetilde{E}$ state and the $\widetilde{E}$ state is coupled with the $\widetilde{X}$, $\widetilde{B}$ and $\widetilde{D}$ states. The $\widetilde{D}$-$\widetilde{E}$, $\widetilde{B}$-$\widetilde{E}$ and $\widetilde{X}$-$\widetilde{E}$ couplings are quite strong. The equilibrium minimum of the $\widetilde{E}$ state is quasi-degenerate with the energetic minimum of the seam of $\widetilde{D}$-$\widetilde{E}$ CIs. The $\widetilde{X}$-$\widetilde{E}$ and $\widetilde{B}$-$\widetilde{E}$ CIs occur at much higher energies and are not relevant in the energy range of the $\widetilde{E}$ band. A similar consideration on energetic ground reveals that the $\widetilde{B}$-$\widetilde{C}$, $\widetilde{C}$-$\widetilde{D}$, $\widetilde{B}$-$\widetilde{D}$ CIs will play important role in the vibronic structure of the $\widetilde{C}$ and $\widetilde{D}$ bands. The band structures of the $\widetilde{C}$, $\widetilde{D}$ and $\widetilde{E}$ electronic states obtained by including the couplings mentioned above are shown in the panel a, b and c of Fig. 4.12, respectively. While the impact of these couplings is not very significant on the $\widetilde{C}$ and $\widetilde{D}$ bands, the structure of the $\widetilde{E}$ band is considerably modified by them.

Internal conversion dynamics

Similar to the case of neutral electronic states of B_4^-, the time-dependence of electronic population of the neutral electronic states of B_5 is recorded, when the WP prepared on $\widetilde{X}$, $\widetilde{A}$, $\widetilde{B}$, $\widetilde{C}$, $\widetilde{D}$ and $\widetilde{E}$ electronic states and is plotted in panels a-f of Fig. 4.13. From the figure, it can be seen that no major flow of electronic population takes place to the other states when the WP is initially prepared on the $\widetilde{X}$, $\widetilde{A}$, $\widetilde{C}$ and $\widetilde{D}$ electronic states. In contrast, the electron population dynamics is quite involved for an initial location of the WP either on the $\widetilde{B}$ and $\widetilde{E}$ electronic states. The latter two cases are shown in panel a and b of Fig. 4.14, respectively. The decay and growth of adiabatic (thick solid line) and

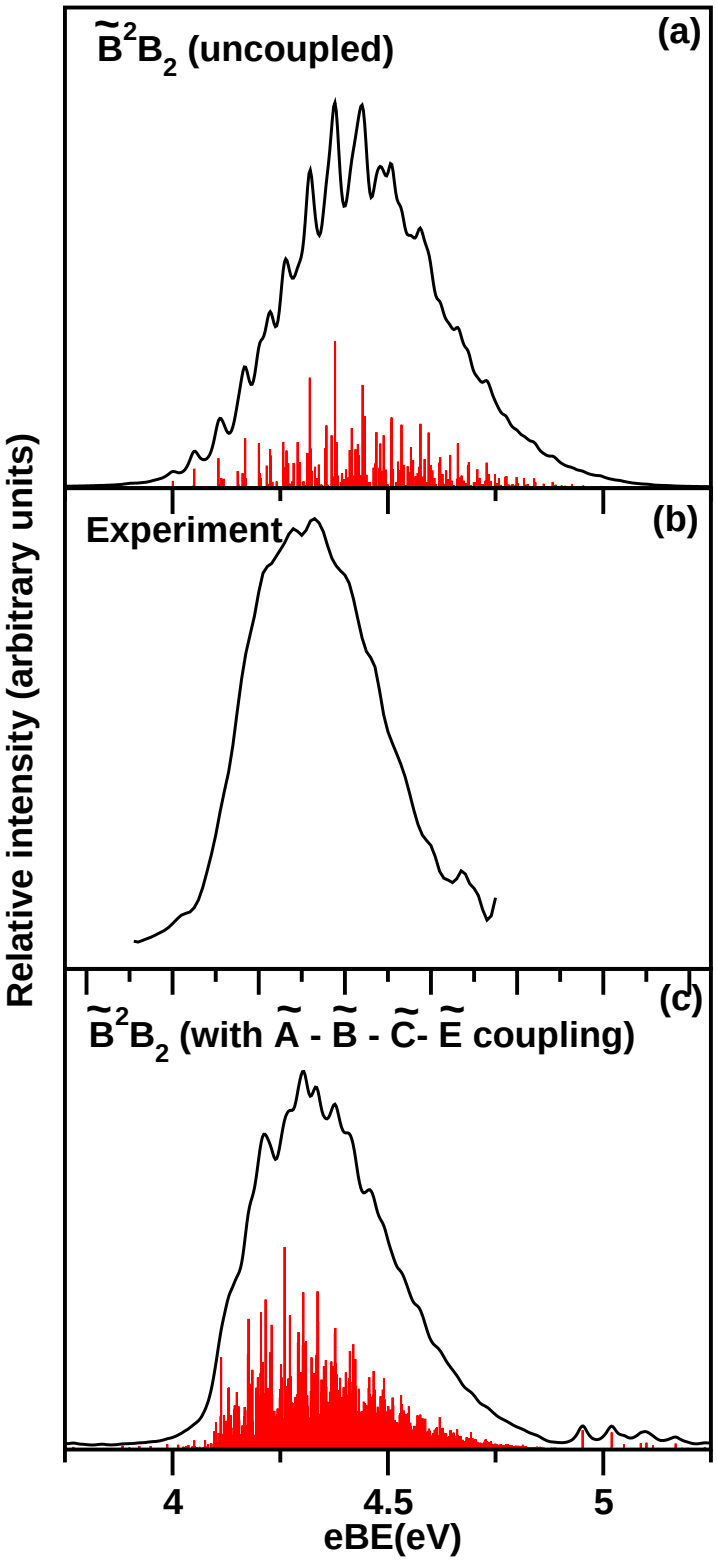

Figure 4.10: Same as in Fig. 4.8 for the $\widetilde{B}^2B_2$ state of B_5. The $\widetilde{B}$ band obtained in the uncoupled and coupled ($\widetilde{A}$-$\widetilde{B}$-$\widetilde{C}$-$\widetilde{E}$) states situations is shown in panel a and c, respectively. The 193 nm experimental recording is reproduced from Ref. [3] and shown in panel b.

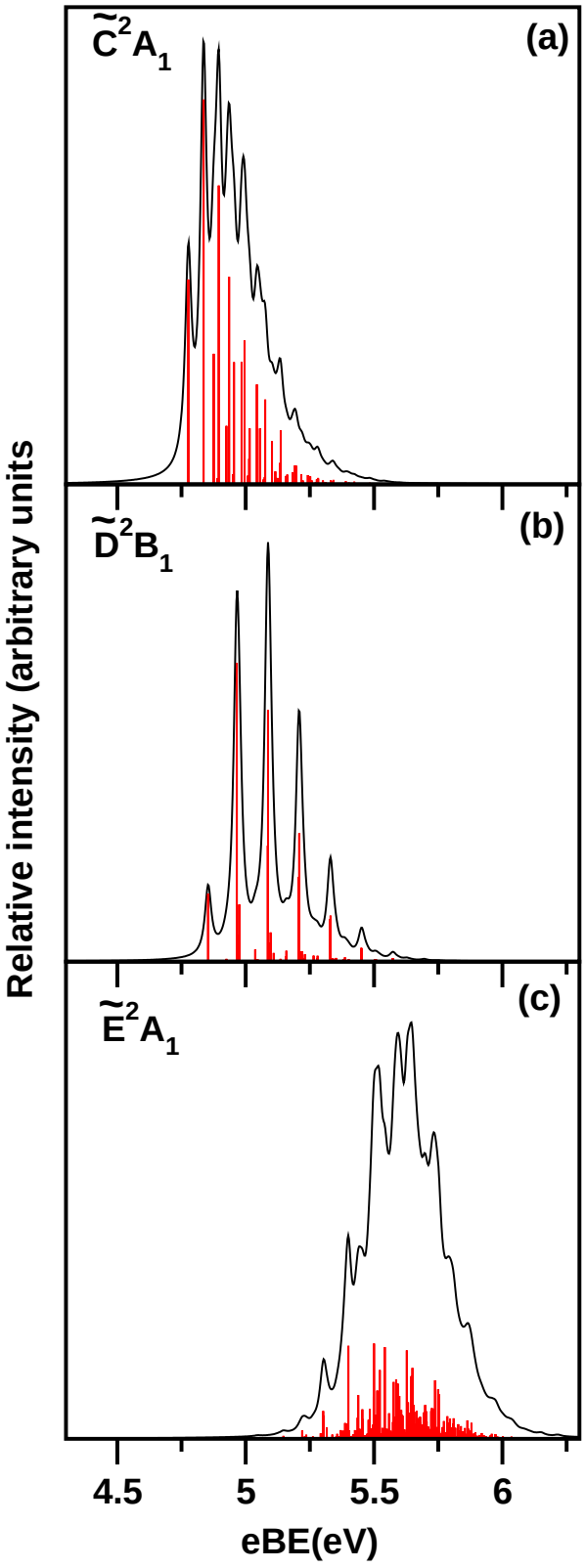

Figure 4.11: Same as in Fig. 4.8 for the uncoupled $\widetilde{C}^2A_1$, $\widetilde{D}^2B_1$ and $\widetilde{E}^2A_1$ electronic states of B_5.

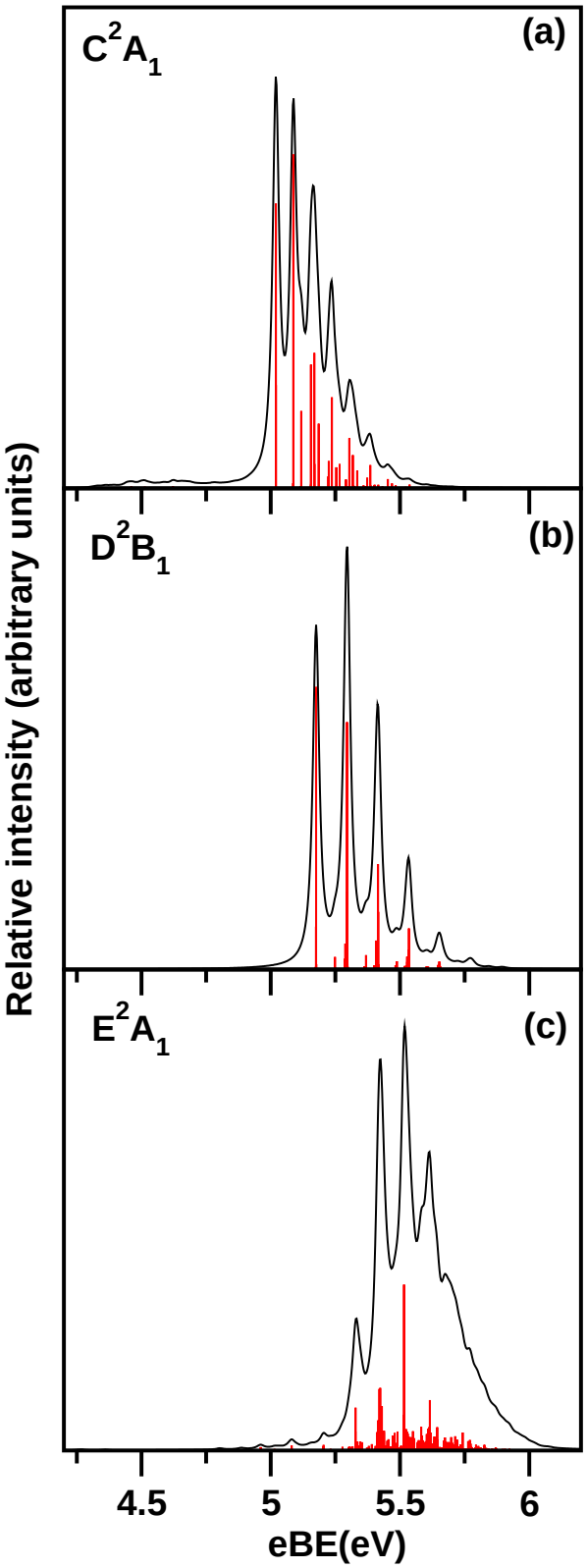

Figure 4.12: The same $\widetilde{C}^2A_1$, $\widetilde{D}^2B_1$ and $\widetilde{E}^2A_1$ states in fully coupled situation is shown in panel a, b and c respectively. These simulations were done by MCTDH diagonalization procedure.

diabatic (thin dashed line) electronic populations for an initial location of the WP on the $\widetilde{B}$ state are plotted in panel a of Fig. 4.14. The $\widetilde{B}$ states population starts from 1.0 (diabatic) and 0.96 (adiabatic) at t=0 and rapidly decays to the $\widetilde{A}$ state and relatively slowly to the $\widetilde{X}$ state in time. This is indicated by the growth of populations of the latter two states. The decay of the $\widetilde{B}$ state population is much faster in the adiabatic picture and relates to a decay rate of $\sim$ 12 fs (adiabatic) and $\sim$ 38 fs (diabatic). The coupling between the $\widetilde{A}$-$\widetilde{B}$ state caused by the ν_8 vibrational mode of b_2 symmetry. Although the strength of this coupling is not very large [cf., Table 3.34 of Chapter 3], the energetic minimum of the $\widetilde{B}$ state located only $\sim$ 0.06 eV below the minimum of the $\widetilde{A}$-$\widetilde{B}$ CIs. This causes a fairly strong mixing of the lower vibrational levels of the $\widetilde{B}$ states with higher vibrational levels of $\widetilde{A}$ state and a huge increase of the vibronic line density of the $\widetilde{B}$ state starting from its adiabatic detachment position [cf., Fig. 4.10(c)]. The adiabatic population of the $\widetilde{B}$ state exhibits damped oscillations and saturates at $\sim$ 0.2 at longer time. The damping of the oscillations caused by the strong anharmonicity by the WP in the vicinity of the CIs during its evolution. These quasiperiodic oscillations reveal a period of 36 fs which roughly corresponds to the frequency of the ν_2 vibrational mode. The $\widetilde{B}$ state is not directly coupled to the $\widetilde{X}$ state of B_5. However the small population flow to the $\widetilde{X}$ state seen in panel a of Fig. 4.14 is mediated via the $\widetilde{X}$-$\widetilde{A}$ CIs. It can be seen that within about 10 fs the population start flowing to the $\widetilde{X}$ state indicating an extremely fast internal conversion dynamics. The population of the $\widetilde{X}$ state saturates roughly to the same value as of the $\widetilde{B}$ state at longer time.

Except the $\widetilde{X}$ state the electron population flows to all excited states when the WP is initially prepared on the $\widetilde{E}$ state as can be seen from panel b of Fig. 4.14. The adiabatic population of the $\widetilde{E}$ state decays much faster (in about $\sim$ 12 fs) compared to its diabatic population ($\sim$ 167 fs). The $\widetilde{E}$ state quickly relaxes to the $\widetilde{D}$ state as its equilibrium minimum is quasi-degenerate with the minimum of the $\widetilde{D}$-$\widetilde{E}$ CIs. The damped recurrences in the adiabatic populations of the $\widetilde{D}$ and $\widetilde{E}$ electronic states occur in a period of $\sim$ 26 fs which correlates to the vibrational period of the ν_1 mode. The $\widetilde{X}$-$\widetilde{E}$ CIs occur at higher energies ($\sim$ 2.01 eV above the $\widetilde{E}$ state minimum) and therefore no direct population transfer to the $\widetilde{X}$ state can be seen. The population can however, directly flow to the $\widetilde{B}$ state through the $\widetilde{B}$-$\widetilde{E}$ CIs. The small population flow to the $\widetilde{A}$ and $\widetilde{C}$ states occurs indirectly through the $\widetilde{A}$-$\widetilde{B}$ and $\widetilde{B}$-$\widetilde{C}$ CIs, respectively.

4.2.3 Photodetachment bands of B_7^-

In this section we present and discuss the photodetachment bands of B_7^- originating from its three isomers discussed above. Theoretical results are compared with the experimental band structures and assigned. Wang and co-workers [4] assigned origin of the observed peaks X and D to isomer I, X, E, F, H and I to isomer II and A, B and G to isomer III (*cf.* panel a of Fig. 4.20 and Table 3.15) by performing extensive quantum chemistry calculations of VDEs. In the following, the detachment bands are calculated by employing the vibronic Hamiltonians $\mathcal{H}_{\rm I}$, $\mathcal{H}_{\rm II}$ and $\mathcal{H}_{\rm III}$ developed in section 3.3.3 and both by time-independent and time-dependent quantum mechanical methods. In

the former approach the Hamiltonian matrix is represented in a direct product harmonic oscillator basis of relevant vibrational modes and then diagonalized with the aid of Lanczos algorithm [18] to calculate the precise location of the vibronic eigenvalues. The spectral intensity is calculated by the golden rule equation. In the time-dependent approach WP pertinent to reference initial state of the anion is propagated on the coupled manifold of electronic states of the neutral isomer. At each step of propagation the time autocorrelation function is calculated. The latter is Fourier transformed to calculate the broad band detachment spectrum. The decay of the excited electronic states of the neutral cluster is studied by recording the time-dependence of the electronic population. The WP propagation is carried out within the framework of MCTDH approach employing the Heidelberg MCTDH suite of programs [14–17]. The assignment of the peaks observed in the experimental spectrum (*cf.* Fig. 4.20) in terms of VDEs agrees quite well with our estimate of the same (*cf.* Table 3.15). Therefore, in the remaining of this section we have undertaken the exercise to analyze the details of each of these peaks (rather bands) and discuss the nuclear dynamics on the relevant electronic states of the corresponding neutral isomer. Several reduced dimensional calculations are performed in order to detect the progression of the vibrational modes in each band. To save space the details of this exercise is not presented here for brevity, however, the important findings are discussed and related to the broad and overlapping structure of each band recorded in the experiment. To this effort the vibronic structure of the mentioned electronic states of each of the isomer is first presented and discussed. The overall composite band structure is presented in a later section and compared with experimental results.

Vibronic structure of the electronic states of isomer I

The three degenerate electronic states of the isomer I are JT active. In the absence of intermode bilinear couplings the vibronic Hamiltonian of each of these states is separable in terms of the symmetric a_1 and JT active degenerate e_2 vibrational modes. Therefore, partial spectra considering these modes are calculated separately by the time-independent method. Analysis of these spectra facilitates the assignment of dominant vibrational progression in the final band structure calculated including all relevant couplings among electronic states and vibrational modes. To save space and for brevity we do not show all partial spectra here however, the important finding are discussed below.

The partial spectrum of the symmetric vibrational modes revealed dominant progression of ν_2 vibrational mode in the $\widetilde{X}$ state. This mode is strongly Condon active in this state (*cf.* Table 3.28). The energetic minimum of the $\widetilde{X}$ state shifts considerable away (by $Q_2 = \sim 3.68$) from the reference equilibrium geometry at Q_2=0 along this mode [*cf.* Fig. 3.18 (b)]. As a result, the center-of-gravity of this partial spectrum occurs at the position of the sixth quantum of excitation of this mode. Line spacings of $\sim$206 cm^{-1} corresponding to the frequency of ν_2 vibrational mode is extracted from the spectrum. The vibrational mode ν_1 is very weakly excited in this state. Similar partial spectra of the $\widetilde{A}$ and $\widetilde{B}$ states reveal negligible excitations of the vibrational modes ν_1 and ν_2 in these states.

The vibrational modes of e_2 symmetry are JT active in the $\widetilde{X}$, $\widetilde{A}$ and $\widetilde{B}$ electronic

Table 4.6: The number of HO basis functions used in the calculation of the stick vibronic spectrum of the mentioned electronic states of neutral isomer I of B_7.

State(s)	Lanczos iterations	No. of HO basis ν_1,ν_2,ν_{8x},ν_{8y},ν_{9x},ν_{9y},ν_{10x},ν_{10y}	Figure number
$\widetilde{X}^2E_1$	5000	8, 40, 12, 12, 6, 6, 20, 20	Fig. 4.15(a)
$\widetilde{A}^4E_1$	5000	25, 10, 20, 20, 6, 6, 12, 12	Fig. 4.15(b)
$\widetilde{B}^2E_1$	5000	30, 10, 15, 15, 6, 6, 15, 15	Fig. 4.15(c)

states. The partial spectra of these modes reveal irregular vibronic structures of all three states. As a result of the JT effect the vibronic levels of the upper and lower adiabatic component of the JT split states mix. Such mixing transforms the discrete vibronic lines to a cluster of lines involving quasi bound resonances. A careful examination reveals that the vibrational mode ν_{10} is the most active JT mode in the $\widetilde{X}$ state and line spacing of $\sim$477 cm^{-1} is extracted from the JT spectrum of this state. The JT activity of this mode is much weaker in the $\widetilde{A}$ and $\widetilde{B}$ states. The JT activity of the vibrational mode ν_9 is the weakest in all three states and that of ν_8 is weak but almost similar in magnitude in all three states discussed above.

The photodetachment bands of all three degenerate states considering all relevant couplings introduced in the Hamiltonian $\mathcal{H}_{\rm I}$ are calculated with the aid of the time-independent matrix diagonalization method. The results are presented in Fig. 4.15, for the $\widetilde{X}$, $\widetilde{A}$ and $\widetilde{B}$ states in panel a, b and c, respectively. The numerical details of the size of the harmonic basis and the number of Lanczos iterations are given in Table 4.6.

The composite band structure of the $\widetilde{X}$ state is shown in panel a reveals discrete line progressions at the lower energies and a huge increase of line density at higher energy. At lower energies below $\sim$2.8 eV the clustering of lines occurs because of mixing of the vibrational modes of a_1 and e_2 symmetry. This region of the spectrum portrays the vibronic structure of the lower adiabatic sheet of the JT split $\widetilde{X}$ state. The JT CI with the upper adiabatic sheet is accessible beyond $\sim$2.77 eV. Therefore, the discrete vibronic levels of the upper adiabatic sheet strongly mix with the quasi-continuum levels of the lower sheet and causes a huge increase of line density beyond this energy as shown in the inset of panel a. A similar explanation holds for the vibronic structure of the $\widetilde{A}$ and $\widetilde{B}$ states plotted in panels b and c, respectively. However, in contrast to the $\widetilde{X}$ state the JT coupling in the $\widetilde{A}$ and $\widetilde{B}$ state is much weaker (*cf.* Table 3.28). Therefore, vibronic line density at higher energies in these latter two bands is much less compared to that in the $\widetilde{X}$ band.

Vibronic structure of the electronic states of isomer II

Within $\sim$6 eV electron binding energy range of the photodetachment spectrum of B_7^- apparently five energetically low-lying electronic states of the neutral isomer II participate. The energies (vertical) of these states are given in Table 3.15. The coupling among these states through vibrational modes of appropriate symmetry is also documented in Table 3.33. It can be seen from the data given in this table that an estimate of the

correct vibronic structure of these electronic state requires simultaneous treatment of nuclear dynamics on the five coupled electronic states. This task could not be accomplished using the matrix diagonalization approach discussed above. This is carried out by propagating WPs using the MCTDH method [14–17] and discussed later in the text. However, as stated earlier in order to assess the progression of vibrational modes in each electronic state and the impact of nonadiabatic coupling on them due to neighboring states, calculations are carried out for uncoupled and various reduced dimensional coupled states situation using the matrix diagonalization approach. The vibronic structures of uncoupled $\widetilde{X}^2B_2$, $\widetilde{A}^2B_1$, $\widetilde{B}^2B_2$, $\widetilde{C}^2A_1$ and $\widetilde{D}^2B_1$ electronic states are presented in panels a-e of Fig. 4.16. The important findings of this exercise are discussed below. Analysis of vibronic structure of each of the above states without including the coupling with their neighbors revealed dominant excitation of the symmetric ν_5 vibrational mode in all of them except in the $\widetilde{C}$ state. Excitation of the ν_4 vibrational mode is stronger in the latter electronic state. Line spacings of $\sim$ 288, $\sim$ 156, $\sim$ 233, $\sim$ 290 and $\sim$ 171 cm^{-1} corresponding to the progression of ν_5 vibrational mode in the $\widetilde{X}$, $\widetilde{A}$, $\widetilde{B}$, $\widetilde{C}$ and $\widetilde{D}$ electronic states, respectively, are extracted from the spectrum of these states. Line spacings of $\sim$ 1116 and $\sim$ 350 cm^{-1} corresponding to the progressions of ν_1 and ν_4 vibrational modes, respectively, are also extracted from the spectrum of the $\widetilde{C}$ state.

The impact of nonadiabatic coupling with the neighboring states on the vibronic structure of a given electronic state is examined next. The numerical details of the calculations are given in Table 4.7. The results are presented in Figs. 4.17 (a-e) for the $\widetilde{X}$, $\widetilde{A}$, $\widetilde{B}$, $\widetilde{C}$ and $\widetilde{D}$ electronic states, respectively. It is found that the band structure of the $\widetilde{X}$ state is mostly perturbed by its coupling with the $\widetilde{A}$ and $\widetilde{C}$ states. Although the coupling strength of the a_2 vibrational modes ν_7 and ν_8 is weak (*cf.* Table 3.33) between the $\widetilde{X}$ and $\widetilde{A}$ states, the energetic minimum of the $\widetilde{X}$-$\widetilde{A}$ intersection is close to the equilibrium minimum of the $\widetilde{X}$ state (*cf.* Table 3.35). Therefore, $\widetilde{X}$-$\widetilde{A}$ coupling has quite some impact on the structure of the $\widetilde{X}$ band. The $\widetilde{X}$ and $\widetilde{C}$ states are strongly coupled by the b_2 vibrational mode ν_{15}. the vibrational mode ν_{14} also makes important contribution to this coupling. The vibronic structure of the $\widetilde{X}$ state by retaining its coupling with the $\widetilde{A}$ and $\widetilde{C}$ states is presented in panel a of Fig. 4.17. The calculated stick vibronic lines are convoluted with a Lorentzian function of $\sim$ 30 meV FWHM to generate the spectral envelope. We note that the same Lorentzian function is used to convolute all stick spectra presented in this chapter. Excitation of nontotally symmetric modes ν_7 and ν_8 with peak spacings of $\sim$665 and $\sim$357 cm^{-1}, respectively, is extracted from the $\widetilde{X}$ state spectrum of Fig. 4.17 (a). The vibronic structure of the $\widetilde{A}$ state is shown in Fig. 4.17 (b) is mostly perturbed by its coupling with the $\widetilde{X}$ state. The energetic minimum of $\widetilde{X}$-$\widetilde{A}$ state intersection occurs only $\sim$0.05 eV above the minimum of the $\widetilde{A}$ state. Unlike the case of $\widetilde{X}$ state, the vibronic structure of $\widetilde{A}$ state is also perturbed by its coupling with the $\widetilde{B}$ state. Excitation of nontotally symmetric modes ν_7 and ν_8 is found in the $\widetilde{A}$ state. The vibronic structure of the $\widetilde{B}$, $\widetilde{C}$ and $\widetilde{D}$ electronic states are shown in panel c, d and e of Fig. 4.17, respectively. Coupling of the $\widetilde{B}$ state with $\widetilde{A}$ and $\widetilde{C}$ states contributes to the vibronic structure of the $\widetilde{B}$ state. Similarly, coupling of the $\widetilde{C}$ state with $\widetilde{B}$ state and $\widetilde{D}$ state with $\widetilde{C}$ state contributes to their

Table 4.7: The number of harmonic oscillator basis function used in the calculation of the stick vibronic spectrum of the mentioned electronic states of neutral isomer II of B_7.

State(s)	Laczos iterations	No. of HO basis along symmetric modes ν_1-ν_5	coupling modes	Figure number
$\widetilde{X}^2B_2$	5000	6, 6, 18, 10, 35		4.16(a)
$\widetilde{A}^2B_1$	5000	6, 18, 6, 15, 30		4.16(b)
$\widetilde{B}^2B_2$	5000	18, 6, 6, 12, 40		4.16(c)
$\widetilde{C}^2A_1$	5000	30, 15, 6, 30, 15		4.16(d)
$\widetilde{D}^2B_1$	5000	6, 6, 15, 6, 30		4.16(e)
$\widetilde{X}^2B_2$ -$\widetilde{A}^2B_1$	5000	10, 6, 15, 6, 25	6 (ν_6), 10 (ν_7), 6 (ν_8)	Fig. 4.17(a)
$\widetilde{X}^2B_2$ -$\widetilde{C}^2A_1$	5000	10, 6, 4, 10, 6	6 (ν_{12}), 6 (ν_{13}), 8 (ν_{14}), 10 (ν_{15})	
$\widetilde{X}^2B_2$ -$\widetilde{D}^2B_1$	5000	6, 6, 10, 6, 20	4 (ν_6), 10 (ν_7), 8 (ν_8)	
$\widetilde{A}^2B_1$ -$\widetilde{B}^2B_2$	5000	8, 4, 8, 6, 15	6 (ν_6), 6 (ν_7), 6 (ν_8)	Fig. 4.17(b)
$\widetilde{A}^2B_1$ -$\widetilde{C}^2A_1$	5000	8, 6, 4, 8, 10	4 (ν_9), 4 (ν_{10}), 8 (ν_{11})	
$\widetilde{B}^2B_2$ -$\widetilde{C}^2A_1$	5000	25, 8, 4, 25, 10	4 (ν_{12}), 8 (ν_{13}), 6 (ν_{14}), 15 (ν_{15})	Fig. 4.17(c)
$\widetilde{B}^2B_2$ -$\widetilde{D}^2B_1$	5000	4, 4, 8, 6, 15	4 (ν_6), 8 (ν_7), 4 (ν_8)	
$\widetilde{C}^2A_1$ -$\widetilde{D}^2B_1$	5000	6, 6, 10, 6, 20	6 (ν_9), 10 (ν_{10}), 6 (ν_{11})	Fig. 4.17(d & e)

respective vibronic structure. The vibrational mode ν_{15} of b_2 symmetry strongly couples to $\widetilde{B}$ and $\widetilde{C}$ electronic states and the minimum of the $\widetilde{B}$ and $\widetilde{C}$ intersections is closer to their respective equilibrium minimum (*cf.* Table 3.35). In addition, the $\widetilde{B}$ state is also strongly coupled with the $\widetilde{D}$ state. As a result, its vibronic structure is strongly perturbed by the associated nonadiabatic coupling. Excitations of nontotally symmetric modes ν_8 & ν_{15}, ν_{14} & ν_{15} and ν_7 are found from the spectrum of the $\widetilde{B}$, $\widetilde{C}$ and $\widetilde{D}$ state, respectively.

Vibronic structure of the electronic states of isomer III

The vibronic structure of the $^2A_2$, $^2B_2$, $\widetilde{B'}^2B_1$, $\widetilde{C'}^2A_1$ and $\widetilde{D'}^2A_1$ electronic states is similarly examined as discussed in sections 4.2.3 and 4.2.3 above. While the vibronic structures of uncoupled $^2A_2$, $^2B_2$, $\widetilde{B'}^2B_1$, $\widetilde{C'}^2A_1$ and $\widetilde{D'}^2A_1$ electronic states are presented in Fig. 4.18, the same including the most relevant interstate couplings are shown in Fig. 4.19 (panel a: $^2A_2$, b: $^2B_2$, c: $\widetilde{B'}^2B_1$, d: $\widetilde{C'}^2A_1$, e: $\widetilde{D'}^2A_1$). The coupling schemes as well as the numerical details of the calculations are given in Table 4.8. In comparison with Fig. 4.17, it can be seen that the nonadiabatic coupling effects are generally stronger in the electronic states of isomer III. In contrast to the assignment of Boldyrev and co-workers we find that the A_2 ($\widetilde{X'}$) state is lower in energy than the B_2 ($\widetilde{A'}$) state at the vertical configuration. This aspect is explicitly confirmed by varying the size of the basis set and the active space in the CASSCF/MRCI calculations. A detail comparison with the experimental band structure is discussed in the subsequent section.

A careful examination of various spectra presented in Figs. 4.18 (a-e) and also corresponding uncoupled state spectra reveal the following. The symmetric vibrational modes ν_1 and ν_6 form dominant progression in the $\widetilde{X'}$, $\widetilde{A'}$, $\widetilde{B'}$, $\widetilde{C'}$ and $\widetilde{D'}$ electronic states. Peak spacings of 1331 & 354, 1411 & 301, 1535 & 409, 1280 & 323 and 1337 & 440 cm^{-1} due to ν_1 & ν_6 vibrational modes are found in the vibronic structure of the above states, in that order. The excitation of the mode ν_1 and ν_6 is strongest in the and $\widetilde{C'}$ and $\widetilde{D'}$ states, respectively. The excitation of the remaining symmetric vibrational modes is

Table 4.8: The same data as Tables 4.7 for neutral isomer III of B_7.

State(s)	Lanczos iterations	No. of HO basis: Symmetric modes ν_1-ν_6	No. of HO basis: Coupling modes	Figure numbers
$^2A_2$	5000	20, 8, 8, 8, 20		4.18(a)
$^2B_2$	5000	4, 20, 4, 20, 10, 20		4.18(b)
$\widetilde{B'}^2B_1$	5000	25, 12, 6, 6, 6, 20		4.18(c)
$\widetilde{C'}^2A_1$	5000	20, 12, 6, 6, 6, 40		4.18(d)
$\widetilde{D'}^2A_1$	5000	40, 4, 18, 4, 4, 18		4.18(e)
$^2A_2$ -$^2B_2$	5000	10, 4, 4, 4, 4, 10	6(ν_9), 10 (ν_{10})	Fig. 4.19(a & b)
$^2A_2$ -$\widetilde{B'}^2B_1$	5000	10, 4, 6, 4, 20	0 (ν_{11}), 6 (ν_{12}), 0 (ν_{13}), 0 (ν_{14}), 0 (ν_{15})	
$^2A_2$ -$\widetilde{C'}^2A_1$	5000	10, 6, 4, 6, 4, 15	8 (ν_7), 4 (ν_8)	
$^2A_2$ -$\widetilde{D'}^2A_1$	5000	25, 4, 10, 4, 4, 15	4 (ν_7), 4 (ν_8)	
$^2B_2$ -$\widetilde{C'}^2A_1$	5000	18, 4, 4, 4, 8, 20	6(ν_{11}), 6 (ν_{12}), 0 (ν_{13}), 0 (ν_{14}), 0 (ν_{15})	
$^2B_2$ -$\widetilde{D'}^2A_1$	5000	15, 4, 8, 4, 4, 10	6(ν_{11}), 0 (ν_{12}), 6 (ν_{13}), 8 (ν_{14}), 0 (ν_{15})	
$\widetilde{B'}^2B_1$ -$\widetilde{C'}^2A_1$	5000	10, 6, 4, 4, 4, 10	6 (ν_9), 8 (ν_{10})	Fig. 4.19(c)
$\widetilde{B'}^2B_1$ -$\widetilde{D'}^2A_1$	5000	10, 6, 6, 4, 4, 10	8 (ν_9), 8 (ν_{10})	
$\widetilde{C'}^2A_1$ -$\widetilde{D'}^2A_1$	5000	30, 6, 6, 15, 6, 30		Fig. 4.19(d & e)

weaker in these states. All symmetric vibrational modes are very weakly excited in the $\widetilde{A'}$ state. The impact of the $\widetilde{X'}$-$\widetilde{A'}$ coupling on the vibronic structure of the $\widetilde{X'}$ band [*cf.* Fig. 4.19 (a)] is strongest. This coupling is mainly caused by the ν_{10} vibrational mode of b_1 symmetry. Although the $\widetilde{X'}$ and $\widetilde{C'}$ states are fairly strongly coupled through ν_7 vibrational mode of a_2 symmetry (*cf.* Table 3.33), impact of this coupling on the structure of $\widetilde{X'}$ band is not as profound as due to the $\widetilde{A'}$ state. This is because the energetic minimum of the $\widetilde{X'}$-$\widetilde{C'}$ CIs occurs at much higher energy compared to that of the $\widetilde{X'}$-$\widetilde{A'}$ states. Excitation of nontotally symmetric vibrational modes ν_8 and ν_{10} are found in the $\widetilde{X'}$ band of Fig, 4.19. Peak spacings of ∼245 and ∼131 cm^{-1} due to the above vibrational modes are extracted from the spectrum. The coupling parameters recorded in Table 3.33 reveal that the vibronic structure of the $\widetilde{A'}$ state is perturbed mostly by its coupling with the $\widetilde{X'}$ state. Likewise, $\widetilde{B'}$-$\widetilde{C'}$ coupling mutually perturbs their vibronic structures. In addition, coupling of the $\widetilde{C'}$ state with $\widetilde{X'}$ state also makes significant contributions to the structure of the $\widetilde{C'}$ state. Vibronic structure of the $\widetilde{D'}$ state is mainly perturbed by its coupling with the $\widetilde{A'}$ and $\widetilde{B'}$ states. Although the $\widetilde{C'}$ state has negligible contribution to the structure of the $\widetilde{X'}$ state, its energetic minimum is quasi-degenerate with the minimum of the $\widetilde{X'}$-$\widetilde{C'}$ intersections (*cf.* Table 3.35). As a result $\widetilde{X'}$-$\widetilde{C'}$ coupling through ν_7 vibrational mode of a_2 symmetry makes significant contribution to the vibronic structure of the $\widetilde{C'}$ state. Excitation of nontotally symmetric modes ν_{10}, ν_9 & ν_{10}, ν_7 & ν_{10} and ν_{10} & ν_{14} are found in the $\widetilde{A'}$, $\widetilde{B'}$, $\widetilde{C'}$ and $\widetilde{D'}$ states, respectively.

Composite photodetachment bands versus experiment

The photodetachment bands of all three isomers are calculated separately employing the full Hamiltonians ($\mathcal{H}_{\rm I}$, $\mathcal{H}_{\rm II}$ and $\mathcal{H}_{\rm III}$) and WP propagation method. The MCTDH suite of programs is used for this purpose [14–17]. For each isomer separate calculations are carried out for six different initial locations of the WP. The resulting time autocorrelation functions are then combined and damped with an exponential function ($e^{-\frac{t}{\tau}}$, with τ=33 fs) to generate the broad band spectral envelope. The technical details of the calculations for each isomer are given in Table 4.9. The spectral envelopes of three isomers are plotted

separately in panel b of Fig. 4.20 and shown by black (isomer I), red (isomer II) and blue (isomer III) color lines. The composite theoretical band structure of all three isomers is shown in panel c. The 193 nm experimental recording of Ref. [4] is shown in panel a. As mentioned in the introduction, eleven distinct peaks are identified in the experiment by recording the detachment spectrum with 355, 266 and 193 nm laser photon. These peaks are assigned by calculating the VDEs [4] as illustrated in Table 3.15. The origin of the theoretical spectra plotted in panel b and c is placed at the experimental adiabatic ionization energies reported in Ref. [4].

A careful inspection of the theoretical and experimental results shown in Fig. 4.20 reveal the following. The broad threshold feature representing the X band originates from both isomer I and II. The A, B, C and G bands originate from isomer III. It is mentioned before that a very sharp band with a short progression of ∼480 (40) cm^{-1} was observed in the experiment [4]. This band is identified with the vibronic structure of the $^2B_2$ electronic state of the neutral isomer III supported by the VDE data calculated by the OVGF method [4]. The VDE data calculated by us by the same method also supports this assignment. The very sharp structure of this band is attributed to very small geometry changes of the neutral B_7 in the $^2B_2$ state as compared to the geometry of the electronic ground state of the anionic isomer III. An adiabatic detachment energy of ∼3.44(2) eV is estimated for this band from the experimental data [4]. As discussed in Sec. 4.2.3 and noted in Table 3.15 that the CASSCF-MRCI calculations yield a reverse energetic ordering of the $^2B_2$ and $^2A_2$ electronic states of the neutral isomer III. According to the latter results, the $^2A_2$ state is the electronic ground state of this isomer. Now a close look at the vibronic energy level structure of the $^2A_2$ [Fig. 4.19(a)] and $^2B_2$ [Fig. 4.19(b)] states of the neutral isomer III clearly indicates that the latter structure closely resembles the structure of the observed band A. A short vibronic progression of ∼460 cm^{-1} can also be observed from the band structure of Fig. 4.19(b) in excellent agreement with the experiment. This progression can be attributed to both ν_4 and ν_5 vibrational modes. These modes have fairly large bilinear coupling (*cf.* Table 3.30). Further to this analysis it can be seen from Fig. 3.21 that the equilibrium minimum of the $^2B_2$ state is more closer to the reference equilibrium minimum (at $\mathbf{Q}$=0) than the $^2A_2$ state. The MO sequence of the anionic isomer III given in Sec. 3.2.3 also suggests that the $^2B_2$ electronic state ought to be the electronic ground state of the corresponding neutral isomer. Therefore, all the evidences furnished above suggest a reverse energetic ordering of the first two electronic states of neutral isomer III of B_7 in the CASSCF-MRCI results. A reversal of this energetic ordering and placing the adiabatic detachment position of the $^2B_2$ state at the reported experimental energy of ∼3.44 eV nicely reproduces the structure of the observed band (*cf.* Fig. 4.20). In contrast, the vibronic spectrum calculated for the coupled $^2B_2$-$^2A_2$ states from the OVGF energy data deviates considerably from the observed band structure of these two electronic states. To support this statement the calculated band structures from the OVGF energy data are given from the OVGF energy data are given panel a ($^2B_2$ state) and b ($^2A_2$ state) of Fig. 4.21. Therefore, the results given above clearly indicates that the CASSCF-MRCI energy data are more accurate for this isomer of B_7 despite a reverse energetic ordering of the first two electronic states. Furthermore, a shakeup

Table 4.9: The normal mode combinations, sizes of the primitive and single particle bases used in the WP propagation (using the MCTDH program modules on the $\widetilde{X}$-$\widetilde{A}$-$\widetilde{B}$ electronic states of neutral isomer I, $\widetilde{X}$, $\widetilde{A}$, $\widetilde{B}$, $\widetilde{C}$ and $\widetilde{D}$ electronic states of neutral isomer II and $\widetilde{X'}$, $\widetilde{A'}$, $\widetilde{B'}$, $\widetilde{C'}$ and $\widetilde{D'}$ electronic states of neutral isomer III of B_7 using Hamiltonians of Eq. 3.10a, 3.11a and 3.11b, respectively.

particle no	Normal modes	SPF basis	Primitive basis
		Isomer I	
1	ν_2, ν_{9x}, ν_{8y}, ν_{7x}	[10,10,8,8,8,8]	(10, 6, 10, 4)
2	ν_1, ν_{8x}, ν_{9y},ν_4	[10,10,8,8,8,8]	(6, 10, 6, 4)
3	ν_{10x}, ν_{10y}, ν_3, ν_5	[10,10,6,6,6,6]	(10, 10, 4, 4)
4	ν_{7y},ν_{6y},ν_{6x}	[6,6,6,6,6,6]	(4, 4, 4)
		Isomer II	
1	ν_5, ν_7, ν_{10}, ν_9, ν_{14}	[20, 10, 15, 10, 10]	(18, 10, 8, 8, 8)
2	ν_4, ν_8 ν_{11}, ν_{12}, ν_{15}	[10, 10, 10, 10, 10]	(8, 10, 8, 8, 8)
3	ν_3, ν_2 ν_1, ν_6, ν_{13}	[15, 10, 15, 10, 10]	(10, 10, 8, 10, 8)
		Isomer III	
1	ν_1,ν_7,ν_{11},ν_{13}	[10, 8, 4, 6]	(6, 6, 10, 8, 4)
2	ν_2,ν_6,ν_{12},ν_{15}	[4, 10, 6, 8]	(4, 8, 16, 4, 12)
3	ν_3,ν_5,ν_9,ν_{14}	[6, 4, 10, 4]	(10, 10, 12, 12, 10)
4	ν_4,ν_8,ν_{10}	[6, 4, 8]	(4, 4, 4, 4, 8)

state at ∼4.14 eV VDE is involved in the higher energy bands of this isomer (see the text below) which cannot be obtained by the OVGF method.

While the location of the C band is missing in the 193 nm experimental spectrum, its existence is clearly seen in the 266 nm experimental spectrum (Fig. 1 of Ref. [4]). The B and C bands originate from the $^2A_2$ electronic state of the neutral isomer III. The $\widetilde{B'}$ state of isomer III, which is a shake-up state is strongly coupled with its $\widetilde{C'}$ and $\widetilde{D'}$ states through the vibrational modes ν_9 and ν_{10} of b_1 symmetry (*cf.* Table 3.33). The broad and diffuse structure of the G band (*cf.* Fig. 4.20) arises from the coupled $\widetilde{B'}$-$\widetilde{C'}$-$\widetilde{D'}$ states of this isomer. The D band represents the vibronic structure of isomer I and originates from its $\widetilde{A}^4E_1$ electronic state. The E, F, H and I bands represent predominantly the vibronic structure of the $\widetilde{A}^2B_1$, $\widetilde{B}^2B_2$, $\widetilde{C}^2A_1$ and $\widetilde{D}^2B_1$ electronic states of isomer II respectively. The separations of G and H bands of ∼ 0.7 eV as found in the experimental results can also be found in the theoretical results (∼ 0.66 eV) of Fig. 4.20 (c). Therefore, it can be concluded that the present theoretical results are on the average in excellent accord with the experimental band structure.

Internal conversion dynamics

Dynamics of the electronic excited states of B_7 clusters is examined in terms of time-dependence of diabatic electronic populations recorded in the WP calculations of Sec.

4.2.3. It is discussed in Sec. 4.2.3 that the three electronically degenerate electronic states of isomer I is JT active and JT effect is strongest in the $\widetilde{X}^2E_1$ electronic state of this isomer. Time-dependence of the populations (diabatic) of the two JT split components of this state is shown in panel a of Fig. 4.22. At time t=0 the population of the component on which the WP is prepared (say component 1) starts from 1.0 and the same for the component 2 is 0.0. It can be seen that population of component 1 transfers to component 2 through the JT CIs.in time and they become equal at = ∼100 fs. At longer time the population of component 2 transfers back to component 1 and fluctuate around a value of ∼0.4. Similar variation of electronic populations of the two components of the $\widetilde{A}^4E_1$ and $\widetilde{B}^2E_1$ states is found. In these cases the JT effect is weak and population transfer occur back and forth between the component states over the entire time interval.

The diabatic electronic populations of the $\widetilde{X}^2B_2$, $\widetilde{A}^2B_1$, $\widetilde{B}^2B_2$, $\widetilde{C}^2A_1$ and $\widetilde{D}^2B_1$ electronic states of neutral isomer II of B_7^- when the WP prepared in $\widetilde{X}$, $\widetilde{A}$, $\widetilde{B}$, $\widetilde{C}$ and $\widetilde{D}$ states are given in panel a, b, c, d and e of Fig. 4.23. When the WP is prepared in $\widetilde{X}$ state, panel a of Fig. 4.23 reveal minor population flow to the other states. The $\widetilde{X}$-$\widetilde{A}$ CI is just ∼0.05 eV above the minimum of $\widetilde{A}$ state (*cf.* Table 3.35). The $\widetilde{X}$-$\widetilde{A}$ CI acts as a funnel for the nonradiative transfer of the $\widetilde{A}$ state to $\widetilde{X}$ state shown in Fig. 4.23(b). As the $\widetilde{X}$ and $\widetilde{A}$ states are well separated from each other and the associated interstate coupling parameter is small, the flow of population expected to be moderate. The other intersections with $\widetilde{A}$ state occurs at much higher energies, and are not expected to create impact on the diabatic population of $\widetilde{A}$ state. The initial population value of the $\widetilde{A}$ state is 1 at t=0. Only 30 % of the population of $\widetilde{A}$ transferred to $\widetilde{X}$ state after 150 fs propagation of the WP, due to the weak coupling with $\widetilde{X}$ state. An initial decay of the population relates to ∼503 fs is estimated from Fig. 4.23(b). Significant population flows to the $\widetilde{A}$ state when the $\widetilde{B}$ state is initially populated (Fig. 4.23 (c)). This happens through the $\widetilde{A}$-$\widetilde{B}$ CIs. From Table 3.35, it can be seen that the $\widetilde{A}$-$\widetilde{B}$ CI minimum is just ∼0.02 eV above the minimum of $\widetilde{B}$ state. Similar situation arises when the WP is initially located on the $\widetilde{C}$ (panel d) and $\widetilde{D}$ (panel e) electronic states. In panel d the $\widetilde{B}$ & $\widetilde{A}$ states populated through $\widetilde{A}$-$\widetilde{C}$ & $\widetilde{B}$-$\widetilde{C}$ CIs, respectively. In panel e $\widetilde{C}$ & $\widetilde{B}$ electronic states populated through $\widetilde{B}$-$\widetilde{D}$ & $\widetilde{C}$-$\widetilde{D}$ CIs, respectively. Nonradiative decay rate of ∼72, ∼136 and ∼86 fs are estimated for $\widetilde{B}$, $\widetilde{C}$ and $\widetilde{D}$ electronic states, respectively.

Similarly, the diabatic populations of the states $^2A_2$, $^2B_2$, $\widetilde{B'}^2B_1$, $\widetilde{C'}^2A_1$ and $\widetilde{D'}^2A_1$ electronic states of neutral isomer III of B_7^- when the WP prepared in $\widetilde{X'}$, $\widetilde{A'}$, $\widetilde{B'}$, $\widetilde{C'}$ and $\widetilde{D'}$ states, are given in panel a, b, c, d and e of Fig. 4.24. The panel a reveals no significant population flow to other states. The population flow from $\widetilde{A'}$, $\widetilde{B'}$, $\widetilde{C'}$ and $\widetilde{D'}$ states through $\widetilde{X'}$-$\widetilde{A'}$, $\widetilde{X'}$-$\widetilde{B'}$, $\widetilde{X'}$-$\widetilde{C'}$ & $\widetilde{B'}$-$\widetilde{C'}$, $\widetilde{C'}$-$\widetilde{D'}$ & $\widetilde{A'}$-$\widetilde{D'}$ CIs can be seen from panels b, c, d and e, respectively. Nonradiative decay rate of ∼89, ∼154, ∼41 and ∼22 fs are estimated for $\widetilde{A'}$, $\widetilde{B'}$, $\widetilde{C'}$ and $\widetilde{D'}$ electronic states, respectively.

4.3 Summary

A theoretical study of the photodetachment spectroscopy of boron cluster anion B_n^- (n=4, 5 and 7) is presented in this chapter. The nuclear dynamics underlying the observed complex structure of the photodetachment bands is studied both by time-independent and time-dependent quantum mechanical methods. The vibronic Hamiltonians developed in Chapter 3 are employed in the investigation. The theoretical results are compared with the experimental findings and discussed in detail.

The nonadiabatic coupling effects are generally found to be small in the photodetachment bands of B_4^-. Some significant effect of such coupling is found in the $\widetilde{a}^3B_{2u}$ and $\widetilde{b}^3B_{1u}$ bands of B_4 only. The symmetric vibrational mode ν_1 and ν_2 forms progression in all the low-lying electronic states of B_4 considered here. The theoretical results are found to be in fair agreement with the experiment and the apparent discrepancy between the two is attributed to the neglect of dynamic spin-orbit coupling in the theoretical treatment and small photodetachment cross sections and inadequate energy resolution in the experiment. In order to confirm that the theoretical results of B_4^- photodetachment do not contain any spin contamination, the equilibrium geometry of B_4^- is optimized both by the UB3LYP and ROMP2 methods (cf., Chapter 3). Using these geometry parameters, two sets of Hamiltonian parameters are derived and dynamics study is performed. Consistent results are obtained in both the cases.

In contrast to B_4^-, the nonadiabatic coupling effects are far more significant in the photodetachment bands of B_5^-. The symmetric vibrational modes ν_3 and ν_4 play most crucial role in this case. Visible impact of nonadiabatic coupling and excitations of nontotally symmetric vibrational modes observed in this case. The complex C band (as designated in the experiment) has been partially described to originate from the $\widetilde{C}^2A_1$, $\widetilde{D}^2B_1$ and $\widetilde{E}^2A_1$ electronic states of B_5. Like the shake-up $\widetilde{E}^2A_1$ state, there are many more states of this kind in the energy range of the C band. A complete analysis of this problem is beyond the scope of the present investigation and will be taken up in future.

Neutral B_7 clusters originating from electron detachment of three isomers (C_{6v} hexagonal pyramidal, C_{2v} pyramidal and C_{2v} planar) of anionic B_7^- cluster are examined and their contribution to the composite experimental band structure is elucidated. The theoretical results are shown to be in good accord with the experimental findings. The impact of the nonadiabatic coupling on the vibronic structure of the photodetachment bands is studied and discussed at length. In addition to totally symmetric vibrational modes excitation of several nontotally symmetric modes is found from the theoretical results. The peaks marked in the experimental spectrum of Fig. 4.20(a) (X to I) are found to originate from the C_{6v} isomer (X and D), pyramidal C_{2v} isomer (X, E, F, H and I) and planar C_{2v} isomer (A, B, C and G). The energetic ordering of the $^2A_2$ and $^2B_2$ states of isomer III is assessed through extensive quantum chemistry calculations and experimental band structures. To the best of our knowledge, B_7 represents a unique system for which the complex vibronic structure of the energetically low-lying electronic state arise from anion precursors of different symmetry and a rich variety of vibronic coupling mechanisms in its energetically low-lying electronic states.

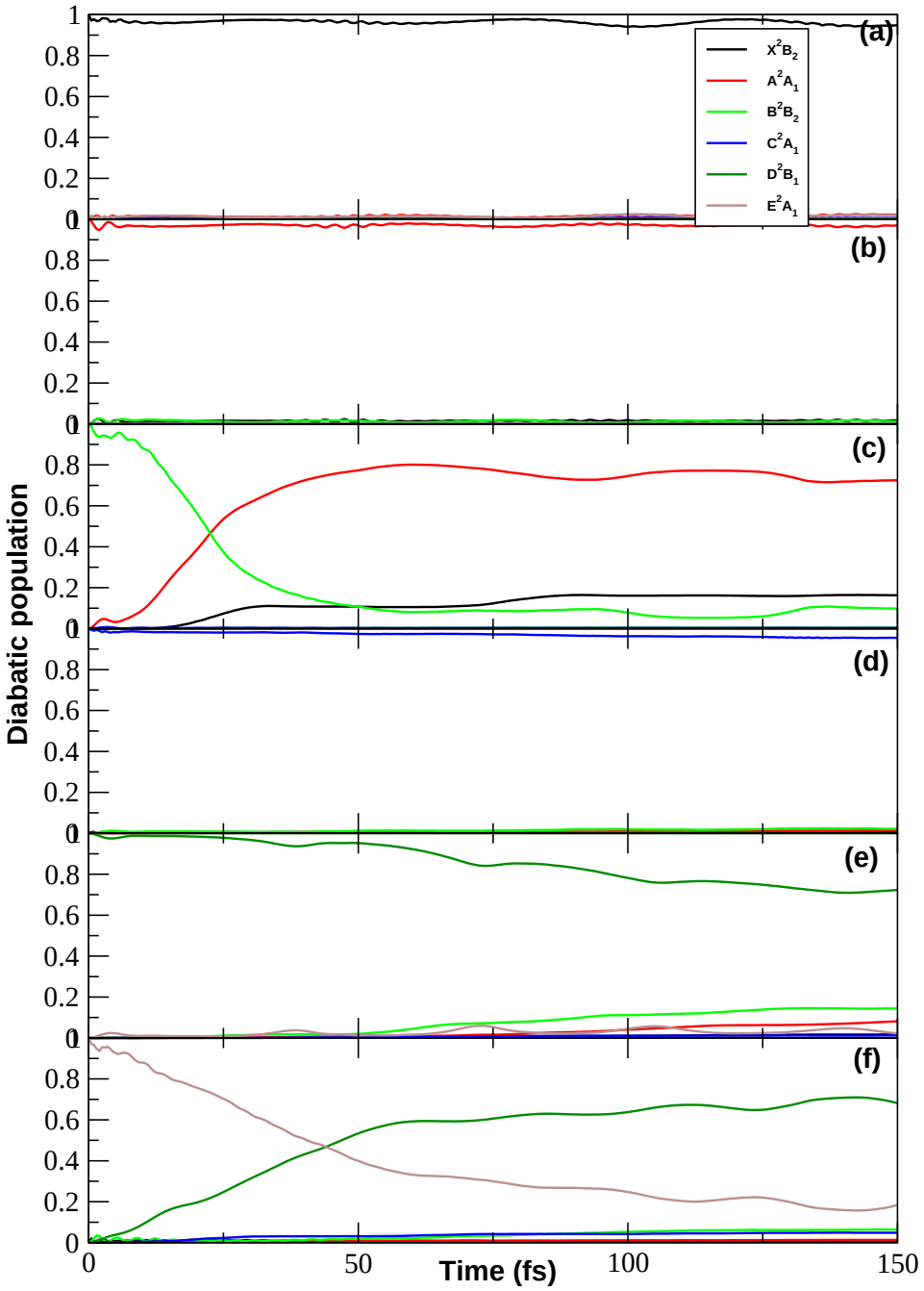

Figure 4.13: Time-dependence of the diabatic electronic populations in the coupled surface dynamics of B_5. The electronic populations for an initial preparation of the WP on the $\widetilde{X}$, $\widetilde{A}$, $\widetilde{B}$, $\widetilde{C}$, $\widetilde{D}$ and $\widetilde{E}$ electronic states are shown in panel a-e, respectively (see text for details).

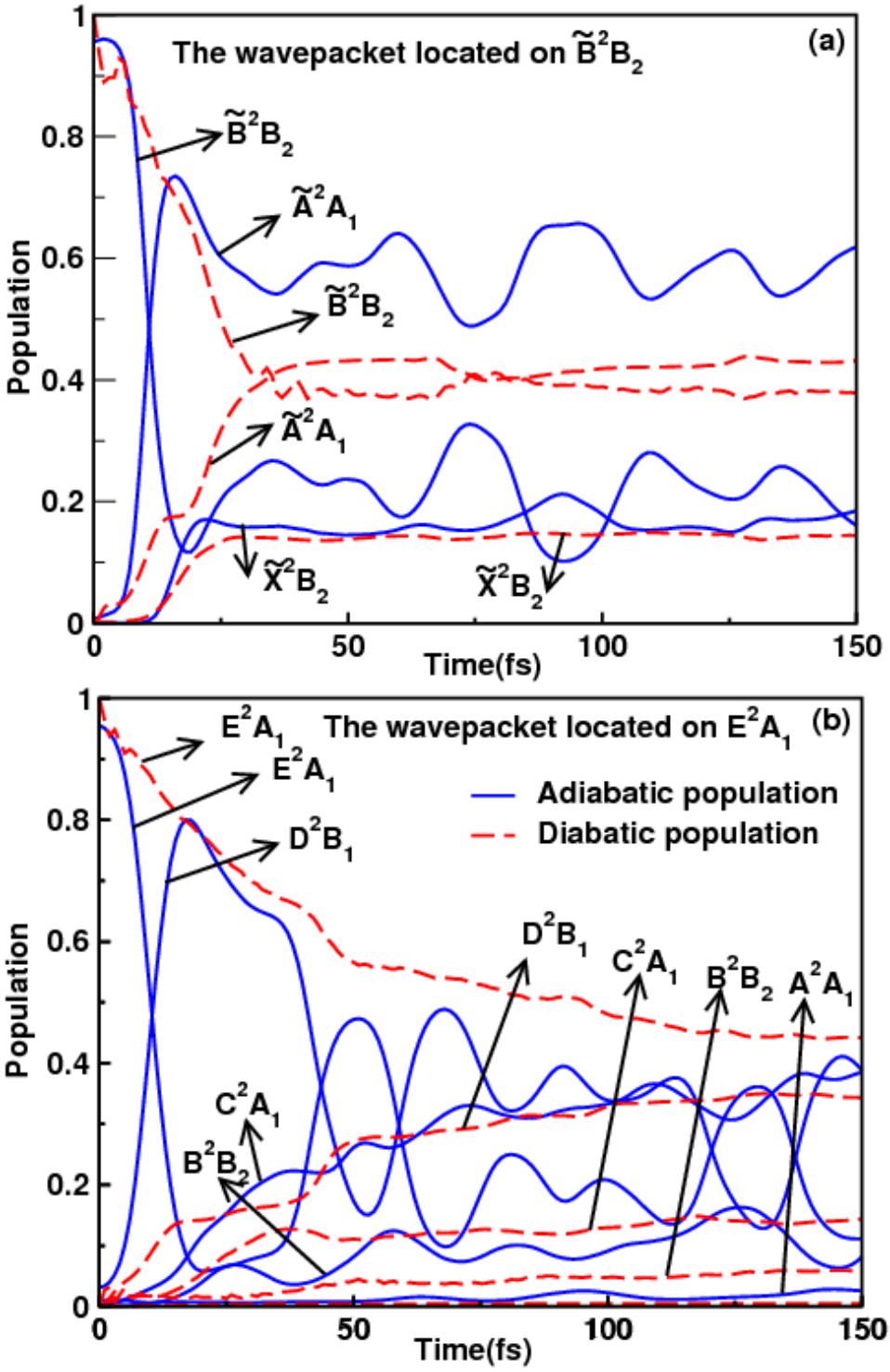

Figure 4.14: Time-dependence of adiabatic (solid lines) and diabatic(dashed lines) for an initial location of the WP on the $\widetilde{B}^2B_2$ (panel a) and $\widetilde{E}^2A_1$ (panel b) electronic states of B_5.

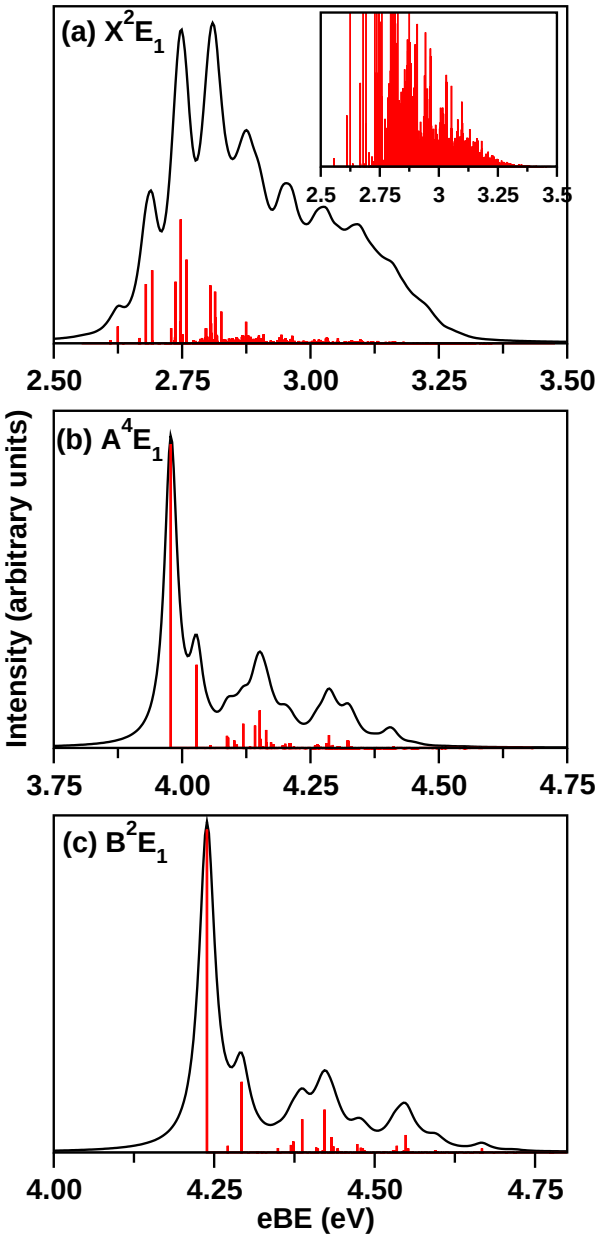

Figure 4.15: Vibronic eigenvalue spectra of $\widetilde{X}^2E_1$, $\widetilde{A}^4E_1$ and $\widetilde{B}^2E_1$ electronic states of the neutral B_7 (isomer I) plotted in panel a, b and c, respectively. The zero of energy correspond to the equilibrium minimum of isomer I of B_7^-. The huge increase of vibronic line density at higher energies resulting from the strong JT effect in the $\widetilde{X}^2E_1$ electronic manifold is shown in the inset of panel a. The numerical details of calculations of the above spectra are given in Table 4.6.

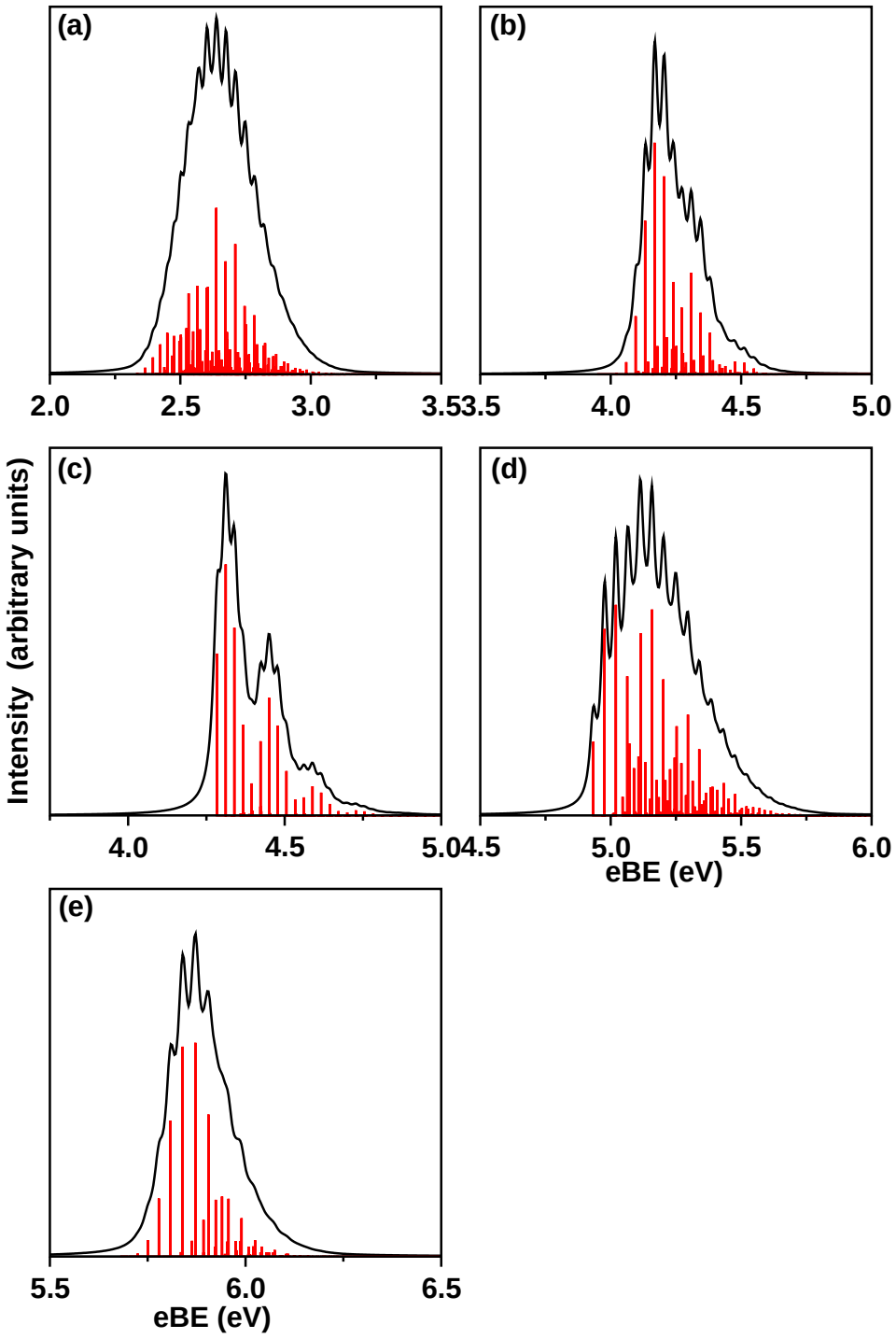

Figure 4.16: Same as in Fig. 4.15, of uncoupled $\widetilde{X}^2B_2$, $\widetilde{A}^2B_1$, $\widetilde{B}^2B_2$, $\widetilde{C}^2A_1$ and $\widetilde{D}^2B_1$ electronic states of B_7 (isomer II). The numerical details of calculations of the above spectra are given in Table 4.7.

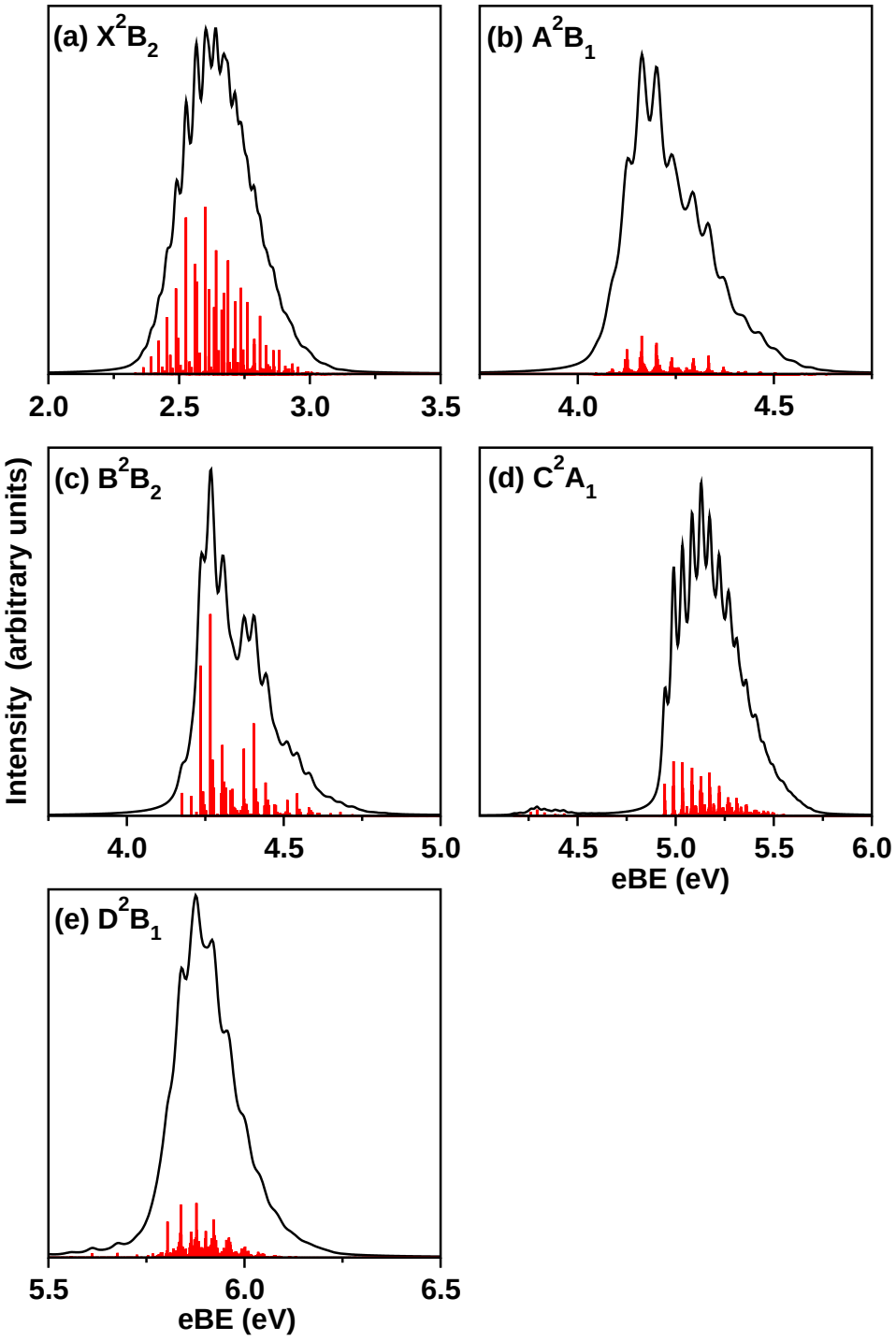

Figure 4.17: Same as in Fig. 4.15, of coupled $\widetilde{X}^2B_2$, $\widetilde{A}^2B_1$, $\widetilde{B}^2B_2$, $\widetilde{C}^2A_1$ and $\widetilde{D}^2B_1$ electronic states of B_7 (isomer II). The numerical details of calculations of the above spectra are given in Table 4.7.

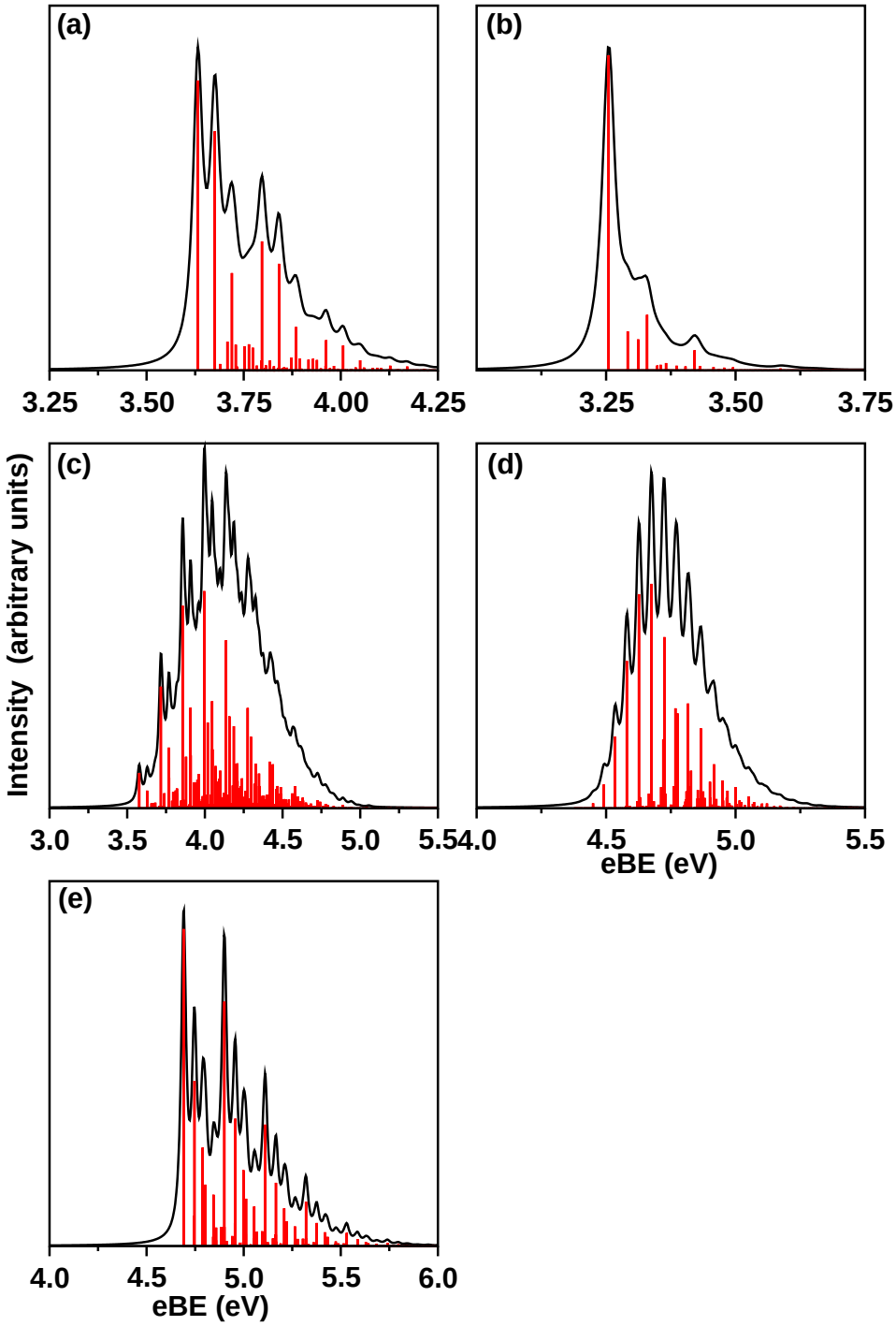

Figure 4.18: Same as in Fig. 4.15, of uncoupled $^2A_2$, $^2B_2$, $\widetilde{B'}^2B_1$, $\widetilde{C'}^2A_1$ and $\widetilde{D'}^2A_1$ electronic states of B_7 (isomer III). The numerical details of calculations of the above spectra are given in Table 4.8.

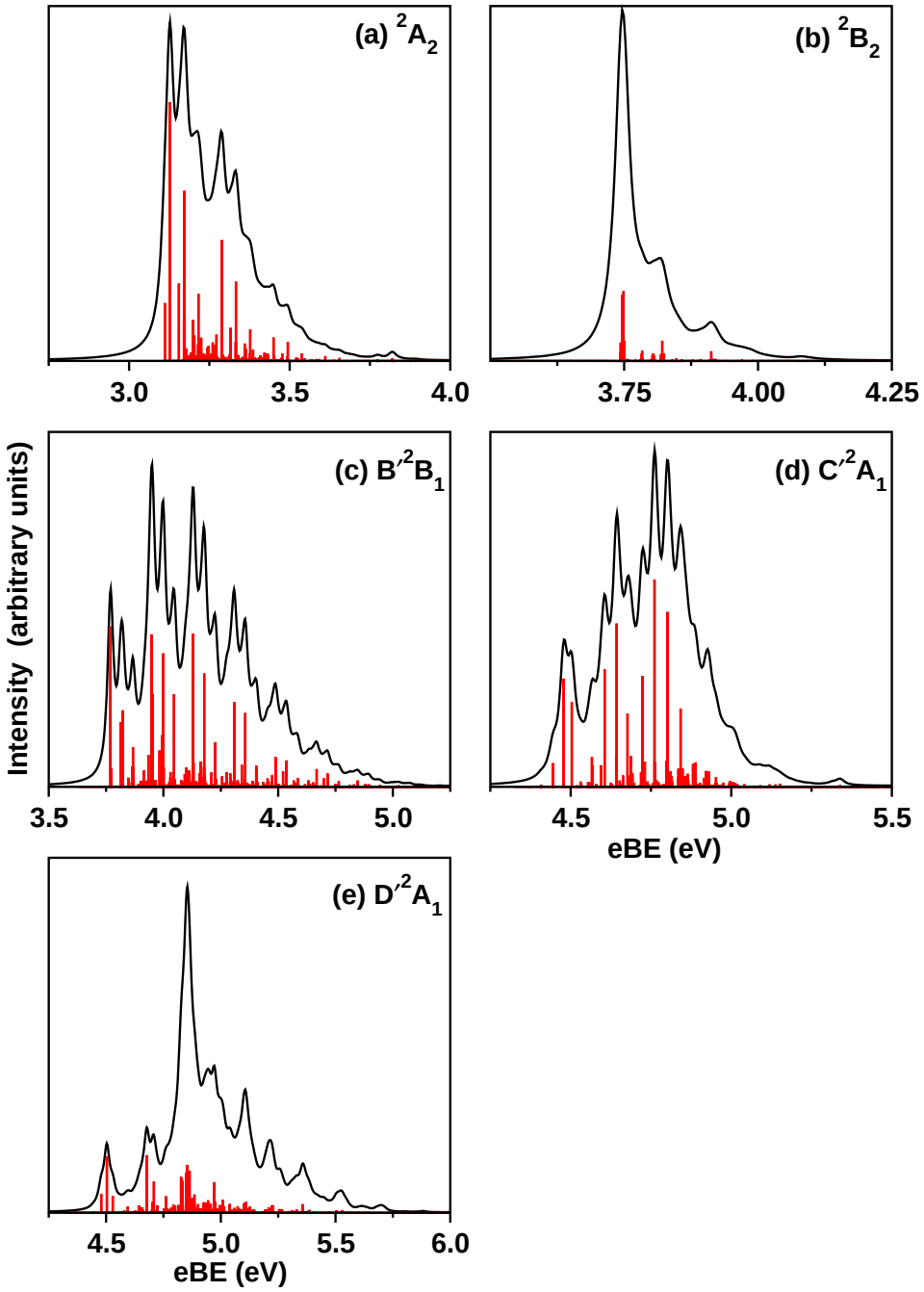

Figure 4.19: Same as in Fig. 4.15, of $^2A_2$, $^2B_2$, $\widetilde{B'}^2B_1$, $\widetilde{C'}^2A_1$ and $\widetilde{D'}^2A_1$ electronic states of B_7 (isomer III). The numerical details of calculations of the above spectra are given in Table 4.8.

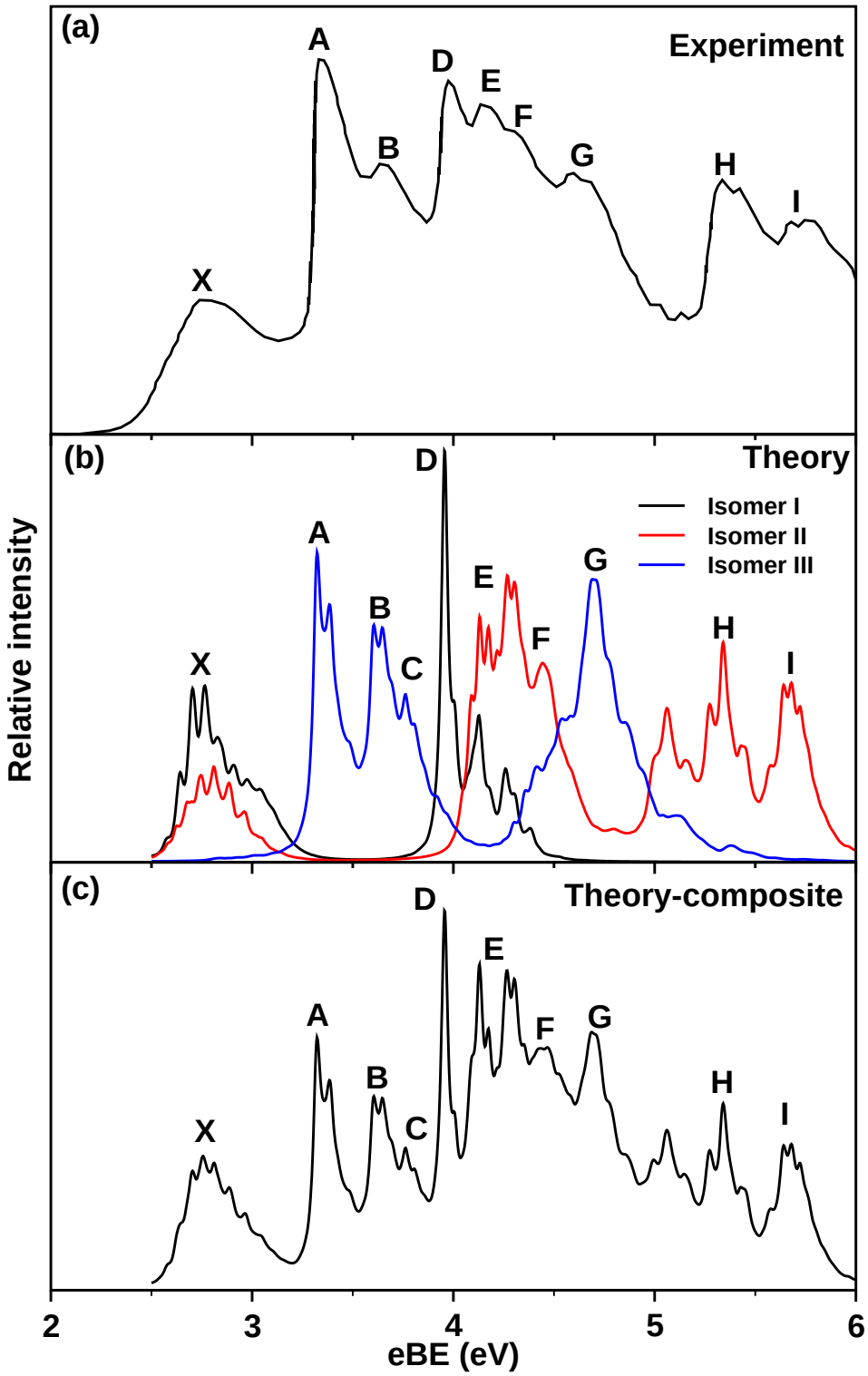

Figure 4.20: Photodetachment spectrum of B_7^-. Relative intensity (in arbitrary units) is plotted as a function of electron binding energy. The 193 nm experimental recording is reproduced from Ref. [4] and plotted in panel a. Theoretical band structure originating from isomer I, II and III of B_7^- is plotted separately in panel b and shown by black, red and blue color lines, respectively (see text for details). The composite theoretical band structure of all three isomers is shown in panel c.

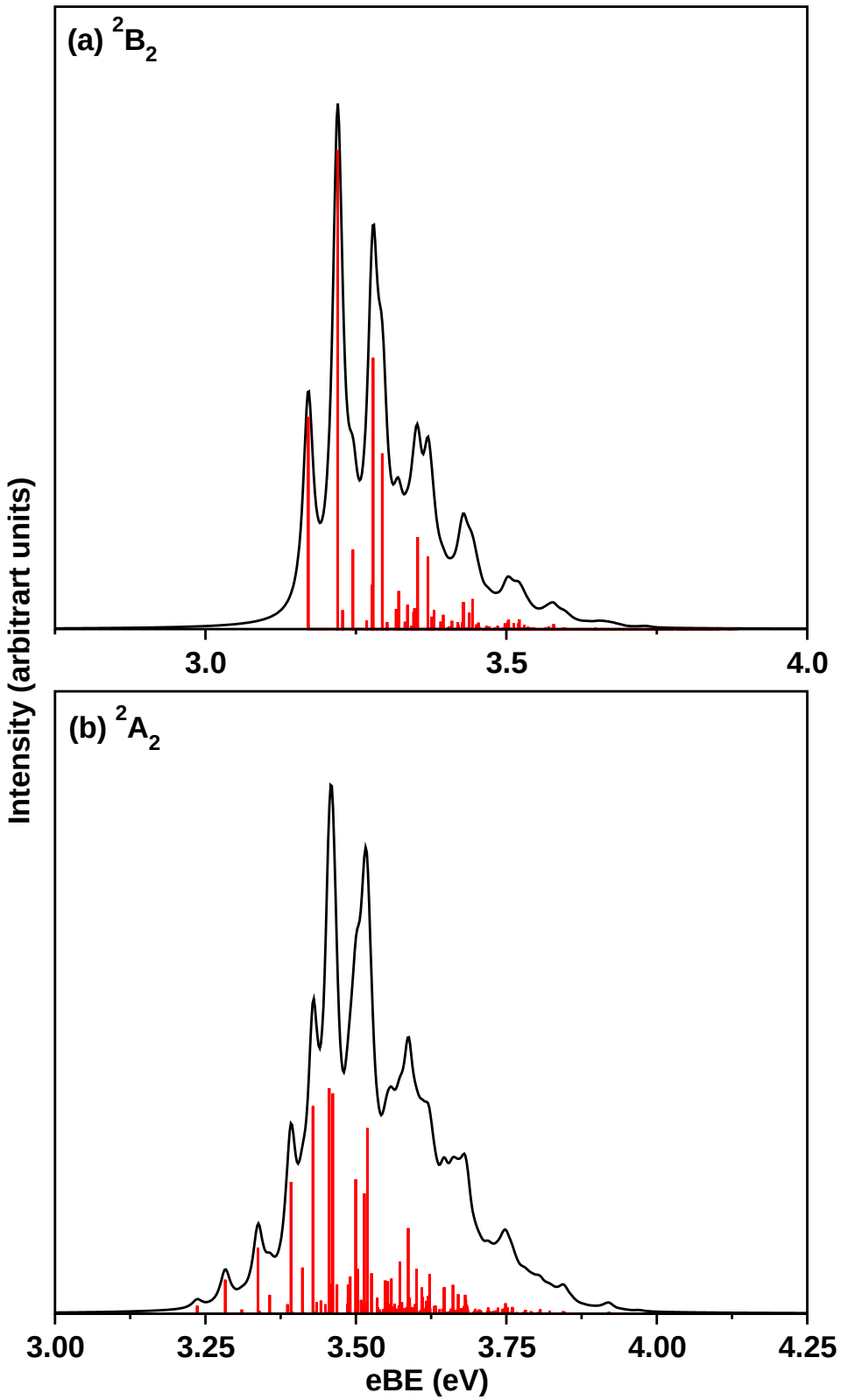

Figure 4.21: Same as in Fig. 4.15, for the $^2B_2$ and $^2A_2$ electronic states of B_7 (isomer III) calculated with the aid of Hamiltonian parameters for the coupled $^2B_2$-$^2A_2$ states extracted from the OVGF energy data.

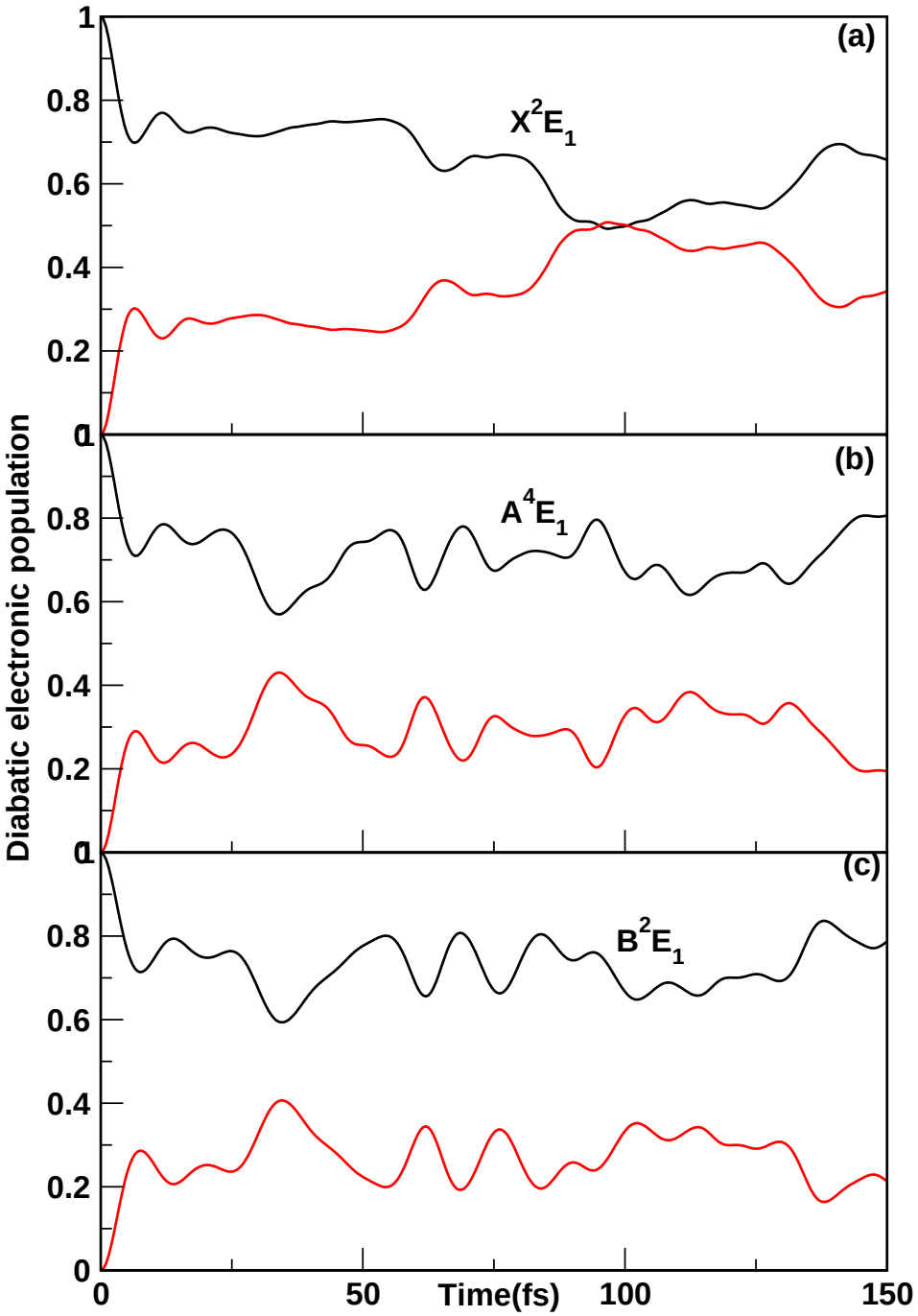

Figure 4.22: Time-dependence of diabatic electronic populations for an initial location of the WP on the $\widetilde{X}^2E_1$ (panel a), $\widetilde{A}^4E_1$ (panel b) and $\widetilde{B}^2E_1$ (panel c) electronic states of B_7 neutral isomer I. The black and red lines in each panel represents the x and y components of the each degenerate state, respectively.

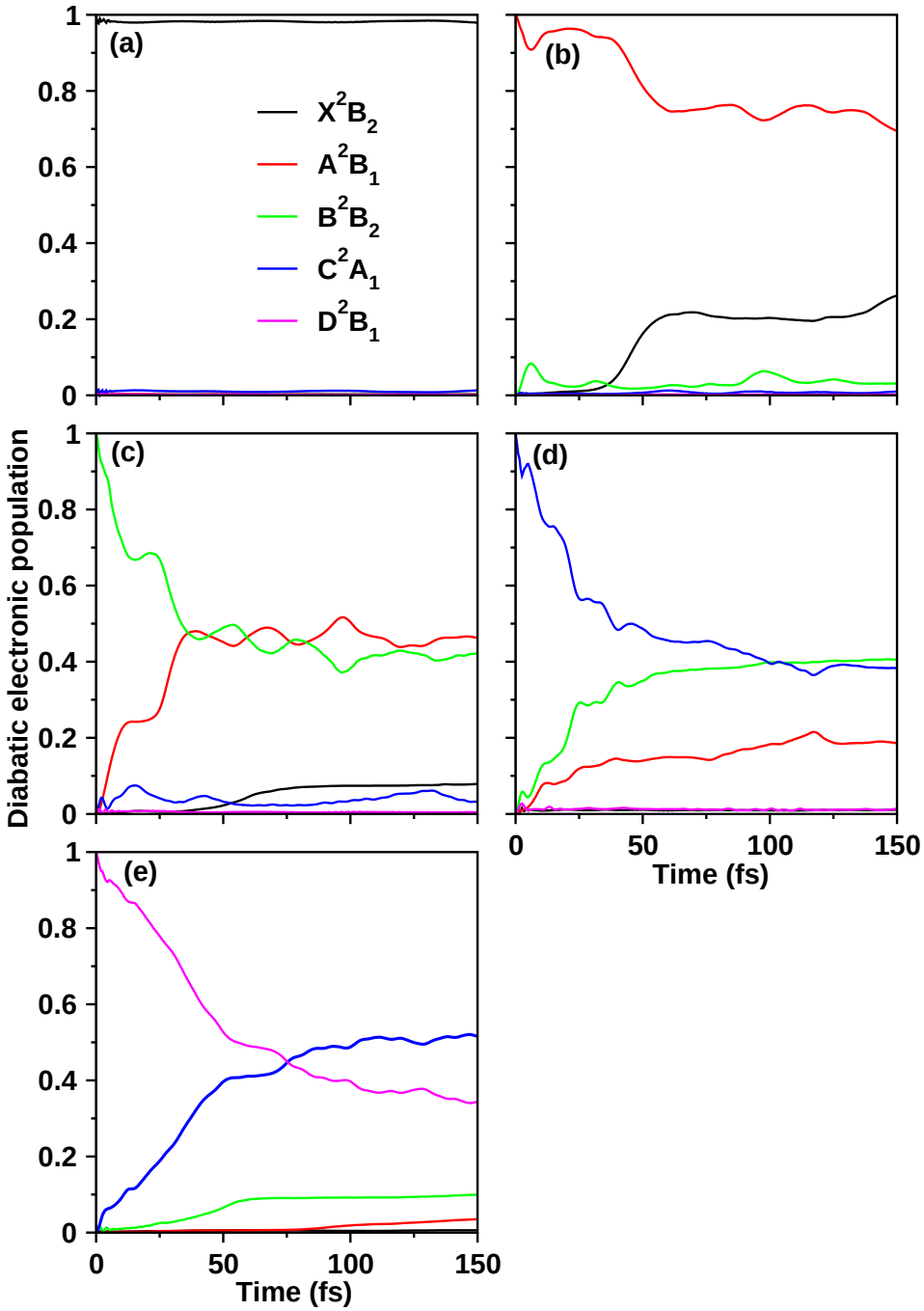

Figure 4.23: Time-dependence of diabatic electronic populations for an initial location of the WP on the $\widetilde{X}^2B_2$ (panel a), $\widetilde{A}^2B_1$ (panel b), $\widetilde{B}^2B_2$ (panel c), $\widetilde{C}^2A_1$ (panel d) and $\widetilde{D}^2B_1$ (panel e) electronic states of neutral isomer II.

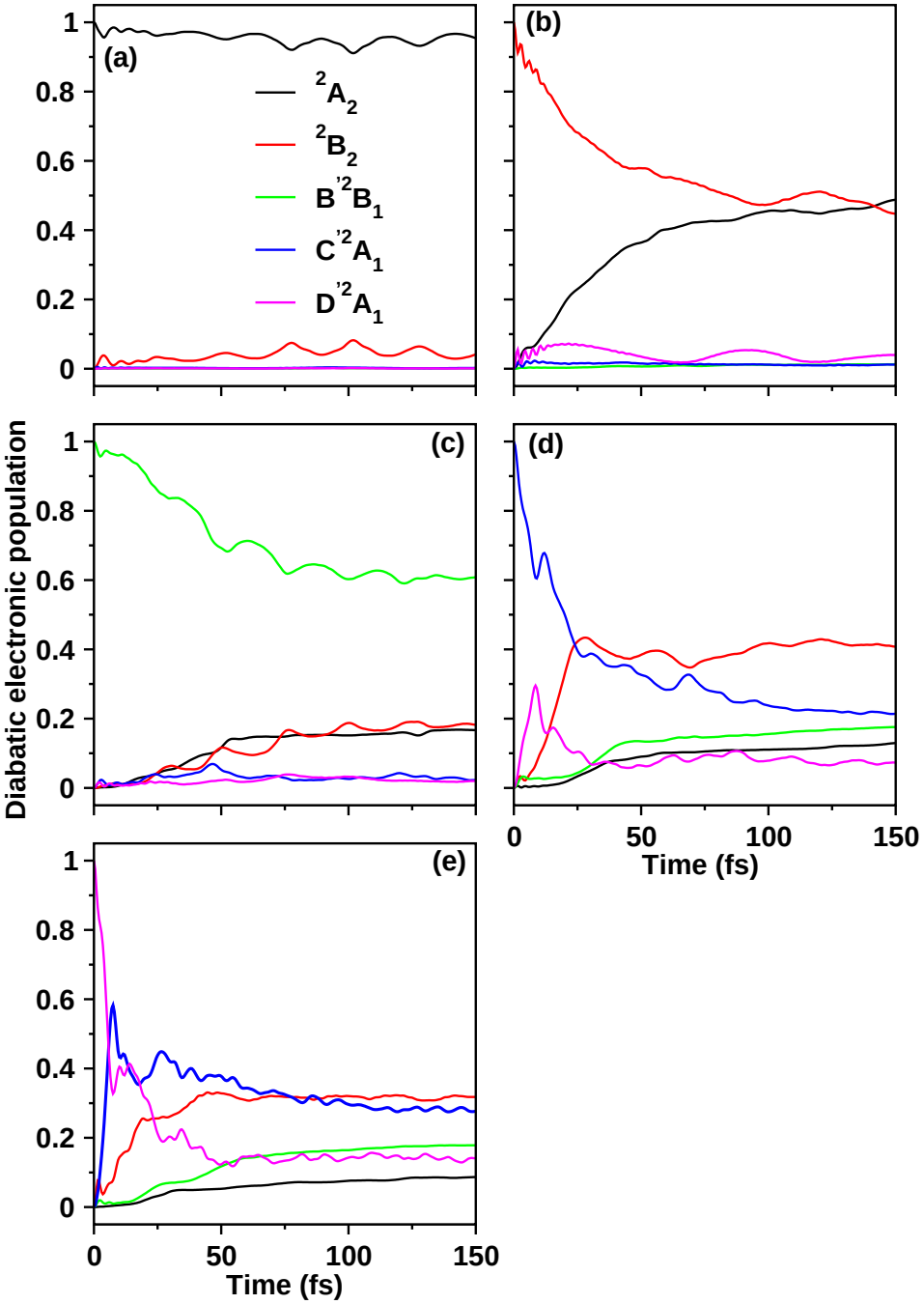

Figure 4.24: Time-dependence of diabatic electronic populations for an initial location of the WP on the $^2A_2$ (panel a), $^2B_2$ (panel b). $\widetilde{B'}^2B_1$ (panel c), $\widetilde{C'}^2A_1$ (panel d) and $\widetilde{D'}^2A_1$ (panel e) electronic states of B_7 neutral isomer III.

References

[1] T. S. Venkatesan, K. Deepika, and S. Mahapatra, J. Comput. Chem. **27**, 1093 (2006).

[2] H. J. Zhai, L. S. Wang, A. N. Alexandrova, A. I. Boldyrev, and V. G. Zakrzewski, J. Phys. Chem. A **107**, 9319 (2003).

[3] H. J. Zhai, L. S. Wang, A. N. Alexandrova, and A. I. Boldyrev, J. Chem. Phys. **117**, 7917 (2002).

[4] H. J Zhai, L-S Wang, A. N. Alexandrova and A. I. Boldyrev, J. Phys. Chem. A **108**, 3509 (2004).

[5] M. T. Nguyen, M. H. Matus, V. T. Ngan, D. J. Grant, and D. A. Dixon, J. Phys. Chem. A **113**, 4895, (2009)

[6] T. B. Tai, D. J. Grant, M. T. Nguyen, and D. A. Dixon, J. Phys. Chem. A **114**,994, (2010)

[7] Conical Intersections: Electronic Structure, Dynamics and Spectroscopy, edited by W. Domcke, D. R. Yarkony, and H. Köppel (World Scientific, Singapore, 2004).

[8] H. Köppel, W. Domcke, and L. S. Cederbaum, Adv. Chem. Phys. **57**, 59 (1984).

[9] M. Born and R. Oppenheimer, Ann. Phys. (Leipzig) **84**, 457 (1927).

[10] M. Born and K. Huang, The Dynamical Theory of Crystal Lattices, (Oxford University Press, Oxford, U.K., 1954).

[11] R. Englman, The Jahn-Teller Effect, (Wiley, New York, 1972).

[12] M. Baer, Beyond Born-Oppenheimer:electronic non-adiabatic coupling terms and conical intersections, (John Wiley and Sons, 2006).

[13] S. Mahapatra, Acc. Chem. Res. **42**, 1004 (2009).

[14] G. A. Worth, M. H. Beck, A. Jäckle, and H.-D. Meyer, The MCTDH Package, Version 8.2, (2000), University of Heidelberg, Heidelberg, Germany. H.-D. Meyer, Version 8.3 (2002), Version 8.4 (2007). See http://mctdh.uni-hd.de.

[15] H.-D. Meyer, U. Manthe, and L. S. Cederbaum, Chem. Phys. Lett. **165**, 73 (1990).

[16] U. Manthe, H.-D. Meyer, and L. S. Cederbaum, J. Chem. Phys. **97**, 3199 (1992).

[17] M. H. Beck, A. Jäckle, G. A. Worth, and H.-D. Meyer, Phys. Rep. **324**, 1 (2000).

[18] J. Cullum and R. Willoughby, Lanczos Algorithms for Large Symmetric Eigenvalue Problems (Birkhäuser, Boston, 1985, Vols. I and II).

5 Theoretical study of photoabsorption spectroscopy of carbon chains. C_{15}

5.1 Introduction

DIBs are absorption features seen in the spectra of reddened stars through diffuse interstellar clouds [1]. Over 400 bands are seen, in ultraviolet, visible and infrared wavelengths. Identification of carriers of DIBs has been a long standing and unresolved issue in the astrophysical spectroscopy. The diffuse structure of these bands is attributed to the very short life times of the excited electronic states of the carrier molecule [2]. Douglas in his seminal paper, suggested that the bare carbon chains C_n, where n may lie in the range 5-15 [3] could show spectroscopic features consistent with the DIBs. The first spectroscopic detection of C_3 in comets in 1881 [4] triggered curiosity among the astronomers, chemists and physicists to further investigate structure and spectroscopy of carbon chains.

Since then many experimental and theoretical studies were reported on the structure of anionic, neutral and cationic bare carbon clusters. Here we refer to two reviews on the rich history of carbon cluster chemistry by Weltner [5] and Orden [6]. Carbon clusters smaller than C_{10} possess low-energy linear structures. Cumulenic bonding (:C=C–C=C:), with nearly equivalent bond lengths, as opposed to acetylenic bonding, (.C≡C-C—C≡C) with alternating bond lengths, was predicted to be the preferred bonding configuration. Linear chains containing odd number of carbon atoms were thought to possess $^1\Sigma_g^+$ ground electronic states, whereas the ground states were $^3\Sigma_g^-$ for the chains with even number of carbon atoms. Clusters larger than C_{10} were believed to occur as monocyclic rings, due to the reduction in angle strain of the larger rings and the added stability arising from an additional C-C bond. Despite this, the cyclic isomers of the neutral clusters reported to be difficult to detect and characterize spectroscopically, and it is the linear isomers that are observed in the vast majority of experimental studies. This is the case even for clusters as large as C_{15}.

The neutral and anions of bare carbon chains are studied with various spectroscopic techniques ranging from pulsed and continuous-wave CRD, R2C2PI, LIF, trapped ion photofragmentation, and electron photodetachment processes during the past decade [7–11] to examine the conjecture of Douglas. It was proved from the study of Maier *et al.* that bare carbon chains C_n upto n=12 can not be carrier for DIBs. The following criteria are formulated by the latter authors for a species to have to be a potential DIB carrier: "(a) absorptions in the 400-800 nm range, (b) oscillator strength f values in the 1-10 range, and (c) an excited electronic-state lifetime longer than a few picoseconds so

Table 5.1: VEEs (in eV) of low-lying excited singlet electronic states calculated at the equilibrium geometry of S_0 state of C_{15}.

Symbol	Excitation energy (eV)	f
$S_1{}^1\Delta_u$	0.6701	0.00
$S_2{}^1\Sigma_u^-$	0.7461	0.00
$S_3{}^1\Sigma_g^-$	2.1277	0.00
$S_4{}^1\Delta_g$	2.1431	0.00
$S_5{}^1\Pi_g$	3.1081	0.00
$S_6{}^1\Pi_u$	3.1097	0.01
$S_7{}^1\Sigma_u^+$	3.2729	12.97
$S_8{}^1\Sigma_u^-$	3.4325	0.00
$S_9{}^1\Sigma_g^-$	3.4485	0.00
$S_{10}{}^1\Delta_g$	3.4800	0.00
$S_{11}{}^1\Delta_u$	3.5148	0.00
$S_{12}{}^1\Sigma_g^+$	3.6132	0.00

that intramolecular broadening would still be compatible with the typical half-widths of the narrower DIBs (i.e., a few wave numbers)" [10]. The longer chains with an odd number of carbon atoms of the length 15, 17, 19 and 21 are expected to satisfy the first two criteria because their transitions are in the 400-800 nm range and their f values scale with the chain length. It remains to be seen by doing nuclear dynamics study, whether the excited electronic state $S_7{}^1\Sigma_u^+$ has a lifetime longer than a few picoseconds to satisfy the third condition listed above.

The low-lying electronic excited states of C_{15} and their oscillator strengths are tabulated in Table 5.1. *Ab initio* calculation of the excited states are described in Section 5.2. As can be seen from the table, the electronic states are very closely spaced, infact 18 electronic states (including degeneracy) appear within 4.0 eV, ideally which need to be studied, for a correct description of the nuclear dynamics. While, consideration all the electronic states would be much appreciated, both the *ab initio* electronic structure calculations and nuclear dynamics simulations would be computationally very challenging and difficult. While the first one (*ab initio* calculations) can be feasible with relatively less expensive yet reliable methods such as equation of motion coupled cluster with single and double excitations (eom-CCSD), the later (nuclear dynamics) with all the 18 electronic states appears to be impossible to study. As our study, primarily focuses on the life time of $S_7{}^1\Sigma_u^+$ electronic state of C_{15}, we retain only those electronic states which couple to $S_7{}^1\Sigma_u^+$ electronic state according to the vibronic coupling selection rules given in Section 5.3. From the selection rules, it can be seen that only $S_5{}^1\Pi_g$, $S_6{}^1\Pi_u$ and $S_{12}{}^1\Sigma_g^+$ electronic states couple to $S_7{}^1\Sigma_u^+$ electronic state.

In this chapter, such study of the nuclear dynamics in the $S_5{}^1\Pi_g$, $S_6{}^1\Pi_u$, $S_7{}^1\Sigma_u^+$ and $S_{12}{}^1\Sigma_g^+$ coupled electronic states of C_{15} carbon chain, by doing rigorous electronic structure calculations is presented. The well celebrated BO approximation fails [18–22]

when two electronic states happen to be degenerate or near degenerate. The reason for such breakdown is the non-adiabatic coupling operator behaves singularly at degeneracy. Familiar examples for such breakdown of BO approximation are JT [23] and RT [24] effects. The RT has been considered as the driving force behind bending instability of linear molecules in degenerate states [31]. Upon bending the molecule, an additional dipole moment is set up in the molecular plane which lifts the electronic degeneracy. In contrast to this, it was proved very recently that the RT effect in fact produces just a splitting of the degenerate term, but not any bending instability. All instabilities and distortions of linear molecules arise due to the mixing with appropriate excited electronic states which is called as the PJT effect [32].

The RT effect in triatomic molecules is extensively studied theoretically by perturbative treatment of the Hamiltonian when expanded in a Taylor series around the linear configuration [24–27]. While there are plethora of studies on the triatomic RT effect, studies on linear polyatomic molecules with atoms more than three, are very less. To the best of our knowledge carbon chains of upto 6 atom length were theoretically studied by including the RT [29, 30] effect. However perturbation theory is known to fail in strong coupling case and when the interacting states are very closely spaced. A quasi-diabatic-Hamiltonian is proposed by Köppel *et al.* to avoid the perturbative treatment of the RT [20, 28] intersections. On rigorous study, this model diabatic Hamiltonian is wide accepted by the scientific community.

This chapter is organized as follows. The details of electronic structure calculations are given in Sec 5.2. The vibronic Hamiltonian is derived in Sec 5.3 by considering the group theoretical approach. The topography of the adiabatic potential energy surfaces are presented in Sec. 5.4. While the theoretical absorption spectrum is discussed in Sec. 5.5, the internal conversion dynamics is discussed in Sec. 5.6.

5.2 Electronic structure calculations

The reference equilibrium geometry of the electronic ground state $S_0\,{}^1\Sigma_g^+$ of C_{15} is optimized by the B3LYP method employing the cc-pVDZ basis set of Dunning [35]. The geometry parameters are tabulated in Table 5.2 along with the literature data. Harmonic frequency (ω_i) of the vibrational modes of C_{15} is calculated by diagonalizing the kinematic and *ab initio* force constant matrix of the reference equilibrium structure. These vibrational frequencies (in eV units) are listed in the third column of Table 5.3. The mass-weighted normal coordinates of the vibrational modes are calculated from the eigenvectors of the force constant matrix. These are then transformed into their dimensionless form ($\mathbf{Q}_i$) by multiplying with $\sqrt{\omega}_i$ (in a_0) [36]. The fundamental vibrational modes of C_{15} decompose into thirteen degenerate and fourteen non degenerate symmetry species of the $D_{\infty h}$ symmetry point group. They transform into the following IREPs of this symmetry point group:

$$\Gamma \;=\; 7\sigma_g(\nu_1-\nu_7)\oplus 7\sigma_u(\nu_8-\nu_{14})\oplus 6\pi_g(\nu_{15}-\nu_{20})\oplus 7\pi_u(\nu_{21}-\nu_{27}). \qquad (5.1)$$

Table 5.2: Optimized equilibrium geometry parameters of the electronic ground state of C_{15}. The results available from the literature [33] are also included in the table for comparison. All units are given in

Parameter	B3LYP/cc-pVDZ [33]	B3LYP/cc-pVDZ This work	MP2/cc-pVDZ This work
R_{12}	1.29	1.29	1.32
R_{23}	1.30	1.30	1.31
R_{34}	1.28	1.27	1.29
R_{45}	1.29	1.29	1.30
R_{56}	1.28	1.28	1.30
R_{67}	1.29	1.29	1.30
R_{78}	1.28	1.28	1.30

The geometry optimization and calculation of the normal modes of vibrations are performed using G03 suit of *ab initio* programs [37]. Adiabatic energies of the low-lying singlet electronic states of C_{15} are calculated *ab initio* along the dimensionless normal coordinates of the 27 (altogether) vibrational degrees of freedom. The VEEs of these electronic states are calculated for $Q_i = \pm 0.10$ and in the range -3.0 to $+3.0$ with an increment 0.25, along i^{th} vibrational mode (keeping others at their equilibrium value) using the EOM-CCSD method as implemented in MOLPRO program package [38]. The excited state symbol, excitation energy and oscillator strength are given in Table 5.1.

5.3 Vibronic Hamiltonian

In this section we construct a Hamiltonian describing the vibronic interactions of $S_5{}^1\Pi_g$, $S_6{}^1\Pi_u$, $S_7{}^1\Sigma_u^+$ and $S_{12}{}^1\Sigma_g^+$ excited electronic states of C_{15} cluster in terms of the normal displacement coordinates of the reference electronic ground state of respective carbon chain, in accordance with the symmetry selection rules. The Hamiltonian is constructed in a diabatic electronic basis [20]. The molecular Hamiltonian in linear vibronic coupling scheme for E_{1g}, E_{1u}, A_{2u} and A_{1g} interacting electronic manifold for Benzene and HFBz are derived thoroughly by Köppel *et al.* and Mahapatra *et al.* [39–41]. In the analogous manner, the molecular Hamiltonian for interacting manifold of excited electronic states of odd numbered carbon chains can be written.

The first-order coupling within (intra) and between (inter) electronic states is governed by the selection rules; $(\Gamma_i)^2 \supset (\Gamma_{\sigma_g^+})$ and $\Gamma_i \otimes \Gamma_j \supset \Gamma_x$, respectively [20]. The symbol, Γ represents the IREP, i and j are the electronic state indices, σ_g^+ represents the totally symmetric vibrational mode and the symbol, x, represents the symmetry of the vibrational mode that transforms according to, $\Gamma_i \otimes \Gamma_x \otimes \Gamma_j \supset \Sigma_g^+$. Now for the degenerate, $S_5{}^1\Pi_g$ and $S_6{}^1\Pi_u$ electronic states the symmetrized direct product transforms into, $(\Pi_g)^2 = (\Pi_u)^2 = \Sigma_g^+ + \Delta_g$. While the vibrational modes of σ_g^+ symmetry can not split the electronic degeneracy (are condon active), and the lack of δ_g modes of symmetry that can lift this electronic degeneracy makes first order RT coupling vanish.

But the electronic degeneracy of Π_g and Π_u states is lifted by the π_g and π_u modes in second order. For the rest of the off-diagonal elements of the Hamiltonian written below the following symmetry rules apply. With the given symmetry representation of the electronic states and the vibrational modes [in Eq. (5.1)] of C_{15} the following rules can be derived from the character table of the $D_{\infty h}$ symmetry point group.

$$\begin{aligned}
\Pi_g \otimes \Pi_u &= \delta_u + \sigma_u^- + \sigma_u^+(8-14),\\
\Pi_g \otimes \Sigma_u^+ &= \pi_u(21-27),\\
\Pi_g \otimes \Sigma_g^+ &= \pi_g(15-20),\\
\Pi_u \otimes \Sigma_u^+ &= \pi_g(15-20),\\
\Pi_u \otimes \Sigma_g^+ &= \pi_u(21-27),\\
\Sigma_u^+ \otimes \Sigma_g^+ &= \sigma_u^+(8-14),
\end{aligned}$$

Where the numbers in the parentheses in the right hand side indicates the vibrational mode number given in Eq. 5.1. The relative sign of various elements of the Hamiltonian is determined by explicitly checking the invariance of the Hamiltonian with respect to the symmetry operations of the D_{6h} point group, following similar works on benzene and cyclopropane radical cation [39–41]. With these considerations the vibronic Hamiltonian can be written as

$$\mathcal{H} = \mathcal{H}_0 \mathbf{1_6} + \mathcal{W}, \tag{5.2a}$$

where

$$\mathcal{W} = \begin{bmatrix}
\mathcal{E}^5 + \mathcal{U}^{5x} & \sum\limits_{i\in\pi_u,\pi_g} \eta_i^{3x,3y} Q_{ix}Q_{iy} & \sum\limits_{i\in\sigma_u^+} \lambda_i^{3x,4x} Q_i & \sum\limits_{i\in\sigma_u^-} \lambda_i^{3x,4y} Q_i & \sum\limits_{i\in\pi_u} \lambda_i^{3x,7} Q_{ix} & \sum\limits_{i\in\pi_x} \lambda_i^{3x,8} Q_{ix} \\
 & \mathcal{E}^3 + \mathcal{U}^{3y} & \sum\limits_{i\in\sigma_u^-} \lambda_i^{3y,4x} Q_{iy} & \sum\limits_{i\in\sigma_u^+} \lambda_i^{3y,4y} Q_i & \sum\limits_{i\in\pi_u} \lambda_i^{3y,7} Q_{iy} & \sum\limits_{i\in\pi_g} \lambda_i^{3y,8} Q_{iy} \\
 & & \mathcal{E}^4 + \mathcal{U}^{4x} & \sum\limits_{i\in\pi_u,\pi_g} \eta_i^{4x,4y} Q_{ix}Q_{iy} & \sum\limits_{i\in\pi_g} \lambda_i^{4x,7} Q_{ix} & \sum\limits_{i\in\pi_g} \lambda_i^{4x,7} Q_{ix} \\
 & & & \mathcal{E}^{4y} + \mathcal{U}^{4y} & \sum\limits_{i\in\pi_g} \lambda_i^{4y,7} Q_{iy} & \sum\limits_{i\in\pi_g} \lambda_i^{4y,8} Q_{iy} \\
 & & h.c. & & \mathcal{E}^7 + \mathcal{U}^7 & \sum\limits_{i\in\sigma_u} \lambda_i^{7,8} Q_i \\
 & & & & & \mathcal{E}^8 + \mathcal{U}^8
\end{bmatrix} \tag{5.2b}$$

In the above, $\mathcal{H}_0 = \mathcal{T}_N + \mathcal{V}_0$, represents the Hamiltonian (assumed to be harmonic) of the reference electronic ground (S_0) state of C_{15} with

$$\mathcal{T}_N = -\frac{1}{2}\sum_{i\ \in\ \sigma_g^+,\ \sigma_u^-} \omega_i \frac{\partial^2}{\partial Q_i^2} - \frac{1}{2}\sum_{i\ \in\ \pi_g,\ \pi_u} \omega_i \left(\frac{\partial^2}{\partial Q_{ix}^2} + \frac{\partial^2}{\partial Q_{iy}^2}\right), \tag{5.3}$$

and

$$\mathcal{V}_0 = \frac{1}{2}\sum_{i\,\in\,\sigma_g^+,\,\sigma_u^-}\omega_i Q_i^2 + \frac{1}{2}\sum_{i\,\in\,\pi_g,\,\pi_u}\omega_i\left(Q_{ix}^2+Q_{iy}^2\right). \tag{5.4}$$

The quantity $\mathbf{1_6}$ is a 6×6 diagonal unit matrix. The nondiagonal matrix Hamiltonian in Eq. (5.2b) describes the PESs of the excited electronic states of C_{15} and their coupling surfaces. The quantity $\mathcal{E}^j$ in this matrix is the VEE of the j^{th} electronic state. The elements of this matrix are expanded in a standard Taylor series around the reference equilibrium geometry at, $\mathbf{Q}=\mathbf{0}$, in the following way

$$\mathcal{U}^j = \sum_{i\,\in\,\sigma_g^+}\kappa_i^j Q_i + \frac{1}{2}\sum_{i\,\in\,\sigma_g^+,\,\sigma_u^-}\gamma_i^j Q_i^2 + \frac{1}{2}\sum_{i\,\in\,\pi_g,\,\pi_u}[\gamma_i^j(Q_{ix}^2+Q_{iy}^2)] \tag{5.5a}$$

$$\mathcal{U}^{jx/jy} = \sum_{i\,\in\,\sigma_g^+}\kappa_i^j Q_i \pm \sum_{i\,\in\,\pi_g,\,\pi_u}\eta_i^j(Q_{ix}^2-Q_{iy}^2) + \frac{1}{2}\sum_{i\,\in\,\sigma_g^+,\,\sigma_u^-}\gamma_i^j Q_i^2 + \frac{1}{2}\sum_{i\,\in\,\pi_g,\,\pi_u}[\gamma_i^j(Q_{ix}^2+Q_{iy}^2)];$$
$$j\in 1 \text{ and } 2. \tag{5.5b}$$

In above equations the two components of the degenerate states and modes are labeled with x/y. The quantity κ_i^j and η_i^j represents the linear intrastate and quadratic RT coupling parameters [20] for the symmetric (σ_g^+) and degenerate (π_g,π_u) vibrational modes, respectively, for the j^{th} electronic state. The first-order PJT coupling parameter of the i^{th} vibrational mode between the electronic states j and k is given by λ_i^{j-k} and γ_i^j are the second-order parameters of the i^{th} vibrational mode for the j^{th} electronic state. The summations run over the normal modes of vibration of specified symmetry in the index. The + and - sign in Eq. (5.5b) is applicable to the x and y components of the degenerate state, respectively. The VEEs calculated in Sec. 5.2 are fitted to the adiabatic counterpart of diabatic electronic Hamiltonian of Eq. 5.2 by a least squares procedure to estimate the parameters of the Hamiltonian defined above. The estimated parameters along the relevant vibrational modes are given in Tables 5.3 and 5.4. A careful inspection of the coupling parameters suggests that not all 40 vibrational modes play significant role in the nuclear dynamics on the electronic states of C_n cluster considered in this chapter. Therefore, only the relevant modes having significant coupling strengths are retained in the nuclear dynamics study presented below.

Table 5.3: *Ab initio* calculated linear and quadratic coupling constants for the $S_5{}^1\Pi_g$, $S_6{}^1\Pi_u$, $S_7{}^1\Sigma_u^+$ and $S_{12}{}^1\Sigma_g^+$ electronic states of C_{15} cluster. All data are given in the eV unit.

Symm	Mode	Freq	κ_i or η_i	γ_i	κ_i or η_i	γ_i	κ_i	γ_i	κ_i	γ_i
			$S_5{}^1\Pi_g$		$S_6{}^1\Pi_u$		$S_7{}^1\Sigma_u^+$		$S_{12}{}^1\Sigma_g^+$	
σ_g^+	ν_1	0.2780	0.0956 (0.06)	-0.0110	0.0956 (0.06)	-0.0110	-0.0068 (0.00)	-0.0147	-0.0168 (0.00)	-0.0034
	ν_2	0.2748	0.2381 (0.37)	0.0397	0.2372 (0.37)	0.0409	0.0356 (0.01)	-0.0441	-0.0276 (0.01)	-0.0478
	ν_3	0.2549	0.1529 (0.18)	-0.0112	0.1523 (0.18)	-0.0119	0.0028 (0.00)	-0.0038	-0.0275 (0.01)	-0.0045
	ν_4	0.2175	-0.0854 (0.08)	-0.0038	-0.0851 (0.08)	-0.0038	0.0017 (0.00)	-0.0029	0.0192 (0.00)	-0.0020
	ν_5	0.1622	0.0483 (0.04)	-0.0006	0.0481 (0.04)	-0.0005	-0.0044 (0.00)	-0.0017	-0.0156 (0.01)	-0.0014
	ν_6	0.1014	0.0171 (0.01)	0.0002	0.0170 (0.01)	0.0002	-0.0077 (0.00)	-0.0012	-0.0190 (0.02)	-0.0004
	ν_7	0.0349	-0.0026 (0.00)	0.0001	-0.0026 (0.00)	0.0001	-0.0272 (0.30)	0.0001	-0.0221 (0.20)	0.0002
σ_u^+	ν_8	0.2802	-	-0.0153	-	-0.0151	-	-0.0193	-	-0.0080
	ν_9	0.2687	-	-0.0123	-	-0.0125		-0.0120	-	-0.0165
	ν_{10}	0.2481	-	-0.1746	-	-0.0186	-	-0.4697	-	0.0607
	ν_{11}	0.2386	-	-0.0352	-	0.0032	-	-0.0641	-	0.0150
	ν_{12}	0.1903	-	-0.0013	-	-0.0015	-	-0.0027	-	-0.0016
	ν_{13}	0.1325	-	-0.0001	-	-0.0001	-	-0.0014	-	-0.0013
	ν_{14}	0.0688	-	-0.0008	-	0.0012	-	-0.0020	-	0.0007
π_g	ν_{15}	0.0943	0.0095 (0.01)	-0.0096	-0.0074 (0.00)	-0.0137	-	-0.0015	-	-0.0057
	ν_{16}	0.0735	0.0083 (0.01)	-0.0055	-0.0069 (0.00)	-0.0101	-	-0.0049	-	-0.0073
	ν_{17}	0.0569	0.0078 (0.01)	-0.0061	-0.0076 (0.01)	-0.0072	-	-0.0073	-	-0.0094
	ν_{18}	0.0341	0.0007 (0.00)	0.0266	-0.0007 (0.00)	0.0305	-	-0.0028	-	-0.0021
	ν_{19}	0.0190	0.0004 (0.00)	0.0205	-0.0004 (0.00)	0.0209	-	-0.0046	-	-0.0060
	ν_{20}	0.0064	0.0003 (0.00)	0.0130	-0.0003 (0.00)	0.0129	-	-0.0054	-	-0.0073
π_u	ν_{21}	0.1063	0.0083 (0.00)	-0.0067	-0.0083 (0.00)	-0.0108	-	-0.0053	-	-0.0000
	ν_{22}	0.0838	0.0083 (0.01)	-0.0108	-0.0082 (0.01)	-0.0090	-	-0.0033	-	0.0000
	ν_{23}	0.0648	0.0077 (0.01)	-0.0074	-0.0077 (0.01)	-0.0054	-	-0.0061	-	-0.0091
	ν_{24}	0.0397	0.0017 (0.00)	0.0133	-0.0018 (0.00)	0.0195	-	-0.0072	-	-0.0031
	ν_{25}	0.0268	0.0014 (0.00)	0.0250	-0.0013 (0.00)	0.0267	-	-0.0039	-	-0.0057
	ν_{26}	0.0121	0.0007 (0.00)	0.0164	-0.0007 (0.00)	0.0165	-	-0.0049	-	-0.0065
	ν_{27}	0.0023	0.0001 (0.00)	0.0099	-0.0001 (0.00)	0.0098	-	-0.0070	-	-0.0090

Table 5.4: Interstate coupling parameters (in eV) of the vibronic Hamiltonian of Eq. 5.2 for the $S_5{}^1\Pi_g$, $S_6{}^1\Pi_u$, $S_7{}^1\Sigma_u^+$ and $S_{12}{}^1\Sigma_g^+$ electronic states of C_{15} cluster estimated from the *ab initio* electronic structure results (see text for details).

Mode	$\lambda_i^{1,2}$	$\lambda_i^{1,3}$	$\lambda_i^{1,4}$	$\lambda_i^{2,3}$	$\lambda_i^{2,4}$	$\lambda_i^{3,4}$
ν_8	0.1439 (0.13)	-	-	-	-	-
ν_9	0.1229 (0.10)	-	-	-	-	-
ν_{10}	0.1531 (0.20)	-	-	-	-	0.2227 (0.40)
ν_{11}	0.1653 (0.23)	-	-	-	-	-
ν_{12}	0.0662 (0.06)	-	-	-	-	0.0112 (0.00)
ν_{13}	0.0341 (0.03)	-	-	-	-	0.0039 (0.00)
ν_{14}	0.0058 (0.00)	-	-	-	-	0.0159 (0.03)
ν_{15}	-	-	0.0331 (0.06)	-	-	-
ν_{16}	-	-	0.0278 (0.07)	0.0190 (0.03)	-	-
ν_{17}	-	-	0.0234 (0.09)	-	-	-
ν_{18}	-	-	-	-	-	-
ν_{19}	-	-	-	-	-	-
ν_{20}	-	-	-	-	-	-
ν_{21}	-	0.0206 (0.02)	-	-	-	-
ν_{22}	-	0.0257 (0.20)	-	-	-	-
ν_{23}	-	0.0183 (0.04)	-	-	0.0206 (0.05)	-
ν_{24}	-	-	-	-	-	-
ν_{25}	-	-	-	-	-	-
ν_{26}	-	-	-	-	-	-
ν_{27}	-	-	-	-	-	-

5.4 Adiabatic potential energy surfaces

In this section we examine the topography of the adiabatic PESs of the four excited singlet electronic states $S_5{}^1\Pi_g$, $S_6{}^1\Pi_u$, $S_7{}^1\Sigma_u^+$ and $S_{12}{}^1\Sigma_g^+$ of C_{15} obtained by diagonalizing the electronic Hamiltonian of the diabatic model developed above. The nonradiative decay of the diabatic population of the $S_7{}^1\Sigma_u^+$ electronic state is calculated and found to depend strongly on the topography of the PESs.

According to the selection rules, given in Sec 5.3, the totally symmetric modes ν_1-ν_7 of C_{15} cannot split the degeneracy of $S_5{}^1\Pi_g$ and $S_6{}^1\Pi_u$ electronic states, while the degenerate bending π_g and π_u modes split the degeneracy of $S_5{}^1\Pi_g$ and $S_6{}^1\Pi_u$ electronic state. One dimensional cuts of the potential energy hypersurfaces of C_{15} are viewed along the given totally symmetric modes (σ_g^+) vibrational mode keeping others at their equilibrium values at, $\mathbf{Q}$=0, are shown in panels (a-g) of Fig. 5.1. In the figure the solid curves represent the adiabatic potential energy functions obtained from the model developed in Sec 5.3 and the points superimposed on them are obtained from *ab initio* quantum chemical calculations discussed in Sec. 5.2. It can be seen from Fig. 5.1 that the *ab initio* energies are very well reproduced by the model.

The energetic minimum of the seam of various CIs and the minimum of the upper adiabatic electronic states are estimated. The resulting data are collected in Table 5.5. The diagonal entries in this table are the energy at the minimum of a state. Whereas, the off-diagonal entries represent the minimum of the seam of CIs. The electronic states S_5 and S_6 are almost degenerate, they are just separated by $\sim$ 0.002 eV from each other. The minimum of S_5 -S_6 intersections is just $\sim$0.28 above the minimum of the upper adiabatic S_6 electronic state. From Table 5.4 it can be seen that interstate coupling between these states is moderately strong along ν_{10} and ν_{11} normal modes of vibrations of symmetry σ_u^+. Similarly the minimum of S_5 -S_7 CIs occurs just $\sim$0.04 eV above the minimum of S_7 electronic state and coupling between these states is facilitated by π_g modes with a strong coupling along ν_{11}. Hence the right wing of S_5 absorption band and the left wing of S_6 and S_7 absorption bands are expected to be strongly perturbed by the S_5 -S_6 and S_5 -S_7 interstate couplings, respectively. Similarly, the minimum of S_5 -S_{12} CIs is $\sim$0.14 eV above the minimum of S_5 electronic state. The interstate coupling between them is negligible. So, the non-adiabatic interactions between them can be safely ignored. As can be seen from the Table 5.5, the minimum of S_6 is just $\sim$0.04, $\sim$0.14 eV below it's CIs with the S_7 and S_{12} electronic states, respectively. The interstate coupling between S_6 -S_7 and S_6 -S_{12} electronic states is negligible (*cf.* Table 5.4). The minimum of S_7 -S_{12} CIs is $\sim$1.81 eV above the minimum of the upper adiabatic sheet of the S_{12} state. This separation is relatively high when compared to the remaining energetic positions discussed above. However, the strong coupling between S_7 -S_{12} makes the nonadiabatic interactions stronger in these coupled electronic states.

The RT effect lifts the degeneracy of S_5 and S_6 electronic states when the molecule is distorted along π_g (ν_{15}-ν_{20}) and π_u (ν_{21}-ν_{27}) normal coordinates of vibration in second order. Now let us consider the topography of S_5 and S_6 electronic states. The Hamiltonian for degenerate electronic state (S_5 or S_6) including only the π_g modes is given

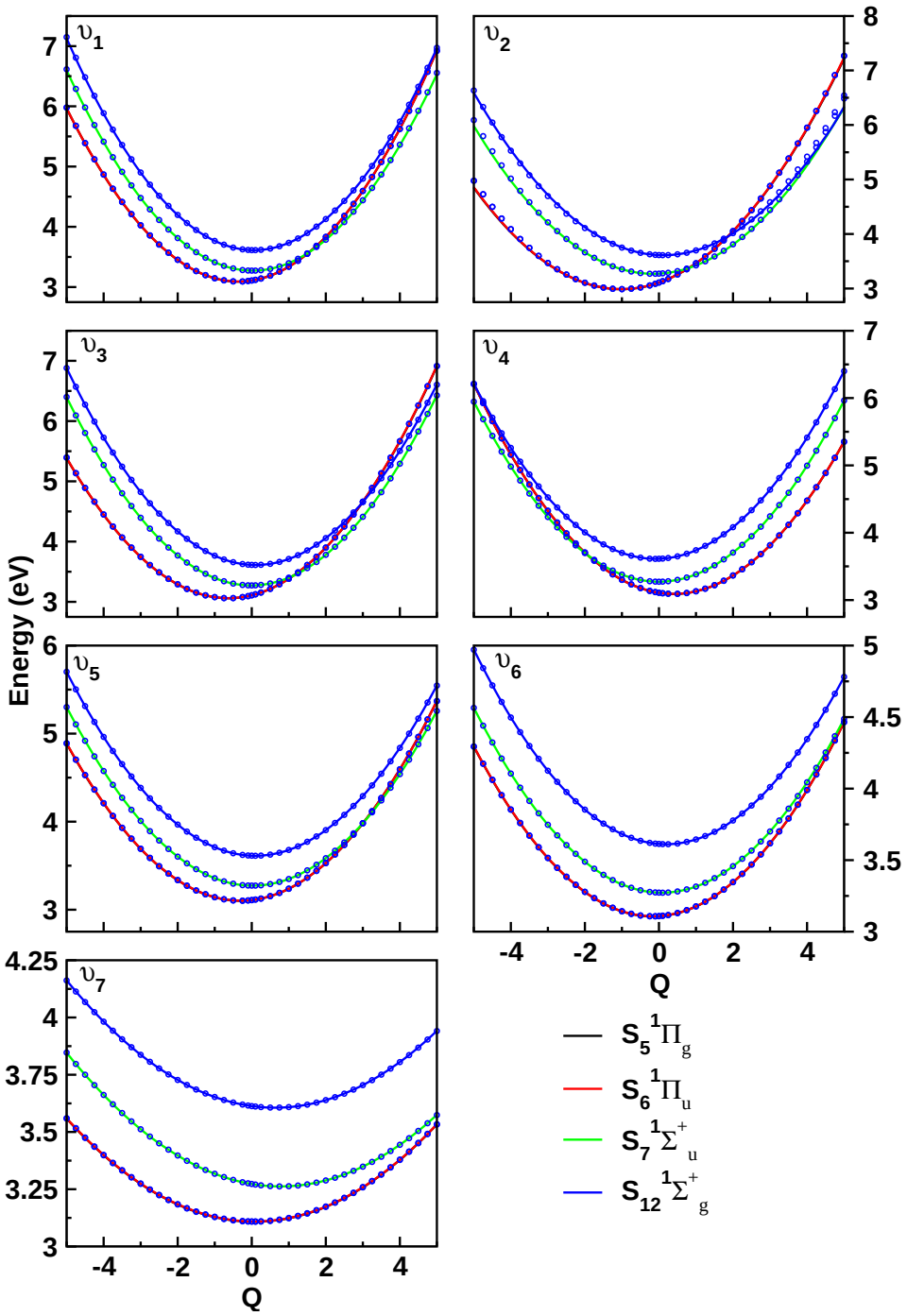

Figure 5.1: Adiabatic potential energies of the low-lying excited singlet electronic states of C_{15}, along the normal coordinates of totally symmetric vibrational modes. The potential energies obtained from the present vibronic model are shown by the solid lines and the computed *ab initio* energies are shown by the circles.

Table 5.5: Estimated equilibrium minimum (diagonal entries) and minimum of the seam of various CIs (off-diagonal entries) of the electronic states of C_{15} within a quadratic coupling model. All quantities are given in eV.

	$S_5\,^1\Pi_g$	$S_6\,^1\Pi_u$	$S_7\,^1\Sigma_u^+$	$S_{12}\,^1\Sigma_g^+$
$S_5\,^1\Pi_g$	2.89	3.17	3.30	3.74
$S_6\,^1\Pi_u$	-	2.89	3.30	3.74
$S_7\,^1\Sigma_u^+$	-	-	3.26	5.41
$S_{12}\,^1\Sigma_g^+$	-	-	-	3.60

as

$$\mathcal{H} = \begin{bmatrix} E + \frac{1}{2}(\omega+\gamma)(Q_x^2+Q_y^2) + \frac{1}{2}\eta(Q_x^2-Q_y^2) & \eta Q_x Q_y \\ \eta Q_x Q_y & E_1 + \frac{1}{2}(\omega+\gamma)(Q_x^2+Q_y^2) - \frac{1}{2}\eta(Q_x^2-Q_y^2) \end{bmatrix}$$

Diagonalization the above diabatic Hamiltonian results adiabatic PESs

$$V_{\pm} = E + \frac{1}{2}(\omega+\gamma-\eta)(Q_x^2+Q_y^2)$$

Minimization of V_- with respect to Q_x suggest V_- is minimum or maximum (at Q_x=0) depending on whether the quantity $\omega+\gamma-\eta$ is greater or less than zero. From the above expression, it is quite clear that RT effect can not induce a new minimum for the degenerate electronic state (S_5 or S_6) and it can not explain the bent geometries of the excited states of the linear polyatomic molecules unless strong anharmonicity terms are presented in the PESs [32].

To explain the bent geometries of the excited states, one has to resort to $\Pi-\Sigma$ coupling mechanism. To obtain the adiabatic PES of C_{15} along π_g mode, one needs to diagonalize the Hamiltonian 5.2b containing only the x components of π_g mode. The analytical expression for the resultant PESs are given in Eq. 5.7 and are plotted in Fig. 5.2. Similarly the one dimensional cuts of the adiabatic PESs of electronic states of C_{15} along π_u vibrational normal coordinates are given in Eq. 5.8 and are plotted in Fig. 5.3.

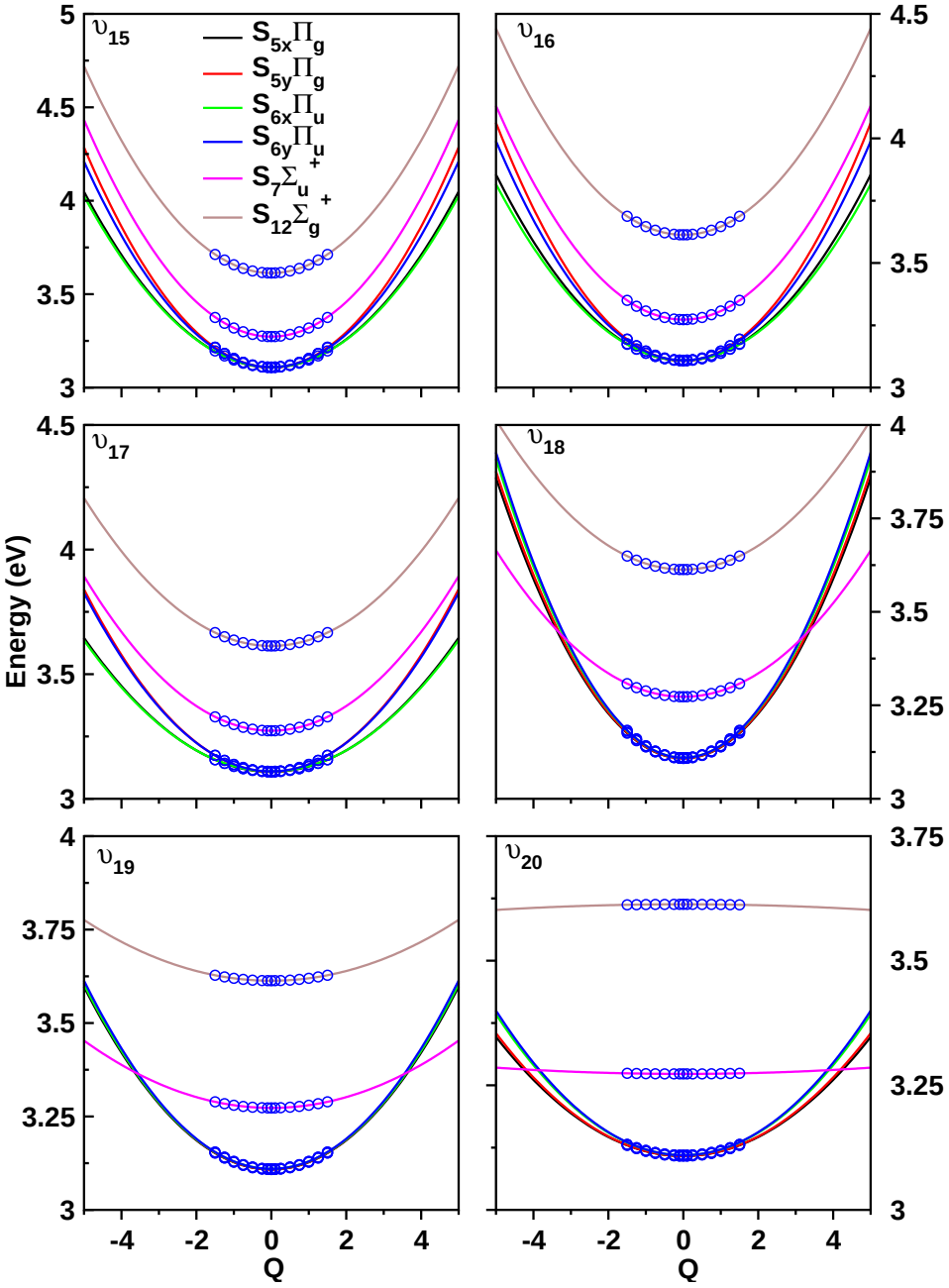

Figure 5.2: Adiabatic potential energies of S_5 , S_6 , S_7 and S_{12} electronic states of C_{15}, along the normal coordinates of degenerate bending π_g vibrational modes. The potential energies obtained from the present vibronic model are shown by the solid lines and the computed *ab initio* energies are shown by the circles.

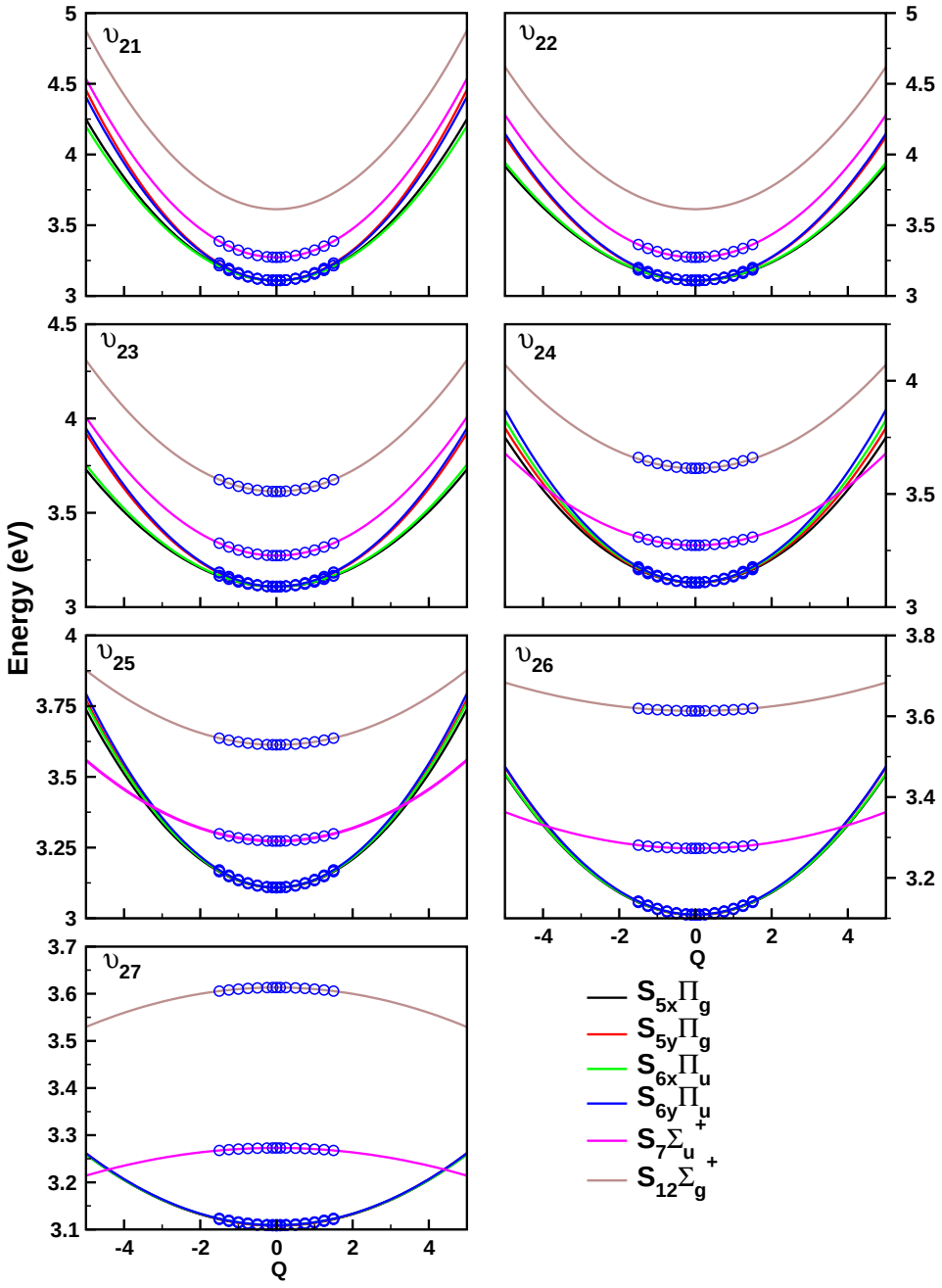

Figure 5.3: Same as Fig. 5.2 for C_{15} along π_u modes.

$$\mathcal{W} = \begin{bmatrix} \mathcal{E}^5 + \frac{1}{2}(\omega_i + \gamma_i^5 + \eta^5)Q_{ix}^2 & 0 & 0 & 0 & 0 & \lambda_i^{5x,12}Q_{ix} \\ 0 & \mathcal{E}^5 + \frac{1}{2}(\omega_i + \gamma_i^5 - \eta_i^5)Q_{ix}^2 & 0 & 0 & 0 & 0 \\ 0 & 0 & \mathcal{E}^6 + \frac{1}{2}(\omega_i + \gamma_i^6 + \eta_i^6)Q_{ix}^2 & 0 & \lambda_i^{6x,7}Q_{ix} & 0 \\ 0 & 0 & 0 & \mathcal{E}^6 + \frac{1}{2}(\omega_i + \gamma_i^6 - \eta_i^6)Q_{ix}^2 & 0 & 0 \\ 0 & 0 & \lambda_i^{6x,7}Q_{ix} & 0 & \mathcal{E}^7 + \frac{1}{2}(\omega_i + \gamma_i^7)Q_{ix}^2 & 0 \\ \lambda_i^{5x,12}Q_{ix} & 0 & 0 & 0 & 0 & \mathcal{E}^{12} + \frac{1}{2}(\omega_i + \gamma_i^{12})Q_{ix}^2 \end{bmatrix} \tag{5.6}$$

This is a $6 \otimes 6$ matrix. By diagonalizing this matrix we will get 6 equations. They are

$$\begin{aligned} V_1 &= \mathcal{E}^5 + \frac{1}{2}(\omega_i + \gamma_i^5 - \eta_i^5)Q_{ix}^2 \\ V_2 &= \mathcal{E}^6 + \frac{1}{2}(\omega_i + \gamma_i^6 - \eta_i^6)Q_{ix}^2 \\ V_{3\pm} &= \frac{\mathcal{E}^5 + \mathcal{E}^{12}}{2} + \frac{2\omega_i + \gamma_i^5 + \eta_i^5 + \gamma_i^{12}}{4}Q_{ix}^2 \pm \sqrt{\left(\frac{\mathcal{E}^{12} - \mathcal{E}^5}{2} + \frac{\gamma_i^{12} - \gamma_i^5 - \eta^5}{4}Q_{ix}^2\right)^2 + (\lambda^{5x,12}Q_{ix})^2} \\ V_{4\pm} &= \frac{\mathcal{E}^6 + \mathcal{E}^7}{2} + \frac{2\omega_i + \gamma_i^6 + \eta_i^6 + \gamma_i^7}{4}Q_{ix}^2 \pm \sqrt{\left(\frac{\mathcal{E}^7 - \mathcal{E}^6}{2} + \frac{\gamma_i^7 - \gamma_i^6 - \eta_i^6}{4}Q_{ix}^2\right)^2 + (\lambda_i^{6x,7}Q_{ix})^2} \end{aligned} \tag{5.7}$$

Similarly the adiabatic PESs along π_u modes obtained by the following equations

$$\begin{aligned} V_1 &= \mathcal{E}^5 + \frac{1}{2}(\omega_i + \gamma_i^5 - \eta_i^5)Q_{ix}^2 \\ V_2 &= \mathcal{E}^6 + \frac{1}{2}(\omega_i + \gamma_i^6 - \eta_i^6)Q_{ix}^2 \\ V_{3\pm} &= \frac{\mathcal{E}^5 + \mathcal{E}^7}{2} + \frac{2\omega_i + \gamma_i^5 + \eta_i^5 + \gamma_i^7}{4}Q_{ix}^2 \pm \sqrt{\left(\frac{\mathcal{E}^7 - \mathcal{E}^5}{2} + \frac{\gamma_i^7 - \gamma_i^5 - \eta^5}{4}Q_{ix}^2\right)^2 + (\lambda^{5x,7}Q_{ix})^2} \\ V_{4\pm} &= \frac{\mathcal{E}^6 + \mathcal{E}^{12}}{2} + \frac{2\omega_i + \gamma_i^6 + \eta_i^6 + \gamma_i^{12}}{4}Q_{ix}^2 \pm \sqrt{\left(\frac{\mathcal{E}^{12} - \mathcal{E}^6}{2} + \frac{\gamma_i^{12} - \gamma_i^6 - \eta_i^6}{4}Q_{ix}^2\right)^2 + (\lambda_i^{6x,12}Q_{ix})^2} \end{aligned} \tag{5.8}$$

Since we found quadratic RT coupling parameters are very small and do not induce a new minimum, here we neglect them in Eq. 5.7

$$V_{3-} = \frac{\mathcal{E}^1 + \mathcal{E}^4}{2} + \frac{1}{2}\omega Q_x^2 \pm \sqrt{\left(\frac{\mathcal{E}^4 - \mathcal{E}^1}{2}\right)^2 + (\lambda^{1x,4} Q_x)^2}$$

Differentiation of V_{3-} with respect to Q_x, yield a minimum at

$$Q_x = \sqrt{\left(\frac{(\lambda^{1x,4})^2}{\omega^2} - \left(\frac{\mathcal{E}^4 - \mathcal{E}^1}{2\lambda}\right)^2\right)}$$

provided the following condition is satisfied

$$2(\lambda^{(1x,4)})^2 > \omega(\mathcal{E}^4 - \mathcal{E}^1).$$

5.5 Absorption spectrum

Vibronic energy levels of the $S_5{}^1\Pi_g$, $S_6{}^1\Pi_u$, $S_7{}^1\Sigma_u^+$ and $S_{12}{}^1\Sigma_g^+$ electronic states of C_{15} are shown and discussed here. These are calculated by the quantum mechanical methods described in Chapter 2 using the parameters of Tables 5.3-5.4. To start with, we construct various reduced dimensional models and examine the vibrational energy levels of each of these electronic states by excluding the PJT coupling with their neighbors. These results help us to understand the role of various vibrational modes and electronic states in the complex vibronic structures of C_{15}. The final simulation of nuclear dynamics is, however, carried out by including all relevant couplings of the Hamiltonian and propagating wave packets using the MCTDH suite of programs [12–15] to elucidate the nonadiabatic coupling effects on the spectral envelopes. The theoretical results are finally compared with the available experimental absorption spectrum of C_{15} [34].

In the uncoupled states situation and in absence of any intermode coupling terms, the Hamiltonian for the $S_5{}^1\Pi_g$ and $S_6{}^1\Pi_u$ states are separable in terms of the σ_g^+, π_g and π_u vibrational modes. One can therefore calculate partial spectra separately for the σ_g^+, π_g and π_u and convolute them to generate the complete spectrum, for these degenerate electronic states. Such a separation reduces the dimension of the secular matrix and facilitates the numerical computation. The vibronic energy level spectrum of the $S_5{}^1\Pi_g$ electronic state is shown in Fig. 5.4. The partial spectra of σ_g^+, π_g and π_u vibrational modes are shown in panels a and b, respectively. The results of convolution of the three partial spectra are shown in panel c. The vibronic energy eigenvalues are obtained by diagonalizing the Hamiltonian matrix using the Lanczos algorithm [42] and are shown as the stick lines in the figure. The envelopes are obtained by convoluting these stick lines with a Lorentzian function with a FWHM of 10 meV. Further details of the calculations are given in Table 5.6. The partial spectrum of the π_g and π_u (panel b) is essentially structureless because of their weak RT coupling (Since RT coupling is quadratic and

weak, it is expected not to contribute much to the spectrum except giving a small shift to the energies). The vibrational modes (panel a), ν_1-ν_7 form progressions and the peaks are ∼2197, ∼2050, ∼2010, ∼1739, ∼1306, ∼819 and ∼282 cm^{-1}, respectively spaced in energy corresponding to the frequencies of these vibrational modes (cf., Table 5.3). The vibrational modes ν_2 and ν_3 forms dominant progression in the band. Very weak fundamental transition due to the bending modes is observed in the spectrum of π_g and π_u modes.

Similar spectra for the RT split $S_6\,^1\Pi_u$ electronic manifold of C_{15} are shown in Fig. 5.5 (a-c). The coupling parameters (see Table 5.3) suggests the vibrational progressions in the $S_6\,^1\Pi_u$ electronic state are very similar to the $S_5\,^1\Pi_g$ electronic state. The vibrational modes ν_2 and ν_3 forms dominant progressions with energy spacings ∼2045 and ∼2007 cm^{-1}, respectively. The excitations from the bending (π_g and π_u) modes is very weak.

The vibrational structure of the S_7 electronic state in absence of coupling with its neighboring states is shown in panel a and the resolved 355 nm experimental recording of Ref [34] is shown in panel b of Fig. 5.6. It can be seen in comparison that the theoretical results are in very good agreement with the experimental band structure of the S_7 state. From the data given in Table 5.3, the excitation of vibrational modes ν_3, ν_4 and ν_5 can be expected in this band. The excitation of the ν_3, ν_5 modes is stronger than that of ν_4. Line spacings of ~ 607, ~ 429 and ~ 288 cm^{-1} corresponding to the frequency of these modes, respectively, are extracted from the theoretical spectrum. Similarly, the spectrum of $S_{12}\,^1\Sigma_g^+$ electronic state is shown in Fig. 5.7 reveals progressions ∼286 and ∼816 cm^{-1} along the vibrational modes ν_6 and ν_5, respectively.

So far we did not consider the PJT coupling of various electronic states in the numerical calculations. On inclusion of this coupling, the separation of the Hamiltonian in terms of the symmetric and degenerate vibrational modes for the degenerate electronic states as explored above is no longer possible. It is therefore necessary to follow the nuclear dynamics simultaneously on six coupled electronic states (four from the two RT split S_5 and S_6 states plus two non degenerate S_7 and S_{12} electronic states) including all relevant vibrational degrees of freedom. Computationally, it turns out to be a daunting task to simulate the nuclear dynamics quantum mechanically by the matrix diagonalization approach employed above. We therefore resort to the MCTDH algorithm [12–15], and propagate WPs on six coupled electronic states including all vibrational degrees of freedom in order to arrive at the desired goal. Even with MCTDH, simulations with 40 vibrational modes is not possible. By looking at the coupling strength of the vibrational modes in Tables 5.3 and 5.4, it is clear that, not all the vibrational modes are important in the nuclear dynamics simulations. We selected thirty vibrational modes (including x and y components of the degenerate vibrational modes) on the basis of the coupling strength. The thirty vibrational degrees of freedom are grouped into four three dimensional particles. The combination scheme of the vibrational modes is given in Table 5.7, along with the sizes of the primitive and SPF bases. The parameters documented in Table 5.7 are optimally chosen to ensure the numerical convergence of the vibronic bands shown in Fig. 5.8. The WP in each calculation is propagated for 200 fs. Fig. 5.8 displays the present theoretical absorption bands of C_{15} in the energy range ∼3-4 eV. The theoretical results of 5.8 are obtained by including the coupling

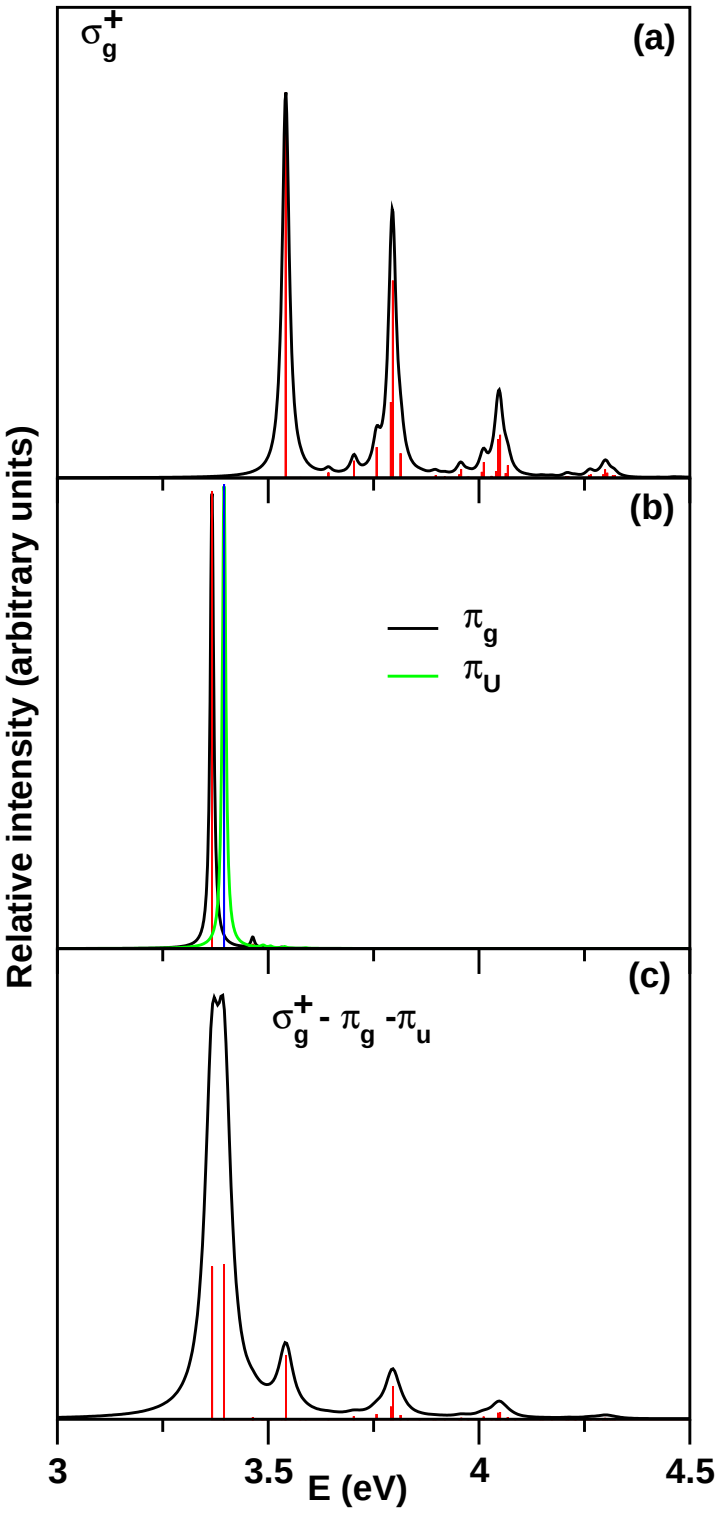

Figure 5.4: The stick vibronic spectra and their convoluted envelopes for the $S_5{}^1\Pi_g$ electronic state of C_{15} calculated with σ_g^+, π_g and π_u modes (indicated in the panel) plotted in panels a and b respectively. The composite spectrum of $S_5{}^1\Pi_g$ by including all the above modes is given in panel c.

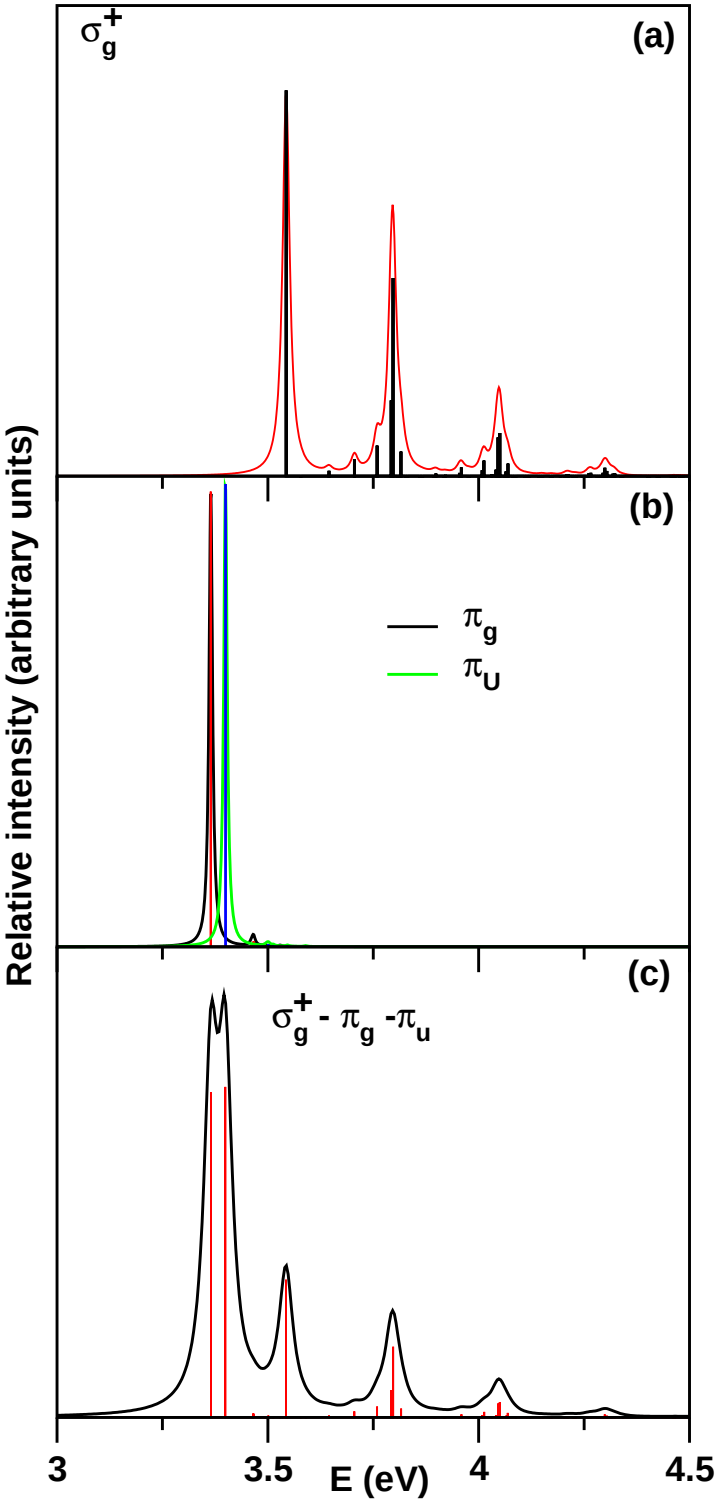

Figure 5.5: Similar as Fig. 5.4 for $S_6{}^1\Pi_u$ electronic state.

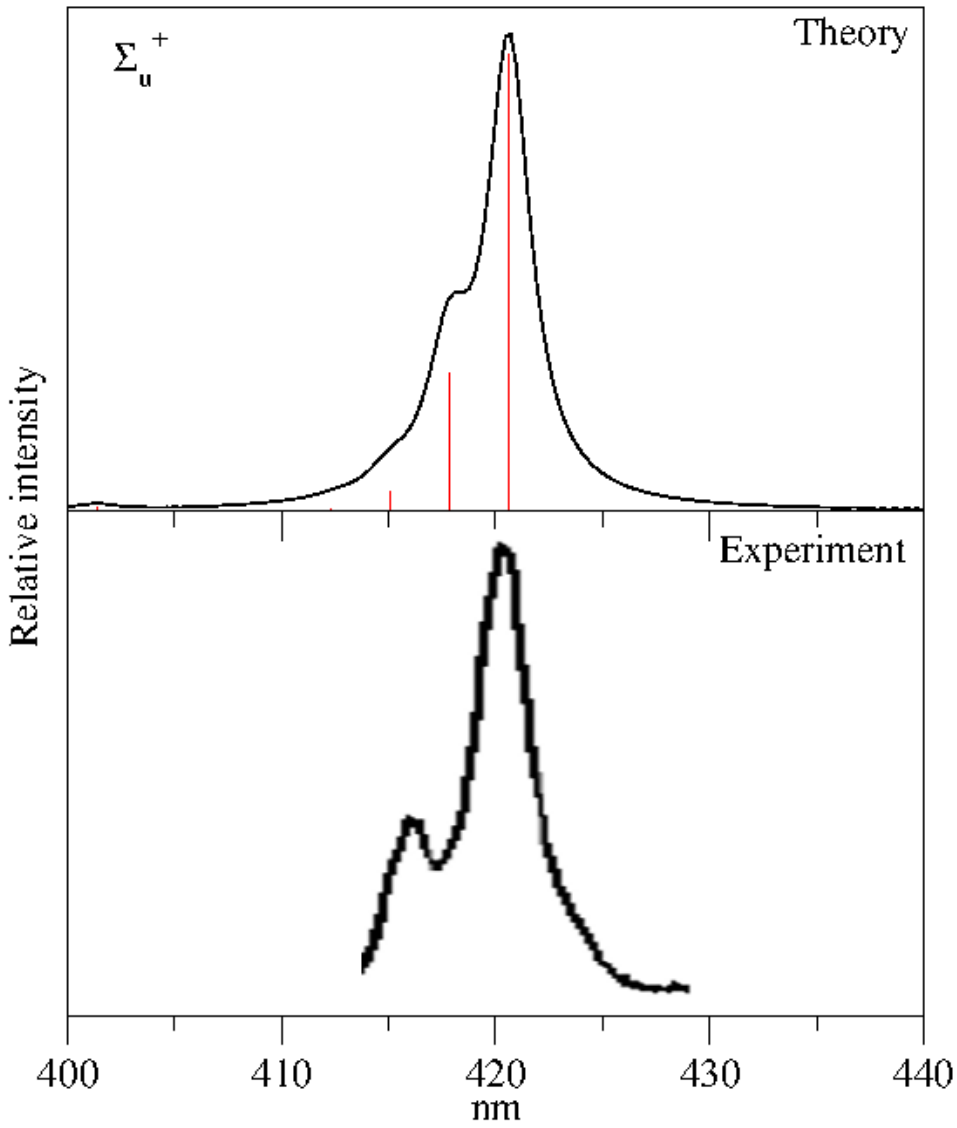

Figure 5.6: The stick vibronic spectrum and the convoluted envelope of the $S_7\,^1\Sigma_u^+$ electronic state of C_{15} calculated with the σ_g^+ vibrational modes plotted in panel a. The 355 nm experimental spectrum is reproduced from Ref. [34] and shown in panel b.

among the states. Six WP propagations in the coupled S_5 -S_6 -S_7 -S_{12} electronic manifold are carried out by initially preparing the WP separately on each of the component state of this manifold. Finally, results from these six calculations are combined. The resulting time autocorrelation function is damped with an exponential function $e^{\frac{-t}{\tau}}$ with τ=66 fs (which corresponds to a 20 meV FWHM Lorentzian function) before Fourier transformation to generate the spectral envelopes of Fig. 5.8.

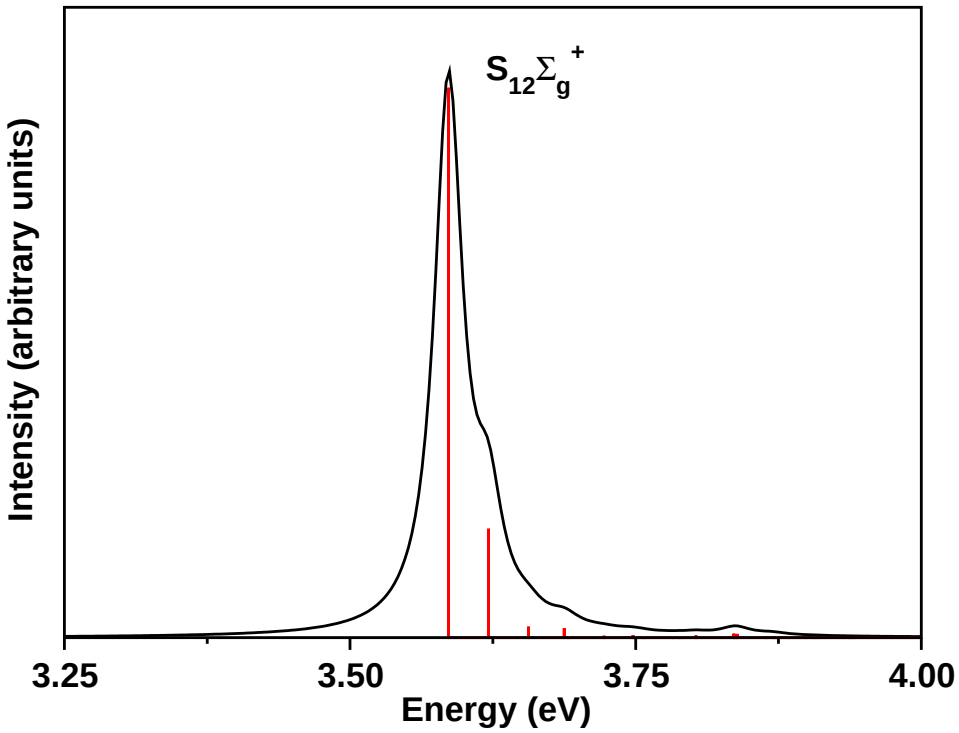

Figure 5.7: Same as Fig. 5.6 for electronic state $S_{12}{}^1\Sigma_g^+$.

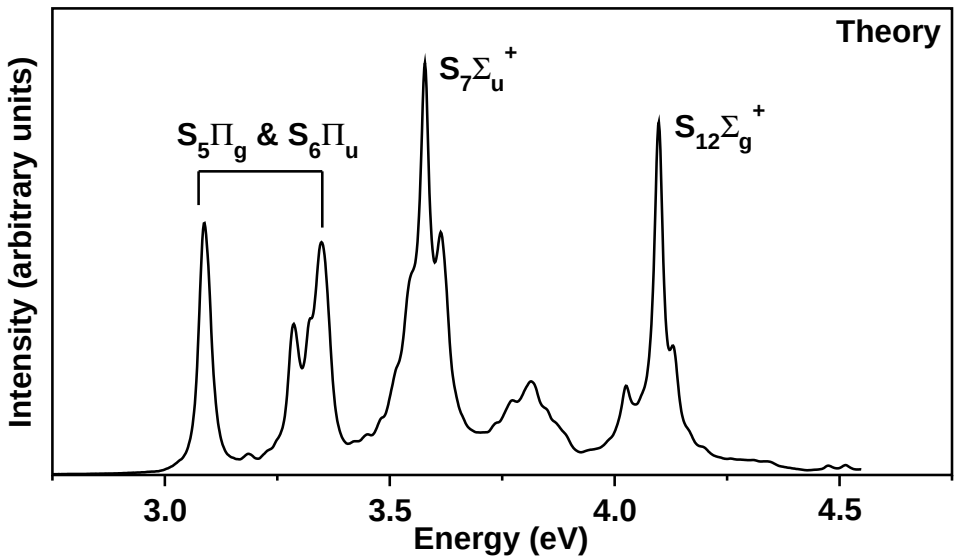

Figure 5.8: The absorption bands of C_{15} obtained from the coupled state dynamics study (see text for details). The intensity in arbitrary units is plotted as as function of the energy of the final vibronic states.

Table 5.6: The number of HO basis functions along with the vibrational mode and the dimension of the secular matrix used in the calculation of the stick vibronic spectra shown in various figures noted below.

Vibrational modes	No. of HO basis	Dimension of secular matrix	Figure(s)
ν_1, ν_2,ν_3,ν_4,ν_5,ν_6,ν_7	8,25,15,8,8,4,4	3072000	5.4 (a)
ν_{15},ν_{16},ν_{17},ν_{18}	8,8,8,8	16777216	5.4 (b)
ν_{21},ν_{22},ν_{23},ν_{24}	8,8,8,8	16777216	5.4 (b)
ν_1, ν_2,ν_3,ν_4,ν_5,ν_6,ν_7	8,25,15,8,8,4,4	3072000	5.5 (a)
ν_{15},ν_{16},ν_{17},ν_{18}	8,8,8,8	16777216	5.5 (b)
ν_{21},ν_{22},ν_{23},ν_{24}	8,8,8,8	16777216	5.5 (b)
ν_1, ν_2,ν_3,ν_4,ν_5,ν_6,ν_7	30,8,8,8,8,8,8	7864320	5.6 (a)
ν_1, ν_2,ν_3,ν_4,ν_5,ν_6,ν_7	30,6,6,6,6,6,6	1399680	5.7

Table 5.7: Normal mode combinations, sizes of the primitive and the single particle basis used in the WP propagation within the MCTDH framework in the six coupled electronic manifold using the complete vibronic Hamiltonian of Eq. (5.2b). First column denotes the vibrational DOF which are combined to particles. Second column gives the number of primitive basis functions for each DOF. Third column gives the number of SPFs for each electronic state.

Normal modes	Primitive basis	SPF basis
ν_1,ν_6,ν_{11},ν_{15y},ν_{16y},ν_{23y}	(6,6,6,6,6,6)	[8,8,8,8,8,8]
ν_2,ν_7,ν_{12},ν_{18x},ν_{17y},ν_{22y}	(6,6,6,6,6,6)	[8,8,8,8,8,8]
ν_3,ν_8,ν_{13},ν_{17x},ν_{v18y},ν_{21y}	(6,6,6,6,6,6)	[8,8,8,8,8,8]
ν_4,ν_9,ν_{14},ν_{16x},ν_{21x},ν_{24x}	(6,6,6,6,6,6)	[8,8,8,8,8,8]
ν_5,ν_{10},ν_{15x},ν_{20x},ν_{23x},ν_{24y}	(6,6,6,6,6,6)	[8,8,8,8,8,8]

5.6 Internal conversion dynamics

As stated in the introduction, the lifetime of the $S_7{}^1\Sigma_u^+$ excited electronic state of C_{15} is of importance for it to qualify as a potential DIB carrier. To be a good carrier for DIBs, the nonradiative decay of the diabatic population of $S_7{}^1\Sigma_u^+$ electronic state is expected [11] be around 70-200 fs. Here in this section, we present the time-dependence of the diabatic electronic populations in the S_5 -S_6 -S_7 -S_{12} electronic states. In order to calculate the latter we recorded the time-dependence of the diabatic electronic populations for an initial transition to each of the above electronic states separately. The results are shown in Fig. 5.9 (a-d). Interesting observations on the dynamical mechanism can be obtained from these population curves in conjunction with the coupling parameters given in Tables 5.3 and 5.4 and the stationary points on the PESs detailed in Section 5.4.

In panel a, the population dynamics is shown for an initial transition of the WP to one of the two RT split components of the $S_5{}^1\Pi_g$ electronic state. In contrast to the well-

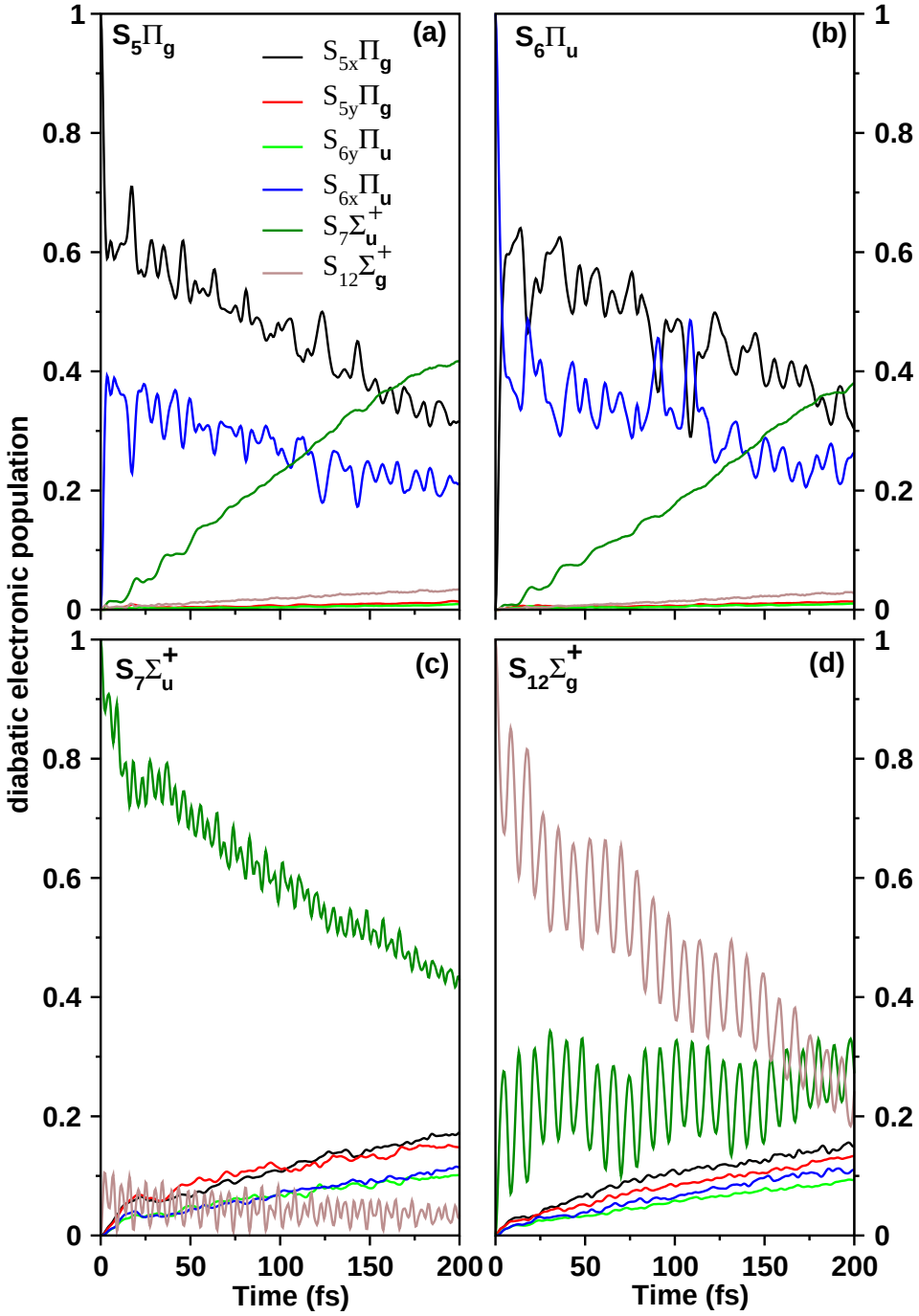

Figure 5.9: The time-dependence of diabatic electronic populations in the S_5 -S_6 -S_7 -S_{12} coupled states nuclear dynamics of C_{15}. The results obtained by initially locating the WP on the x and y components of S_5 and S_6 states and S_7 and S_{12} states are shown in panels (a-d), respectively.

known JT effect where the decay and growth of the population of x and y components of the degenerate electronic can be seen, the population transfer to the counter component is very minimal in the RT case. This is due to the small RT coupling found in the $S_5{}^1\Pi_g$ and $S_6{}^1\Pi_u$ electronic states. The $S_5{}^1\Pi_g$ and $S_6{}^1\Pi_u$ electronic states are coupled by σ_u^+ modes and it can be seen from the Table 5.4 that this coupling is strong along ν_{10} and ν_{11} vibrational modes. From Table 5.5, it can be seen that the location of the energetic minimum of S_5 -S_6 and S_5 -S_7 CIs lie just ∼0.33 eV and ∼0.40 eV above the minimum of the S_5 electronic state. Hence population transfer to S_6 and S_7 state is expected in this case. The decay of population of the x component of S_5 state and the growth of the S_6 (x component) and S_7 state population can be clearly seen from the diagram (panel a). The population of S_{12} electronic state show only minor variations in this case as the minimum of S_5 -S_{12} CIs lie ∼0.84 eV above the minimum of S_5 electronic state and they are weakly coupled. It is therefore clear that the electronic nonadiabatic dynamics in this situation is predominantly governed by the PJT coupling with S_6 and S_7 electronic states. The initial decay of the population of the $S_5{}^1\Pi_g$ state relates to a decay rate of ∼56 fs.

Panel b of Fig. 5.9 portrays the population dynamics when the WP is initially prepared on the x component of S_6 state. The S_5 and S_6 states are nearly degenerate at the vertical configuration. The initial depletion of the diabatic electronic population of S_6 state amounts to a nonradiative decay rate of ∼ 25 fs. It can be seen that the decay of the S_6 population mainly contributes to the growth of the population of x component of the S_5 state and S_7 state. This reflects that the coupling of the S_6 state with S_5 and S_7 states is much stronger (cf., Table 5.4) than the RT coupling within the S_6 state.

The population dynamics of the WP initially prepared on the S_7 is shown in panel c. In this case the electronic diabatic population of S_7 state transfers to S_5 and S_6 electronic states. The decay rate of the S_7 electronic state are estimated to be ∼ 110 fs. This population decay is indeed within the proposed range of ∼70-200 fs [10, 11]. It is already stated that while the PJT coupling between S_5 and S_7 states is strong, the PJT coupling between S_6 and S_7 electronic states is weak. The minimum of S_5 -S_7 and S_6 -S_7 are just ∼0.04 eV above the minimum of S_7 electronic state. Hence the population of the S_7 state is expected to transfer to S_5 state. The S_5 state in-turn coupled strongly to S_6 state via σ_u^+ modes. A population transfer to S_6 state from S_7 state can also be seen.

Finally, the electronic population dynamics for an initial propagation of the WP on S_{12} state is shown in panel d. It can be seen that the S_{12} state decays at a much faster rate ∼ 63 fs compared to the S_7 state. This is due to the relatively stronger PJT coupling between the S_7 -S_{12} states. Only minor population transfer takes place to the S_5 and S_6 coupled electronic manifold in this case

5.7 Summary

A detailed theoretical account of the multimode RT and PJT interactions in some selected electronic states of linear C_{15} cluster is presented here to elucidate the lifetimes of its excited electronic state $S_7{}^1\Sigma_u^+$. The vibronic Hamiltonian is constructed in a diabatic

electronic basis, including the RT coupling within the degenerate S_5 and S_6 electronic states and the PJT couplings of these RT split states with the nondegenerate S_7 and S_{12} electronic states of C_{15}. The coupling parameters of the vibronic Hamiltonian are determined by calculating the adiabatic PESs of the $S_5\,^1\Pi_g$, $S_6\,^1\Pi_u$, $S_7\,^1\Sigma_u^+$ and $S_{12}\,^1\Sigma_g^+$ electronic states along each of the 40 vibrational modes. First principles nuclear dynamics calculations are carried out both via time-independent and time-dependent quantum mechanical methods to simulate the nonadiabatic nuclear motion on the coupled manifold of these electronic states. The theoretical results are found to be in good accord with the available experimental results. The final theoretical simulations using the full Hamiltonian of Eqs. 5.2-5.5b can only be carried out by propagating WPs employing the MCTDH algorithm [12–15]. A careful examination of various theoretical results enabled us to arrive at the following conclusions. The RT effect in the S_5 and S_6 electronic states of C_{15} is very weak. The PJT coupling between the S_5 and S_6 dominates the RT coupling. Due to the clustering of the four excited states within $\sim$ 1.0 eV, the nonradiative processes are found to be dominanting in predicting the vibronic structure and the transfer of diabatic electronic population among these states. The initial decay of the diabatic population of $S_7\,^1\Sigma_u^+$ is estimated to be $\sim$110 fs, which lie in the much anticipated range $\sim$70-200 fs [10, 11].

References

[1] T. P. Snow and B. J. McCall, Annu. Rev. Astron. Astrophys **44**, 367, (2006).

[2] W. H. Smith, T. P. Snow and D. G. York, Astrophys. J. **218**, 124 (1977).

[3] A. E. Douglas. Nature **269** 130 (1997).

[4] W. Huggins, Proc. R. Soc. Landon **33**, 1 (1982); G. Herzberg, Astophys. J. **96**, 314 (1942).

[5] W. Weltner, Jr. and R. J. van Zee, Chem. Rev. **89**, 1713 (1989).

[6] A. V. Orden and R. J. Saykally, Chem. Rev. **98**, 2313 (1998).

[7] J. P. Maier Chem. Soc. Rev. **17**, 45, (1988).

[8] J. P. Maier Chem. Soc. Rev. **26**, 21, (1997).

[9] J. P. Maier J. Phys. Chem. A **102** 3462 (1998).

[10] E. B. Jochnowitz and J. P. Maier, Annu. Rev. Phys. Chem. **59**, 519 (2008).

[11] C. A. Rice and J. P. Maier, J. Phys. Chem. A **117**, 5559 (2013).

[12] G. A. Worth, M. H. Beck, A. Jäckle, and H. -D. Meyer, The MCTDH Package, Version 8.2, (2000), University of Heidelberg, Heidelberg, Germany. H. -D. Meyer, Version 8.3 (2002), Version 8.4 (2007). See http://mctdh.uni-hd.de.

[13] H. -D. Meyer, U. Manthe, and L. S. Cederbaum, Chem. Phys. Lett. **165**, 73 (1990).

[14] U. Manthe, H. -D. Meyer, and L. S. Cederbaum, J. Chem. Phys. **97**, 3199 (1992).

[15] M. H. Beck, A. Jäckle, G. A. Worth, and H. -D. Meyer, Phys. Rep. **324**, 1 (2000).

[16] M. Born and R. Oppenheimer, Ann. Phys. **84**, 457 (1927).

[17] C. J. Ballhausen and A. E. Hansen, Ann. Rev. Phys. Chem. **23**, 15 (1972).

[18] R. Englman, The Jahn-Teller Effect, (Wiley, New York, 1972).

[19] M. Baer, Beyond Born-Oppenheimer:electronic non-adiabatic coupling terms and conical intersections, (John Wiley and Sons, 2006).

[20] H. Köppel, W. Domcke and L. S. Cederbaum, *Adv. Chem. Phys.* **57**, 59 (1984).

[21] S. Mahapatra, Acc. Chem. Res. **42**, 1004 (2009).

[22] Conical Intersections: Electronic Structure, Dynamics and Spectroscopy, edited by W. Domcke, D. R. Yarkony, and H. Köppel (World Scientific, Singapore, 2004).

[23] H. A. Jahn and E. Teller, Proc. R. Soc. London, Ser. A **161**, 220. (1937).

[24] R. Renner, Z. Physik **92**, 172 (1934).

[25] J. A. Pople, Mol. Phys.**3**, 16, (1960).

[26] A. J. Merer and D. N. Travis, Can. J. Phys. **43**, 1795 (1965).

[27] J. A. Pople and H. C. Louguet-Higgins, Mol. Phys. **1**, 372 (1958).

[28] H. Köppel, W. Domcke and L. S. Cederbaum, J. Chem. Phys. **74**, 2945 (1991).

[29] M. Perić, M. Petković and S. Jerosimić, Chem. Phys. **343**, 141 (2008).

[30] M. Perić, R. Ranković and S. Jerosimić, Chem. Phys. **344**, 35 (2008)

[31] I. B. Bersuker, *The Jahn-Teller effect*, (Cambridge University Press, Cambridge (U.K), 2006).

[32] P. Garcia-Fernandez and I. B. Bersuker, Int, Jou, Quant, Chem, **112**, 3025 (2012).

[33] J. M. L. Martin, J. E. Yazal and J-P Francois, Chem. Phys. Lett. **252**, 9, (1996).

[34] D. Forney, P. Freivogel, M. Grutter, and J. P. Maier, J. Chem. Phys. **104**, 4954 (1996);

[35] T. H. Dunning, Jr., J. Chem. Phys. **90**, 1007 (1989).

[36] E. B. Wilson Jr., J. C. Decius and P. C. Cross, *Molecular vibrations* (McGraw-Hill, New York, 1955).

[37] M. J. Frisch, *et al.* Gaussian 03, Revision B. 05, Gaussian, Inc., Pittsburgh, PA, 2003.

[38] H. -J. Werner, P. J. Knowles, R. D. Amos, A. Bernhardsson, and others, MOLPRO-2002, a package of ab initio programs; Universitat Stuttgart: Stuttgart, Germany; University of Birmingham:Birmingham, United Kingdom, 2002.

[39] M. Döscher, H. Köppel, and P. Szalay, J. Chem. Phys. **117**, 2645, (2002)

[40] T. S. Venkatesan, H.-D. Meyer, H. Köppel, L. S. Cederbaum and S. Mahapatra, J. Phys. Chem. A, **111**, 1746, (2007).

[41] T. Mondal, S. R. Reddy and S. Mahapatra, J. Chem. Phys. **137**, 054311 (2012)

[42] J. Cullum and R. Willoughby, Lanczos Algorithms for Large Symmetric Eigenvalue Problems (Birkhäuser, Boston, 1985, Vols. I and II).

6 Photophysics of hexafluorobenzene

6.1 Introduction

Fluorine atom substitution in the Bz ring leads to a stabilization of the σ orbitals which consist mostly the fluorine orbitals. In a more general context this phenomenon is known as perfluoro effect in the literature [1]. Several experimental and theoretical studies on neutral FBz molecules have appeared in the literature over the past decades [2–24], a detailed understanding of the spectroscopic and dynamical properties of their electronic excited states is still missing. Despite this, some detailed theoretical studies attempting to understand these properties of neutral FBzs and their radical cations have appeared in the recent past [25–31]. In continuation to earlier works of this group on MFBz, *o*-DFBz, *m*-DFBz, PFBz [25,26] and $TFBz^+$ [30] we attempt here to investigate the structure and dynamics of the energetically low-lying electronic states of HFBz by quantum mechanical methods. Like the parent Bz, HFBz also belongs to the D_{6h} symmetry point group at its equilibrium geometry. Because of high symmetry like Bz, many optical transitions are electric-dipole forbidden in HFBz also. Vibronic interaction is an important mechanism that causes a symmetry mixing and allows optically dark transitions. This statement dates back to the work of Sponer *et al.* , in which the optically dark transition of Bz was reported [32] for the first time. Furthermore, because of high symmetry, many of the low-lying electronic states of these molecules are orbitally degenerate and prone to the JT distortion [33]. The latter introduces a rich variety of vibronic coupling mechanisms which are fundamentally important in the spectroscopic and dynamical properties of these polyatomic molecular systems.

Spectroscopic [9, 13] and photophysical [5, 7] studies on FBz molecules have revealed that the features of the electronic absorption and emission bands and lifetimes of fluorescence emission strongly depends on the number of substituted fluorine atoms. For example, C_6F_n with n $\leq$ 4 exhibit structured $S_1 \leftarrow S_0$ absorption band, large quantum yield and nanosecond lifetime of fluorescence. On the other hand, C_6F_n with n=5 and 6 exhibit structureless $S_1 \leftarrow S_0$ absorption band [9, 13], low quantum yield [5, 7], picosecond and nanosecond lifetime of fluorescence emission [16]. Furthermore, a biexponential decay of fluorescence is observed for the latter molecules [16]. Experimental measurements of Philis *et al.* [13] revealed that a lowering of D_{6h} symmetry of Bz by fluorine substitution leads to the appearance of additional bands within 8.0 eV which do not have a Bz parentage. For example, apart from three singlet-singlet transitions analogous to the $B_{2u} \leftarrow A_{1g}$, $B_{1u} \leftarrow A_{1g}$ and $E_{1u} \leftarrow A_{1g}$ transitions in Bz, one additional band has been observed in MFBz and in *o*-DFBz in the region of the $^1B_{1u}$ band [13]. This band is correlate with the 3s ($^1E_{1g}$) Rydberg state of Bz molecule [13]. Likewise,

one additional band has been identified in PFBz and HFBz at ∼5.85 and ∼5.36 eV, respectively, and is designated as the unassigned C-band [13]. Recent theoretical studies [25, 26] on the FBz molecules have settled the ambiguities over the justification of the origin of these additional bands and several other issues mentioned above for C_6F_n with n upto 5. It appears from the work done by Mondal *et al.* [25, 26] that along with vibronic coupling, perfluoro effect [1] also plays an important role on the dynamics of the low-lying excited electronic states of these FBz molecules. In case of HFBz (where all the hydrogen atoms are replaced by fluorine atoms and the perfluoro effect is expected to have the maximum impact), there exist no clear-cut understanding of the origin of the additional bands (when compared to Bz) and several anomalous experimental observations about it's fluorescence lifetime and biexponential decay dynamics in gas phase absorption spectrum [13]. Furthermore, the additional band (C-band) observed in HFBz, unlike PFBz, exhibits a twin structure and there is no unambiguous interpretation exists for the observed twin to date.

The lowering of energy of the two lowest $\pi\sigma^*$ states upon increasing fluorination is discussed in our previous work [25]. For completeness, we plot in Fig. 6.1, the energy of the first few electronic states of Bz and HFBz calculated at the equilibrium geometry of the respective S_0 state. The energies are calculated by the EOM-CCSD method using the aug-cc-pVDZ basis set. It can be seen from the diagram that the $\pi\sigma^*$ state becomes S_2 in case of HFBz. In the latter, two $\pi\sigma^*$ states are degenerate at the equilibrium configuration of the S_0 state. They represent the two components of the degenerate $^1E_{1g}$ electronic state of HFBz [25]. These findings are in excellent accord with those of Philis *et al.* [13], Motch *et al.* [20] and Holland *et al.* [21] but are in contrast to those of Zgierski *et al.* [19] and Temps *et al.* [22]. The lowest $\pi\sigma^*$ state was found to be the S_1 (in PFBz and HFBz) in the latter studies [19, 22].

The absorption bands observed within 8.0 eV for HFBz are highly diffuse and exhibit irregular structures which hardly allow any definitive vibrational assignments. Therefore, a detail theoretical investigation of the nuclear dynamics is undertaken to understand the these observations. The complex and diffuse nature of the gas phase absorption spectrum of HFBz [13, 19–22] suggests vibronic coupling among the underlying excited electronic states which makes an optically dark transition allowed. Such coupling induces nonadiabatic transitions among different electronic states and a mixing of the energy levels of different vibronic symmetries. A typical signature of vibronic interactions is the occurrence of CIs [34, 37–42] of electronic PESs in multi-dimensions. These intersections become the mechanistic bottleneck for ultrafast relaxation and energy transfer between electronic states [34]. Occurrence of CIs causes a breakdown of the adiabatic BO approximation [43]. The nonadiabatic coupling terms are singular in the adiabatic electronic basis. For numerical convenience, a diabatic electronic basis [44] is preferred in the dynamics study. In the latter basis, the coupling between states is described by the electronic Hamiltonian and the coupling elements are smooth functions of nuclear coordinates.

The aim of the present chapter is to understand some of the unresolved issues on the observed optical absorption spectrum of HFBz and to provide a comparative account on the impact of fluorine atom substitution on the optical absorption spectrum

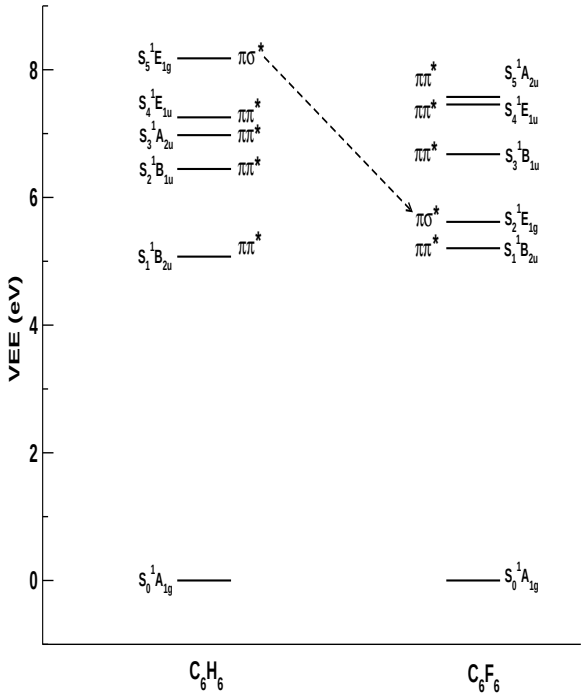

Figure 6.1: Schematic diagram of the energetically low-lying electronic states of Bz and HFBz. The adiabatic electronic energies are calculated at the equilibrium configuration of the respective S_0 state. The zero of energy corresponds to the equilibrium minimum of the S_0 state of Bz and HFBz. Further details of the diagram are given in Sec. 6.2 of the text.

of Bz. This task is accomplished by performing detail *ab initio* electronic structure calculations and first principles simulations of nuclear dynamics. The electronic structure calculations for the low-lying electronic states of HFBz are carried out to construct an appropriate parametrized model vibronic Hamiltonian of HFBz. In this model the PESs and the coupling surfaces of the relevant electronic states are constructed by calculating the VEEs with the aid of EOM-CCSD method [45] implemented in MOLPRO suite of program [46]. The VEEs are calculated along the dimensionless normal displacement coordinates of all the vibrational modes. The calculated adiabatic energy points are fitted to the theoretical model developed in this chapter. The coupling between different electronic states is taken into consideration in accordance with the symmetry selection rules [54] and the relative phases of the coupling terms of the Hamiltonian are derived from group theory considerations analogous to that carried out for the benzene radical cation (Bz^+) [35].

On the technical aspects, a time-independent matrix diagonalization approach to treat the coupled-state nuclear dynamics including all the relevant vibrational modes is beyond the capability of the present computer hardware. This task is therefore accomplished with a time-dependent WP propagation approach employing the MCTDH scheme developed at Heidelberg [47–50]. This scheme has been very successful particularly in treating

the multi-state and multi-mode vibronic coupling problems of large dimension [47–50]. While the final results of this chapter are obtained by this method, comparison calculations are carried out in reduced dimensions by the time-independent matrix diagonalization method in order to arrive at unambiguous assignments (whenever possible) of the vibronic structure of the observed absorption bands.

6.2 Details of electronic structure calculations

The reference equilibrium geometry of the electronic ground state [S_0 ($^1A_{1g}$)] of HFBz is optimized by the MP2 theory method employing the aug-cc-pVDZ basis set of Dunning [51]. The Gaussian-03 suite of program [52] is used for this purpose. The optimized reference equilibrium geometry converged to the D_{6h} symmetry point group. The optimized structural parameters, $r_{C-C} = 1.401$ angstrom and $r_{C-F} = 1.346$ angstrom, are in fair agreement with their experimental values [53] of, 1.391 ± 0.007 angstrom and 1.327 ± 0.007 angstrom, respectively.

Harmonic frequency (ω_i) of the vibrational modes of HFBz is calculated by diagonalizing the kinematic and *ab initio* force constant matrix of the reference equilibrium structure. These vibrational frequencies are listed in Table 6.1. The mass-weighted normal coordinates of the vibrational modes are calculated from the eigenvectors of the force constant matrix. These are then transformed into their dimensionless form ($\mathbf{Q}_i$) by multiplying with $\sqrt{\omega}_i$ (in a_0). The fundamental vibrational modes of HFBz belong to ten degenerate and ten nondegenerate symmetry species of the D_{6h} point group. They decompose into the following IREPs of this symmetry point group [54]:

$$\begin{aligned}\Gamma &= 2a_{1g}(\nu_1,\nu_2) \oplus a_{2g}(\nu_3) \oplus a_{2u}(\nu_4) \oplus 2b_{1u}(\nu_5,\nu_6) \oplus 2b_{2g}(\nu_7,\nu_8) \oplus 2b_{2u}(\nu_9,\nu_{10}) \oplus \\ &\quad e_{1g}(\nu_{11}) \oplus 3e_{1u}(\nu_{12},\nu_{13},\nu_{14}) \oplus 4e_{2g}(\nu_{15},\nu_{16},\nu_{17},\nu_{18}) \oplus 2e_{2u}(\nu_{19},\nu_{20}). \qquad (6.1)\end{aligned}$$

The description of the vibrational modes of Eq. (6.1) is given in Table 6.1 along with their numbering as proposed by Herzberg [55] and also by Wilson [56].

Adiabatic energies of the low-lying singlet electronic states of HFBz are calculated *ab initio* along the dimensionless normal coordinates of the 30 (altogether) vibrational degrees of freedom. The VEEs of these electronic states are calculated for $Q_i = \pm 0.25$ and in the range -3.00 to $+3.00$ with an increment 0.50, along i^{th} vibrational mode (keeping others at their equilibrium value) using the EOM-CCSD method as implemented in MOLPRO program package [46]. Like in our previous studies on FBzs [25,26,30] the aug-cc-pVDZ basis set is used for the C atoms and the energy-consistent pseudopotentials of Stuttgart/Cologne group [58] are used for the fluorine atoms.

In order to ensure a reliable basis for using ECPs for fluorine atoms, we have done test calculations of the VEEs of the low-lying electronic states of HFBz with and without ECPs. The results are given in Table 6.2. It can be seen that the change in VEE for all five states is very minor (the average deviation is $\sim$0.04 eV), indicating the reliability of ECPs to describe the excited state PESs of HFBz.

Table 6.1: Description of the vibrational modes of the electronic ground state of HFBz calculated at the MP2/aug-cc-pVDZ level of theory.

Symmetry	Nomenclature		Vibrational Frequency(ω_i/eV)		Predominant nature
	Herzberg [55]	Wilson [56]	present	Experiment [57]	
a_{1g}	ν_1	ν_1	0.1874	0.1847	C-F stretching in-phase
	ν_2	ν_2	0.0686	0.0693	Ring breathing
a_{2g}	ν_3	ν_3	0.0968	0.0857	C-F in-plane bending, in-phase
a_{2u}	ν_4	ν_{11}	0.0261	0.0267	C-F out-of-plane bending, in-phase
b_{1u}	ν_5	ν_{12}	0.1507	0.1640	C-F trigonal stretching
	ν_6	ν_{13}	0.0727	0.0793	C-C-C trigonal bending
b_{2g}	ν_7	ν_4	0.0577	0.0885	C-F out-of-plane trigonal
	ν_8	ν_5	0.0222	0.0309	C-C-C Puckering
b_{2u}	ν_9	ν_{14}	0.1825	0.1553	C-C stretching (kekule)
	ν_{10}	ν_{15}	0.0341	0.0258	C-F in plane trigonal bending
e_{1g}	ν_{11}	ν_{10}	0.0448	0.0459	C-F out-of-plane bending
e_{1u}	ν_{12}	ν_{20}	0.1921	0.1897	C-C stretching
	ν_{13}	ν_{19}	0.1236	0.1263-0.1232	C-F stretching
	ν_{14}	ν_{18}	0.0387	0.0391	C-F in-plane bending
e_{2g}	ν_{15}	ν_6	0.2093	0.2052	C-C stretching
	ν_{16}	ν_9	0.1420	0.1434	C-F stretching
	ν_{17}	ν_8	0.0541	0.0549	C-C-C in-plane bending
	ν_{18}	ν_7	0.0328	0.0327	C-F in-plane bending
e_{2u}	ν_{19}	ν_{16}	0.0757	0.0738	C-C-C out-of-plane
	ν_{20}	ν_{17}	0.0169	0.0217	C-F out-of-plane

Table 6.2: Vertical excitation energy (in eV) of the five low-lying four excited singlet electronic states calculated at the equilibrium geometry of S_0 state of HFBz.

State	aug-cc-pVDZ	ECP
$S_1(^1B_{2u})$	5.204	5.168
$S_2(^1E_{1g})$	5.617	5.678
$S_3(^1B_{1u})$	6.677	6.646
$S_4(^1A_{2u})$	7.456	7.556
$S_5(^1E_{1u})$	7.574	7.542

6.3 The vibronic Hamiltonian and nuclear dynamics

In this section we construct a Hamiltonian in the normal displacement coordinates of the reference electronic ground state of HFBz in accordance with the symmetry selection rule. The nuclear dynamics in its excited electronic states is studied subsequently using this Hamiltonian. The Hamiltonian is constructed in a diabatic electronic basis [44]. Within $\sim$ 8.0 eV excitation energy range signature of five excited singlet electronic states (viz., $S_1{}^1B_{2u}$, $S_2{}^1E_{1g}$, $S_3{}^1B_{1u}$, $S_4{}^1E_{1u}$ and $S_5{}^1A_{2u}$) emerged in the experimental absorption spectrum [13]. The symmetry of these electronic states indicates that the JT and PJT interactions are the two fundamentally important mechanisms that would primarily govern the overall shape and the assignment of the electronic absorption bands of HFBz. With the given symmetry representation of the electronic states and the vibrational modes, the following rules can be derived from the character table of the D_{6h} symmetry point group.

The first-order coupling within (intra) and between (inter) electronic states is governed by the selection rules; $(\Gamma_i)^2 \supset (\Gamma_{a_1})$ and $\Gamma_i \otimes \Gamma_j \supset \Gamma_x$, respectively [34]. The symbol, Γ represents the IREP, i and j are the electronic state indices, a_1 represents the totally symmetric vibrational mode and the symbol, x, represents the symmetry of the vibrational mode that transforms according to, $\Gamma_i \otimes \Gamma_x \otimes \Gamma_j \supset A_1$. Now for the degener-

ate, $^1E_{1g}$ (S_2) and $^1E_{1u}$ (S_4) electronic states the symmetrized direct product transforms into, $(E_{1g})^2 = (E_{1u})^2 = a_{1g} + e_{2g}$. While the vibrational modes of a_{1g} symmetry can not split the electronic degeneracy (are condon active), the modes of e_{2g} symmetry can lift this electronic degeneracy and are JT active. For the rest of the off-diagonal elements of the Hamiltonian written below the following symmetry rules apply.

$$B_{2u} \otimes E_{1g} = e_{2u}\ (\nu_{19}, \nu_{20}), \tag{6.2a}$$
$$B_{2u} \otimes B_{1u} = a_{2g}\ (\nu_3), \tag{6.2b}$$
$$B_{2u} \otimes E_{1u} = e_{2g}\ (\nu_{15}, \nu_{16}, \nu_{17}, \nu_{18}), \tag{6.2c}$$
$$B_{2u} \otimes A_{2u} = b_{1g}, \tag{6.2d}$$
$$E_{1g} \otimes B_{1u} = e_{2u}\ (\nu_{19}, \nu_{20}), \tag{6.2e}$$
$$E_{1g} \otimes E_{1u} = e_{2u}\ (\nu_{19}, \nu_{20}) + a_{2u}\ (\nu_4) + a_{1u}, \tag{6.2f}$$
$$E_{1g} \otimes A_{2u} = e_{1u}\ (\nu_{12}, \nu_{13}, \nu_{14}), \tag{6.2g}$$
$$B_{1u} \otimes E_{1u} = e_{2g}\ (\nu_{15}, \nu_{16}, \nu_{17}, \nu_{18}), \tag{6.2h}$$
$$B_{1u} \otimes A_{2u} = b_{2g}\ (\nu_7, \nu_8), \tag{6.2i}$$
$$E_{1u} \otimes A_{2u} = e_{1g}\ (\nu_{11}). \tag{6.2j}$$

According to Eq. (6.1) HFBz does not have any vibrational mode of either b_{1g} or a_{1u} symmetry. Therefore, the coupling of the electronic states as given in Eqs. (6.2d) and (6.2f), through these modes do not appear in the electronic Hamiltonian given below. The relative sign of various elements of the Hamiltonian is determined by explicitly checking the invariance of the Hamiltonian with respect to the symmetry operations of the D_{6h} point group, following similar works on Bz and cyclopropane radical cation [35, 36]. With these considerations the vibronic Hamiltonian can be written as

$$\mathcal{H} = \mathcal{H}_0 \mathbf{1}_7 + \mathcal{W}, \tag{6.3a}$$

where

$$\mathcal{W} = \begin{bmatrix}
\mathcal{E}^1 + \mathcal{U}^1 & \sum_{i\in e_{2u}} \lambda_i^{1,2x} Q_{ix} & \sum_{i\in e_{2u}} -\lambda_i^{1,2y} Q_{iy} & \sum_{i\in a_{2g}} \lambda_i^{1,3} Q_i & \sum_{i\in e_{2g}} \lambda_i^{1,4x} Q_{ix} & 0 & \sum_{i\in e_{2g}} -\lambda_i^{1,4y} Q_{iy} \\
h.c. & \mathcal{E}^2 + \mathcal{U}^{2x} & \sum_{i\in e_{2g}} \lambda_i^{2x,2y} Q_{iy} & \sum_{i\in e_{2u}} \lambda_i^{2x,3} Q_{ix} & \sum_{i\in a_{2u}} \lambda_i^{2x,4x} Q_i & \sum_{i\in e_{1u}} \lambda_i^{2x,5} Q_{ix} & \sum_{i\in e_{2u}} \lambda_i^{2x,4y} Q_{iy} + \sum_{i\in a_{1u}} \lambda_i^{2x,4y} Q_i \\
 & h.c. & \mathcal{E}^2 + \mathcal{U}^{2y} & \sum_{i\in e_{2u}} -\lambda_i^{2y,3} Q_{iy} & \sum_{i\in e_{2u}} \lambda_i^{2y,4x} Q_{iy} - \sum_{i\in e_{1u}} \lambda_i^{2y,4x} Q_i & \sum_{i\in e_{1u}} -\lambda_i^{2y,5} Q_{iy} & \sum_{i\in e_{2u}} \lambda_i^{2y,4y} Q_{ix} + \sum_{i\in a_{2u}} \lambda_i^{2y,4y} Q_i \\
 & & h.c. & \mathcal{E}^3 + \mathcal{U}^3 & \sum_{i\in e_{2g}} \lambda_s^{3,4x} Q_{ix} & \sum_{i\in b_{2g}} \lambda_i^{3,5} Q_i & \sum_{i\in e_{2g}} -\lambda_i^{3,4y} Q_{iy} \\
 & & & h.c. & \mathcal{E}^{4x} + \mathcal{U}^{4x} & \sum_{i\in e_{1g}} \lambda_i^{4x,5} Q_{ix} & \sum_{i\in e_{2g}} \lambda_i^{4x,4y} Q_{iy} \\
 & & & & h.c. & \mathcal{E}^5 + \mathcal{U}^5 & \sum_{i\in e_{1g}} -\lambda_i^{4y,5} Q_{iy} \\
 & & & & & h.c. & \mathcal{E}^{4y} + \mathcal{U}^{4y}
\end{bmatrix} \tag{6.3b}$$

In the above, $\mathcal{H}_0 = \mathcal{T}_N + \mathcal{V}_0$, represents the Hamiltonian (assumed to be harmonic) of the reference electronic ground (S_0) state of HFBz with

$$\mathcal{T}_N = -\frac{1}{2}\sum_{i\,\in\,a_{1g},\,a_{2g},\,b_{2g},\,b_{2u}} \omega_i \frac{\partial^2}{\partial Q_i^2} - \frac{1}{2}\sum_{i\,\in\,e_{2g},\,e_{2u},\,e_{1g},\,e_{1u}} \omega_i \left(\frac{\partial^2}{\partial Q_{ix}^2} + \frac{\partial^2}{\partial Q_{iy}^2}\right), \quad (6.4)$$

and

$$\mathcal{V}_0 = \frac{1}{2}\sum_{i\,\in\,a_{1g},\,a_{2g},\,b_{2g},\,b_{2u}} \omega_i Q_i^2 + \frac{1}{2}\sum_{i\,\in\,e_{2g},\,e_{2u},\,e_{1g},\,e_{1u}} \omega_i \left(Q_{ix}^2 + Q_{iy}^2\right). \quad (6.5)$$

The quantity $\mathbf{1_7}$ is a 7×7 diagonal unit matrix. The nondiagonal matrix Hamiltonian in Eq. (6.3b) describes the PESs of the excited electronic states of HFBz and their coupling surfaces. The quantity $\mathcal{E}^j$ in this matrix is the VEE of the j^{th} electronic state. The elements of this matrix are expanded in a standard Taylor series around the reference equilibrium geometry at, $\mathbf{Q} = \mathbf{0}$, in the following way

$$\mathcal{U}^j = \sum_{i\,\in\,a_{1g}} \kappa_i^j Q_i + \frac{1}{2}\sum_{i\,\in\,a_{1g},\,a_{2g},\,b_{2g},\,b_{2u}} \gamma_i^j Q_i^2 + \frac{1}{2}\sum_{i\,\in\,e_{2g},\,e_{2u},\,e_{1g},\,e_{1u}} [\gamma_i^j (Q_{ix}^2 + Q_{iy}^2)] + \frac{1}{24}[\zeta_{15}^{(3)}(Q_{15x}^4 + Q_{15y}^4)]; j \in 1, 3 \text{ and } 5, \quad (6.6a)$$

$$\mathcal{U}^{jx/jy} = \sum_{i\,\in\,a_{1g}} \kappa_i^j Q_i \pm \sum_{i\,\in\,e_{2g}} \lambda_i^j Q_{ix} + \frac{1}{2}\sum_{i\,\in\,a_{1g},\,a_{2g},\,b_{2g},\,b_{2u}} \gamma_i^j Q_i^2 + \frac{1}{2}\sum_{i\,\in\,e_{2g},\,e_{2u},\,e_{1g},\,e_{1u}} [\gamma_i^j (Q_{ix}^2 + Q_{iy}^2)]; j \in 2 \text{ and } 4. \quad (6.6b)$$

In above equations the two components of the degenerate states and modes are labeled with x/y. The quantity κ_i^j and λ_i^j represents the linear intrastate and interstate (JT) coupling parameters [34] for the symmetric (a_{1g}) and degenerate (e_{2g}) vibrational modes, respectively, for the j^{th} electronic state. The first-order PJT coupling parameter of the i^{th} vibrational mode between the electronic states j and k is given by λ_i^{j-k}; γ_i^j and ζ_i^j are the second-order and fourth-order coupling parameters of the i^{th} vibrational mode for the j^{th} electronic state. The summations run over the normal modes of vibration of specified symmetry in the index. The + and - sign in Eq. (6.6b) is applicable to the x and y components of the degenerate state, respectively. A fourth-order term along the degenerate ν_{15} vibrational mode is included in Eq. (6.6a), in order to account for the anharmonicity of the S_3 state along this vibrational mode (discussed later in the text). The VEEs calculated in Sec. 6.2 are fitted to the adiabatic counterpart of diabatic electronic Hamiltonian of Eq. 6.3 by a least squares procedure to estimate the parameters of the Hamiltonian defined above. The estimated parameters along the relevant vibrational modes are given in Tables 6.3 and 6.4. A careful inspection of the

coupling parameters suggests that not all 30 vibrational modes play significant role in the nuclear dynamics on the electronic states of HFBz considered in this chapter. Therefore, only the relevant modes having significant coupling strengths are retained in the nuclear dynamics study presented below. The VEEs of the electronic excited states of HFBz are given in Table 6.5 along with the theoretical and experimental excitation energies available from the literature.

Table 6.3: Ab initio calculated linear and quadratic coupling constants for the $S_1{}^1B_{2u}$, $S_2{}^1E_{1g}$, $S_3{}^1B_{1u}$, $S_4{}^1E_{1u}$ and $S_5{}^1A_{2u}$ electronic states of HFBz. All data are given in the eV unit.

Symm-etry	Mode	κ_i	γ_i	κ_i or λ_i	γ_i	κ_i	γ_i	κ_i or λ_i	γ_i	κ_i	γ_i
		S_1		S_2		S_3		S_4		S_5	
a_{1g}	ν_1	-0.1565 (0.3)	0.0059	0.0791(0.1)	-0.0288	-0.1357(0.3)	0.0038	-0.1467(0.3)	0.0001	-0.0225(0.0)	-0.0587
	ν_2	-0.1055 (1.2)	-0.0022	-0.0517(0.3)	-0.0038	-0.0827(0.7)	0.0008	-0.0931(0.9)	-0.0023	-0.0576(0.4)	-0.0085
a_{2g}	ν_3		-0.0068		-0.0113		-0.0062		-0.0075		-0.0143
a_{2u}	ν_4		-0.0125		-0.0143		-0.0114		-0.0169		-0.0063
b_{1u}	ν_5		-0.0007		-0.0374		-0.0017		-0.0042		-0.0212
	ν_6		-0.0011		-0.0222		-0.0045		-0.0056		-0.0174
b_{2g}	ν_7		-0.0510		-0.0266		-0.0494		-0.0530		0.0212
	ν_8		-0.0144		-0.0193		-0.0174		-0.0145		0.00001
b_{2u}	ν_9		0.1514		0.0501		0.0691		0.0624		0.0139
	ν_{10}		0.0009		-0.0006		0.0004		-0.0007		-0.0058
e_{1g}	ν_{11}		-0.0643		0.0301		-0.0749		-0.1505		-0.2649
e_{1u}	ν_{12}		-0.0080		-0.0610		-0.0131		-0.0260		-0.0359
	ν_{13}		-0.0038		-0.0199		-0.0045		-0.0136		-0.0218
	ν_{14}		-0.0008		-0.0096		-0.0013		-0.0024		-0.0037
e_{2g}	ν_{15}		0.0147	0.1490(0.26)	-0.0167		0.0758	0.0672(0.06)	0.0476		-0.0310
	ν_{16}		-0.0007	0.0380(0.04)	-0.0285		-0.0233	0.0112(0.01)	0.0091		-0.0274
	ν_{17}		-0.0130	0.0717(0.88)	-0.0119		-0.0112	0.0195(0.06)	-0.0018		-0.0115
	ν_{18}		-0.0032	0.0309(0.44)	-0.0027		-0.0036	0.0075(0.02)	-0.0010		-0.0081
e_{2u}	ν_{19}		-0.0622		-0.0575		-0.0071		-0.0527		-0.0338
	ν_{20}		-0.0151		-0.0090		0.0060		-0.0141		-0.0134

Table 6.4: The interstate coupling parameters (in eV) of the vibronic Hamiltonian of Eq. 6.3 for the $S_1{}^1B_{2u}$, $S_2{}^1E_{1g}$, $S_3{}^1B_{1u}$, $S_4{}^1E_{1u}$ and $S_5{}^1A_{2u}$ electronic states of HFBz, estimated from the *ab initio* electronic structure results (see text for details).

Mode	$\lambda_i^{1,2}$	$\lambda_i^{1,3}$	$\lambda_i^{1,4}$	$\lambda_i^{2,3}$	$\lambda_i^{2,5}$	$\lambda_i^{3,4}$	$\lambda_i^{3,5}$	$\lambda_i^{4,5}$
ν_3		0.0139 (0.01)						
ν_7							0.1649 (3.92)	
ν_8							0.0526 (4.01)	
ν_{11}								0.1022 (2.60)
ν_{12}					0.1110 (0.09)			
ν_{13}					-			
ν_{14}					0.0631 (0.94)			
ν_{15}			0.2003 (0.44)			0.2610 (0.78)		
ν_{16}			0.0820 (0.16)			0.0902 (0.20)		
ν_{17}			0.0814 (1.14)			0.0470 (0.38)		
ν_{18}			0.0326 (0.50)			0.0244 (0.28)		
ν_{19}	0.1548 (2.10)							
ν_{20}	0.0619 (6.70)			0.0626 (6.86)				

Table 6.5: Vertical excitation energies (in eV) of the lowest five electronic states of HFBz.

	S_1 ($^1B_{2u} \leftarrow \tilde{X}\ ^1A_{1g}$) $\pi^* \leftarrow \pi$	S_2 ($^1E_{1g} \leftarrow \tilde{X}\ ^1A_{1g}$) $\sigma^* \leftarrow \pi$	S_3 ($^1B_{1u} \leftarrow \tilde{X}\ ^1A_{1g}$) $\pi^* \leftarrow \pi$	S_4 ($^1E_{1u} \leftarrow \tilde{X}\ ^1A_{1g}$) $\pi^* \leftarrow \pi$	S_5 ($^1A_{2u} \leftarrow \tilde{X}\ ^1A_{1g}$) $\pi^* \leftarrow \pi$
Ref. [11]	4.80	5.32	6.36	7.10	-
Ref. [14]	4.70	5.39	6.25	7.00	-
	-	5.72	-	-	-
Ref. [13, 15]	(4.28)	5.38	6.40	7.11	7.70
	-	5.75	-	-	-
Ref. [20]	4.86	5.38	6.39	7.11	7.70
	-	5.66	-	-	-
Ref. [21] EXPT	4.86	5.38	6.37	7.095	7.70
Ref. [21] TDDFT	4.91	5.05	5.90	-	-
Ref. [19] EXPT	4.48	4.34	4.90		
Ref. [19] TD/BP86	4.915	4.539	-	-	-
Ref. [22] TD/BP86	5.025	4.641	5.853	-	-
This work	5.168	5.678	6.646	7.542	7.556
Adjusted VEEs	5.032	5.594	6.776	7.256	7.706

6.4 Potential energy surfaces

In this section we examine the topography of the adiabatic PESs of the ground and first five excited singlet electronic states of HFBz obtained by diagonalizing the electronic Hamiltonian of the diabatic model developed above. The complex features of the vibronic bands recorded in the experiment [12, 13, 19–22] and the relaxation mechanisms are governed by the detail topography of these electronic states. One dimensional cuts of the full dimensional potential energy hypersurfaces of HFBz viewed along the given vibrational mode keeping others at their equilibrium values at, $\mathbf{Q}$=0, are shown in Figures 6.2 and 6.3. In these figures the solid curves represent the adiabatic potential energy functions obtained from the model developed in Sec 6.3 and the points superimposed on them are obtained from *ab initio* quantum chemical calculations discussed in Sec. 6.2.

In Figs. 6.2(a-b), the potential energies of the S_0, S_1, S_2, S_3, S_4 and S_5 electronic states (indicated in the panel) are plotted along the symmetric vibrational modes ν_1 and ν_2, respectively. It can be seen that the model reproduces the calculated *ab initio* data extremely well. The degeneracy of the S_2 and S_4 state remains unperturbed upon distortion along these symmetric vibrational modes. While the crossing of S_0 state with S_1 seems not very important, the crossing of S_1 and S_2 electronic states (panel a) appears to be important for the detailed structure of the first vibronic band. We note that these states are largely separated in the parent Bz molecule and therefore a structured S_1 band observed for this molecule [13] (cf. Fig. 6.1 drawn at the vertical configuration). The curve crossing between the S_1 and S_2 electronic states seen in Fig. 6.2(a) along ν_1 leads to energetically low-lying accessible CIs in multi-dimensions. It is to be noted again that, the S_1 state is of $\pi\pi^*$ origin where as, the S_2 state is of $\pi\sigma^*$ type. The schematic diagram given in Fig. 6.1 reveals that the $\pi\sigma^*$ state comes down in energy drastically (compared to the parent Bz molecule) due to perfluoro effect. Now it is intriguing to note that [cf. Fig. 6.2(a)] S_1 and S_2 state indeed cross at a distorted (from the reference equilibrium) geometry of HFBz. A similar situation was encountered in case of PFBz molecule, although the curve crossing was found at a much larger displacement from the vertical configuration for this molecule [25, 26]. The S_1 and S_2 states of HFBz are coupled (in first-order) through the PJT type of interactions by the vibrational modes ν_{19} and ν_{20} of e_{2u} symmetry (cf. Table 6.4). The two $\pi\sigma^*$ states become energetically

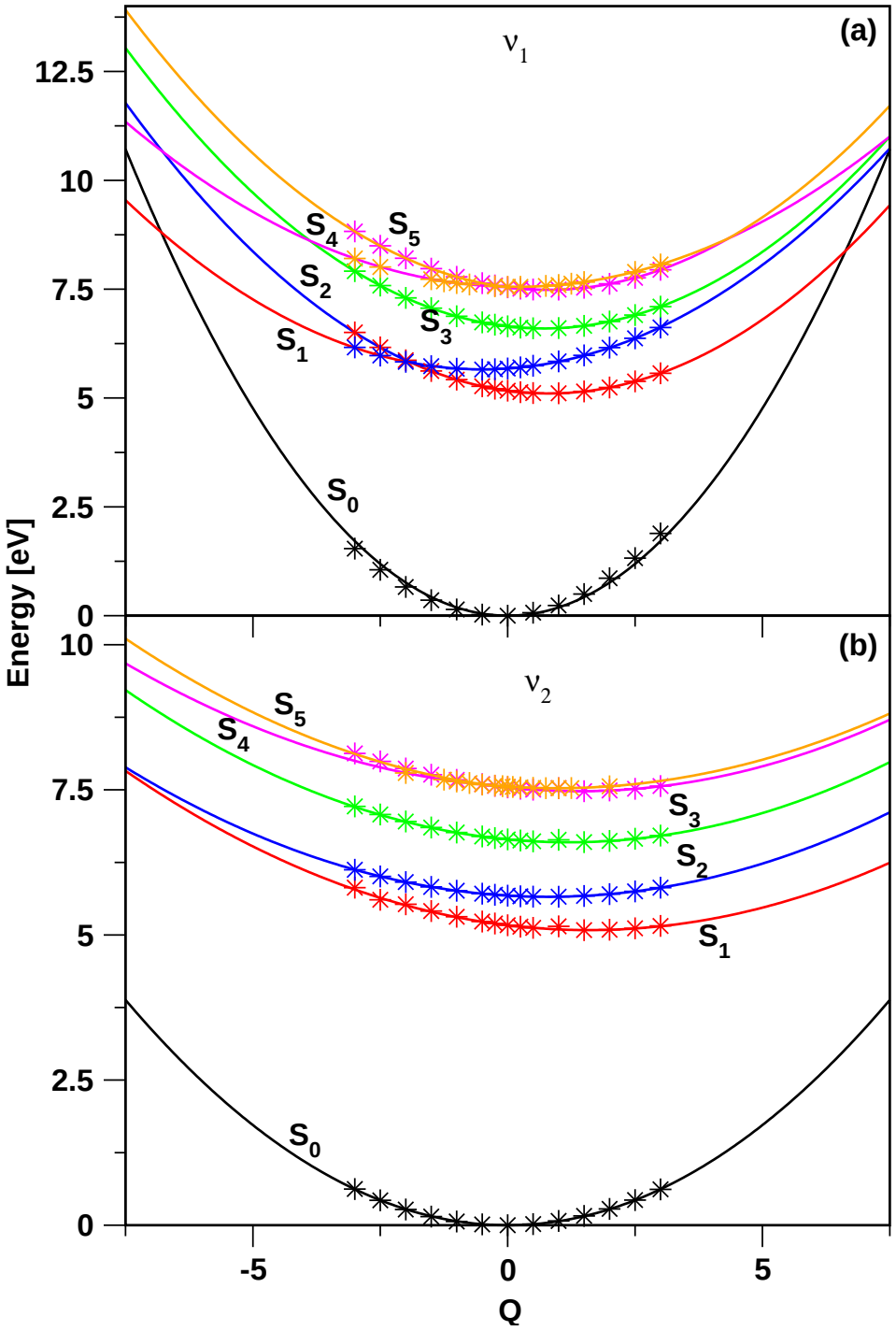

Figure 6.2: Adiabatic potential energies of ground and low-lying excited singlet electronic states of HFBz, along the normal coordinates of totally symmetric vibrational modes. The potential energies obtained from the present vibronic model are shown by the solid lines and the computed *ab initio* energies are shown by the asterisks.

degenerate and form the JT active S_2 state of HFBz. Apart from S_2, S_4 is also a JT ative state in HFBz. This state undergoes PJT crossings with the S_3 and S_5 states as clearly revealed by the potential energy curves shown in Fig. 6.2(a). In contrast to ν_1, the curve crossings are seldom visible along ν_2 in Fig. 6.2(b). The near degeneracy of the S_4 and S_5 states around the reference equilibrium configuration can be clearly seen from both the panels (a and b) of Fig. 6.2.

The locus of the degeneracy of the two components of the S_2 and also S_4 electronic states defines the seam of the JT CIs within these degenerate electronic states at the D_{6h} symmetry configuration of HFBz. Including the second-order diagonal coupling terms of symmetric modes, the energetic minimum on these seams is found at ∼5.64 and ∼7.42 eV for the S_2 and S_4 electronic state, respectively. The electronic degeneracy of the S_2 and S_4 state is split upon distortion along the degenerate (e_{2g}) vibrational modes $\nu_{15} - \nu_{18}$. This leads to a total of seven states altogether to be considered to treat the nuclear dynamics in the S_1-S_2-S_3-S_4-S_5 coupled electronic manifold of HFBz. The potential energies of these electronic states of HFBz are shown in Figs. 6.3(a-d) along the x component of the degenerate vibrational modes $\nu_{15} - \nu_{18}$, respectively. The symmetry rule forbids a first-order coupling of these vibrational modes in the nondegenerate S_1, S_3 and S_5 electronic states. However, these modes are JT active in first-order in the S_2 and S_4 electronic states. It can be seen from Fig. 6.3 that, the JT splitting is very small in the S_4 electronic state in contrast to a relatively larger splitting found in the S_2 state. Moreover, the quartic term of the Taylor expansion (Eqs. 6.6a) seems to have significant role in representing the potential energies of the S_3 state, along the vibrational mode of ν_{15}. It is well known that the JT distortion causes a symmetry breaking [34,40] and as a result the new minima on the lower adiabatic sheet of the JT split S_2 and S_4 states occur at ∼5.50 and ∼7.41 eV, respectively. The JT stabilization energies amount to ∼0.14 and ∼0.01 eV, respectively, for these two degenerate electronic states in that order.

It is obvious from the potential energy plots given in Figs. 6.3(a) and 6.3(b) (above) that, apart from the JT interactions within the degenerate electronic states (S_2 and S_4), curve crossings of the nondegenerate electronic states (S_1, S_3 and S_5) either among themselves or with the components of the JT split degenerate electronic states also exist. The latter describes the PJT interactions and the energetic minimum of the seam of S_1-S_2 PJT CIs is found at ∼ 5.51 eV. This minimum is ∼ 0.13 eV below the seam of JT CIs within the S_2 electronic manifold. The minimum of the S_2-S_3 CIs is found at ∼ 1.65 eV above the minimum of the JT CIs within the S_2 electronic manifold. This minimum is ∼ 0.60 eV above the minimum of the S_3 electronic state. Likewise, the minimum of the S_3-S_5 and S_4-S_5 CIs occurs at ∼ 1.08 and ∼ 0.01 eV above the minimum of the S_5 electronic state. We reiterate that the potential energy curves of Fig. 6.3 also confirms the near degeneracy of the S_4 and S_5 electronic states around the reference equilibrium configuration of HFBz. The energetic proximity of the minimum of an intersection seam to the equilibrium minimum of a state plays very important role in the nuclear dynamics as discussed below.

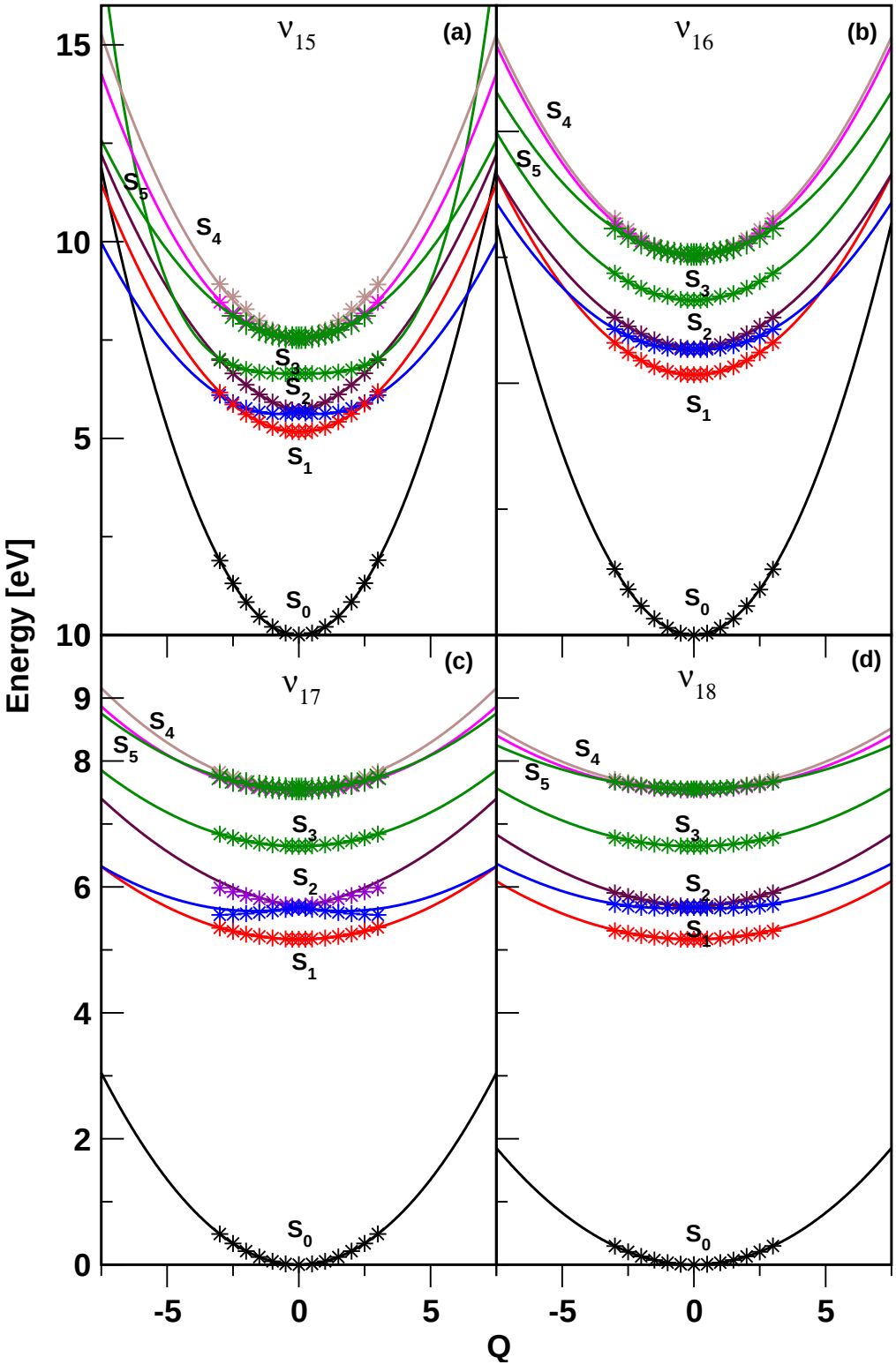

Figure 6.3: Same as in Fig. 6.2, along the dimensionless normal coordinates of the x component of the degenerate e_{2g} vibrational modes ν_{15}-ν_{18}.

6.5 Electronic absorption spectrum

As stated in the introduction, spectroscopic [9, 13] and photophysical [5, 7] studies have revealed that C_6F_n with n $\leq$ 4 exhibits structured $S_1 \leftarrow S_0$ absorption band where as,C_6F_n with n=5 and 6 exhibits structureless $S_1 \leftarrow S_0$ absorption band. It is already established in our previous work [25,26] that the coupling between S_1 state with the rest of the higher excited states occurs much beyond the energy range of the first electronic absorption band of MFBz, *o*-DFBz and *m*-DFBz molecules. The coupling strength of the relevant vibrational modes is also very weak [25, 26]. These findings explained the observed structure in the first absorption band of these molecules. Contrary to this, in case of PFBz occurrence of low-energy CIs between the S_1 and S_2 states (due to increased perfluoro effect) the first absorption band becomes structureless and diffuse [25,26]. The S_1-S_2 nonadiabatic coupling in PFBz is also much stronger compared to the other three molecules mentioned above [25,26]. However, in case of HFBz the present findings reveal that the energetic minimum of $S_1 - S_2$ CIs occurs at further lower energy compared to PFBz. As a result the seam of $S_1 - S_2$ CI is expected to be more readily accessible to the nuclear motion on the S_1 electronic state. Therefore, much profound effect on the spectral envelope of the first and second absorption bands of HFBz can be expected. In order to confirm this, we in the present study first construct various reduced dimensional models and examine the vibrational energy levels of each of these electronic states by excluding the PJT coupling with their neighbors. These results help us to understand the role of various vibrational modes and electronic states in the complex vibronic structures of HFBz. The final simulation of nuclear dynamics is, however, carried out by including all relevant couplings of the Hamiltonian and propagating wave packets using the MCTDH suite of programs [47–50] to elucidate the nonadiabatic coupling effects on the spectral envelopes. The theoretical results are finally compared with the available experimental absorption spectrum of HFBz [13].

The optical absorption spectrum of the uncoupled (without PJT coupling) nondegenerate S_1, S_3 and S_5 electronic states is shown in panel a, b and c of Fig. 6.4, respectively. According to the symmetry selection rule, only totally symmetric vibrational modes can have non-zero first-order (intrastate) coupling in these nondegenerate electronic states. We therefore considered both linear and quadratic coupling terms due to these modes in the nuclear dynamics study on these electronic states. The theoretical stick spectrum of the S_1 state (panel a of Fig. 6.4) is obtained by considering a vibrational basis consisting of 9 and 27 harmonic oscillator functions along ν_1 and ν_2 vibrational modes, respectively. The resulting secular matrix is diagonalized using 5000 Lanczos iterations. The theoretical stick spectrum is convoluted with a Lorentzian line shape function of 40 meV FWHM to generate the spectral envelope. The same convolution procedure is applied to all later stick data presented in this chapter. The vibronic structure of uncoupled S_1 electronic state (panel a) reveals peak spacings corresponding to the frequencies of ν_1 and ν_2 vibrations of $\sim$0.1328 and $\sim$0.0664 eV, respectively. The dominant progression is formed by the ν_2 vibrational mode. Similarly, the spectra of the S_3 and S_5 states presented in panels b and c are obtained by diagonalizing the secular matrix employing 5000 Lanczos iterations using 9 and 27 harmonic oscillator functions for S_3 and 10 and

40 harmonic oscillator functions for S_5 electronic state, respectively along the ν_1 and ν_2 vibrational modes. The vibrational mode ν_2 forms the dominant progression in both these electronic states. Peak spacings of ~ 0.0694 and ~ 0.0600 eV corresponding to the frequency of this mode can be extracted from the spectrum of the S_3 (panel b) and S_5 (panel c) electronic states, respectively. The vibrational mode ν_1 is very weakly excited in all these nondegenerate electronic states.

While the totally symmetric (a_{1g}) vibrational modes are coupled in first-order in the nondegenerate S_1, S_3 and S_5 states only, the JT active (e_{2g}) vibrational modes can have non-zero first-order coupling in the degenerate S_2 and S_4 states in addition. Therefore, all the a_{1g} and e_{2g} vibrational modes are considered to examine the nuclear dynamics in the latter two electronic states. We note that in absence of PJT and bilinear coupling terms, the Hamiltonian for the degenerate (S_2 and S_4) electronic state is separable in terms of the a_{1g} and e_{2g} vibrational modes. Therefore, in the dynamics study the partial spectrum for the a_{1g} and e_{2g} vibrational modes are calculated separately and finally convoluted to generate a composite vibronic band to describe the overall picture. The vibrational structure of the S_2 electronic manifold of HFBz is shown in Fig. 6.5. The partial spectra due to a_{1g} and e_{2g} vibrational modes and their composite are presented in panels a, b and c of Fig. 6.5, respectively. The stick spectra presented in Fig. 6.5 and all latter ones shown below are converged with respect to the size of the harmonic oscillator basis as well as number of Lanczos iterations. The dominant progression in the band of panel a is caused by the ν_2 vibrational mode. Peak spacing of $\sim$0.0647 eV corresponding to the frequency of the ν_2 vibrational mode can be estimated from the spectrum. Fundamental transition due to ν_{15}, ν_{16} and ν_{18} vibrational modes are observed in the partial spectrum of the degenerate e_{2g} vibrational modes shown in panel b. Lines are $\sim$0.1956, $\sim$0.0435 and $\sim$0.0376 eV spaced in energy and correspond to the frequency of the ν_{15}, ν_{16} and ν_{18} vibrational modes, respectively. The clumping of spectral lines under each peak and a huge increase of line density indicates strong JT coupling effects due to the vibrational modes ν_{15}, ν_{16} and ν_{18}, respectively. Such a coupling leads to the appearance of a long series of resonances corresponding to the vibrational motion on the lower JT sheet of the S_2 electronic manifold for energies below $\sim$5.6 eV. Similarly for energies above $\sim$5.6 eV, the upper sheet of S_2 electronic manifold plays a role. Nevertheless, the strong nonadiabatic effects mix the discrete vibrational levels of upper adiabatic sheet with the quasi-continuum levels of lower adiabatic sheet, and therefore, the nuclei undergo simultaneous transitions to both sheets of the JT split PES. The occurrence of higher energy maximum in the spectral envelope of Fig. 6.5(b) is due to metastable resonances of the upper adiabatic cone where as, the lower energy maximum arises from the lower adiabatic sheet. The broadening mechanism and the appearance of high energy peaks are just the strong nonadiabatic coupling effects characteristic for JT intersections [34, 37, 40]. These high energy peaks are referred to as Slonczewski resonances, and the evidence of these resonances was reported in the literature for several (E $\times$ e)-JT problems [61–63].

Similar spectra of the JT split S_4 electronic manifold of HFBz are shown in Figs. 6.6(a-c). The symmetric vibrational modes, ν_1, ν_2, and their combinations form the progressions (panel a) in this case also. The excitation strength of the ν_1 mode is $\sim$ 3

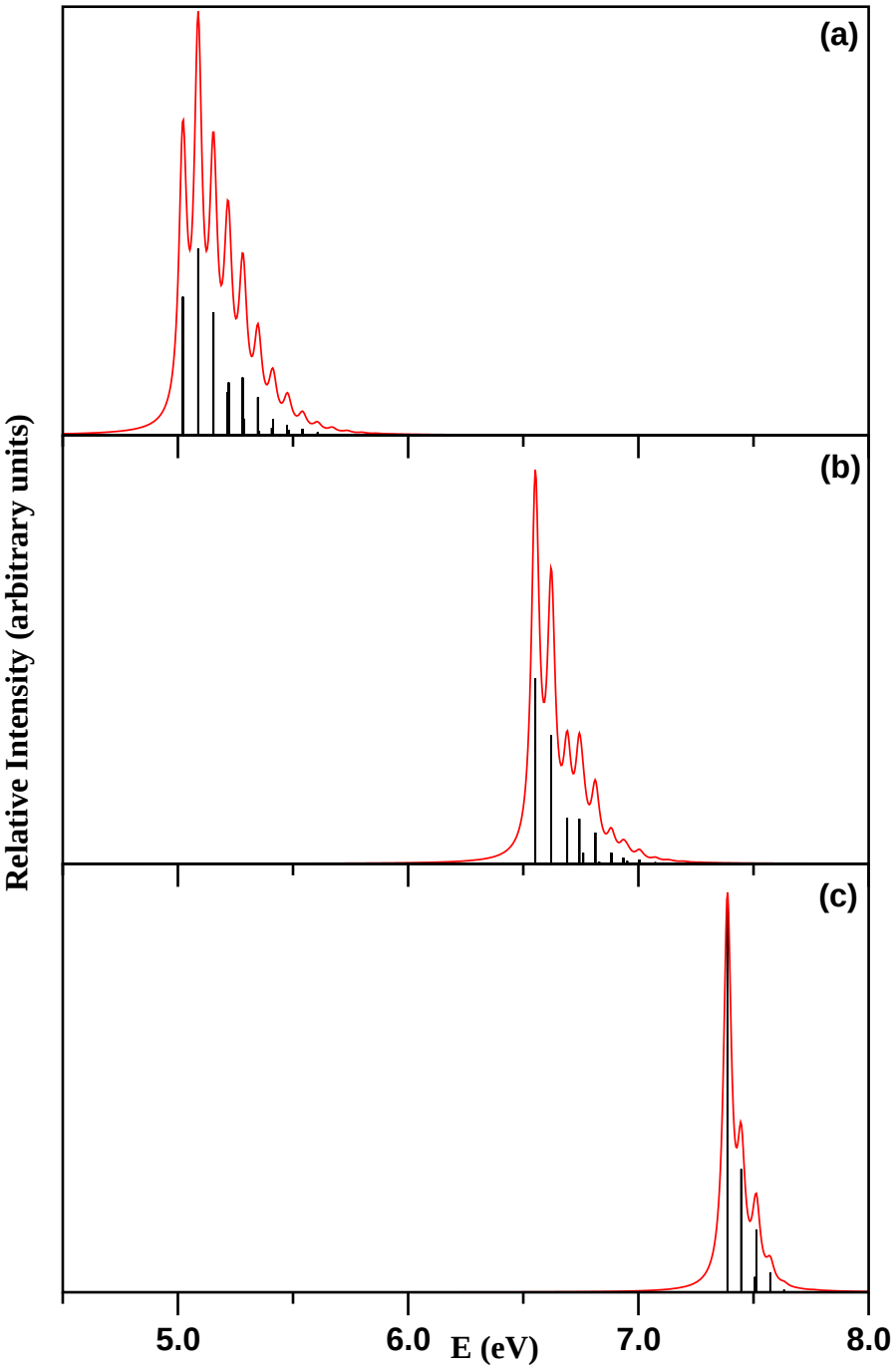

Figure 6.4: ${S_1}^1B_{2u} \leftarrow \mathrm{S}_0$ (panel a), ${S_3}^1B_{1u} \leftarrow \mathrm{S}_0$ (panel b) and ${S_5}^1A_{2u} \leftarrow \mathrm{S}_0$ (panel c) electronic absorption spectrum (excluding all interstate couplings) of HFBz. The above spectra are calculated with the symmetric vibrational modes ν_1 and ν_2 only. The relative intensity (in arbitrary units) is plotted as a function of the energy of the final electronic state. The zero of the energy corresponds to the equilibrium minimum of the electronic ground state (S_0) of HFBz. The theoretical stick spectrum in each panel is convoluted with a Lorentzian function of 40 meV FWHM to generate the corresponding spectral envelope.

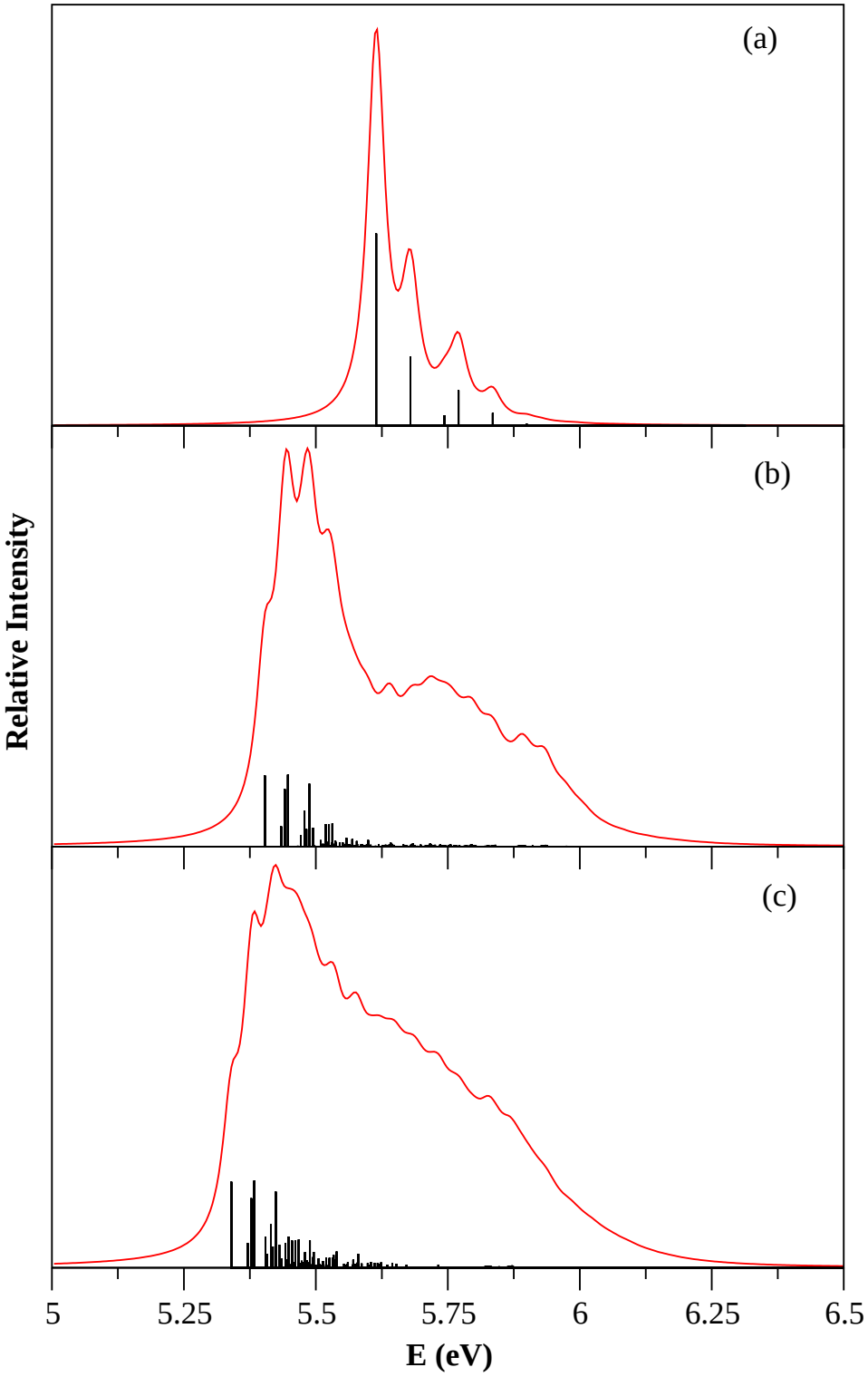

Figure 6.5: Same as in Fig. 6.4 for the $S_2\,^1E_{1g} \leftarrow S_0$ electronic transition in HFBz : (a) partial spectrum computed with the two totally symmetric a_{1g} vibrational modes ν_1 and ν_2, (b) partial spectrum computed with the four JT active degenerate e_{2g} vibrational modes ν_{15}-ν_{18}, and (c) the composite theoretical spectrum obtained by convoluting the above two partial spectra. The stick spectrum of panel c is multiplied by a factor of 3 for a better clarity.

times weaker than that of the ν_2 mode. The intense lines in panel a are ∼0.1874 and ∼0.0662 eV spaced relative to the band origin and correspond to the frequency of the ν_1 and ν_2 vibrational modes, respectively, in the S_4 state.

In contrast to the S_2 state spectrum of Fig. 6.5(a), the spectrum in Fig 6.6(a) exhibits an extended progression owing to a relatively larger coupling strength of ν_1 and ν_2 modes (cf. Table 6.3) in the S_4 state. On the other hand,the spectrum for the JT active e_{2g} vibrational modes for the S_2 state, shown in Fig. 6.5(b), exhibits much more complex structure compared to that for the S_4 state (cf. Fig. 6.6(b)). The complex energy level structure of Fig. 6.5(b) clearly reveals stronger JT coupling effects in the S_2 state and as a result the composite band of this state (panel c of Fig. 6.5) becomes highly diffuse and structureless. Since the JT effect in the S_4 state is extremely weak, the composite band structure of this state [cf. Fig. 6.6(c)] essentially resembles the symmetric mode spectrum of Fig. 6.6(a).

While the spectrum of the individual states presented above contains rich information on the excitation of various vibrational modes, their overall structure is far from the one recorded in the experiment [12, 13, 19–22]. Apart from the JT coupling within the degenerate electronic states, several other interstate couplings (cf. Table 6.4) are important and need to be considered to arrive at a satisfying agreement with the experiment [12, 13, 19–22]. The important interstate couplings are discussed in Sec. 6.4 in terms of the topological characteristics of the adiabatic potential energy surfaces. The dynamical consequences of these couplings are examined and discussed in the following. Twenty three relevant vibrational modes and all relevant couplings of the vibronic Hamiltonian of Eqs. (6.2-6.3) are considered for this exercise. Such a consideration leads to a huge increase of the dimension of the vibronic secular matrix and a diagonalization of it is numerically impossible with the available computer hardware. We therefore use the Heidelberg MCTDH suite of program [47–50], and propagate WPs to calculate the broad band spectrum considering all the required degrees of freedom. The numerical details of these calculations are given in Table 6.6. We note that, it was necessary to adjust the vertical excitation energies within the error limit of EOM-CCSD data to reproduce the adiabatic excitation energies at their experimental values [13, 20, 21]. Apart from this, no other parameters are adjusted in our theoretical calculations. The adjusted vertical excitation energies are given in Table 6.5.

Seven calculations are carried out by initially preparing the WP separately on each component of the S_1-S_2- S_3-S_4-S_5 electronic manifold. The WP in each case is propagated for 200 *fs*. Numerically converged spectra for the S_1 and S_2 states obtained from these calculations are shown in panel c of Fig. 6.7 along with the experimental results in panel a and b reproduced from Ref. [13] and Ref. [20], respectively. The time autocorrelation function is damped with an exponential function, ($e^{-\frac{t}{\tau}}$, with τ_r= 33 fs), prior to its Fourier transformation to calculate the spectrum. Such a damping is equivalent to a convolution of the energy spectrum with a Lorentzian lineshape function of 20 meV FWHM. It can be seen that the theoretical result of panel c is in very good accord with the old and recent experiments [13, 20, 21]. The structured absorption band of the uncoupled S_1 state (cf. Fig. 6.4(a)) becomes essentially structureless upon considering its coupling with the other states. The PJT coupling of S_1 state with S_2 along the ν_{19}

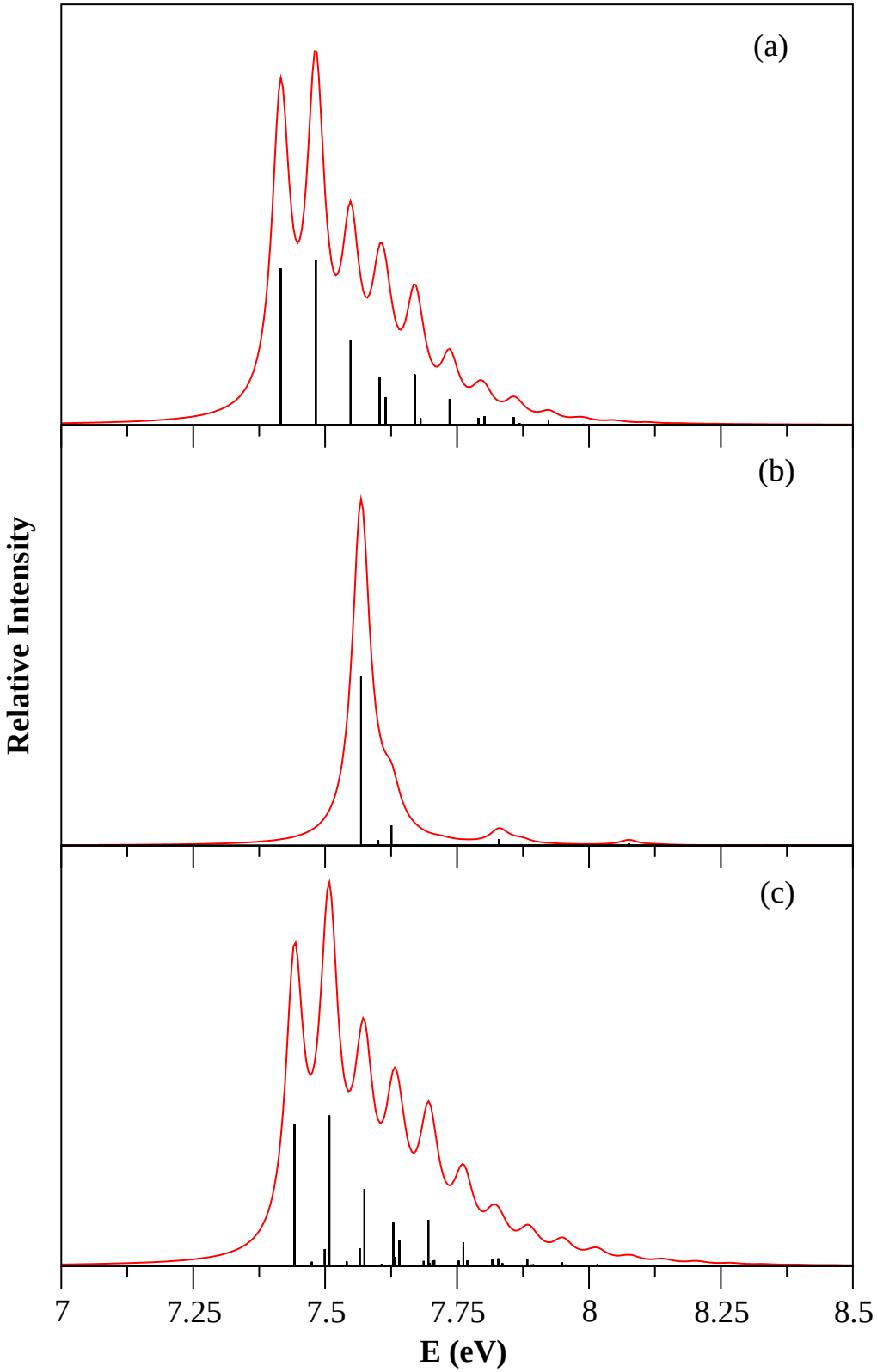

Figure 6.6: Same as in Fig.6.4 for the $S_4\,^1E_{1u} \leftarrow S_0$ electronic transition in HFBz

and ν_{20} vibrational modes [cf. Table 6.4] is very strong. As discussed in Sec. 6.4 the energetic minimum of the S_1 and S_2 CIs occurs at lower energy and the seam of CIs is therefore readily accessible to the nuclear motion on the S_1 electronic state. The intersections of S_1 state with S_3, S_4 and S_5 occur at much higher energies and do not have any impact on the nuclear dynamics on the S_1 state.

The broad band above $\sim$ 5 eV in Fig. 6.7 represents the vibronic structure of the JT active S_2 state. It can be seen from the spectra plotted in panel b and c of Fig. 6.5 for the S_2 state that the JT effect itself is very strong within this state, as a result a bimodal vibronic band is obtained for this electronic state. The S_1-S_2 PJT coupling further broadens the band structure of this state. The energetic minimum of the S_1-S_2 curve crossings is very close to the minimum of the JT intersections within the S_2 electronic state (cf. Sec. 6.4). The two peaks in the bimodal spectral profile arise from the two JT split adiabatic electronic sheets of the S_2 state. These peaks located at $\sim$ 5.35 and $\sim$ 5.75 eV and are in excellent accord with their experimental values [cf. Table 6.5 for a detailed comparison].

The third and fourth absorption bands of HFBz obtained with the full Hamiltonian of Eq. 6.3 are shown in panel b of Fig. 6.8. These bands are formed by the S_3, S_4 and S_5 electronic states of HFBz. All these states are of $\pi\pi^*$ type (cf. Fig.6.1). The corresponding experimental results are reproduced from Ref. [13] and shown in panel a of Fig. 6.8. The two curves in panel a emerged from a decomposition of experimental spectrum [13]. This was done to eliminate the overlapping components and to correctly estimate the oscillator strengths of the two curves of $^1B_{1u}$ and $^1E_{1u}$ Bz parentage [13]. It can be seen from Fig. 6.8 that theoretical results are in satisfactory agreement with the low-resolution experimental data. In case of Bz the signature of the $^1A_{2u}$ state was not seen distinctly as it was buried within the spectral envelope of the JT active E_{1u} state. In case of HFBz the $^1A_{2u}$ state appears vertically at an energy above the JT active $^1E_{1u}$ state (cf. Fig. 6.1). As a result the distinct feature seen at an energy beyond $\sim$ 7.5 eV appears due to the $^1A_{2u}$ electronic state of HFBz (cf. Fig. 6.8). This feature was tentatively assigned at $\sim$7.7 eV in the experimental results (cf. Table 6.5) originating from this state and the present findings confirms this assignment. It is important to note that we carried out various two-coupled states calculations in order to confirm the assignment of the peaks appeared in the broad envelopes of Fig. 6.8(b).

At this point, it is worthwhile to compare the present theoretical results to those available in the literature. The lowering of the $\pi\sigma^*$ state energy with increasing fluorination have been predicted by Zgierski *et al.* [19] and by Studzinski *et al.* [22] through TDDFT calculations. Their results show that this $\pi\sigma^*$ state becomes the lowest excited state in case of HFBz at the equilibrium geometry of the S_0 state. By comparing the features observed in the fluorescence and absorption spectra of jet cooled PFBz and HFBz with other FBz derivatives with less number of fluorine atoms Zgierski *et al.* concluded that the S_1 state of the former molecules deserves a $\pi\sigma^*$ assignment [19]. This assignment is also supported by performing TDDFT calculations by Studzinski *et al.* [22]. However, this assignment differs from that of Motch *et al.* [20] and Holland *et al.* [21] who established with the aid of a combined experimental and computational study that the LUMO of HFBz is of π^* character. The present findings reveal that the lowest $\pi\sigma^*$ state

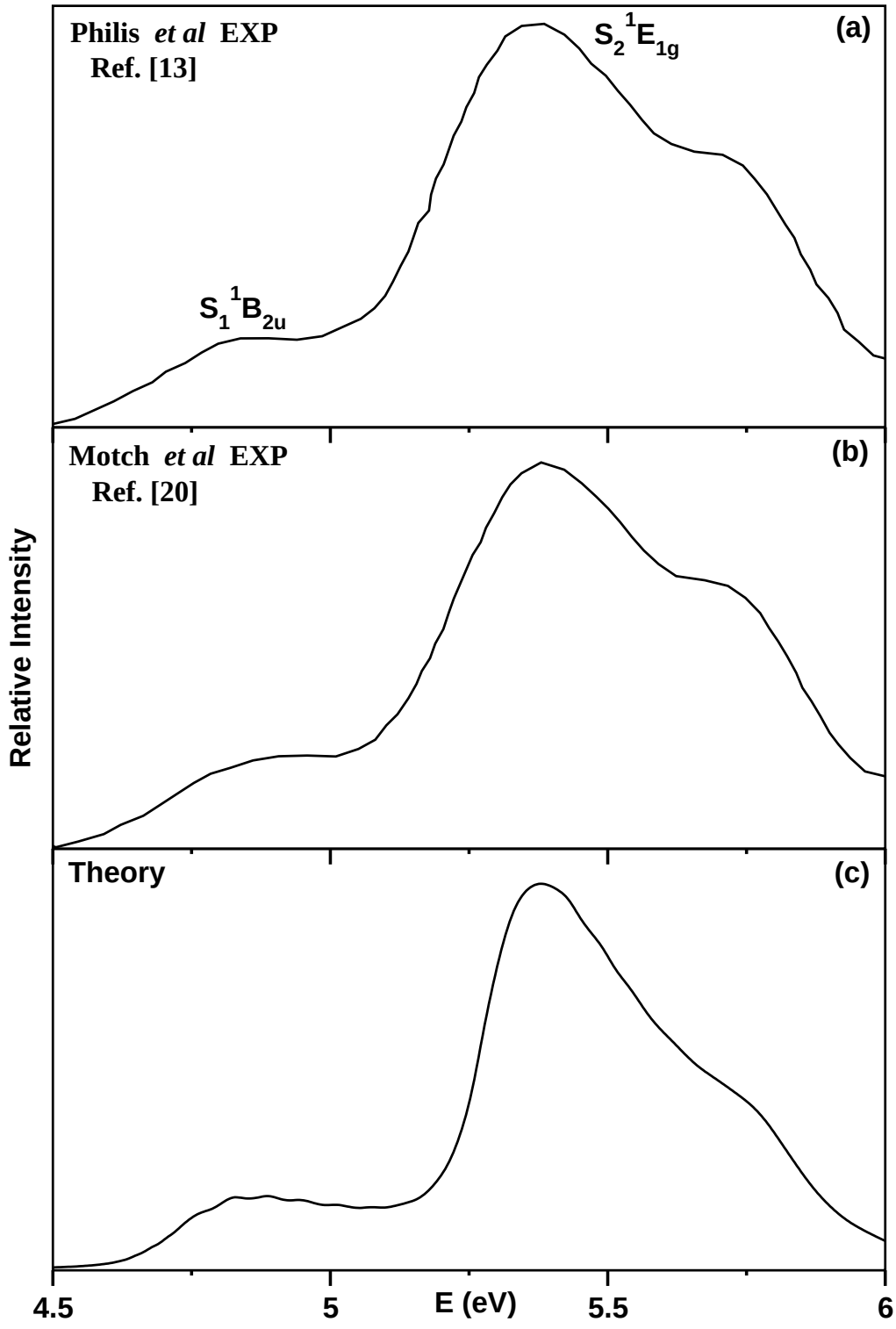

Figure 6.7: Vibronic bands of the S_1-S_2 states of HFBz calculated using seven states and twenty three vibrational modes using MCTDH algorithm with a damping time of 33 *fs*. The experimental [13, 20] and theoretical results are shown in panel a, b and c, respectively. The intensity (in arbitrary unit) is plotted along the energy (relative to minimum of the $^1A_{1g}$ state of HFBz) of the final vibronic states.

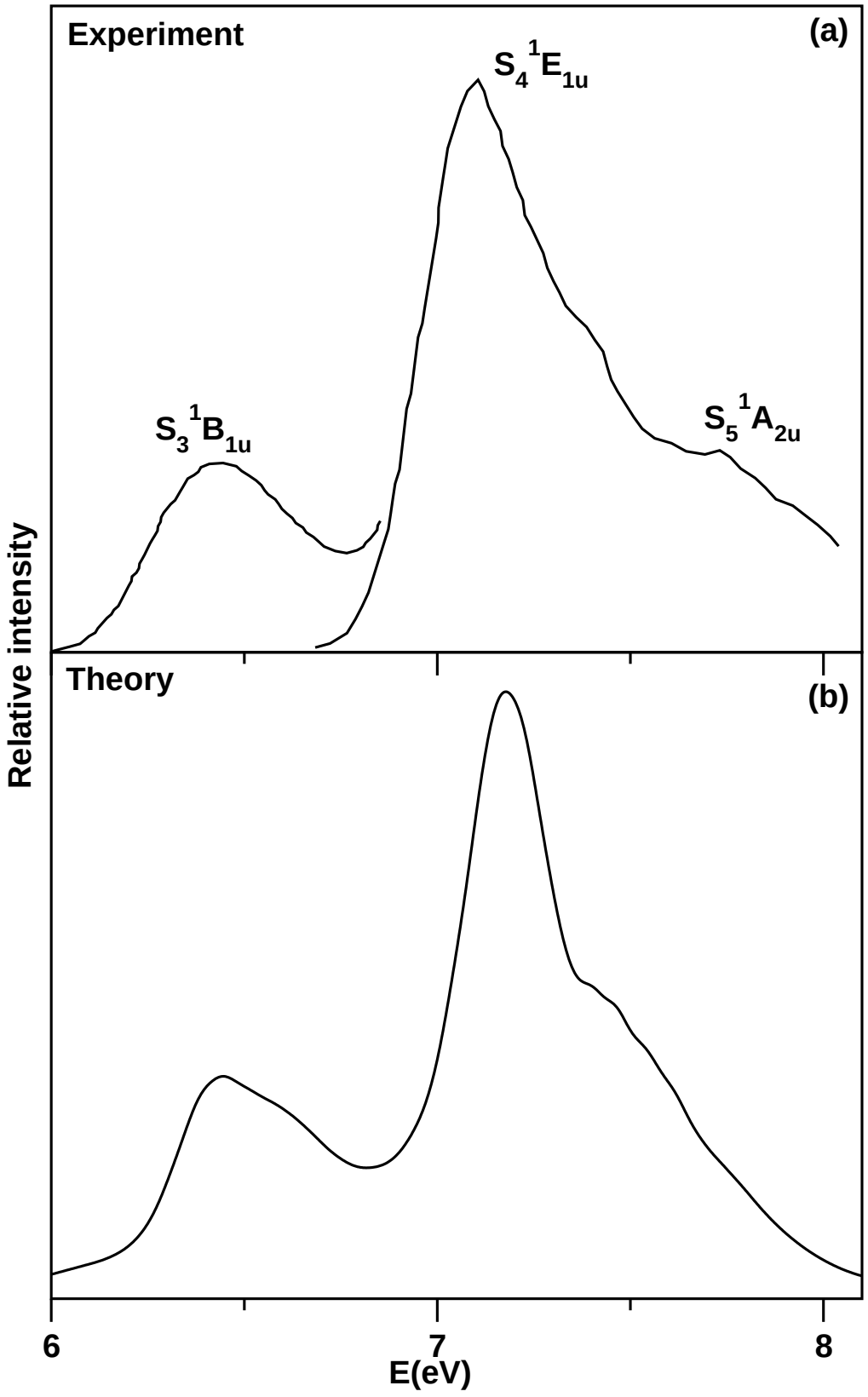

Figure 6.8: Same as Fig. 6.7, for S_3-S_4-S_5 electronic states of HFBz with a damping time of 12 *fs*.

Table 6.6: Normal mode combinations, sizes of the primitive and the single particle basis used in the wave packet propagation within the MCTDH framework in the seven coupled electronic manifold using the complete vibronic Hamiltonian of Eq. (6.3). Second column denotes the vibrational DOF which are combined to particles. Third column gives the number of primitive basis functions for each DOF. Fourth column gives the number of SPFs for each electronic state.

Molecule	Normal modes	Primitive basis	SPF basis
HFBz	(ν_1, ν_{18y}, ν_{20y}, ν_{11y})	(8, 6, 10, 4, 6)	[8,25,25,6,6,6,6]
	(ν_2, ν_{16x}, ν_{20x}, ν_{11x}, ν_{12y})	(10, 5, 10, 4, 6)	[9,6,6,6,12,12,6]
	(ν_{18x}, ν_{17y}, ν_{19x}, ν_{14x}, ν_7)	(6, 8, 10, 4, 6)	[18,18,18,25,6,6,18]
	(ν_{17x}, ν_{16y}, ν_{19y}, ν_{14y}, ν_8)	(8, 5, 10, 4, 8)	[18,8,8,18,9,9,18]
	(ν_{15x}, ν_{15y}, ν_3, ν_{12x})	(8, 8, 4, 6)	[8,6,6,6,6,6,6]

becomes S_2 in HFBz and the assignments of the structure appearing in photoabsorption spectrum between ∼4.5 and ∼6 eV in the present study [25, 26] are consistent with the findings of Philis *et al.* [13], Motch *et al.* [20] and Holland *et al.* [21]. It is intriguing to note that the age old experimental results of Refs. [12, 13] are in very good agreement with those obtained in the modern experiments [20, 21] and it can be seen form Fig. 6.7 that our theoretical results are in perfect accord with the findings from all these experiments. In order to reconfirm, we carried out calculations of VEEs using five other different wavefunction based approaches (as possible for this large system) and also using the TDDFT method. The magnitude of the VEEs differ in each calculations but they confirm that S_1 and S_2 states of HFBz is of $\pi\pi^*$ and $\pi\sigma^*$ character, respectively. The TDDFT calculations using the G03 program package [52] indeed gave a reverse energetic ordering of these two states as reported in Refs. [19, 22]. To save space and brevity we do not include here all the test results obtained by us using different electronic structure methods. Instead, we note that the electronic structure results employed in this work offers the best agreement with the experiment for this "large"molecular system. The detailed analysis carried out here along with the literature results (both theory and experiments, see Table 6.5) confirm that the S_2 state is $\pi\sigma^*$ in HFBz at the equilibrium geometry of the S_0 state. This state comes down in energy with increasing fluorination and forms the lowest energy CIs with the S_1 state in HFBz. Further support to the above assignment of the state order arise from a recent experimental and computation study on perfluorinated oligophenylenes. For these higher homologues of HFBz the S_1 state is found to be of $\pi\pi^*$ type [64].

Temps *et al.* have studied ultrafast nonradiative dynamics of electronically excited HFBz [22]. These authors arrived at the same results as reported by Zgierski *et al.* [19]. The S_1 state was found to be of $\pi\sigma^*$ type ($^1E_{1g}$ symmetry) through TDDFT calculations [22]. Four peaks were reported in the optical absorption spectrum of HFBz recorded by Temps *et al.* (cf. Fig. 1 of Ref. [22]) in the ∼ 210-280 nm wavelength region. Apparently, the weakest one appearing at the longest wavelength was assigned to the $S_1(^1E_{1g}) \leftarrow S_0(^1A_{1g})$ transition. This transition is dipole forbidden. The weak absorption and low-

quantum yield of fluorescence of this optically dark state is attributed to its strong nonadiabatic coupling with the $^1B_{2u}(S_2)$ state of $\pi\pi^*$ origin. The next three peaks were assigned to the $S_2(^1B_{2u}) \leftarrow S_0(^1A_{1g})$, $S_3(^1B_{1u}) \leftarrow S_0(^1A_{1g})$ and $S_4(^1E_{1u}) \leftarrow S_0(^1A_{1g})$ transition, respectively. The present electronic structure and dynamics results reported in Figs. 6.1, 6.5 and 6.7 differ considerably from this assignment. We reiterate that the S_1 state is a $\pi\pi^*$ state and NOT a $\pi\sigma^*$ state at the equilibrium configuration the S_0 state of HFBz (cf. Fig. 6.1). A wave function based approach of quantum chemical calculations, therefore predicted that the S_1 state is of $^1B_{2u}$ symmetry. Unlike in Ref. [22], the three peaks observed in the spectrum plotted in the panel c of Fig. 6.7 are assigned to a transition to the $^1B_{2u}(S_1)$ and $^1E_{1g}(S_2)$ electronic states of HFBz. The bimodal structure of the latter band arises due to strong JT splitting of 1^1E_{1g} state along the vibrational modes of e_{2g} symmetry. These assignments are also consistent with the experimental results of Philis *et al.* [13], Motch *et al.* [20] and Holland *et al.* [21]. The splitting between the two maxima of the theoretical spectrum of ∼0.40 eV of the $S_2{}^1E_{1g}$ [*cf.* Fig. 6.7(c)] state compares well with it's experimental value [13].

6.6 Internal conversion dynamics

In order to understand the impact of complex nonadiabatic coupling on the dynamics of the coupled S_1-S_2-S_3-S_4-S_5 excited electronic states, the time-dependence of diabatic electronic populations is plotted in Fig. 6.9. These electronic populations are obtained by initially locating the WP on the S_1 state, one component of the JT split S_2 state, the S_3 state, one component of the JT split S_4 state and the S_5 state and shown in Fig. 6.9, respectively. It can be seen from panel a of Fig. 6.9 that the electronic population transfer occurs only to the S_2 state when the WP is initially prepared on the S_1 state. It was found in our previous work [26] that the energetic minimum of S_1-S_2 CIs decreases gradually from MFBz to PFBz due to the lowering of S_2 state energy by the perfluoro effect. The present calculations reveal that the minimum of the S_1-S_2 CIs in HFBz occurs at ∼5.51 eV, which is even lower in energy compared to that of PFBz occurring at ∼ 6.92 eV (see Table VIII of Ref. [25]). Therefore, the S_1-S_2 CI is more readily accessible to the WP moving on the S_1 state of HFBz when compared to PFBz. The initial decay of the population relates to a nonradiative internal conversion rate of ∼ 153 *fs* of the S_1 state. The femtosecond time-resolved experiment of Temps *et al.* [22] predicts a decay rate of ∼ 172 fs of this initially excited state. We reiterate that this state is designated as $\pi\sigma^*$ in contrast to our designation as $\pi\pi^*$.

The CIs of S_1 state with S_3, S_4 and S_5 states occur at high energies and these are not accessible to the WP prepared on the S_1 state as clearly indicated by the population diagram shown in Fig. 6.9. It is discussed above that the S_1-S_2 CIs are the bottleneck underlying the broadening of the $S_1 \leftarrow S_0$ absorption band in HFBz. The WP initially prepared on the S_2 state moves very fast to the S_1 state (panel b). A nonradiative decay rate of ∼22 *fs* can be estimated from the population curve of S_2 state given in panel b. It is to be noted from the population diagram of Fig. 6.9, that the population of the second component of the JT split S_2 state also grows in time. However, the population

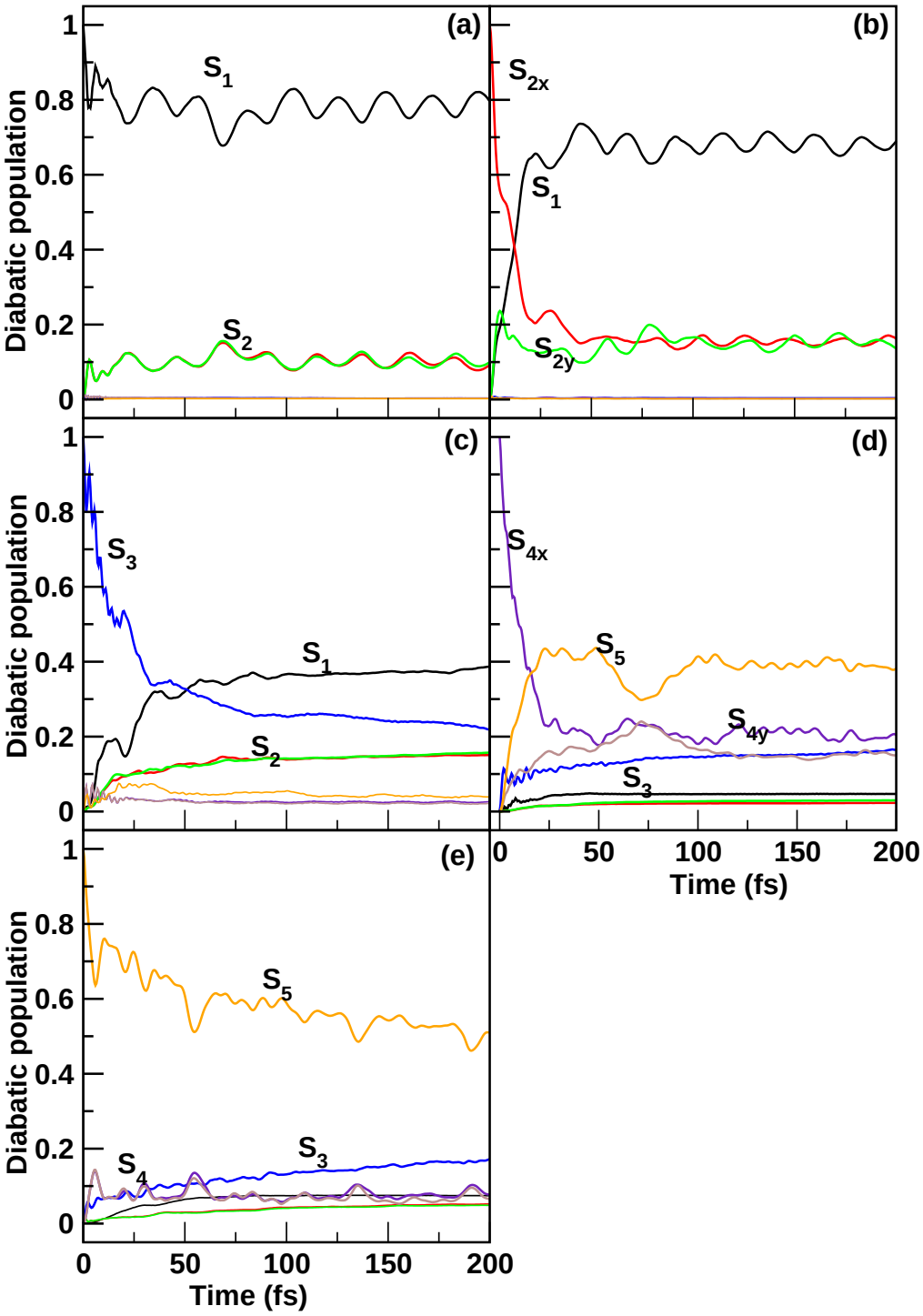

Figure 6.9: Time-dependence of diabatic electronic populations in the S_1-S_2-S_3-S_4-S_5 coupled state nuclear dynamics of HFBz. The results obtained by initially locating the WP on the S_1 state, one component of the JT split S_2 state, S_3 state, one component of the JT split S_4 state and S_5 state are shown in panel a-e, respectively.

growth of the latter state is much slower than that of the S_1 state. This indicates that the S_1-S_2 PJT coupling is much stronger than the JT coupling within the S_2 electronic manifold. The electronic structure data given in Tables 6.3 and 6.4 are in accord with these findings. Therefore it is clear that much of the broadening of the spectral envelope of the S_1 and S_2 state is caused by the strong S_1-S_2 PJT coupling particularly, along the ν_{20} vibrational mode of e_{2u} symmetry.

The electron population dynamics becomes more complex and involved when the WP is initially prepared either on the S_3 (panel c), S_4 (panel d) or S_5 (panel e) electronic state. In the former case most of the population transfers to S_1 state via two consecutive low-energy S_3-S_2 and S_2-S_1 CIs. Similarly, when the WP is prepared on the S_4 state the internal conversion to the S_3 and S_5 states occurs due to strong S_4-S_3 and S_4-S_5 interstate coupling (cf. Table 6.4). The initial sharp decay of the population of the S_3 and S_4 states in panels c and d relates to the nonradiative decay rate of $\sim$67 and $\sim$28 *fs* of these states, respectively. When the WP is prepared on the S_5 state, the population transfers to the S_3 and S_4 states only. A nonradiative decay rate of $\sim$110 *fs* is found for this state.

A few remarks are in order at this point. The electronic structure and quantum dynamics results presented above revealed excellent agreement with the experimental findings. The detailed comparative account on the energetic location of the bands presented in Table 6.5 reveals that the present theoretical results are in perfect accord with the experimental findings of Frueholz *et al.* [11,12], Philis *et al.* [13], Motch *et al.* [20] and Holland *et al.* [21]. Apart from a reverse energetic ordering of the two lowest excited electronic states of HFBz the other observations made in the experiment of Ref. [19, 22] can very well be understood from the present theoretical results. It is shown that the PJT coupling between the S_1 and S_2 states of HFBz is much stronger than the JT coupling within the S_2 electronic state. It is discussed in section 6.4 that the energetic minimum of the S_1-S_2 intersection is near degenerate to the minimum of the S_2 state. This energetic minimum of the S_2 state occurs at a displaced geometry at Q_1=-0.79, Q_2=0.66, Q_{15x}=-0.94, Q_{16x}=-0.41, Q_{17x}=-1.99, Q_{18x}=-1.21, Q_{19x}=0.0, Q_{20x}=0.0 from the original vertical configuration (at Q=0). It can be seen that $\sim$ 20 % of the electronic population flows to the S_2 state (cf. panel a of Fig.6.9) upon an initial Franck-Condon transition to the S_1 ($\pi\pi^*$) state. A part of this 20% population trapped in the vicinity of the minimum of the S_2 ($\pi\sigma^*$) state gives rise to fluorescence emission. Since this part is expected to be quite small, extremely low quantum yield of fluorescence is obtained in the experimental measurements [19]. Also, since this emission occurs from a geometry away from the vertical configuration (as stated above), overlap of the absorption and emission band is not observed [19]. Strong S_1-S_2 nonadiabatic interaction causes a mixing of the energetically low-lying vibronic levels of the S_2 state with the continuum levels of the S_1 state and gives rise to a large spectral width. The relatively weaker JT coupling within the S_2 state also contributes to the spectral broadening as discussed in Sec 6.5 above.

6.7 summary

A detailed theoretical account of multi-mode JT and PJT interactions in five lowest excited singlet electronic states of HFBz is presented in this contribution. Extensive electronic structure calculations are performed to develop a model diabatic vibronic coupling Hamiltonian (Eqs. 6.2-6.6b), and first-principles dynamics calculations are carried out both via time-independent and time-dependent quantum mechanical methods. The calculated adiabatic potential energies of five electronic states are parametrized to establish the diabatic vibronic Hamiltonian. Using the constructed Hamiltonian the nuclear dynamics is systematically studied to reveal impact of electronic nonadiabatic coupling on the dynamics. The electronic structure data reveal multiple CIs among these excited electronic states of HFBz. The theoretical findings are found to be in good accord with the available experimental results.

Several issues regarding the complex vibronic dynamics of HFBz (as compared to Bz) are addressed and resolved in this chapter. The major findings are the following.
1. The S_2 state of HFBz is JT active, two $\pi\sigma^*$ states are energetically degenerate in this case. This is not the case for any other fluoro derivatives of Bz with number of fluorine atoms less than 6.
2. Some of the earlier works [19, 22] predicted that the S_1 state is of $\pi\sigma^*$ type in PFBz and HFBz. This assignment has been found to be incorrect in the present study. The S_1 state is of $\pi\pi^*$ type for all FBz molecules. This result is also in accord with the recent findings in the literature [21].
3. The present assignment of the peaks in the photoabsorption spectrum of HFBz is in agreement with the experimental results of Philis *et al.* [13] but is in contradiction with that of Temps *et al.* [22].
4. The structureless S_1 band of HFBz originates from energetically low-lying CIs of the S_1 and S_2 states and very strong PJT coupling among them.
5. The bimodal shape of the second photoabsorption band originates from the orbitally degenerate JT active $^1E_{1g}$ electronic state of HFBz. The energetic location of these two peaks is in good agreement with the experimental results of Philis *et al.* [13]. The JT coupling is strong in this electronic state which causes a bimodal shape of the absorption profile, the PJT coupling of this state with S_1 is even stronger which causes this bimodal spectral profile structureless. We note that this state is optically dark for a transition from the electronic ground state of HFBz. The absorption profile of this state seen in the experiment is due to its vibronic coupling with the optically bright S_1 state.
6. The JT coupling in the $^1E_{1u}$ electronic state is far weaker than in the $^1E_{1g}$ state of HFBz. The $^1E_{1g}$-$^1E_{1u}$ PJT coupling is symmetry allowed and there exist vibrational modes of appropriate symmetry to cause this coupling. The symmetry invariance of $^1E_{1g}$- $^1E_{1u}$ coupling matrix is studied and the relative phases of the coupling elements are derived. However, thorough analysis of the electronic structure data reveal negligible coupling among these degenerate electronic states.
7. The third and forth absorption bands of HFBz are formed by three $\pi\pi^*$ type of orbitals of $^1B_{1u}$, $^1E_{1u}$ and $^1A_{2u}$ symmetry. Unlike in case of Bz, the signature of the $^1A_{2u}$ state is clearly seen in the absorption spectrum of HFBz. This state appears at

$\sim$ 7.7 eV in the experimental spectrum [13] and is in good accord with our theoretical results.
8. Nonradiative decay rate of $\sim$ 153 fs and $\sim$ 22 fs is found for the S_1 and S_2 state, respectively. Electronic population transfer occurs to the S_1 state via S_3-S_2 and S_3-S_1 CIs when the S_3 state is initially populated. Likewise, nonradiative electron population transfer occurs to the S_3, S_5 and S_3, S_4 states when the S_4 and S_5 states are initially populated, respectively. These nonradiative transfer of electron populations relate to decay rate of $\sim$ 67, 28 and 110 fs, respectively, of the S_3, S_4 and S_5 electronic states of HFBz.

6.8 Appendix: Symmetry analysis of $E_{1g} - E_{1u}$ JT and PJT Hamiltonian

The symmetry invariance of the vibronic Hamiltonian of Bz^+ discussed by Köppel and coworkers has been found to be applicable in case of HFBz also as both the systems belong to D_{6h} symmetry point group. In this appendix we examine the symmetry invariance of the $E_{1g} - E_{1u}$ PJT coupling block of the vibronic Hamiltonian of Eq. 6.3b. Since HFBz belongs to same D_{6h} symmetry point group as Bz^+, the JT coupling matrix derived for the E_{1g} and E_{1u} states in Ref. [35] is applicable to those states of HFBz also. The D_{6h} symmetry point group can be represented as $D_{6h} = D_6 \otimes i$; Where i represents the inversion operation. Like Bz^+ the latter operation is trivial for HFBz also. The principal rotation axis C_ϕ can be 2, 3 and 6 fold. The other symmetry operations are E, C_2' and C_2''. It is stated in the introduction that the symmetry rule allows the vibrational modes of e_{2u}, a_{2u} and a_{1u} to be PJT active in first-order in the $E_{1g} - E_{1u}$ coupled electronic manifold. Considering only the linear coupling terms the following analysis can be made.

A coupled Hamiltonian in the E_{1g} and E_{1u} electronic function spaces can be represented in terms of the electronic projection operators. Let the kets $|x_1\rangle$, $|y_1\rangle$ and $|x_2\rangle$, $|y_2\rangle$ and the corresponding bras represent the first and second rows/columns of the E_{1g} and E_{1u} representation matrices as given in Ref. [35]. Let us also denote the components of the degenerate vibrational modes by Q_x and Q_y. The following transformations hold.

First we will derive the vibronic Hamiltonian for JT active E_{1g} and E_{1u} electronic states.

$$\begin{aligned}
[|x_1\rangle\langle x_1| - |y_1\rangle\langle y_1|] \xrightarrow{C_\phi} & [cos^2(\phi) - sin^2(\phi)][|x_1\rangle\langle x_1| - |y_1\rangle\langle y_1|] \\
& +(2cos(\phi)sin(\phi))[|x_1\rangle\langle x_1| + |y_1\rangle\langle y_1|] \\
= & \; cos(2\phi)[|x_1\rangle\langle x_1| - |y_1\rangle\langle y_1|] \\
& +sin(2\phi)[|x_1\rangle\langle y_1| + |y_1\rangle\langle x_1|] \qquad \text{(A1)}
\end{aligned}$$

$$\begin{aligned} |x_1\rangle\langle y_1| + |y_1\rangle\langle x_1| &\xrightarrow{C_\phi} -2cos(\phi)sin(\phi)[|x_1\rangle\langle x_1| - |y_1\rangle\langle y_1|] \\ &\quad +(cos^2(\phi) - sin^2(\phi))[|x_1\rangle\langle y_1| - |y_1\rangle\langle x_1|] \\ &= -sin(2\phi)[|x_1\rangle\langle x_1| - |y_1\rangle\langle y_1|] \\ &\quad +cos(2\phi)[|x_1\rangle\langle y_1| + |y_1\rangle\langle x_1|] \end{aligned} \tag{A2}$$

From Eq. (A1) and Eq. (A2),

$$\begin{aligned} \begin{bmatrix} |x_1\rangle\langle x_1| - |y_1\rangle\langle y_1| \\ |x_1\rangle\langle y_1| + |y_1\rangle\langle x_1| \end{bmatrix} &\xrightarrow{C_\phi} \begin{bmatrix} cos(2\phi) & sin(2\phi) \\ -sin(2\phi) & cos(2\phi) \end{bmatrix} \begin{bmatrix} |x_1\rangle\langle x_1| - |y_1\rangle\langle y_1| \\ |x_1\rangle\langle y_1| + |y_1\rangle\langle x_1| \end{bmatrix} \\ &= Q_x[|x_1\rangle\langle x_1| - |y_1\rangle\langle y_1|] + Q_y[|x_1\rangle\langle y_1| + |y_1\rangle\langle x_1|] \end{aligned}$$

$Q_x[|x_1\rangle\langle x_1| - |y_1\rangle\langle y_1|] + Q_y[|x_1\rangle\langle y_1| + |y_1\rangle\langle x_1|]$, is invariant with respect to C_ϕ. Where Q_x and Q_y represent the x and y components of either e_{2g} or e_{2u} mode. Under inversion operator ($|x_1\rangle$, $|y_1\rangle$) and (Q_x, Q_y) transform as ($|x_1\rangle$, $|y_1\rangle$) and ($\pm Q_x$, $\pm Q_y$). To make the function $Q_x[|x_1\rangle\langle x_1| - |y_1\rangle\langle y_1|] + Q_y[|x_1\rangle\langle y_1| + |y_1\rangle\langle x_1|]$ invariant with respect to inversion, (Q_x, Q_y) should transform as (Q_x, Q_y) and hence the normal mode is a gerade e_{2g} representation. Similarly, this function can be shown to invariant with respect to the operations C_2' and C_2''.

Considering the symmetry invariance with respect to the operations given above, the E_{1g} JT coupling matrix for the e_{2g} vibrational mode is given by

$$\mathcal{H}^{JT}_{e_{2g}} = \begin{pmatrix} \lambda Q_x & \lambda Q_y \\ \lambda Q_y & -\lambda Q_x \end{pmatrix}$$

$$\begin{aligned} |x_1\rangle\langle x_1| + |y_1\rangle\langle y_1| &\xrightarrow{C_\phi} [cos^2(\phi) + sin^2(\phi)][|x_1\rangle\langle x_1| + |y_1\rangle\langle y_1|] \\ &= [|x_1\rangle\langle x_1| + |y_1\rangle\langle y_1|] \end{aligned} \tag{A3}$$

$$\begin{aligned} |x_1\rangle\langle y_1| - |y_1\rangle\langle x_1| &\xrightarrow{C_\phi} [cos^2(\phi) + sin^2(\phi)][|x_1\rangle\langle y_1| - |y_1\rangle\langle x_1|] \\ &= [|x_1\rangle\langle y_1| - |y_1\rangle\langle x_1|] \end{aligned} \tag{A4}$$

It can be proved that $Q_{a_{1g}}[|x_1\rangle\langle x_1| + |y_1\rangle\langle y_1|]$ and $Q_{a_{1u}}[|x_1\rangle\langle y_1| - |y_1\rangle\langle x_1|]$ are invariant with respect to all symmetry operations of D_6 point group. The E_{1g} JT coupling matrix for the a_{1g} and a_{1u} vibrational modes is given by

$$\mathcal{H}^{JT}_{a_{1g}\&a_{1u}} = \begin{pmatrix} \kappa Q_{a_{1g}} & \beta Q_{a_{1u}} \\ -\beta Q_{a_{1u}} & \kappa Q_{a_{1g}} \end{pmatrix}$$

The hermitian property of Hamiltonian requires

$$\begin{aligned}
\mathcal{H}_{12} &= \mathcal{H}_{21}^{*} \\
\beta Q_{a_{1u}} &= (-\beta Q_{a_{1u}})^{*} \\
\beta Q_{a_{1u}} &= -\beta Q_{a_{1u}} \text{ since the Hamiltonian is real} \\
2\beta Q_{a_{1u}} &= 0 \\
\beta &= 0 \text{ since } Q_{a_{1u}} \neq 0
\end{aligned}$$

Similarly the JT hamiltonian for E_{1u} can also be deduced from the symmetry properties. Now we proceed to deduce the E_{1g}-E_{1u} PJT coupling matrix.

$$\begin{aligned}
[|x_1\rangle\langle x_2| - |y_1\rangle\langle y_2|] \xrightarrow{C_\phi} & [cos^2(\phi) - sin^2(\phi)][|x_1\rangle\langle x_2| - |y_1\rangle\langle y_2|] \\
& +(2cos(\phi)sin(\phi))[|x_1\rangle\langle x_2| + |y_1\rangle\langle y_2|] \\
= & \; cos(2\phi)[|x_1\rangle\langle x_2| - |y_1\rangle\langle y_2|] \\
& +sin(2\phi)[|x_1\rangle\langle y_2| + |y_1\rangle\langle x_2|] \qquad \text{(A5)}
\end{aligned}$$

$$\begin{aligned}
|x_1\rangle\langle y_2| + |y_1\rangle\langle x_2| \xrightarrow{C_\phi} & -2cos(\phi)sin(\phi)[|x_1\rangle\langle x_2| - |y_1\rangle\langle y_2|] \\
& +(cos^2(\phi) - sin^2(\phi))[|x_1\rangle\langle y_2| - |y_1\rangle\langle x_2|] \\
= & -sin(2\phi)[|x_1\rangle\langle x_2| - |y_1\rangle\langle y_2|] \\
& +cos(2\phi)[|x_1\rangle\langle y_2| + |y_1\rangle\langle x_2|] \qquad \text{(A6)}
\end{aligned}$$

From Eq. (A5) and Eq. (A6),

$$\begin{aligned}
\begin{bmatrix} |x_1\rangle\langle x_2| - |y_1\rangle\langle y_2| \\ |x_1\rangle\langle y_2| + |y_1\rangle\langle x_2| \end{bmatrix} \xrightarrow{C_\phi} & \begin{bmatrix} cos(2\phi) & sin(2\phi) \\ -sin(2\phi) & cos(2\phi) \end{bmatrix} \begin{bmatrix} |x_1\rangle\langle x_2| - |y_1\rangle\langle y_2| \\ |x_1\rangle\langle y_2| + |y_1\rangle\langle x_2| \end{bmatrix} \\
= & \; Q_x[|x_1\rangle\langle x_2| - |y_1\rangle\langle y_2|] + Q_y[|x_1\rangle\langle y_2| + |y_1\rangle\langle x_2|]
\end{aligned}$$

$Q_x[|x_1\rangle\langle x_2| - |y_1\rangle\langle y_2|] + Q_y[|x_1\rangle\langle y_2| + |y_1\rangle\langle x_2|]$, is invariant with respect to C_ϕ. Where Q_x and Q_y represent the x and y components of the e_{2u} mode.

Now a C_2' rotation transforms $(|x_1\rangle, |y_1\rangle)$, $(|x_2\rangle, |y_2\rangle)$ and (Q_x, Q_y) to $(-|x_1\rangle, |y_1\rangle)$, $(|x_2\rangle, -|y_2\rangle)$ and $(-Q_x, Q_y)$, respectively. Therefore,

$$\begin{aligned}
Q_x[|x_1\rangle\langle x_2| - |y_1\rangle\langle y_2|] + Q_y[|x_1\rangle\langle y_2| + |y_1\rangle\langle x_2|] \xrightarrow{C_2'} & (-Q_x)[(-|x_1\rangle)\langle x_2| - |y_1\rangle(-\langle y_2|)] \\
& +Q_y[(-|x_1\rangle)(-\langle y_2|) + |y_1\rangle\langle x_2|] \\
= & \; Q_x[|x_1\rangle\langle x_2| - |y_1\rangle\langle y_2|] + Q_y[|x_1\rangle\langle y_2| + |y_1
\end{aligned}$$

is also invariant with respect to C_2' rotation.

Similarly a C_2'' rotation transforms $(|x_1\rangle, |y_1\rangle)$, $(|x_2\rangle, |y_2\rangle)$ and (Q_x, Q_y) to $(|x_1\rangle, -|y_1\rangle)$,

$(-|x_2\rangle, |y_2\rangle)$ and $(-Q_x, Q_y)$, respectively. and

$$\begin{aligned} Q_x[|x_1\rangle\langle x_2| - |y_1\rangle\langle y_2|] + Q_y[|x_1\rangle\langle y_2| + |y_1\rangle\langle x_2|] &\xrightarrow{C_2''} (-Q_x)[|x_1\rangle(-\langle x_2|) - (-|y_1\rangle)\langle y_2|] \\ &\quad +Q_y[|x_1\rangle\langle y_2| + (-|y_1\rangle)(-\langle x_2|)] \\ &= Q_x[|x_1\rangle\langle x_2| - |y_1\rangle\langle y_2|] + Q_y[|x_1\rangle\langle y_2| + |y_1\rangle\langle x_2|] \end{aligned}$$

is invariant with respect to C_2'' rotation also.

Considering the symmetry invariance with respect to the operations given above the $E_{1g} - E_{1u}$ PJT coupling matrix for the e_{2u} vibrational mode is given by

$$\mathcal{H}_{e_{2u}}^{PJT} = \begin{pmatrix} E_{E_{1g}}^x & 0 & \lambda Q_x & \lambda Q_y \\ 0 & E_{E_{1g}}^y & \lambda Q_y & -\lambda Q_x \\ \lambda Q_x & \lambda Q_y & E_{E_{1u}}^x & 0 \\ \lambda Q_y & -\lambda Q_x & 0 & E_{E_{1u}}^y \end{pmatrix}$$

The PJT coupling matrix for the a_{2u} mode can be derived similarly as follows.

$$\begin{aligned} |x_1\rangle\langle x_2| + |y_1\rangle\langle y_2| &\xrightarrow{C_\phi} [cos^2(\phi) + sin^2(\phi)][|x_1\rangle\langle x_2| + |y_1\rangle\langle y_2|] \\ &= [|x_1\rangle\langle x_2| + |y_1\rangle\langle y_2|] \end{aligned} \tag{A7}$$

$$\begin{aligned} |x_1\rangle\langle x_2| + |y_1\rangle\langle y_2| &\xrightarrow{E} |x_1\rangle\langle x_2| + |y_1\rangle\langle y_2| \\ |x_1\rangle\langle x_2| + |y_1\rangle\langle y_2| &\xrightarrow[\phi=6,3,2]{C_\phi} |x_1\rangle\langle x_2| + |y_1\rangle\langle y_2| \\ |x_1\rangle\langle x_2| + |y_1\rangle\langle y_2| &\xrightarrow{C_2'} -|x_1\rangle\langle x_2| + |y_1\rangle(-\langle y_2|) = -[|x_1\rangle\langle x_2| + |y_1\rangle\langle y_2|] \\ |x_1\rangle\langle x_2| + |y_1\rangle\langle y_2| &\xrightarrow{C_2''} -[|x_1\rangle\langle x_2| + |y_1\rangle\langle y_2|] \\ |x_1\rangle\langle x_2| + |y_1\rangle\langle y_2| &\xrightarrow{i} -[|x_1\rangle\langle x_2| + |y_1\rangle\langle y_2|] \end{aligned}$$

The characters of the a_{2u} mode are (1,1,1,1,-1,-1,-1) for (E, C_6, C_3, C_2, C_2', C_2'', i) operations in the D_{6h} symmetry point group. Thus $[|x_1\rangle\langle x_2| + |y_1\rangle\langle y_2|]Q_{a_{2u}}$ is invariant with respect to all symmetry operations of the D_{6h} point group. Similarly, it can be trivially shown that $[|x_1\rangle\langle y_2| - |y_1\rangle\langle x_2|]Q_{a_{1u}}$ is invariant with respect to all the symmetry operations of the D_{6h} point group. The PJT coupling Hamiltonian for the a_{2u} and a_{1u} vibrational modes is therefore given by

$$\mathcal{H}_{a_{2u},a_{1u}}^{PJT} = \begin{bmatrix} E_{E_{1g}}^x & 0 & \lambda' Q_{a_{2u}} & \lambda'' Q_{a_{1u}} \\ 0 & E_{E_{1g}}^y & -\lambda'' Q_{a_{1u}} & \lambda' Q_{a_{2u}} \\ \lambda' Q_{a_{2u}} & -\lambda'' Q_{a_{1u}} & E_{E_{1u}}^x & 0 \\ \lambda'' Q_{a_{1u}} & \lambda' Q_{a_{2u}} & 0 & E_{E_{1u}}^y \end{bmatrix} \tag{A8}$$

We mention that analysis of the *ab initio* electronic structure data reveal that the E_{1g}-E_{1u} PJT coupling is not relevant for HFBz.

References

[1] C. R. Brundle, M. B. Robin, and N. A. Kuebler, J. Am. Chem. Soc. **94**, 1466 (1972).

[2] H. Sponer, J. Chem. Phys. **22**, 234 (1954).

[3] C. D. Cooper, J. Chem. Phys. **22**, 503 (1954).

[4] K. N. Rao, H. Sponer, Can. J. Phys. **35**, 332 (1957).

[5] D. Phillips, J. Chem. Phys. **46**, 4679 (1967).

[6] R. Gilbert, P. Sauvageau, and C. Sandorfy, Can. J. Chem. **50**, 543 (1972).

[7] G. L. Loper, and E. K. C. Lee, Chem. Phys. Lett. **13**, 140 (1972).

[8] J. Metcalfe, M. G. Rockley, and D. Philips, J. Chem. Soc. Faraday Trans. 2. **70**, 1660 (1974).

[9] M. B. Robin, *Higher Excited States of Polyatomic Molecules*, Vol. III (Academic, New York, 1975), and references therein.

[10] C. B. Duke, K. L. Yip, G. P. Ceaser, A. W. Potts, and D. G. Streets, J. Chem. Phys. **66**, 256 (1976).

[11] R. P. Frueholz, W. M. Flicker, O. A. Mosher, and A. Kuppermann, J. Chem. Phys. **70**, 3057 (1979).

[12] R.P. Frueholz, W.M. Flicker, O.A. Mosher, A. Kuppermann, Chem. Phys.Lett. **52**, 86. (1977)

[13] J. Philis, A. Bolovinos, G. Andritsopoulos, E. Pantos, and P. Tsekeris, J. Phys. B: At. Mol. Phys. **14**, 3621 (1981).

[14] A. P. Hitchcock, P. Fischer, A. Gedanken, M. B. Robin, J. Phys. Chem. **91**, 531, (1987).

[15] D. R. Smith, J. W. Raymonda, Chem. Phys. Lett. **12**, 269, (1971).

[16] D. V. O'connor, M. Sumitani, J. M. Morris, and K. Yoshihara, Chem. Phys. Lett. **93**, 350 (1982).

[17] O. Plashkevych, L. Yang, O. Vahtras, and L. G. M. Pettersson, Chem. Phys. **222**, 125 (1997).

[18] C. D. Keefe, J. Barrett, and L. L. Jessome, J. Mol. Struc. **734**, 67 (2005).

[19] M. Z. Zgierski, T. Fujiwara, and E. C. Lim, J. Chem. Phys. **122**, 144312 (2005).

[20] C. Motch, A. Giuliani, J. Delwiche, P. Limao-Vieira, N. J. Mason, S. V. Hoffmann, and M. -J. Hubin-Franskin, Chem. Phys. **328**, 183, (2006).

[21] D. M. P. Holland, D. A. Shaw, M. Stener, and P. Decleva, J. Phys. B: At. Mol. Opt. Phys. **42**, 245201 (2009)

[22] H. Studzinski, S. Zhang, Y. Wang, and F. Temps, J. Chem. Phys. **128**, 164314 (2008).

[23] S. H. Lee, C. Y. Wu, S. K. Yang, and Y. P. Lee, J. Chem. Phys. **125**, 144301 (2006).

[24] I. Pugliesi, N. M. Tonge, and M. C. R. Cockett, J. Chem. Phys. **129**, 104303 (2008).

[25] T. Mondal, and S. Mahapatra, J. Chem. Phys. **133**, 084304 (2010).

[26] T. Mondal, and S. Mahapatra, J. Chem. Phys. **133**, 084305 (2010).

[27] E. Gindensperger, I. Bâldea, J. Franz, and H. Köppel, Chem. Phys. **338**, 207 (2007).

[28] S. Faraji, and H. Köppel, J. Chem. Phys. **129**, 74310 (2008).

[29] S. Faraji, H. -D. Meyer, and H. Köppel, J. Chem. Phys. **129**, 74311 (2008).

[30] T. Mondal, and S. Mahapatra, Phys. Chem. Chem. Phys. **11**, 10867 (2009).

[31] J. G. Philis, T. Mondal, and S. Mahapatra, Chem. Phys. Lett. **495**, 187 (2010).

[32] H. Sponer, D. Nordheim, A. L. Sklar and E. Teller, J. Chem. Phys. **7**, 207, (1939)

[33] H. A. Jahn and E. Teller, Proc. R. Soc. London, Ser. A **161**, 220. (1937)

[34] H. Köppel, W. Domcke, and L. S. Cederbaum, Adv. Chem. Phys. **57**, 59 (1984).

[35] M. Döscher, H. Köppel, and P. Szalay, J. Chem. Phys. **117**, 2645, (2002)

[36] T. S. Venkatesan, H.-D. Meyer, H. Köppel, L. S. Cederbaum and S. Mahapatra, J. Phys. Chem. A, **111**, 1746, (2007).

[37] W. Domcke, D. R. Yarkony and H. Köppel, *Conical Intersections: Electronic Structure, Dynamics and Spectroscopy*, World Scientific: Singapore, (2004).

[38] E. Teller, J. Phys. Chem. **41**, 109 (1937); G. Herzberg, and H. C. Longuet-Higgins, Discuss. Farad. Soc. **35**, 77 (1963); T. Carrington, Discuss. Farad. Soc. **53**, 27 (1972); D. R. Yarkony, Acc. Chem. Res. **31**, 511 (1998); F. Bernardi, M. Olivucci, and M. A. Robb, Chem. Soc. Rev. **25**, 321 (1996).

[39] M. Baer and G. D. Billing, *The Role of Degenerate States in Chemistry*:Advances in Chemical Physics, Vol. 124, Wiley: Hoboken, (2002).

[40] H. Köppel, L.S. Cederbaum, and S. Mahapatra, *Theory of the JahnTeller Effect. Handbook of High-resolution Spectroscopy*, John Wiley & Sons, (2011).

[41] S. Mahapatra, Acc. Chem. Res. **42**, 1004 (2009).

[42] S. Mahapatra, Int. Rev. Phys. Chem. **23**, 483 (2004).

[43] M. Born, and R. Oppenheimer, Ann. Physik (Leipzig) **84**, 457 (1927).

[44] W. Lichten, Phys. Rev. **164**, 131 (1967); F. T. Smith, ibid. **179**, 111 (1969); T. F. O'Malley, Adv. At. Mol. Phys. **7**, 223 (1971); T. Pacher, L. S. Cederbaum, and H. Köppel, Adv. Chem. Phys. **84**, 293 (1993).

[45] H. Sekino, and R. J. Bartlett, Int. J. Quantum. Chem., Chem. Symp. **18**, 255 (1984); J. Geertsen, M. Rittby, and R. J. Bartlett, Chem. Phys. Lett. **164**, 57 (1989); J. F. Stanton, and R. J. Bartlett, J. Chem. Phys. **98**, 7029 (1993).

[46] R. D. Amos, A. Bernhardsson, A. Berning, P. Celani, D. L. Cooper, M. J. O. Deegan, A. J. Dobbyn, F. Eckert, C. Hampel, G. Hetzer, et al., MOLPRO, a package of ab initio programs designed by H. -J. Werner, P. J. Knowles, version 2008.1.

[47] G. A. Worth, M. H. Beck, A. Jäckle and H. -D. Meyer, The MCTDH Package, Version 8.2, 2000, University of Heidelberg, Germany. H. -D. Meyer, Version 8.3, 2002. Version 8.4 (2007), See http://www.pci.uni-heidelberg.de/tc/usr/mctdh/

[48] H. -D. Meyer, U. Manthe, and L. S. Cederbaum, Chem. Phys. Lett. **165**, 73 (1990).

[49] U. Manthe, H. -D. Meyer, and L. S. Cederbaum, J. Chem. Phys. **97**, 3199 (1992).

[50] H.-D. Meyer and G. A. Worth, Theor. Chem. Acc. 109, 251 (2003).

[51] T. H. Dunning, Jr., J. Chem. Phys. **90**, 1007 (1989).

[52] M. J. Frisch et al., Gaussian 03, revision B.05; Gaussian, Inc., Pittsburgh, PA, 2003.

[53] A. Almenningen, O. Bastiansen, R. Seip, M. Hans, Acta Chem. Scand. **18**, 2115 (1964).

[54] E. B. Wilson Jr., J. C. Decius and P. C. Cross, *Molecular vibrations* (McGraw-Hill, New York, 1955).

[55] G. Herzberg, *Infrared and Raman Spectra of Polyatomic Molecules, Vol.2 of Molecular Spectra and Molecular Structure* (Van Nostrand, New York, 1945) p. 183.

[56] E. B. Wilson, Jr., Phys. Rev. **45**, 706 (1934).

[57] D. Steele and D. H. Whiffen, Trans. Faraday Soc., **55**, 369 (1959)

[58] A. Bergner, M. Dolg, W. Kuechle, H. Stoll, and H. Preuss, Mol. Phys. **80**, 1431 (1993).

[59] W. Domcke, H. Köppel, and L. S. Cederbaum, Mol. Phys. **43**, 851 (1981).

[60] J. Cullum, and R. Willoughby, *Lanczos Algorithms for Large Symmetric Eigenvalue Problems* (Birkhäuser, Boston, 1985) Vols. I and II.

[61] I. B. Bersuker, *The Jahn-Teller effect*, (Cambridge University Press, Cambridge (U.K), 2006); I. B. Bersuker, Chem. Rev. **101**, 1067, (2001).

[62] J. C. Slonczewski, Phys. Rev. **131**, 1596 (1963); J. C. Slonczewski, and V. L. Moruzzi, Physics **3**, 237 (1967)

[63] P. Habitz, W. H. E. Schwarz, Theo. Chem. Acta. **28**, 267 (1973); H. Köppel, E. Haller, L. S. Cederbaum, and W. Domcke, Mol. Phys. **41**, 669 (1980)

[64] B. Milian-Medina, S. Varghese, R. Ragni, H. Boerner, E. Orti, G. M. Farinola, and J. Gierschner, J. Chem. Phys. **135**, 124509 (2011)

7 Conclusions and future directions

A detailed description of the photoinduced quantum nonadiabatic dynamics of the low lying electronic states of neutral boron B_n (where n=4, 5 and 7) clusters and carbon cluster C_{15} is presented in this thesis. The theoretical study involves construction of vibronic Hamiltonians of the electronic ground and excited states of the corresponding neutral clusters through state-of-the-art ab initio quantum chemistry calculations. Employing these Hamiltonians the nuclear dynamics is studied subsequently from first principles by solving quantum eigenvalue equation. Theoretically calculated vibronic structures of the photodetachment bands are reported and compared with the available experimental recordings. The theoretical results are generally found to be in good accord with the experiment. The main findings of the present work are given below.

B_4:

(a) The symmetric vibrational mode ν_1 and ν_2 forms progression in all the six low-lying electronic states of B_4 considered here.

(b) Peak spacing of $\sim$423 cm^{-1} corresponding to the mode ν_2 was found from the stick spectrum of $\widetilde{X}$ state of B_4. In addition the combination (ν_1+ν_2) mode also forms the $\sim$1590 cm^{-1} progression in this band.

(c) The vibrational mode ν_2 forms the major progression ($\sim$741 cm^{-1}) in the $\widetilde{a}$ state while ν_1 forms very weak excitations ($\sim$1150 cm^{-1}) in the $\widetilde{b}$ state.

(d) The vibrational mode ν_2 in the $\widetilde{A}$ and ν_1 in the $\widetilde{c}$ and $\widetilde{B}$ electronic states from dominant progressions. Peak spacings of $\sim$ 767, $\sim$ 1234 and $\sim$ 1237 cm^{-1} are found corresponding to the frequency of these modes in the mentioned electronic states, respectively.

(e) The nonadiabatic coupling effects are small in the electronic states of B_4^-. Some significant effect of this coupling is found in the $\widetilde{a}^3B_{2u}$ and $\widetilde{b}^3B_{1u}$ states of B_4 only. The excitation of non totally symmetric mode ν_6 with an energy spacing of $\sim$ 1004 cm^{-1} is estimated from the irregular spectral progression of coupled $\widetilde{b}$ electronic state.

(f) The photodetachment spectra calculated by employing reference equilibrium geometries calculated by the UB3LYP and ROMP2 methods are in excellent agreement with experiment indicating negligible effect of spin-contamination in theoretical results.

(g) The effect of $\widetilde{a}$-$\widetilde{b}$ CIs on the adiabatic electronic population of $\widetilde{b}$ electronic state when the WP prepared on $\widetilde{b}$ state is studied in detail. The initial sharp decrease of population of $\widetilde{b}$ electronic state relates to a decay rate of of $\sim$ 14 fs ($\sim$ 7 fs) in the diabatic (adiabatic) picture.

B_5:

(a) Line spacings of $\sim$ 724 and $\sim$ 658 cm^{-1} corresponding to the frequency of ν_3 and ν_4 modes, respectively, extracted from the theoretical spectrum. A vibrational progression of $\sim$ 550 cm^{-1} has been estimated from the experimental band structure of the $\widetilde{X}$ state.

(b) The progression of ν_4 vibrational mode with an energy spacings of $\sim$ 530 cm^{-1} found in theoretical stick spectrum of $\widetilde{A}$ state. An energy spacing of $\sim$ 530 cm^{-1} was reported in the experiment.

(c) Peak spacings of $\sim$1242, $\sim$901, $\sim$723 and $\sim$337 cm^{-1} corresponding to the modified frequency of ν_1, ν_2, ν_3 and ν_4 vibrational modes, respectively, in the $\widetilde{B}$ state are extracted from the stick line spectrum. The excitation of the mode ν_3 is strongest.

(d) Vibrational modes ν_1 & ν_4; ν_2; ν_1, ν_3 & ν_4 form progression in the $\widetilde{C}$, $\widetilde{D}$ and $\widetilde{E}$ states, respectively.

(e) In contrast to B_4, the nonadiabatic coupling effects are far more significant in the photodetachment bands of B_5. In addition to the totally symmetric modes, coupling vibrational modes are also excited in the vibronic bands of B_5.

(f) Nontotally symmetric vibrational modes ν_7, ν_8 and ν_9 are weakly excited in the $\widetilde{X}$ band. Weak excitation of ν_9 vibrational mode is found in $\widetilde{A}$ band.

(g) The effect of $\widetilde{A}$-$\widetilde{B}$ coupling on the structure of the $\widetilde{B}$ band is found to be the strongest. It causes a huge increase in the vibronic line density. therefore the entire $\widetilde{B}$ band is perturbed by the associated nonadiabatic coupling.

(h) The complex C band is formed by the overlapping $\widetilde{C}$, $\widetilde{D}$ and $\widetilde{E}$ electronic states of B_5.

(i) A decay rate of $\sim$12 fs of the adiabatic electronic population is obtained for both $\widetilde{B}$ and $\widetilde{E}$ electronic states.

B_7:

(a) Three isomers of B_7^- viz., a triplet hexagonal pyramidal (C_{6v}, $^3A_1$), a singlet pyramidal (C_{2v}, $^1A_1$) and a singlet planar (C_{2v}, $^1A_1$) contribute most to the recorded photodetachment band structure.

(b) The JT stabilization energies of $\widetilde{X}^2E_1$, $\widetilde{A}^4E_1$ and $\widetilde{B}^2E_1$ electronic states of isomer I of B_7 estimated to be $\sim$0.11, $\sim$0.07 and $\sim$0.06 eV, respectively. The JT activity of $\widetilde{A}^4E_1$ and $\widetilde{B}^2E_1$ electronic states is weak in comparison to that of $\widetilde{X}^2E_1$ state.

(c) The vibrational modes ν_2 and ν_{10} forms dominant progressions in $\widetilde{X}^2E_1$ state with spacings $\sim$206 and $\sim$477 cm^{-1}, respectively.

(d) Analysis of vibronic structure of the electronic states of isomer II without including the coupling with their neighbors revealed dominant excitation of the symmetric ν_5 vibrational mode in all of them except in the $\widetilde{C}$ state. Line spacings of $\sim$ 288, $\sim$ 156, $\sim$ 233, $\sim$ 290 and $\sim$ 171 cm^{-1} corresponding to the progression of ν_5 vibrational mode in the $\widetilde{X}$, $\widetilde{A}$, $\widetilde{B}$, $\widetilde{C}$ and $\widetilde{D}$ electronic states, respectively, are extracted from the spectrum of these states.

(e) Excitation of coupling modes are extracted from various coupled spectra of the the electronic states of isomer II and isomer III.

(f) Excitation of the ν_4 vibrational mode is stronger in the $\widetilde{C}$ electronic state of isomer II. Line spacings of $\sim$ 1116 and $\sim$ 350 cm^{-1} corresponding to the progressions of ν_1 and ν_4 vibrational modes, respectively, are also extracted from the spectrum of the $\widetilde{C}$ state

(g) Peak spacings of 1331 & 354, 1411 & 301, 1535 & 409, 1280 & 323 and 1337 & 440 cm^{-1} due to ν_1 & ν_6 vibrational modes are found in the vibronic structure of the $\widetilde{X'}$, $\widetilde{A'}$, $\widetilde{B'}$, $\widetilde{C'}$ and $\widetilde{D'}$ states of isomer III, respectively.

C_{15}:

(a) A detailed theoretical account of the multimode RT and PJT interactions in some selected electronic states of linear C_{15} cluster is presented here to elucidate the lifetimes of its excited electronic state $S_7\,^1\Sigma_u^+$.

(b) The RT effect in the S_5 and S_6 electronic states of C_{15} is very weak. The PJT coupling between the S_5 and S_6 dominates the RT coupling.

(c) The vibrational modes ν_2 and ν_3 forms dominant progression in both S_5 and S_6 states. Very weak fundamental transition due to the bending modes is observed in the spectrum of π_g and π_u modes.

(d) The excitation of vibrational modes ν_3, ν_4 and ν_5 with line spacings of $\sim$ 607, $\sim$ 429 and $\sim$ 288 cm^{-1}, respectively, are extracted from the theoretical spectrum of S_7 .

(e) The spectrum of $S_{12}\,^1\Sigma_g^+$ electronic state reveals progressions $\sim$286 and $\sim$816 cm^{-1} along the vibrational modes ν_6 and ν_5, respectively.

(f) The initial decay of the diabatic electronic population of S_5 , S_6 , S_7 and S_{12} states amounts to a nonradiative decay rate of $\sim$56, $\sim$25, $\sim$110, $\sim$63 fs, respectively.

HFBz:

(a) The S_2 state of HFBz is JT active, two $\pi\sigma^*$ states are energetically degenerate in this case. This is not the case for any other fluoro derivatives of Bz with number of fluorine atoms less than 6.

(b) Some of the earlier works (J. Chem. Phys. **122**, 144312 (2005) and J. Chem. Phys. **128**, 164314 (2008)) predicted that the S_1 state is of $\pi\sigma^*$ type in PFBz and HFBz. This assignment has been found to be incorrect in the present study. The S_1 state is of $\pi\pi^*$ type for all fluoro-benzene molecules. This result is also in accord with the recent findings in the literature (J. Phys. B: At. Mol. Opt. Phys. **42**, 245201 (2009)).

(c) The present assignment of the peaks in the photoabsorption spectrum of HFBz is in agreement with the experimental results of Philis *et al.* (J. Phys. B: At. Mol. Phys. **14**, 3621 (1981)) but is in contradiction with that of Temps *et al.* (J. Chem. Phys. **128**, 164314 (2008)).

(d) The structureless S_1 band of HFBz originates from energetically low-lying CIs of the S_1 and S_2 states and very strong PJT coupling among them.

(e) The bimodal shape of the second photoabsorption band originates from the orbitally degenerate JT active $^1E_{1g}$ electronic state of HFBz. The energetic location of these two peaks is in good agreement with the experimental results of Philis *et al.* . The JT coupling is strong in this electronic state which causes a bimodal shape of the absorption profile, the PJT coupling of this state with S_1 is even stronger which causes this bimodal spectral profile structureless. We note that this state is optically dark for a transition from the electronic ground state of HFBz. The absorption profile of this state seen in the experiment is due to its vibronic coupling with the optically bright S_1 state.

(f) The JT coupling in the $^1E_{1u}$ electronic state is far weaker than in the $^1E_{1g}$ state of HFBz. The $^1E_{1g}$-$^1E_{1u}$ PJT coupling is symmetry allowed and there exist vibrational modes of appropriate symmetry to cause this coupling. The symmetry invariance of $^1E_{1g}$-$^1E_{1u}$ coupling matrix is studied and the relative phases of the coupling elements are derived. However, thorough analysis of the electronic structure data reveal negligible coupling among these degenerate electronic states.

(g) The third and forth absorption bands of HFBz are formed by three $\pi\pi^*$ type of orbitals of $^1B_{1u}$, $^1E_{1u}$ and $^1A_{2u}$ symmetry. Unlike in case of Bz, the signature of the $^1A_{2u}$ state is clearly seen in the absorption spectrum of HFBz. This state appears at $\sim$ 7.7 eV in the experimental spectrum and is in good accord with our theoretical results.

(h) Nonradiative decay rate of $\sim$ 153 fs and $\sim$ 22 fs is found for the S_1 and S_2 state, respectively. Electronic population transfer occurs to the S_1 state via S_3-S_2 and S_3-S_1 CIs when the S_3 state is initially populated. Likewise, nonradiative electron population transfer occurs to the S_3, S_5 and S_3, S_4 states when the S_4 and S_5 states are initially populated, respectively. These nonradiative transfer of electron populations relate to decay rate of $\sim$ 67, 28 and 110 fs, respectively, of the S_3, S_4 and S_5 electronic states of HFBz.

In conclusion, the effect of nonadiabatic interactions on the photoinduced processes of (boron and carbon) clusters and HFBz molecule is examined by establishing model diabatic Hamiltonians. First principles nuclear dynamical simulations are carried out both within the time-independent and time-dependent frameworks. The present study clearly indicates the importance of electronic nonadiabatic interactions in the broad and diffuse nature of the observed vibronic bands, ultrafast nonradiative decay of electronically excited states of boron and carbon clusters. The fluorescence quenching of the excited electronic states of HFBz is also a signature of the vibronic interactions. The chemical impact of increasing fluorine substitution on the electronic structure and nuclear dynamics of HFBz is established.

To this end the we mention that the present work is restricted to the VC of electronic states with same spin multiplicities (e.g., singlet-singlet or triplet-triplet VC). This study can be further extended to the systematic investigation of VC for electronic states of different spin multiplicities (e.g., singlet-triplet VC). An initiative in this direction is taken by us and is presented in Chapter 3. The selection rules for static and dynamics

spin-orbit coupling are derived. Another possible extension of this work is the inclusion of rotational degrees of freedom in the present model VC Hamiltonian to obtain information on rovibronic levels of isolated molecules.

The photophysics study of C_{15} in Chapter 5 is carried out by considering $S_5{}^1\Pi_g$, $S_6{}^1\Pi_u$, $S_7{}^1\Sigma_u^+$ and $S_{12}{}^1\Sigma_g^+$ electronic states only. For an ideal description of the photophysics all the relevant low-lying excited states have to be included in the nuclear dynamics. This study can further be extended to the investigation of photo-physics of the low-lying excited states of carbon chains with carbon atoms 17, 19 and 21. While the nuclear dynamics of $S_7{}^1\Sigma_u^+$ electronic state is more sought in C_{15}, in C_{17}, C_{19} and C_{21} clusters the nuclear dynamics of $S_5{}^1\Sigma_u^+$ electronic state is more important. Further more, this problem can be extended to design a suitable laser pulse to control the diabatic electronic population decay of ${}^1\Sigma_u^+$ electronic state using optimal control theory.

List of publications

[1] S. Rajagopala Reddy and S. Mahapatra, '*Theoretical study of photodetachment processes of anionic boron clusters. I. Structure*', J. Chem. Phys. 136, 024322 (2012).

[2] S. Rajagopala Reddy and S. Mahapatra, '*Theoretical study of photodetachment processes of anionic boron clusters. II. Nuclear dynamics*', J. Chem. Phys. 136, 024323 (2012).

[3] S. Rajagopala Reddy and S. Mahapatra, '*A theoretical account of the photodetachment spectroscopy of anionic boron clusters*', S. M. C. Bulletin, **4**, 5, (2013).

[4] S. Rajagopala Reddy and S. Mahapatra, '*Theoretical study of photodetachment processes of anionic boron clusters. III.* B_7^-', (manuscript submitted).

[5] T. Mondal, S. Rajagopala Reddy and S. Mahapatra, '*Photophysics of fluorinated benzene. III. Hexafluorobenzene*', J. Chem. Phys. 137, 054311 (2012).

[6] S. Rajagopala Reddy and S. Mahapatra, '*Photophysics of carbon chain* C_{15}', (manuscript under preparation).

[7] S. Rajagopala Reddy, S. Mahapatra and G. N. Patwari, '*On the fluoroscence behaviour of phenylacetylene and methyl amine complexes*', (manuscript under preparation).

[8] R. Sarkar, S. Rajagopala Reddy and S. Mahapatra '*Nonadiabatic interactions in* CH_3F *radical cation*', (manuscript under preparation).

Posters presented in conferences/Symposia

[1] Poster presented in Discussion meeting on spectroscopy and dynamics of molecules and clusters held during 18th-21st, February, 2010 at The International Centre, Goa.

[2] Poster presented in Theoretical Chemistry Symposium 2010 held during 08th-12th, December, 2010 at IIT Kanpur, India

[3] Poster presented in Applies theory on molecular systems held during 02nd-05th November 2011 at IICT Hyderabad, India

[4] Poster presented in Electronic structure and Dynamics of Molecules and Clusters held during 17th-20th February 2013 at IACS, Kolkata, India

[5] Poster presented in Chemfest 2010, 2011 and 2012 an in-house symposium held at School of Chemistry, University of Hyderabad, India.